

**Mixed Oxidant Corrosion in
Nonequilibrium Syngas at 540°C**

**Corrosie van roestvast staal in
"nonequilibrium" syngas op 540°C
(met een samenvatting in het nederlands)**

PROEFSCHRIFT

ter verkrijging van de graad van doctor aan de Technische Universiteit te Delft,
op gezag van de Rector Magnificus, Prof. ir. K.F. Wakker
In het openbaar te verdedigen ten overstaan van een commissie,
aangewezen door het College van Dekanen op 8 mei, 1995 te 1600 uur

door
Wate Thewis BAKKER
mijnbouwkundig ingenieur
geboren te Stiens

Wate Thewis Bakker

Dit proefschrift is goedgekeurd door de promotor Prof. dr. J.H.W. de Wit

The research reported in this thesis has been carried out as part of EPRI's exploratory research program on materials technology for use by electric utilities, under contract RP 8041-01 with Lockheed Missile and Space Co., Inc., Palo Alto, CA.

ABSTRACT

High temperature metal alloys in gasifiers are mostly used in heat exchangers for cooling hot syngas, consisting mainly of CO and H₂ with smaller amounts of H₂O and CO₂ and minor quantities of H₂S and HCl. Metal temperatures range from 250 to 600°C, gas temperatures from 250 to 1200°C. Because of rapid cooling the composition of the gas does not follow, resulting in a non equilibrium situation at the metal surface. Calculations show that such gases have lower oxygen and sulfur pressures than equilibrated gases at the same temperature. This makes the results of previous laboratory studies less appropriate for predicting mixed oxidant corrosion in gasifiers. For this reason the present study was carried out using non equilibrium gas mixtures, similar to syngases, produced in entrained slagging gasifiers. Most corrosion experiments were carried out at 540°C as this is a common temperature for superheaters and hot gas cleanup systems. Corrosion test duration ranged from 1.5 to 1350 hours. Iron based model alloys containing 35% Ni, 20% Cr and various minor alloying additions were studied.

Three different corrosion regimes were identified over the range of conditions studied, depending on the sulfur to oxygen pressure ratio of the gas and the alloy composition. At very low PS₂/PO₂ ratios a somewhat protective FeCr₂S₄ scale is formed, leading to near parabolic corrosion rates, with Kp's ranging from 1 to 17 (μm)²/hr. At higher PS₂/PO₂ ratios nonprotective Fe(Ni,Cr)S external scales are formed. These allow rapid internal oxidation of the chromium in the alloy. This results in high corrosion rates. Under the same conditions very low subparabolic corrosion rates are obtained, when strong oxide formers are added to the alloy, most likely because of the presence of a dense layer of oxide precipitates in the alloy surface. Thus the same corrosion model is operative in all 3 corrosion regimes: external sulfidation of iron and nickel, together with internal oxidation of chromium and other strong oxide formers.

EXECUTIVE SUMMARY

INTRODUCTION

It is generally expected that the world will use fossil fuels as its main source of energy for at least 50 years. Coal will be the dominant fuel, despite significant growth in renewable energy and nuclear power. Present large scale electric power generation from coal requires removal of pollutants after combustion. This is costly and can only remove 90-95% of major pollutants such as NO_x and SO_x . Coal gasification provides a means to clean coal prior to combustion. Thus 99+% of all major pollutants can be removed at reasonable cost. Coal gasification power plants are also more efficient than conventional power plants. Therefore it is expected that coal gasification will become the preferred way to produce electricity in the 20th century. Most coal gasifiers will require metal heat exchangers to remove sensible heat from the raw syngas. Expected metal temperatures are 300 to 600°C, while the surrounding gas temperature will range from 400 to 1100°C. The syngas consists mainly of CO and H_2 , with smaller amounts of CO_2 and H_2O and minor quantities of H_2S and HCl. The heat exchanger alloys will therefore be exposed to simultaneous corrosion by sulfur, oxygen and chlorine bearing species. It is the purpose of this study to examine mixed oxidant corrosion in non equilibrium gases closely resembling those in commercial gasifiers.

EXPERIMENTAL APPROACH

The composition of syngas depends on the coal and the coal gasification process. The H_2S and HCl contents of the gas depend mainly on the sulfur and chlorine content of the coal. Thus 0.2 and 0.8% H_2S were selected to represent gas derived from low and high sulfur coal respectively. HCl was not a variable in this study, 400 ppmv was added to all gas mixtures. This represents a coal with a chlorine content in the 0.1 to 0.15% range. The CO, CO_2 , H_2 and H_2O content of syngas depend mainly on the coal gasification process. Dry coal fed slagging gasifiers produce syngas with low CO_2 and H_2O contents, while gas produced in coal-water slurry fed gasifiers contains about 10% CO_2 and 13-23% H_2O . Therefore gas mixtures with variable CO/ CO_2 and H_2 / H_2O ratios were selected in the range shown above.

Oxygen and sulfur pressures of the gases were calculated using a procedure modified by Perkins for non equilibrium gases. Figure S-1 shows the oxygen pressure of syngas as a function of water content. Since the hydrogen content of the gases did not vary much with oxygen pressure, the sulfur pressure was only dependent on the H₂S content.

An austenitic alloy (A) containing 20% Cr, 35% Ni, 1% Mn, 0.3% Si, bal. Fe was selected as the base alloy for this study. Other alloys, containing 3% additions of V, Ti, Si and Al, were included to study the effect of sulfide and oxide forming elements. (Alloys B, C, D and E)

12.5 × 9 × 2.5 mm samples of the alloys were exposed to syngas, flowing at 1000 cc/min. at 540°C for 1.5 to 1350 hours. The high gas flow rate is needed to prevent shifts in gas composition. After exposure scale thickness and metal loss is determined. The highest of the two measurements is considered the corrosion loss. The major analytical tool to determine corrosion mechanisms was scanning electron microscopy with energy dispersive X-ray spectroscopy, capable of quantitatively determining all elements except carbon, which was rarely present. In addition optical microscopy, X-ray diffraction and Auger spectroscopy were used.

RESULTS

Figure S-2 shows the corrosion loss of various alloys as a function of the steam content of the gas, at a constant sulfur pressure ($\text{Log } P_{\text{S}_2} = -9.3$). The base alloy (A) and alloys containing vanadium (B) or titanium (C) show maximum corrosion losses when the syngas contains 3% water. At this point the $\text{Log } P_{\text{S}_2}/P_{\text{O}_2} = 18$. Alloys containing Si or Al (D & E) experience a moderately high corrosion loss when the steam content is less than 2%. The corrosion loss becomes insignificant when the steam content of the gas is 2% or higher. At this point the $\text{Log } P_{\text{S}_2}/P_{\text{O}_2}$ is 18.5. Changes in the sulfur pressure of the gas or changes in the type of oxidant used (CO₂ instead H₂O) do not change the overall corrosion behavior of the alloy, when plotted as a function of the $P_{\text{S}_2}/P_{\text{O}_2}$ ratio. However the scatter in the data increases considerably. This indicates that corrosion rates are not only a function of the oxygen and sulfur pressure of the gas, but also depend on the type of oxygen species present as well as the H₂S partial pressure.

The corrosion behavior, described above, can be rationalized by the following model: When exposed to syngas all alloys form porous outward growing ("epitactical") iron-nickel sulfide scales, which also may contain minor amounts of chromium. At high $P_{\text{S}_2}/P_{\text{O}_2}$ ratios, where Cr_xS_y is a stable phase, a dense layer of Fe Cr₂S₄ is formed at the scale/metal interface. When the $P_{\text{S}_2}/P_{\text{O}_2}$ ratio is lowered this layer becomes progressively thinner and incorporates a considerable amount of oxygen. Below the external sulfide scale, internal oxidation of chromium occurs in the alloy surface. Some Cr_xS_y may also form at high $P_{\text{S}_2}/P_{\text{O}_2}$ ratios. This results in an inward growing ("topotactical") scale formed by coalescence of oxide precipitates and intergranular

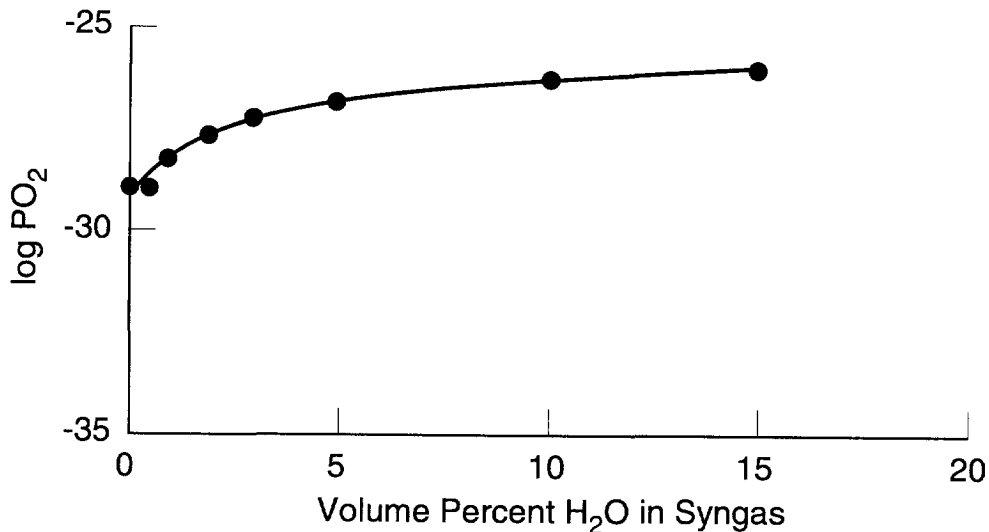


Figure S-1
Nonequilibrium Oxygen Pressure of Syngas as a Function of Steam Content at 550°C

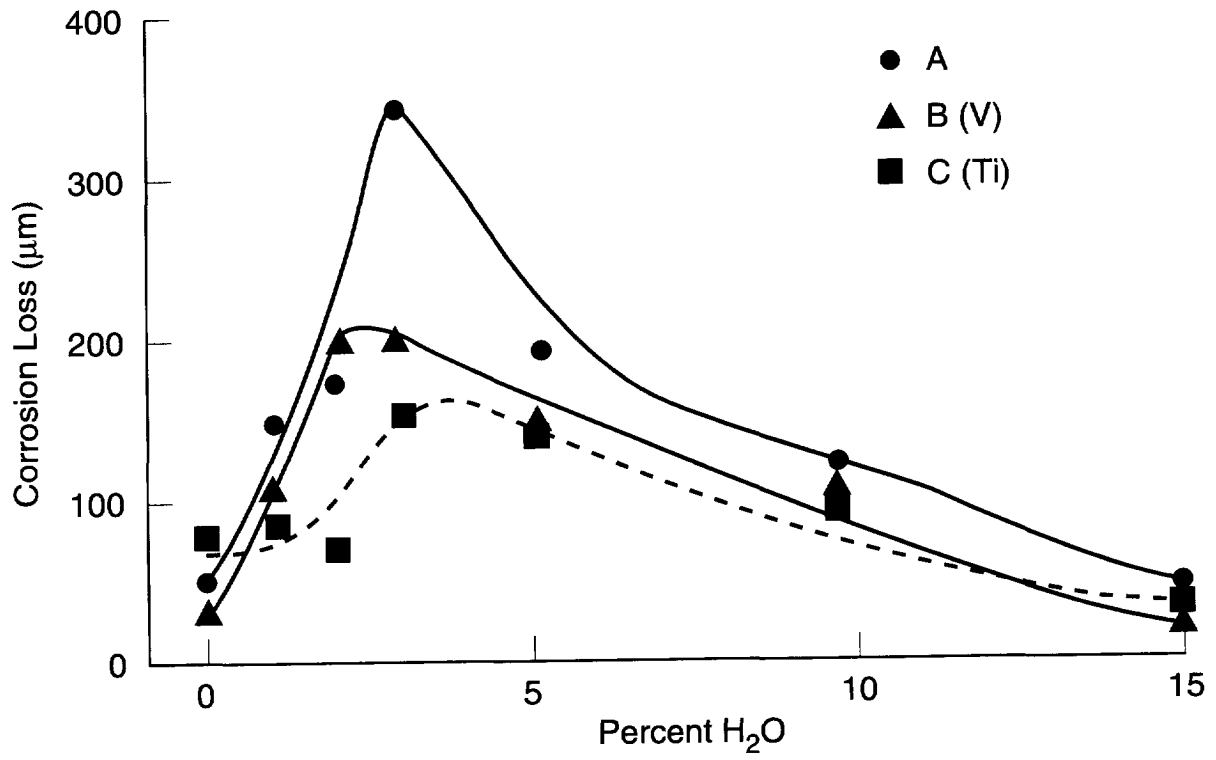
corrosion products. This scale may contain a considerable amount of unconverted metal, mainly iron. This corrosion model leads to 3 distinct corrosion regimes, depending on gas and alloy composition. These are labeled type A, B and C corrosion and are shown schematically in Figure S-3.

Type A corrosion occurs in all alloys at high PS_2/PO_2 ratios. Here the $Fe Cr_2S_4$ subscale is somewhat protective. This results in relatively low near parabolic corrosion rates, with K_p 's ranging from 1-17 $(\mu m)^2/hr$. Calculated corrosion rates range from 0.1-0.4 mm/yr.

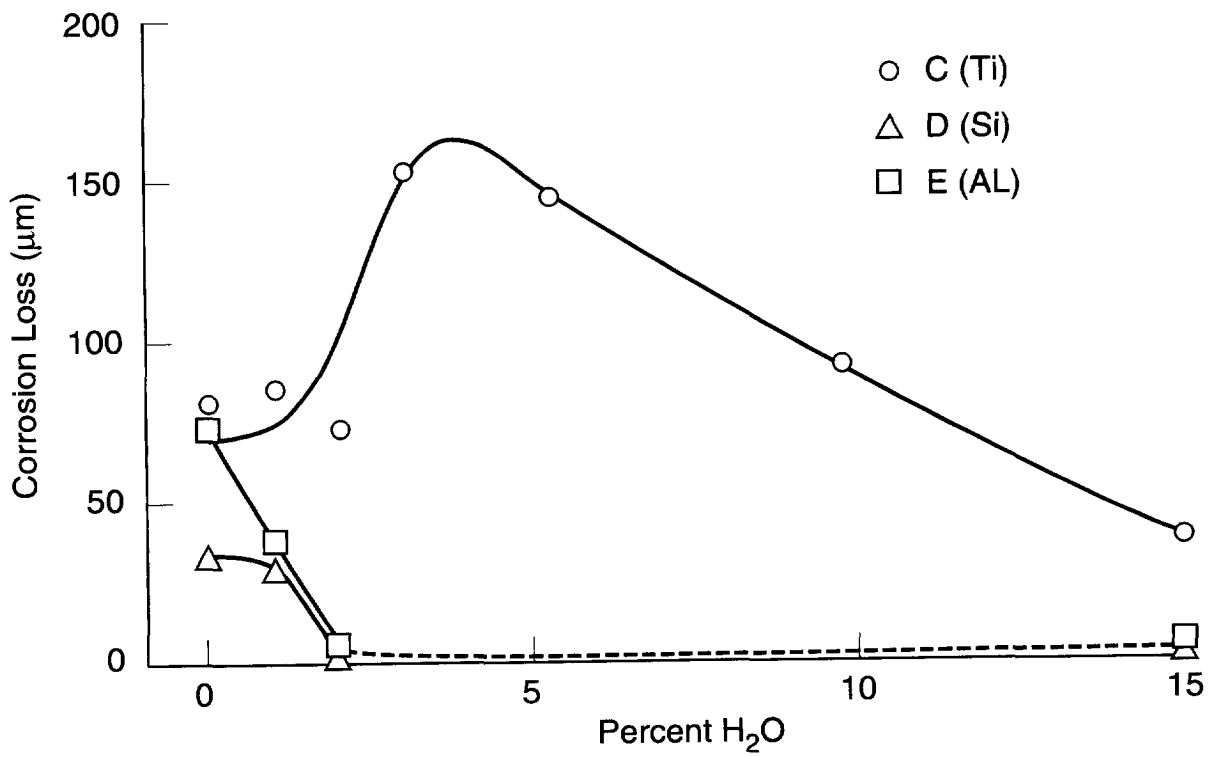
Type B corrosion occurs in alloys A, B and C in gases with PS_2/PO_2 ratios, where Cr_2O_3 becomes the stable phase and $Fe Cr_2S_4$ does not form. This results in rapid internal oxidation of chromium, concurrent with outward diffusion of Fe and Ni, which form sulfides at the outer scale/gas interface. The resulting Cr_2O_3 rich inner scale containing 5-15% FeS is porous and non protective. Corrosion losses as high as 0.3 mm/600 hrs have been observed. Such scales spall frequently and give rise to pseudolinear corrosion rates.

Type C corrosion occurs in alloys D and E containing additions of strong oxide formers. Simultaneous precipitation of SiO_2 or Al_2O_3 and Cr_2O_3 in the alloy surface below a porous external (Fe, Ni) S scale, leads to a very dense precipitation zone, which largely inhibits outward diffusion of Fe and Ni and inward diffusion of oxidant. Thus very low corrosion rates are observed. Corrosion kinetics are probably subparabolic and lead to corrosion rates less than 0.1 mm/yr.

Further decreases in PS_2/PO_2 ratio do not affect type C corrosion. Type B corrosion losses gradually decrease and become variable. This frequently leads to a pitting type of

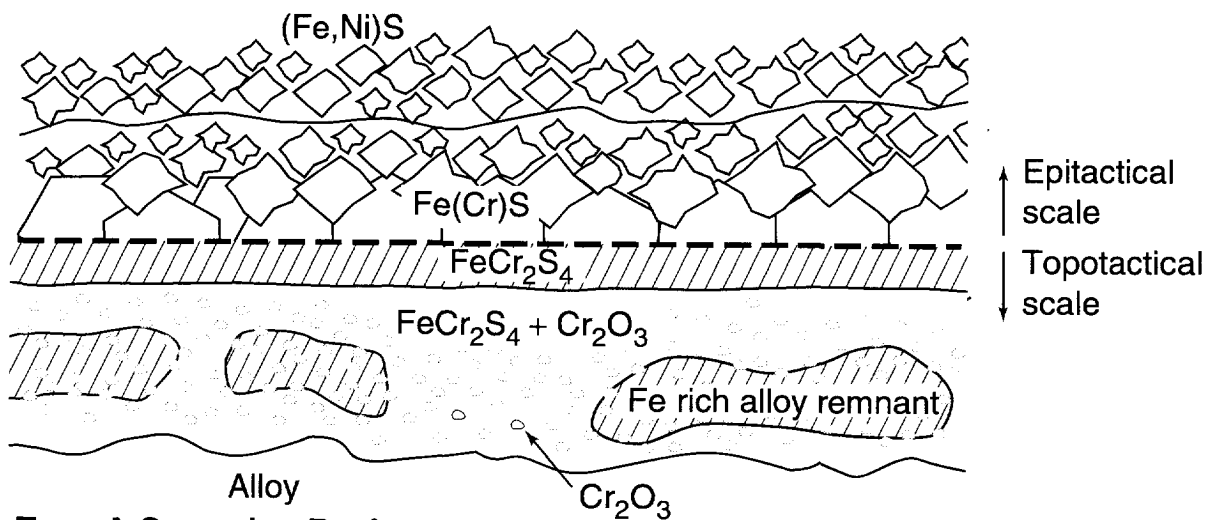


(a)

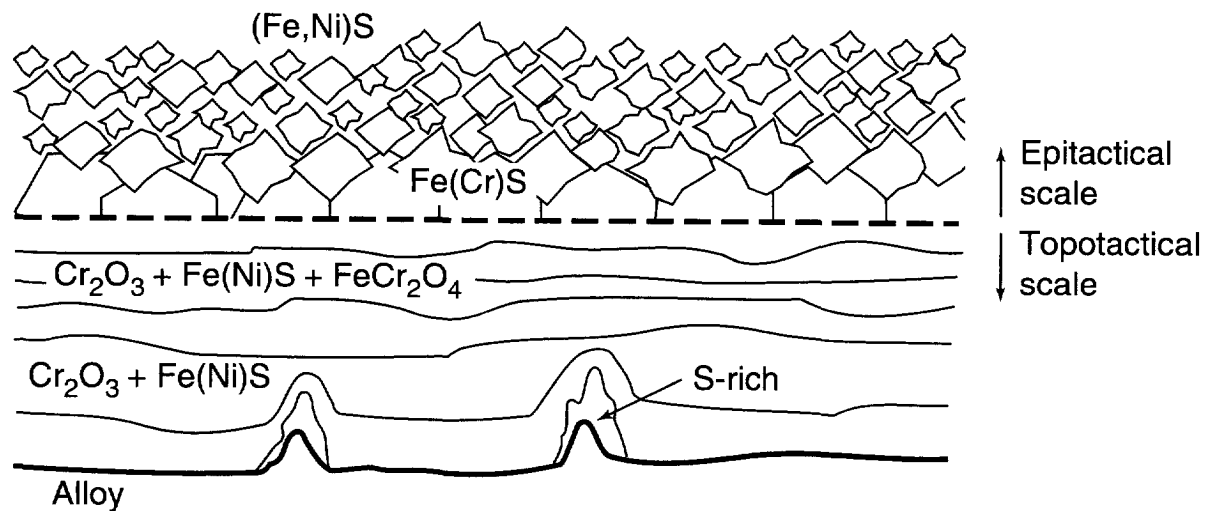


(b)

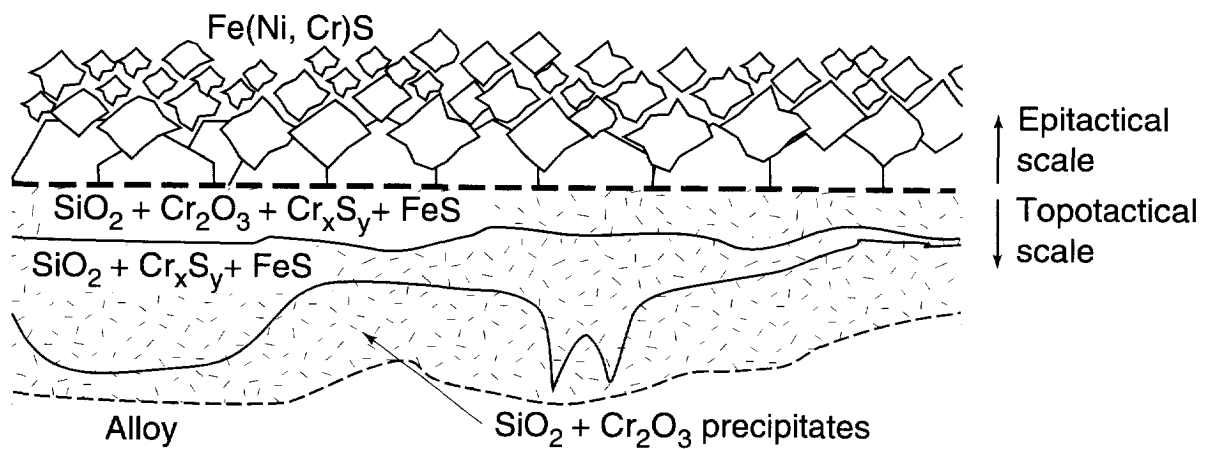
Figure S-2
Corrosion As a Function of H₂O Content of Syngas (0.8% H₂S)



Type A Corrosion Regime



Type B Corrosion Regime



Type C Corrosion Regime

Figure S-3
Schematic of Scale Morphology and Composition

corrosion attack, probably caused by the local formation of a protective Cr_2O_3 layer at the scale/metal interface. Data from a concurrent study indicate that the presence of 400 ppmv HCl in the gases used in this study increased the corrosion losses considerably, especially in the Type B regime. It is speculated that the presence of HCl facilitates the outward transportation of Fe and Ni as chlorides. It may also increase the porosity of the Cr_2O_3 rich inward growing scale formed by the coalescence of Cr_2O_3 precipitates

The corrosion model described above is similar to that of the oxidation of dilute austenitic Ni-Cr and Ni-Co alloys, investigated previously by Wood, et al.⁶⁷⁻⁶⁹ and Kofstad, et al.⁶⁶. When the chromium content of such alloys falls below a critical level, usually in the 20% Cr range, protective external Cr_2O_3 scales cannot form, but internal oxidation will occur instead, according to Wagner's classical theory⁷². However Cr_2O_3 precipitates in the alloy surface as well as precipitates converted to spinels in the inner scale, substantially reduce corrosion rates in dilute alloys with moderate Cr contents in the 12-20% range. Work by Perkins, et al.^{73,74} has shown that protective external scale growth may change to non protective internal oxidation at lower temperatures. Thus internal oxidation of Cr, Si and Al appears feasible at the low temperatures used in this study. Unfortunately applicable solubility and diffusion data of the various species involved are not available for a mathematical treatment.

The corrosion model developed in this study is able to explain most mixed oxidant corrosion features, observed on alloys after service in gasifiers, which could not be explained by the "kinetic boundary" model, presently, widely used to describe mixed oxidant corrosion at higher temperatures. Examples are the rapid corrosion of the 20% Cr-Ni INCO 82 weld metal, which is clearly Type B corrosion, the presence of partially converted inward growing scales on type 310 stainless steel and pitting attack of alloy 800 in gasifier environments with high steam contents.

ACKNOWLEDGMENTS

This thesis is the result of the cooperation of many people in different organizations, which enabled me to complete this study, while carrying out my regular duties as Manager of High Temperature Materials Technology in the Strategic Development group at EPRI.

First of all I want to thank Roger Perkins for introducing me to the arcane world of high temperature oxidation and corrosion many years ago and for being my mentor ever since.

Secondly I like to thank John Stringer at EPRI for encouraging me to personally do some research instead of managing it, and for providing funds to carry out the experimental work at the Lockheed Space and Missile Laboratory.

I like to especially thank Jane Bonvallet and her associates at Lockheed, A. Heynen, Len Ioste, Arles Parrish, Joe Cullinan and several others for carrying out most of the experimental work. Without their devotion and attention to detail I would not have succeeded.

The invaluable help of Ilene Fish of MacPublish and EPRI's publications and visual communications group in preparing a fully electronic manuscript is hereby gratefully acknowledged.

I like to thank several colleagues in the high temperature corrosion field for thoughtful discussions, especially Ian Wright at ORNL, Jim Norton, Tana Levi, Kathleen Stein and Victor Guttman at JRC, Petten, and Jerry Meier at the Pittsburgh University. Wally Huybregts and his colleagues at KEMA provided the colorful "Dicom" cover photograph.

Finally I like to thank my promotor, Professor Hans de Wit, for taking on an over age graduate student, and for his thoughtful guidance and discussions during my visits to Delft.

CONTENTS

Section	Page
1	Introduction 1-1
2	Technology Background 2-1
	2.1 Gasification Technology 2-1
	2.1.1 Process Development 2-1
	2.1.2 Materials Experience 2-7
	2.2 Laboratory Corrosion Studies 2-12
3	Research Objectives 3-1
4	Experimental Procedures and Concepts 4-1
	4.1 Gas Composition Analysis and Selection 4-1
	4.2 Alloy Selection and Preparation 4-9
	4.2.1 Alloy Selection 4-9
	4.2.2 Alloy Preparation 4-12
	4.3 Corrosion Test Procedures 4-13
	4.3.1 Corrosion Test Furnace Description and Test Procedures 4-13
	4.3.2 Gas Flow Control 4-15
	4.3.3 Water Addition Procedure and Control 4-17
	4.4 Analytical Procedures 4-20
	4.4.1 Sample Preparation and Optical Microscopy 4-20
	4.4.2 SEM/EDS/WDS Analysis 4-24
	4.4.3 X-Ray Diffraction 4-30
5	Results 5-1
	5.1 Corrosion Kinetics in Water Free Gas Mixtures 5-1
	5.2 Effect of Oxygen Pressure on Corrosion 5-8
	5.2.1 Corrosion as a Function of Steam Content of Syngas 5-9
	5.2.2 Corrosion as a Function of the CO ₂ /CO Ratio of the Gas 5-11

5.2.3	Corrosion in Gases Containing 0.2% H ₂ S	5-13
5.3	Scale Analysis.....	5-13
5.3.1	General Description of Typical Scale	5-16
5.3.2	Effect of Exposure Time on Scale Development.....	5-16
5.3.3	Effect of Variation in Steam Content on Scale Development, 600 hr Exposure; 0.8% H ₂ S, 540°C	5-39
5.3.4	Effect of Changes in the CO/CO ₂ Ratio in Steam Free Gases.....	5-59
5.3.5	Effect of H ₂ S Content in Syngas.....	5-68
6	Interpretation and Discussion	6-1
6.1	Identification of Corrosion Mechanisms.....	6-1
6.1.1	Corrosion as a Function of PS ₂ and PO ₂	6-1
6.1.2	Scale Growth and Corrosion Mechanisms for Base Alloy A.....	6-4
6.1.3	Effect of Minor Alloying Additions.....	6-10
6.1.4	Corrosion Kinetics	6-14
6.2	Comparison With Previous Work.....	6-16
6.2.1	Laboratory Studies	6-16
6.2.2	Plant Experience	6-25
6.3	Unified Corrosion Model.....	6-28
7	Conclusions.....	7-1
8	References	8-1
9	Samenvatting	9-1
10	Curriculum Vitae.....	10-1

LIST OF FIGURES

Figure	Page
1-1 Evolution of World Energy Utilization.....	1-2
1-2 Global Energy Resources.....	1-2
1-3 Efficiency Improvements of Coal Fired Plants.....	1-3
2-1 Schematic of Integrated Gasification Combined Cycle (I.G.C.C.) Power Plant.....	2-4
2-2 Schematic of Advanced I.G.C.C. Plant.....	2-4
2-3 Temperature Distribution of Uncooled Corrosion Coupons, Nominally Operating at 570°C.....	2-9
2-4 Corrosion of Low Alloy Steels in Syngas Coolers of Coal-Water Slurry Fed Gasifiers.....	2-11
2-5 Stability Diagram for the Cr-S-O System at 849°K (621°C).....	2-13
2-6 Kinetic Boundaries for Some Alloys.....	2-15
4-1 Equilibrium Constants of CO ₂ /CO and H ₂ O/H ₂ Reactions.....	4-4
4-2 Equilibrium and Nonequilibrium Oxygen Pressures of Syngas	
a. Dry Syngas.....	4-5
b. Wet Syngas.....	4-5
4-3 Equilibrium Constants of H ₂ S/H ₂ Reaction.....	4-6
4-4 Equilibrium and Nonequilibrium Sulfur Pressure of Syngas.....	4-7

4-5	Nonequilibrium Oxygen Pressure of Syngas as a Function of Steam Content at 550°C.....	4-7
4-6	Cr-O-S Phase Diagram at 550°C	4-8
4-7	Condensed Phase Equilibria for the V-O-S System at 550°C (823°K).....	4-10
4-8	Condensed Phase Equilibria for the Ti-O-S System at 550°C (823°K)	4-10
4-9	Modified Schaeffler Diagram	4-11
4-10	Microstructure of Experimental Alloys.....	4-14
4-11	Schematic of Corrosion Test Furnace.....	4-15
4-12	Gas Control and Flow Diagram.....	4-16
4-13	Schematic of Water Addition System.....	4-17
4-14	Steam Addition vs. Temperature at Hydrogen Flow Rate of 210 cc/min. Total Gas Flow 1000 cc/min.....	4-20
4-15	Schematic Diagram of Sample in Metallographic Mount.....	4-21
4-16	Measurement of Remaining Sound Metal.....	4-22
4-17	Measurement of Thickness of Topotactical Scale on Alloy A.....	4-23
4-18	Phase Stability Fields of Cr, Fe and Ni at 622°C	4-27
4-19	EDS Spectrum for V ₂ O ₅ Near K Line of Oxygen, Showing Oxygen K Lines and Vanadium L Lines.....	4-29
4-20	EDS Spectrum for Cr, Fe, Ni, O, S Scale Near K Line of Oxygen, Showing Oxygen K Lines and L Lines of Cr, Fe Mn and Ni	4-29
4-21	XRD Analysis of Scale on Sample 92.1282, Scale Thickness 7–12µm	4-33
4-22	XRD Analysis of Scale on Sample 91.0722 Scale Thickness 30–40µm	4-34
4-23	XRD Analysis of 50Cr–50Ti Mixture After 15 hr Exposure to Gas 1	4-35
4-24	XRD Analysis of 50Cr–50V Mixture After 15 hr Exposure to Gas 1.....	4-35

4-25	Granular Ti-Cr and V-Cr Mixtures After 15 hr Exposure to Gas 1, 0% H ₂ O	
	a. 50 Ti - 50 Cr.....	4-36
	b. 50V - 50 Cr	4-36
5-1	Accelerated Sulfidation of Low Alloy Steel by Thermal Cycling.....	5-2
	a. Proposed model.....	5-2
	b. Experimental Verification of Model	5-2
5-2A	Corrosion Loss as a Function of Time	5-4
5-2B	Corrosion Loss as a Function of Time, Log-Log Plot	5-5
5-3	Corrosion loss as a Function of \sqrt{T}	5-7
5-4	Corrosion as a Function of H ₂ O Content of Syngas (0.8% H ₂ S)	5-10
5-5	Corrosion as a Function of CO ₂ /CO Ratio of Syngas (0.8% H ₂ S, 0% H ₂ O).....	5-12
5-6	Corrosion as a Function of H ₂ O Content in Syngas (0.2% H ₂ S).....	5-14
5-7	Optical Photomicrograph of Scale on Alloy A, 1350 hr Exposure, Gas 1A	5-17
5-8	Back Scattered Electron (BSE) Image of Scale on Alloy A, 15 hr Exposure, Gas 1, 540°C	5-18
5-9	BSE Image of Scale on Alloy A, 150 hr Exposure, Gas 1, 540°C	5-19
5-10	Photomicrographs of Scale on Alloy A, 600 hr Exposure, Gas 1, 540°C	
	a. Optical Photomicrograph.....	5-21
	b. BSE Image of Topotactical Scale	5-21
5-11	BSE Image of Scale on Alloy A, 1224 hr Exposure, Gas 1, 540°C	5-22
5-12	BSE Image of Scale on Alloy B, 15 hr Exposure, Gas 1, 540°C	5-24
5-13	BSE Image of Scale on Alloy B, 600 hr Exposure, Gas 1, 540°C	5-24
5-14	Photomicrographs of Scale on Alloy B, 1224 hr Exposure, Gas 1, 540°C	
	a. BSE Image.....	5-25
	b. Elemental Maps	5-25

5-15	BSE Image of Scale on Alloy C, 15 hr Exposure, Gas 1, 540°C	5-27
5-16	BSE Image of Scale on Alloy C, 150 hr Exposure, Gas 1, 540°C.....	5-27
5-17	BSE Image of Scale on Alloy C, 600 hr Exposure, Gas 1, 540°C.....	5-29
5-18	BSE Image of Scale on Alloy C, 1224 hr Exposure, Gas 1, 540°C.....	5-29
5-19	BSE Image of Corroded Surface on Alloy D, 1.5 hr Exposure, Gas 1, 540°C	5-30
5-20a	BSE Image of Scale on Alloy D, 15 hr Exposure, Gas 1, 540°C	5-31
5-20b	Elemental Maps of Scale on Alloy D, 15 hr Exposure, Gas 1, 540°C	
	a. BSE Image of Scale	5-32
	b. Elemental Maps	5-32
5-21	BSE Image of Scale on Alloy D, 600 hr Exposure, Gas 1, 540°C.....	5-33
5-22	BSE Image of Scale on Alloy E, 15 hr Exposure, Gas 1, 540°C	5-34
5-23	BSE Image of Scale on Alloy E, 600 hr Exposure, Gas 1, 540°C.....	5-35
5-24	BSE Image of Scale on Alloy A, 15 hr Exposure, Gas 4, 540°C	5-37
5-25	BSE Image of Scale on Alloy B, 15 hr Exposure, Gas 4, 540°C	5-37
5-26	BSE Image of Scale on Alloy C, 15 hr Exposure, Gas 4, 540°C.....	5-38
5-27	BSE Image of Scale on Alloy D, 15 hr Exposure, Gas 4, 540°C.....	5-39
5-28	BSE Image of Scale on Alloy A, 600 hr Exposure, Gas 2, 540°C	5-40
5-29a	Photomicrographs of Scale on Alloy A, 600 hr Exposure, Gas 4, 540°C Optical Photomicrograph	5-41
5-29b	Photomicrographs of Scale on Alloy A, 600 hr Exposure, Gas 4, 540°C BSE Image	5-42
5-30	BSE Image of Scale on Alloy A, 600 hr Exposure, Gas 6, 540°C	5-43
5-31	BSE Image of Scale on Alloy A, 600 hr Exposure, Gas 7, 540°C	5-44

5-32	BSE Image of Scale on Alloy B, 600 hr Exposure, Gas 2, 540°C	5-45
5-33	Elemental Maps of Scale on Alloy B, 600 hr Exposure, Gas 2, 540°C.....	5-46
	a. BSE Image of Scale	5-46
	b. Elemental Maps	5-46
5-34	BSE Image of Scale on Alloy B, 600 hr Exposure, Gas 4, 540°C	5-48
5-35	BSE Image of Scale on Alloy B, 600 hr Exposure, Gas 6, 540°C	5-48
5-36	BSE Image of Scale on Alloy B, 600 hr Exposure, Gas 7, 540°C	5-49
5-37	BSE Image of Scale on Alloy C, 600 hr Exposure, Gas 2, 540°C	5-50
5-38	BSE Image of Scale on Alloy C, 600 hr Exposure, Gas 7, 540°C	5-51
5-39	Photomicrographs of Scale on Alloy D, 600 hr Exposure, Gas 2, 540°C	
	a. BSE Image.....	5-52
	b. Elemental Maps	5-52
5-40	BSE Image of Scale on Alloy D, 600 hr Exposure, Gas 3, 540°C.....	5-54
5-41	Line Scans by Auger Spectroscopy Across Scale-Metal Interface of Alloy D After 600 hr Exposure to Gas 3 at 540°C	5-55
5-42	Photomicrographs of Scale on Alloy D, 600 hr Exposure, Gas 7, 540°C.....	5-56
5-43	BSE Image of Scale and Alloy Surface on Alloy D, 600 hr Exposure, Gas 7, 540°C	5-57
5-44	BSE Image of Scale on Alloy E, 600 hr Exposure, Gas 2, 540°C	5-58
5-45	BSE Image of Scale on Alloy E, 600 hr Exposure, Gas 3, 540°C	5-59
5-46	Photomicrographs of Scale on Alloy E, 600 hr Exposure, Gas 7, 540°C	
	a. BSE Image.....	5-60
	b. Elemental Maps	5-60
5-47	Photomicrographs of Scale on Alloy A, 600 hr Exposure, Gas 0, 540°C	
	a. BSE Image of Topotactical Scale	5-62
	b. Optical Photomicrograph.....	5-62
5-48	BSE Image of Scale on Alloy B, 600 hr Exposure, Gas 0, 540°C	5-63

5-49	BSE Image of Scale on Alloy C, 600 hr Exposure, Gas 0, 540°C.....	5-63
5-50	BSE Image of Scale on Alloy D, 600 hr Exposure, Gas 0, 540°C.....	5-64
5-51	BSE Image of Scale on Alloy C	
	a. 600 hr, Gas 5, 540°C (5% H ₂ O)	5-66
	b. 600 hr, Gas 9, 540°C (CO ₂ /CO=0.64).....	5-66
5-52	BSE Image of Scales on Alloys A and C, 600 hr Exposure, Gas 8, 540°C	
	a. Alloy A.....	5-67
	b. Alloy C	5-67
5-53	Photomicrographs of Scale on Alloy A, 600 hr Exposure, Gas 1A, 540°C	
	a. BSE Image of Scale	5-69
	b. Elemental Maps	5-69
5-54	BSE Image of Scale on Alloy A, 1350 hr Exposure, Gas 1A, 540°C	5-70
5-55	BSE Image of Scale on Alloy A, 600 hr Exposure, Gas 2A, 540°C.....	5-71
5-56	BSE Image of Scale on Alloy A, 600 hr Exposure, Gas 4A, 540°C.....	5-71
5-57	BSE Image of Scale on Alloy B, 1350 hr Exposure, Gas 1A, 540°C	5-73
5-58	BSE Image of Scale on Alloy B, 600 hr Exposure, Gas 2A, 540°C	5-73
5-59	BSE Image of Scale on Alloy B, 600 hr Exposure, Gas 4A, 540°C	5-74
5-60	BSE Image of Scale on Alloy C, 600 hr Exposure, Gas 1A, 540°C	5-75
5-61	BSE Image and Elemental Maps of Scale on Alloy C, 1350 hr Exposure, Gas 1A, 540°C.....	5-76
5-62	BSE Image of Scale on Alloy C, 600 hr Exposure, Gas 2A, 540°C	5-77
5-63	BSE Image of Scale on Alloy C, 600 hr Exposure, Gas 4A, 540°C	5-78
5-64	BSE Image of Scale on Alloy D, 600 hr Exposure, Gas 2A, 540°C	5-79
6-1	Corrosion Loss as a Function of Log PS ₂ /PO ₂ , Alloys A & B.....	6-2
6-2	Corrosion Loss as a Function of Log PS ₂ /PO ₂ , Alloys C, D & E.....	6-2

6-3	Schematic of Scale Development on Alloy A in Syngas With a High PS ₂ /PO ₂ Ratio (Type A Corrosion).....	6-6
6-4	Schematic Stability diagrams for Al, Si, Cr, Fe and Ni at 550°C.....	6-7
6-5	Schematic of Scale Development on Alloy A in Syngas With Intermediate to Low PS ₂ /PO ₂ Ratio (Type B Corrosion)	
	a. Intermediate PS ₂ /PO ₂ Ratio (3% H ₂ O,0.8% H ₂ S)	6-9
	b. Low PS ₂ /PO ₂ Ratio (3% H ₂ O,0.2% H ₂ S)	6-9
6-6	Schematic of Scale Development on Alloy D	
	a. Type A Corrosion.....	6-13
	b. Type C Corrosion.....	6-13
6-7	Corrosion Losses of Alloys 800 and SS 310 as a Function of Water Content on Syngas 600 hrs, 540°C (0.8% H ₂ S)	6-16
6-8	BSE Image and EDS Analyses of Scales on SS 310 after 600 hr Exposure in Gas 4, 540°C (3% H ₂ O, 0.8% H ₂ S).....	6-17
6-9	Isothermal Corrosion Losses of Alloy 800 and SS 310 at 540°C in Gas 1A (0% H ₂ O, 0.2% H ₂ S)	6-18
6-10	Scale on Alloy 310 After Exposure to Syngas 1A, With and Without 400 ppmv HCl	
	a. No HCL (From Ref. 58).....	6-20
	b. 400 ppmv HCL (This Study).....	6-20
6-11	EPMA Line Scans of Cronifer and SS 310 CbN After Exposure to Gas 1A Without HCL After Norton. ⁵⁸	
	a. Cronifer 45, 1000 hr Exposure	6-24
	b. Cronifer 45, 2000 hr Exposure	6-24
	c. 310 CbN, 2000 hr Exposure.....	6-24
6-12	BSE Image of SS 310 After 2100 hr Exposure in the PRENFLO Demonstration Plant at 570°C.....	6-25
6-13	BSE Image of Alloy 800 After 2600 hr Exposure in SAR Gasification Plant at 523°C.....	6-26
6-14	INCO 82 Weld Metal After 3600 hr Exposure in SAR Gasification Plant, 406°C	
	a. Optical Photomicrograph.....	6-27
	b. BSE Image.....	6-27

LIST OF TABLES

Table	Page
2-1 Number of Reported Incidents of Failures in Coal Conversion Plants	2-8
4-1 Typical Syngas Compositions (vol %).....	4-2
4-2 Model Syngas Compositions (vol %)	4-3
4-3 Nonequilibrium Gas Compositions Used in This Study (vol %).....	4-8
4-4 Composition of Experimental Alloys.....	4-12
4-5 Water Vapor Pressure as a Function of Temperature	4-19
4-6 Semiquantitative EDS Analysis of Standards	4-25
4-7 Probable Mineral Composition of Scale Calculated from EDS Analysis (at %).....	4-28
4-8 Oxygen Content Scales of Measured by EDS and WDS	4-30
4-9 Mass Absorption Coefficients and Densities for Some of the Elements Considered in This Study.....	4-31
4-10 Penetration Depth for Different Corrosion Products. The 1/e Depth is Defined as the Depth at Which the Planes are Illuminated by a Beam Reduced in Intensity by a Factor of e. There is Additional Reduction of the Diffracted Beam by Another Amount Dependent on the Exit Angle	4-32
4-11 Chemical Composition of Scales on Ti-Cr and V-Cr Mixtures After 15 hr Exposure to Gas 1.....	4-37

5-1	Corrosion Loss and Linear Corrosion Rates of Some Alloys After 600 hr. Cyclical Exposure in Dry Syngas, 0.8% H ₂ S	5-3
5-2	Metal Recession (μm) After Continuous Corrosion Tests 550°C Gas 1	5-6
5-3	Approximate Parabolic Corrosion Constants and Corrosion Rates	5-8
5-4	Corrosion Loss in 600 hrs Laboratory Tests at 540°C (μm)	5-9
5-5	Scale Analysis. Effect of Exposure Time. Test Matrix	5-15
5-6	Scale Analysis. Effect of Oxidants. Test Matrix	5-15
5-7	Scale Analysis. Effect of H ₂ S Content. (0.2 H ₂ S). Test Matrix.....	5-15
5-8	Scale Composition on Alloy A. 1.5 hrs Exposure, Gas 1, 540°C (at %).....	5-18
5-9	Scale Composition on Alloy A. 150 hrs Exposure, Gas 1, 540°C (at %).....	5-19
5-10	Composition of Topotactical Scale on Alloy A. 600 hr Exposure, Gas 1, 540°C (at %).....	5-20
5-11	Composition of Topotactical Scale on Alloy A. 1224 hr Exposure, Gas 1, 540°C (at %).....	5-22
5-12	Composition of Scale on Alloy B. 15 hr Exposure, Gas 1, 540°C (at %).....	5-23
5-13	Composition of Scale on Alloy B After 600 hr Exposure, Gas 1, 540°C (at %).....	5-23
5-14	Composition of Scale on Alloy B. 1224 hrs Exposure, Gas 1 540°C (at %).....	5-26
5-15	Scale Composition on Alloy C, 15 hrs Exposure, Gas 1 540°C (at %).....	5-26
5-16	Composition on Scale on Alloy C, 150 hrs Exposure, Gas 1, 540°C (at %).....	5-28

5-17	Composition of Topotactical Scale on Alloy C, 1224 hr Exposure, Gas 1, 540°C (at %)	5-28
5-18	Scale Composition on Alloy D, 15 hr Exposure, Gas 1, 540°C (at %)	5-30
5-19	Composition of Topotactical Scale on Alloy D, 600 hr Exposure, Gas 1, 540°C (at %)	5-33
5-20	Scale Composition on Alloy E, 15 hr Exposure, Gas 1, 540°C (at %)	5-34
5-21	Scale Composition on Alloy E, 600 hrs Exposure, Gas 1 540°C (at %)	5-35
5-22	Composition of Topotactical Scale on Alloy B, 15 hrs, Gas 4, 540°C (at %)	5-36
5-23	Composition of Topotactical Scale on Alloy C, 15 hrs, Gas 4, 540°C (at %)	5-36
5-24	Composition of Scale/Alloy Interface on Alloy D, 15 hrs, Gas 4, 540°C (at %)	5-38
5-25	Composition of Topotactical Scale on Alloy A, 600 hrs Exposure, 540°C, Gas 2 (at %)	5-39
5-26	Composition of Topotactical Scale on Alloy A, 600 hr Exposure, Gas 4 540°C (at %)	5-42
5-27	Composition of Topotactical Scales on Alloy B, 600 hr, Gas 2 540°C (at %)	5-44
5-28	Composition of Topotactical Scales on Alloy B, 600 hr Exposure, Gas 4, 540°C (at %)	5-47
5-29	Composition of Topotactical Scale on Alloy B, 600 hrs, Gas 6, 540°C (at %)	5-47
5-30	Scale Composition on Alloy B, 600 hrs, Gas 7, 540°C (at %)	5-47
5-31	Typical Composition of Topotactical Scale on Alloy C After Exposure to Gases Containing 0, 1, 2, 3, 10 and 15% H ₂ O, 600 hrs, 540°C (at %)	5-49

5-32	Composition of Scales on Alloy D, 600 hr Exposure, Gas 2 540°C (at %)	5-51
5-33	Composition of Topotactical Scale on Alloy D, 600 hr Exposure, Gas 3, 540°C (at %)	5-53
5-34	Composition of Scale on Alloy D, 600 hr Exposure, Gas 7 540°C (at %)	5-53
5-35	Composition of Alloy Surface Layer, Alloy D, 600 hrs, Gas 7 (at %)	5-56
5-36	Scale Composition on Alloy E, 600 hr Exposure, Gas 2, 540°C (at %)	5-57
5-37	Scale Composition on Alloy E, 600 hrs, Gas 3, 540°C (at %)	5-58
5-38	Scale Composition on Alloy B, 600 hrs, Gas 0, 540°C (at %)	5-61
5-39	Scale Composition on Alloy C, 600 hrs Exposure, Gas 0, 540°C (at %)	5-61
5-40	Scale Compositions on Alloy D, 600 hrs Exposure, Gas 0, 540°C (at %)	5-64
5-41	Typical Composition of Topotactical Scales on Alloy C After 600 hr Exposure to Syngas with PO ₂ of 10 ⁻²⁷ at 540°C (at %)	5-65
5-42	Typical Compositions of Topotactical Scale on Alloys A and C after 600 hr Exposure to Syngas with PO ₂ of 10 ⁻²⁶ at 540°C (at %)	5-65
5-43	Composition of Topotactical Scale on Alloy A, 600 hrs, 540°C Gas 1A (0.2% H ₂ S) At%	5-68
5-44	Composition of Topotactical Scale on Alloy A, 1350 hrs, 540°C, Gas 1A (at %)	5-68
5-45	Composition of Scale on Alloy A, 600 hrs, 540°C, Gas 2A (at %)	5-70
5-46	Composition of Scale on Alloy A, 600 hrs, 540°C, Gas 4A (at %)	5-72
5-47	Scale and Alloy Compositions of Alloy B, 1350 hrs, 540°C, Gas 1A (at %)	5-72

5-48	Composition of Scale on Alloy B, 600 hrs, 540°C, Gas 2A (at %)	5-72
5-49	Composition of Scale on Alloy B, 600 hrs, 540°C, Gas 4A (at %)	5-74
5-50	Composition of Topotactical Scale on Alloy C, 1350 hrs, 540°C, Gas 1A (at %)	5-75
5-51	Scale Composition on Alloy C, 600 hrs, 540°C, Gas 2A (at %)	5-77
5-52	Composition of Scale on Alloy C, 600 hrs, 540°C, Gas 4A (at %)	5-78
5-53	Composition of Scale on Alloy D, 600 hrs, 540°C, Gas 2A (at %)	5-79
6-1	Corrosion Losses (μm) in Dry Syngas 1A, With and Without 400 ppmv HCl	6-19
6-2	Corrosion Losses in Wet Syngas 4, With and Without 400 ppmv HCl 3% H ₂ O, 0.8% H ₂ S, 600 hrs, 540°C	6-22

SYMBOLS AND ABBREVIATIONS

BSE	Back Scattered Electron (image)
CGCC	Coal gasification combined cycle (power plant)
EDS	Energy Dispersive (X-ray) Spectroscopy (microanalysis)
FGD	Flue gas desulfurization
GTOe	Gigaton oil equivalent
HRB	Heat recovery boiler
IGCC	Integrated (coal) gasification combined cycle (plant)
IGFC	Integrated (coal) gasification fuel cell (plant)
IGHAT	Integrated (coal) gasification humid air turbine (plant)
Kp (1)	Parabolic corrosion rate constant (μm^2)hr
Kp (2)	Gas equilibrium reaction constant (at constant pressure)
KV-STEG	Kolen vergasser—Stoom en gas turbine (centrale)
mil	0.001 inch
MPC	Metals Properties Council
NIST	National Institute of Standards and Technology
PCF	Pulverized Coal Fired (Power plant)

PO ₂	Oxygen pressure (atm)
PS ₂	Sulfur pressure (atm)
Quad	Quadrillion BTU (British thermal unit)
SEM	Scanning Electron Microscope
SNG	Synthetic Natural Gas
WDS	Wave Length Dispersive (X-ray) Spectroscopy (microanalysis)
XRD	X-Ray Diffraction

1

INTRODUCTION

Most energy utilization scenarios confirm that the world will rely on fossil fuels as its major source of energy for at least 50 years¹. The limited availability of oil and gas is expected to make coal the predominant fuel during this time period. This is illustrated in Figure 1.1, which shows expected future consumption of the major energy sources in the 1960-2060 time frame. It is noted that coal will become the dominant energy resource, despite significant growth in both nuclear and renewable energy. The reasons for this are its huge available and widely distributed reserves and relatively low cost (Figure 1.2)². Coal is already the predominant fuel for electric power generation in most countries and is expected to increase its market share, especially after the supply of readily available and low cost natural gas is decreasing. It is also expected that the majority of the new coal fired capacity will be erected in developing countries, as they try to raise their standard of living.

It is well known that coal has its drawbacks as clean and convenient fuel, even when used in large scale industrial installations such as electric utility plants. Like most fossil fuels, coal is an intimate mixture of hydrocarbons and impurities, many of which have undesirable side effects when released back to the environment. Unlike impurities in liquid and gaseous fossil fuels, which can be readily removed by refining prior to combustion, most impurities in coal are not readily removed before combustion and are released as solid, liquid and gaseous substances during combustion. Over the years it has become increasingly more unacceptable to release these byproducts to the environment. Thus, the emission of particulates was restricted early on from about the 1940's. Restrictions on sulfur oxide (SO_x) emissions appeared in the late sixties, while nitrogen oxide (NO_x) abatement devices are currently introduced worldwide. Unfortunately, the ability to remove undesirable impurities after combustion is limited. It is estimated that the cost of removing more than 95% of sulfur from coal in the conventional pulverized coal - flue gas desulfurization scrubber - power plant will be prohibitive, if technically feasible at all³. Post combustion NO_x cleanup is equally limited, both economically and technically.

Coal gasification provides a means to clean coal prior to combustion. The solid fuel is transformed to gaseous fuel, from which obnoxious impurities such as H_2S can be readily removed, with processes used commercially in refineries and sour natural gas

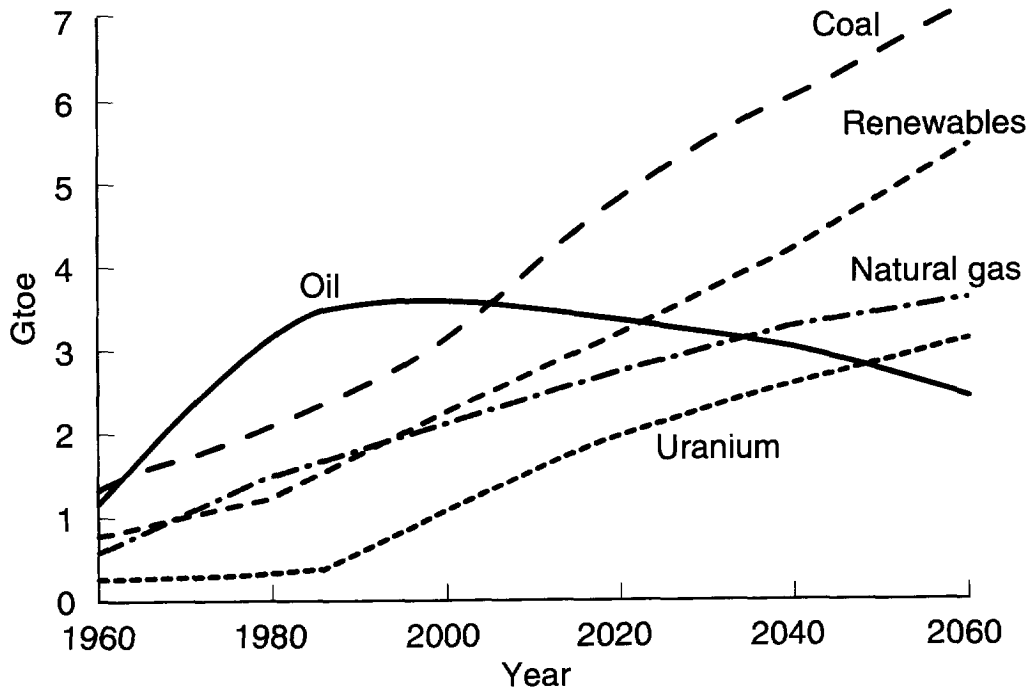


Figure 1.1
Evolution of World Energy Utilization

World Energy Conference - Conservation Commission, 1986

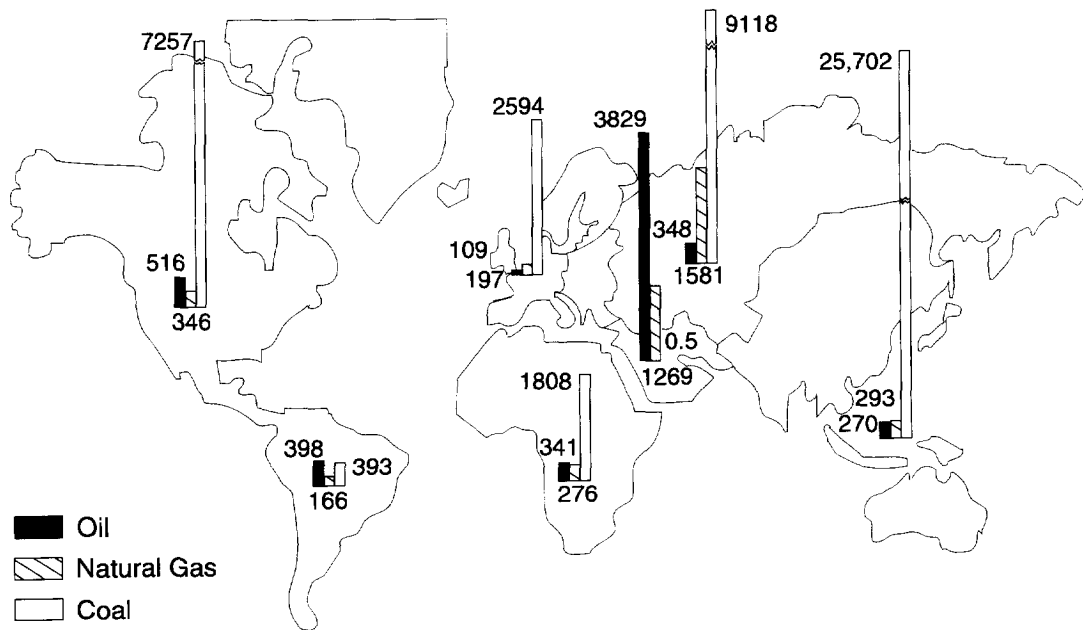


Figure 1.2
Global Energy Resources, Proven Reserves in Quads

purification plants, where removal of 99+% of the sulfur species is routine. By manipulating the combustion process in the gas turbine, it is further possible to suppress NO_x emissions to less than 10 ppm, without additional NO_x removal equipment⁴. Thus, coal gasification provides a way to utilize the world's most abundant fossil fuel resource while reducing air pollutants to levels equal to or less than those of plants using natural gas, which is the cleanest fossil fuel presently available.

Another drawback of coal is its high carbon content. Thus, combustion of coal will inherently produce more CO_2 than more hydrogen rich oil and natural gas fuels. At present the only practical way to decrease CO_2 emission is to increase the overall efficiency of the energy conversion process. Here again coal gasification combined cycle power plants have an edge. Van Lier³ projects that coal gasification plants may have a 2-5% advantage in efficiency, which can be further increased in the future by using fuel cells to produce electricity instead of gas turbines (Figure 1.3).

Thus, there are very sound reasons to develop coal gasification technology as a future means to convert coal to electricity. However, the cost of electricity will probably remain the main criterion to select future coal based power plant, especially in developing countries with scarce resources. At this moment coal gasification plants are still

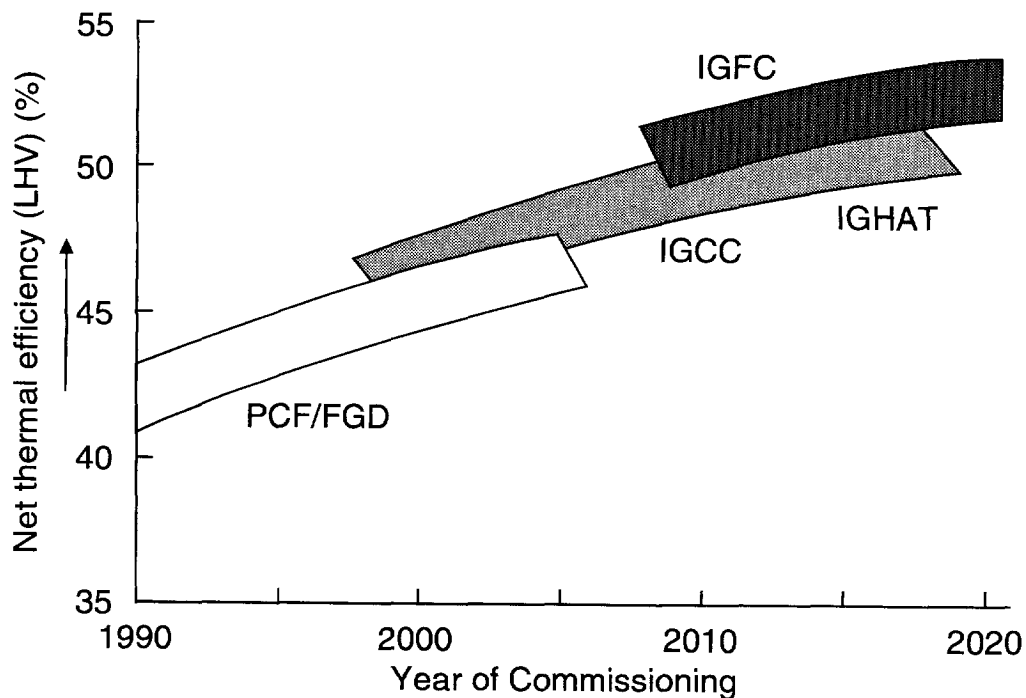


Figure 1.3
Efficiency Improvement of Coal Fired Plants

considerably more expensive to build than conventional plants⁵. Part of this is the newness of the technology, which results in higher costs for the first plants. Part of it are the greater complexity and more corrosive conditions present in coal gasification. Further R&D is needed to reduce the latter cost. By choosing mixed oxidant corrosion in environments prevailing in coal gasifiers as a research topic, this thesis hopes to contribute to our understanding of materials performance in gasifiers. Eventually this should result in more durable and less expensive materials for coal gasifiers, thus improving its competitive advantage.

2

TECHNOLOGY BACKGROUND

2.1 GASIFICATION TECHNOLOGY

2.1.1 Process Development

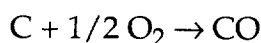
Gasification has been around for a long time⁶. It supplied lighting and heating since the 19th Century in the form of town gas. Most of the processes used then were quite inefficient and highly detrimental to the environment. The main legacy of these older plants are highly contaminated plant sites awaiting removal of carcinogenic tars and other gasification residues. Fortunately readily available, low cost natural gas shut down town gas plants first in the USA and shortly thereafter in Europe.

The first oil crisis in 1973 revived interest in coal and in methods to obtain liquid and gaseous fuels from coal, which was seen as the only abundant fossil fuel resource, fully controlled by the consuming countries. At that time there was also a perceived shortage of natural gas. Thus, most technology development, at least in the U.S. was directed towards processes yielding significant quantities of methane directly, i.e., low temperature processes. The natural gas shortage proved to be non existent and most research on low temperature processes disappeared with this knowledge.

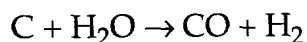
At about the same time the concept of a coal gasification combined cycle (C.G.C.C.) power plant as an alternative to conventional power plants was promoted by EPRI, where a systematic R&D program was started, which eventually led to the first large scale 1000 ton/day demonstration plant of the technology at the Coolwater site of Southern California Edison Company, which operated from 1984-1989⁷.

At present a coal gasification combined cycle power plant consists of the following major units:

1. The coal gasification plant, including the coal grinding and feed system, the gasifier itself, heat recovery systems and a water quench system to remove particulates and water soluble impurities such as HCl and NH₃. Here the coal is converted to gas by partial oxidation:



Hydrocarbons in the coal are generally converted to hydrogen at high temperatures or to methane (CH₄) at lower temperatures. Water or steam is generally added in various quantities to control the gasification temperature as the reaction



is endothermic. Thus, the resulting gas mixture consists mainly of CO and H₂ with lesser quantities of CO₂ and H₂O. Sulfur species in the coal are mainly converted to H₂S, with a minor amount of COS. Nitrogen species are converted to NH₃ and chlorine species to HCl. More details on the gas compositions resulting from various coal gasification processes and their corrosive potential are given later in Section 4.1.

2. The sulfur removal and recovery system. This system was originally developed for the desulfurization of sulfur rich hydrocarbon streams in oil refineries and sour natural gas. It consists of the following three, mostly proprietary, systems.
 - a. The main sulfur removal system. Here sour gases, mainly H₂S are extracted from the gas using organic liquids, which are later recovered for reuse. Thus, a gas with a high concentration of H₂S is obtained.
 - b. The fuel gas clean up and conversion system. It recovers additional sulfur species such as COS to maximize sulfur recovery. In some cases it can also be used to remove sulfur species from the tail gas of the sulfur recovery unit.
 - c. The sulfur recovery unit. Here the H₂S rich gas is converted to elemental sulfur, or sulfuric acid which are saleable byproducts.
3. The gas turbine combined cycle power plant. The purified gas is fed to a gas turbine and combusted to produce electric power. Generally it is rehumidified using low level waste heat from the gasifier to reduce the flame temperature and thus the NO_x content in the flue gas to very low levels. The exhaust from the gas turbine is cooled down in a heat recovery boiler where steam is produced to drive a steam turbine for additional power production. Steam produced in the heat recovery system of the gasifier is generally superheated here also before entering the steam turbine.
4. The oxygen plant. The oxidant for the gasification process can be either air or oxygen. Which system will eventually prove to be the most cost effective, is still under debate. However, all major processes, presently close to commercialization use

oxygen, except one, which can use both. The major arguments for the use of oxygen are as follows:

- a. The use of oxygen reduces the size of the gasifier significantly as the gas flow is reduced four fold. This reduces equipment cost sufficiently to offset the high cost of the oxygen plant.
- b. The use of oxygen increases the overall efficiency of the gasification plant. Large amounts of nitrogen do not need to be heated up, with the necessity to recover its latent heat later on. Thus, heat losses are reduced and the size of the heat recovery system can be reduced. This largely offsets the energy needed to produce oxygen.
- c. The gas produced in oxygen blown gasifiers can be used for the production of chemicals, like methanol, fertilizers, oxochemicals and the like, as well as for power production. Thus, development cost can be shared. Most commercially operating coal gasification plants presently produce chemicals not electricity: e.g., UBE in Japan (ammonia), Eastman Kodak USA (photochemicals) and SAR in Germany (oxochemicals, hydrogen).

In this thesis we will therefore limit ourselves to corrosion in syngas derived from oxygen blown gasifiers, i.e., gas mixtures consisting mainly of CO and H₂, with H₂S as the main corrosive impurity.

In summary, in a coal gasification combined cycle power plant, the inevitable energy losses associated with conversion of coal to gas are offset by the inherently higher efficiency of the gas turbine (Brayton) cycle in comparison with the steam (Rankine) cycle. Further improvements are obtained by closely integrating the waste heat recovery in the gasification unit with that of the heat recovery boiler of the gas turbine, to produce the maximum amount of additional power via a steam turbine. Figure 2.1 shows a schematic of such a plant layout, which basically represents that of the Cool water demonstration plant⁷. Additional efficiencies and increases in power output can be obtained by using the compressor of the gas turbine to compress air for the oxygen plant and to add the nitrogen separated in this plant back to the clean gas prior to combustion. This advanced integration scheme will be used in the SEP 250 MWe (2000 tpd) demonstration plant presently operating in Buggenum the Netherlands. Its schematic is shown in Figure 2.2⁸.

The efficiency of an integrated coal gasification plant will be considerably higher than that of a conventional pulverized coal power plant, especially when the latter is equipped with flue gas scrubbers to remove SO_x and selective catalytic reduction equipment to remove NO_x⁵. In the early 1980's, when everybody believed that fuel prices would escalate faster than the rate of inflation forever, it was thought that this would be enough to make coal gasification the technology of choice. The collapse of energy prices put an end to this dream.

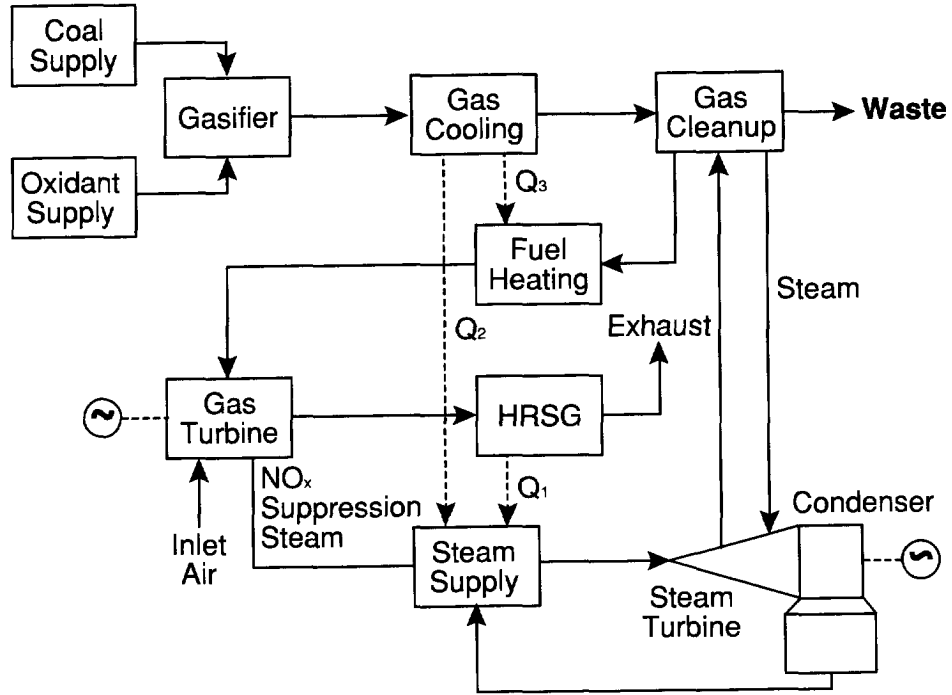


Figure 2.1
Schematic of Integrated Gasification Combined Cycle Power Plant (I.G.C.C.)

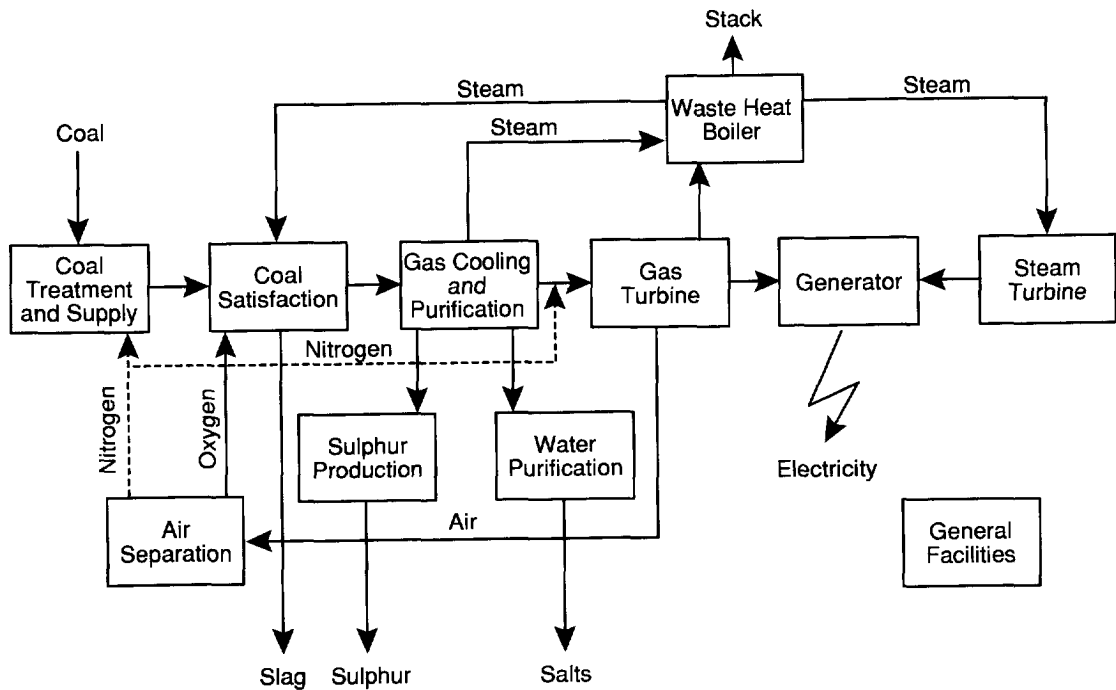


Figure 2.2
Schematic of Advanced I.G.C.C. Plant

In recent years the need to greatly decrease the emission of pollutants has revived interest in coal gasification technology. Undesirable pollutants in the coal, mainly sulfur, nitrogen and chlorine are removed from the fuel prior to combustion. Thus, it is possible to remove such impurities at the 99+% level without excessive cost. Methods to remove the same impurities after combustion eliminate at present only about 90% of the pollutants. Removal up to 95% appears possible in the near future. In addition, the thermal NO_x in the combustion turbine can be suppressed to very low levels by diluting the gas with steam or nitrogen. Finally, the higher efficiency of the IGCC plant will reduce the emission of CO_2 , which will abate real or perceived global warming. Thus, there are sound societal and economic reasons for the commercial success of this technology. This is demonstrated by the fact that there are now 5 large (>250 MWe) and numerous smaller IGCC plants in various stages of design, construction and operation throughout the world.

Various gasification processes can be used more or less interchangeably in the gasification section. They share the following common characteristics:

1. A high overall efficiency, generally greater than 90%. This is achieved by an efficient gasification process and a good heat recovery system. The efficiency of the gasification process is measured by the cold gas efficiency, i.e., the energy lost by gasification prior to heat recovery, and a high carbon conversion, which should exceed 99%. Cold gas efficiency ranges from 75-83%, and is mostly dependent on the amount of water used during gasification. The latent heat of the gas is mostly recovered by raising steam in syngas coolers, which may consist of radiant, convective or fire tube boilers. The syngas coolers are among the most expensive components of the gasification plant. Here metal alloys in the form of heat exchanger tubes are directly exposed to the hot corrosive fuel gas (syngas) at 400-1200°C (gas temperature). Contrary to general perception, the efficiency of the gasifier is not very dependent on the temperature at which the latent heat is recovered, since the steam produced is integrated with steam production in the heat recovery boiler (HRB) of the gas turbine. Thus, most of the steam superheating can be done in the HRB, where conditions are less corrosive and most of the heat exchangers in the syngas coolers are used to generate steam. The temperature of the heat exchanger depends mainly on the pressure of the steam produced and the temperature of the gas. It ranges generally from 350 to maximum 450°C. For some systems a limited amount of superheating in the syngas coolers is desirable. This will require higher temperatures, but generally below 600°C, since high temperature steam conditions are not considered cost effective⁹.
2. No production of hazardous liquid or solid wastes. This favors the use of high temperature gasification systems in which all hazardous byproducts, such as tars, phenols, etc. are destroyed.

2. Technology Background

3. Production of minimum volume of inert ash or slag. This favors the use of slagging gasifiers, which produce a glassy slag, from which hazardous heavy metal cannot be readily leached.
4. Operation at a pressure high enough to feed the clean gas directly to the gas turbine. This requires operation in the 20-40 bar range. Operation at high pressure also reduces equipment size and is therefore desirable by itself.
5. Ability to use various types of coal from lignite to bituminous grades.

The requirements outlined above generally favor slagging gasifiers, especially entrained slagging gasifiers. In such gasifiers the finely ground coal is fed to a burner, where it is mixed with oxygen and sometimes steam to be gasified in suspended state in a gasifier at a temperature well above the melting point of the mineral matter of the coal, generally at 1300-1600°C, depending on coal type and gasification process. Entrained slagging gasifiers can gasify most coals, without major process changes. The gasifier itself is relatively small as the gasification reactions are very rapid at high temperature. The major difference between entrained slagging gasification processes is the way in which coal is fed to the gasifier. Coal can be fed dry, through a system of lock hoppers, using nitrogen as the carrier gas, or in the form of a coal-water slurry, generally containing 60-70% coal and 30-40% water. The Shell and Krupp-Koppers gasification processes are examples of dry fed gasifiers, while the Dow and Texaco processes use a coal-water slurry. The gas produced in a dry fed gasifier contains more CO and less CO₂ and H₂O than gas produced in a slurry fed gasifier. This has a considerable effect on the corrosivity of the resulting gas, which is studied in detail in this thesis and is further discussed in Section 4.1 on "Gas Composition Analysis and Selection".

Purification of raw syngas is presently done at room temperature or below. The efficiency of an C.G.C.C. plant can further be improved by removing the impurities at elevated temperature. This may also reduce capital cost somewhat as the size of the heat recovery system becomes smaller. Laboratory to pilot scale R&D is presently underway to make hot gas clean up feasible. Considerable progress has been made, especially in the area of sulfur removal¹⁰. The preferred temperature for hot gas clean up has not yet been fully established, but probably will be in the 500-600°C range, i.e., the same temperature as that required for superheating steam. Removal of other critical contaminants, halogens, alkalis, ammonia, has not been studied in the same detail as sulfur removal, but is equally critical, to protect the gas turbine from corrosion and to keep total NO_x emissions low. Since the main advantage of CGCC plants is their lack of emissions, hot gas clean up must be able to deliver the same level of impurity removal as the present proven technology. Thus, it is unlikely that hot gas clean up will be used in the first generation of CGCC plants.

2.1.2 Materials Experience

Papers on laboratory corrosion studies, claiming to simulate coal gasification environments by far outnumber papers on actual plant experience. There are several reasons for this. Firstly, materials experience and know how is often considered proprietary, by the developers of gasification process technology. Secondly, plant operating conditions, especially in pilot plants are often variable, and ill defined. This makes it often difficult to report the observed materials behavior in a meaningful way. Finally the primary focus of materials engineers concerned with plant operations, is to keep the plant operating not to write papers. Thus if failures occur, the decision on how to proceed - repair, replace, etc., must be made quickly, based on cursory investigations. In depth studies to discover the root cause of problems are often considered an unnecessary luxury, which is only done when recurring problems seriously affect the availability of the plant.

In the USA several attempts were made to systematically study materials behavior and performance in gasifiers. Dr. Frankel of DOE organized a failure reporting and analysis system for various DOE-sponsored pilot plants in the 70's and early eighties. The project was managed by the National Bureau of Standards (N.B.S., now the National Institute of Standards and Technology (N.I.S.T.)), with assistance of the Argonne and Oak Ridge National laboratories in the area of failure analysis. Efforts to extend the program worldwide were not successful. A computerized data base was established at NIST which was available to the public. Table 2.1¹¹ gives an overview of all failures up to 1978. It can be seen that the reported failures cover all possible failure modes one can imagine. Many of them are the result of human error or lack of knowledge. For instance, there are still 48 reported instances of stress corrosion cracking, 105 instances of manufacturing defects and 48 instances of equipment malfunctioning. As a class, corrosion had the largest number of reported failures (151) of which 36 were contributed to sulfidation and, therefore, most likely occurred in the gasifier and related equipment. D.R. Diercks¹² describes some of the failures in more detail. The more spectacular ones were caused by sulfidation and polythionic stress corrosion cracking, a form of aqueous corrosion during downtime.

A large effort to study materials behavior in gasifier type environments was started by the Metals Properties Council (M.P.C.) in 1971 under sponsorship of the American Gas Association and later GRI and DOE. This program also included exposure of corrosion coupon racks in various pilot plants operating at that time. Most of these pilot plants were designed to produce synthetic natural gas (SNG), i.e., mostly methane. The initial raw gas compositions prior to methanation generally contained much more steam (up to 40%) and were thus more oxidizing. Interest at that time was mainly in uncooled metal components at gasifier operating temperature, i.e., 800-1000°C. Results have been reported in several publications^{13,14}. Exposure times ranged up to about 3000 hrs, but most were less than 2000 hrs. Results were quite variable, even for duplicate exposures.

Table 2-1
Number of Reported Incidents of Failures in Coal Conversion Plants

Failure Mode	Failure Mode Analysis										Total
	Bigas	Battelle	CO ₂	Cresap	Hygas	SRC	Synthane	Westinghouse	Other		
Corrosion	0	2	37	4	30	8	22	6	42	151	
Aqueous	0	0	0	0	1	0	0	0	3	4	
Carburization	0	0	8	0	1	0	0	1	2	12	
Metal Dusting	0	0	4	0	0	0	0	0	3	7	
Oxidation	0	0	2	0	4	0	0	1	4	11	
Pitting	0	0	3	1	4	3	6	0	8	25	
Sulfidation	0	0	13	0	12	0	6	1	4	36	
General	0	2	7	3	8	5	10	3	18	56	
Erosion	2	4	7	9	12	6	26	6	20	92	
Equipment Malfunction*	5	4	6	3	9	2	9	2	6	46	
Manufacturing Defect	8	10	11	9	7	8	28	5	19	105	
Design	5	6	5	8	4	8	17	5	14	72	
Fabrication	0	1	3	0	2	0	4	0	2	12	
Quality Control	3	3	3	1	1	0	7	0	3	21	
Stress Corrosion	2	0	5	1	6	5	6	8	15	48	
Chloride	0	0	4	0	6	2	4	0	9	25	
Other	2	0	1	1	0	3	2	8	6	23	
Stress/Temp. Failure	0	2	1	0	6	0	6	6	8	29	
Creep	0	0	0	0	1	0	0	0	3	4	
Fatigue	0	2	0	0	2	0	3	4	4	15	
Thermal Stress/Shock	0	0	1	0	3	0	3	2	1	10	

*Failures from temperature/pressure excursions.

This is partly because of the use of different coals, and associated changes in sulfur content, partly due to intermittent operation, where corrosion rates can be influenced by aqueous corrosion during downtime and finally due to considerable variations in operating temperature. Corrosion data from uncooled corrosion coupons are especially sensitive to temperature excursions, as even short time excursions at high temperature can destroy protective scales¹³. Figure 2.3 taken from a later study by Ullrich¹⁵ et al., shows the temperature distribution of an uncooled corrosion coupon rack nominally operating at about 570°C for about 2000 hrs. For more than 7% of the time the temperature actually exceeded 670°C. Thus, corrosion data from uncooled specimens can generally not be used for materials selection to design commercial plants.

In general, the corrosion rate data obtained were quite high, especially on alloys with a high Ni and relatively low Cr content and quite often exceeded the 0.5 mm/yr acceptance criterion, which at that time was considered an acceptable maximum corrosion rate.

Since that time interest in the production of synthetic natural gas has all but disappeared. Coal gasification systems for electric power production, mainly entrained slagging gasifiers produce a much more reducing and sulfidizing gas which makes the use of uncooled metal alloys in the hot gas stream unrealistic at temperatures much above 600°C. Thus emphasis in corrosion testing has switched mainly to steam evaporator

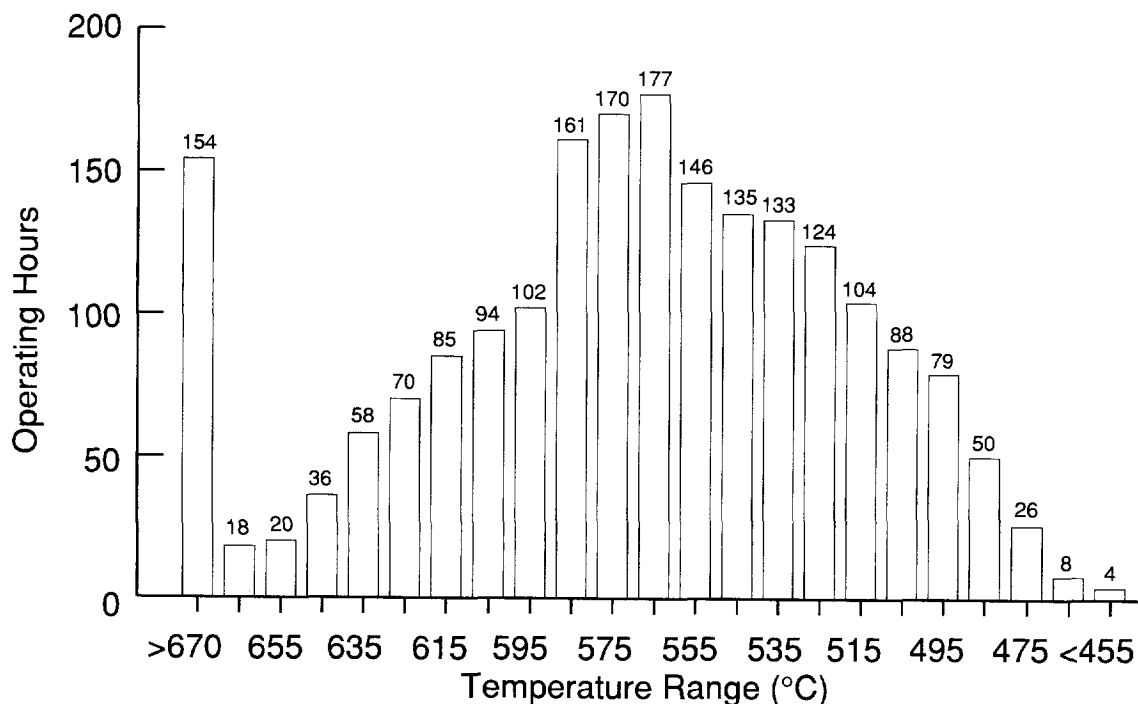


Figure 2.3
Temperature Distribution of Uncooled Corrosion Coupons, Nominally Operating at 570°C

temperatures ~250-450°C, with some additional work at superheater temperatures ~500-600°C. Typically corrosion test spools are built into existing heat exchangers or separate water or steam cooled test loops are used^{15,16,17}. Unfortunately, details of the test results are quite often kept confidential, especially corrosion rate data, although some data continue to be published.

The target maximum allowable corrosion rate has also changed over the years. Metallic components in fluid bed gasifiers are generally small and can be easily exchanged during scheduled outages. They usually are not required to contain high pressure steam or gas. A large corrosion allowance is also feasible. At present most alloys directly exposed to hot syngas are heat exchanger tubes, containing high pressure water or steam. These heat exchangers are large and cannot be easily replaced. Therefore, they are designed for a 20-30 year life. Corrosion allowances are generally limited to 2-3 mm. Thus, the target acceptable corrosion rate has been reduced to 0.1 mm/yr.

At first it was thought that carbon or low alloy steels would be acceptable heat exchanger materials, especially at temperatures below 300°C. This proved to be a fallacy¹⁶. Initially very high corrosion rates far exceeding 1 mm/yr were experienced in coal-water slurry fed gasifiers. After an extensive laboratory evaluation, it was concluded that the excessive corrosion rates experienced early on were caused mainly by aqueous corrosion during downtime and possibly operation below the dewpoint of the syngas for short periods of time. Corrosion during downtime is a well-recognized failure mechanism in H₂-H₂S environments in refineries, where it can lead to polythionic stress corrosion cracking. Methods to reduce or eliminate it have been developed. For gasifiers, blanketing with dry nitrogen or nitrogen with NH₃ added during down periods where access to the syngas cooler is not required or the use of dry air during periods when access is required, will largely eliminate the occurrence of aqueous corrosion during downtime. Corrosion during downtime will also be less of a problem in commercial plants with infrequent stoppages.

Corrosion tests on low alloy steels indicated results which were in good agreement with laboratory data, but generally too high to make the use of low alloy steels practical (Figure 2.4)¹⁸. Thus, attention was directed towards stainless steels as candidate materials for heat exchangers in syngas coolers. Initial tests^{17,19} were not promising in that corrosion rates generally exceeded 1 mm/yr for common stainless steels such as 304 and 310 even at 340-370°C. Best performance was obtained by alloys with a high molybdenum content such as alloys 28 (3.5%Mo 27%Cr) and 625 (9%Mo 20%Cr) in long term tests up to 5000 hrs. Examination of the alloys after service and the fact that Mo containing alloys had the lowest corrosion rates indicated that corrosion during downtime-pitting and occasional stress corrosion cracking - were still the major factors affecting the corrosion rate. During the exposure period, large quantities of liquefaction

residues were gasified which had high chlorine and sulfur contents, which made it more difficult to avoid corrosion during downtime²⁰.

Finally a long term test is reported in a commercial gasifier fueled with a typical bituminous coal containing about 1% S and 0.2% chlorine¹⁸, using a steam cooled separate test loop in the syngas cooler. Here corrosion during downtime was completely avoided by keeping the test loop hot during shutdown. Exposure time was 3600 hrs. Under these conditions, corrosion rates were greatly reduced. Less than 0.1 mm/yr at temperatures below 450°C and about 0.2 mm/yr at 550°C for alloy 310 (25%Cr - 20%Ni). However, some signs of carburization were found in alloy 800 (20Cr-31Ni) at temperatures as low as 550°C and definite carburization was noted in alloy 310 at temperatures over 600°C²¹. Thus, 600°C may well be the practical use limit for most commercial alloys, at least in high pressure heat exchangers where embrittlement of the pressure boundary is not allowed.

All the tests reported above were carried out in coal-water slurry fed entrained slagging gasifiers which produce a syngas with about 15% steam. Dry coal fed gasifiers produce a much drier syngas (0-3% H₂O) with a lower oxygen pressure, which is potentially more sulfidizing. Unfortunately, less has been published about materials performance here. Data from a 2300 hr exposure test of steam cooled samples²² indicated corrosion rates of 0.4 mm/yr for alloy 800 and 0.2 mm/yr for alloy 310 at 420°C. These rates are about the

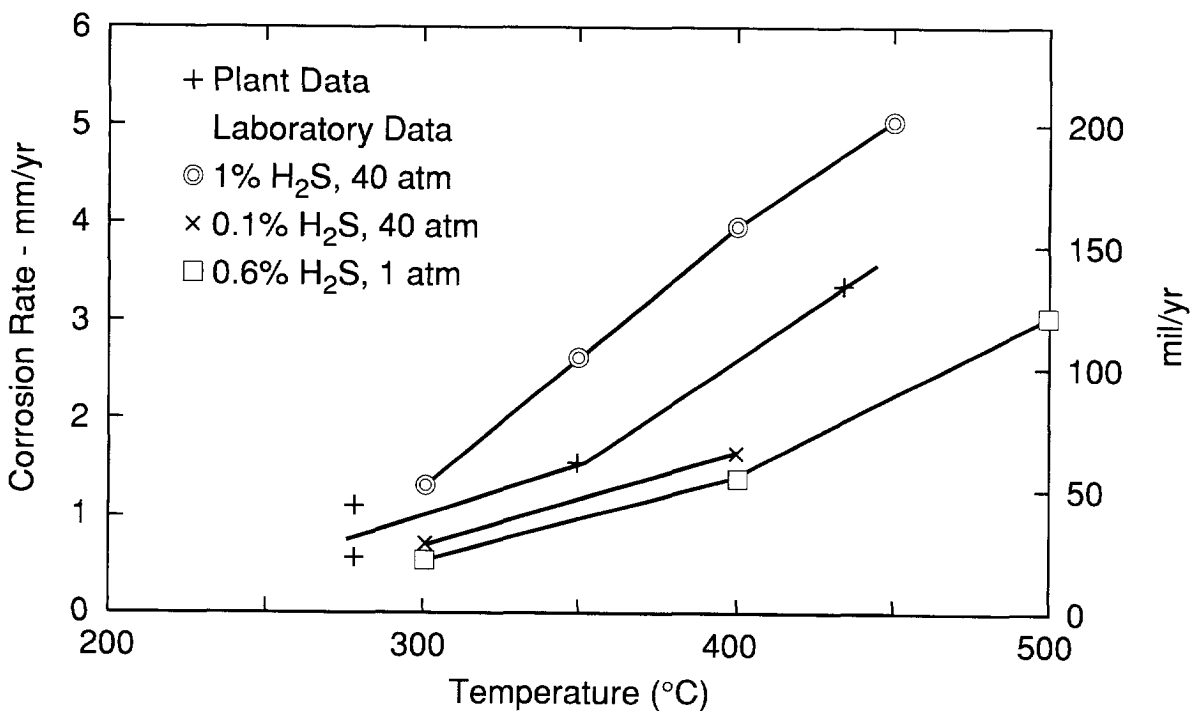


Figure 2.4
Corrosion of Low Alloy Steels in Syngas Coolers of Coal-Water Slurry Fed Gasifiers

same as those observed in a coal-water slurry fed gasifier at 550°C, indicating that corrosion rates are indeed somewhat higher here. No obvious signs of downtime corrosion were observed, despite relatively long periods of downtime.

Based on the above observations, it is concluded that commercial austenitic stainless steels may be suitable for use in evaporators in syngas coolers, provided downtime corrosion is largely suppressed. The use of Mo containing stainless steels such as alloy 28 (27Cr-31Ni-3.5Mo) is preferred to further minimize downtime corrosion problems. In the past such alloys generally would be applied as the outer layer of duplex, coextruded tubes. However, coextruded tubes are expensive and occasionally cause fabrication problems during bending (disbonding) and welding. Therefore, single alloy, austenitic stainless steel tubes such as alloys 800 and 28, which will resist corrosion and stress corrosion cracking at the water side are now preferred.

For superheater service the choice of materials is less clear at present, as many common alloys show marginal corrosion rates at temperatures over 500°C. For this reason the corrosion studies reported here were carried out at 540°C, and will provide useful background information for materials selection for superheater components.

2.2 LABORATORY CORROSION STUDIES

Innumerable studies of mixed oxidant corrosion have been carried out in the last 20-25 years. Most have been concerned with gases containing S and O as the main oxidants, but there are also a number of studies dealing with O and C as the main oxidants. We will discuss only studies on oxygen-sulfur systems here. The majority of these studies have the following features in common.

1. They were carried out in equilibrium gas mixtures, in which the oxygen and sulfur pressures are used as the main criteria to predict corrosion rates. The usually unspoken assumption is that gases with the same PO_2 and PS_2 will have similar corrosivity.
2. They were carried out at elevated temperatures, generally above 600°C and usually in the 800-1000°C range, especially in the older studies. Although these studies are not directly applicable to present day gasifiers, where cooled heat exchanger tubes are exposed to nonequilibrium gases at 400-600°C, they have resulted in three useful concepts and tools to interpret high temperature gaseous corrosion data. They are:

1) The Use of Phase Stability Diagrams

Phase stability diagrams in which the stability regions of sulfides and oxides of a given metal are plotted as a function of oxygen and sulfur partial pressure are widely used to determine potential reaction products in gasification

environments. A comprehensive review of derivation and application of stability diagrams to the analysis of oxidation and sulfidation reaction was given by Gulbransen and Janson²³. Similar analyses have been used by Perkins, Stringer, Meier and Natesan²⁴⁻²⁷ among others. A typical phase equilibrium diagram for the Cr-O-S system is shown in Figure 2.5²⁴ for 621°C²⁴. The stability region of Cr₂O₃ will increase with decreasing temperature. However, oxygen and sulfur pressures of the equilibrium gas composition (represented by point 1) will also decrease with decreasing temperature so that the position of the gas composition relative to the Cr₃S₄/Cr₂O₃ boundary remains roughly the same.

Many authors²⁴⁻²⁷ have pointed out that the stability diagrams of metals can be used to predict which reaction products are possible, not those which are actually formed in a given experiment for a given multicomponent alloy. The first reason for this is that the formation of a protective scale, for instance, Cr₂O₃ on Cr will change the gas composition at the scale metal interface. For instance if the diffusion of sulfur ions through the scale would be faster than that of oxygen, sulfides could form under the Cr₂O₃ scale. Thus, kinetics of the diffusion of corrosive gases will influence the formation of the corrosion products. Secondly, most alloys contain several alloying elements, some of which will produce stable oxides, e.g., Cr, some stable sulfides, e.g., Fe. Superimposing stability diagrams of alloying elements present in the alloy is only of limited value as various mixed

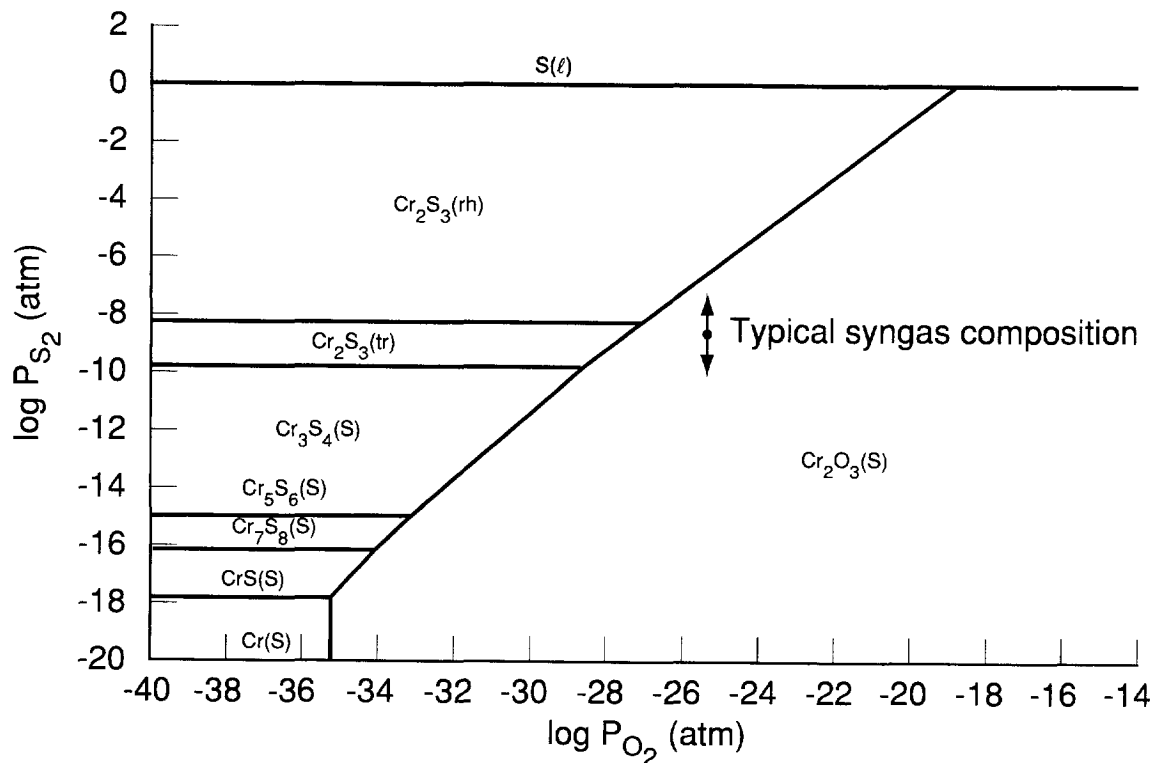


Figure 2.5
Stability Diagram for the Cr-S-O System at 894°K (621°C)

oxides (e.g., FeCr_2O_4) and Sulfides e.g., FeCr_2S_4 , are stable and cannot be predicted from the stability of the constituents alone. Finally during initial transient stages a variety of oxides and sulfides will form, which will gradually be replaced by the slowest growing stable oxide usually Cr_2O_3 . However, Meier²⁶ points out that the resulting Cr_2O_3 layer may contain impurities which makes the Cr_2O_3 scale less impervious, thus allowing the ingress of sulfur or the outward diffusion of Fe or Ni to form an external Fe(Ni)S scale as demonstrated by Perkins²⁴. This argument has led to the second major concept used in describing mixed oxidant corrosion.

2) The Kinetic Boundary

This concept was originally introduced by Perkins²⁴ and has been widely applied by Natesan²⁷. Because of the kinetic considerations discussed above, the oxygen pressure of a given syngas must be several orders of magnitude higher than that existing at the $\text{Cr}_x\text{S}_y/\text{Cr}_2\text{O}_3$ boundary, before the formation of Cr_2O_3 is rapid enough to form an impervious barrier to the influx of sulfur and the outward difference of Fe and Ni. Figure 2.6 shows "kinetic boundaries" for a few alloys from experiments by Perkins²⁴. To the left of the boundary impervious Cr_2O_3 or Al_2O_3 scales are not formed. This leads to the formation of Fe Ni sulfides either above or below the Cr_2O_3 scale which will lead to destructive corrosion, especially above the melting point of NiS containing eutectics. Unfortunately, the location of the kinetic boundary depends on the duration of the corrosion experiment and tends to shift to more oxidizing conditions with longer exposure time. This leads to the third major concept used in describing mixed oxidant corrosion.

3) "Break Away" Corrosion

This concept has previously been used to describe the onset of sudden catastrophic corrosion after a long period of passive behavior. A classic example is the corrosion of carbon steel in the CO_2 environment of gas cooled nuclear reactors²⁵. Alloys exposed to a gas composition to the right of the kinetic boundary in Figure 2.6 initially develop a protective scale and show low corrosion rates sometimes for several thousand hours, before the protective scale breaks down and allows the formation of Fe and Ni sulfides. Catastrophic sulfidation will then occur especially at elevated temperatures. The phenomenon of break away corrosion was demonstrated frequently in long term corrosion experiments by V. Hill et al., under sponsorship of the Metals Properties Councils²⁸.

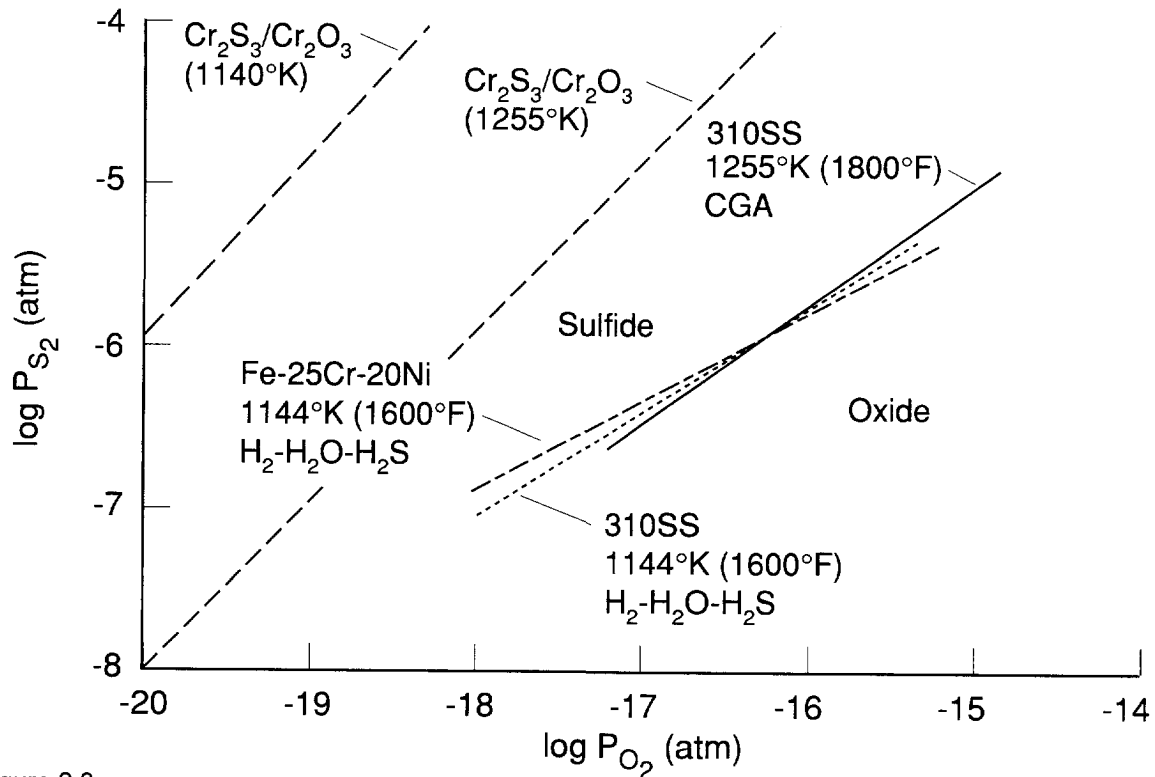


Figure 2.6
Kinetic Boundaries for Some Alloys

The experimental approach and concepts discussed above have served well in elucidating corrosion in mixed oxidant environments at high temperatures. Here the temperature is high enough to attain gas equilibrium rapidly and sulfidation rates are rapid enough to lead to unacceptably high corrosion rates. Thus, the main purpose of corrosion research was to define conditions under which protective oxide scales could be expected to remain intact for sufficiently long time to provide an acceptable service life. It was found that high chromium austenitic alloys, with low Ni and Fe contents were the most promising^{28,29}. Al and Si additions to such alloys tended to stabilize the Cr_2O_3 scale of such alloys, possibly by forming a SiO_2 or Al_2O_3 rich subscale^{29,30}. However in general it was found difficult to define alloy compositions, which form completely impervious scales over long periods of time. Recently this has become even more difficult, because the gas compositions produced by the present generation of entrained gasifiers have a much lower oxygen partial pressure than those of processes designed to produce synthetic natural gas. Therefore, most designers of gasification equipment have eliminated uncooled alloy components from the hot gas path and allow only water or steam cooled metallic parts, mostly as heat exchangers, i.e., waterwalls, convection bundles and fired tube boilers.

Perkins and Bakker³¹ have considered in how far the knowledge obtained from high temperature corrosion experiments will apply to corrosion observed at lower temperatures, where a cooled metallic component is in contact with considerably hotter syngas. They found considerable differences:

- 1) At lower temperatures the syngas composition will not readily come to equilibrium. This will reduce the oxygen pressure of the gas further and make it more corrosive³¹. This was also observed by John³².
- 2) Because of the lower oxygen pressure of the nonequilibrium syngas, produced in entrained gasifiers, most commercial high chromium alloys cannot form a sulfur free protective oxide scale^{31,32} i.e., the gas composition falls to the left of the kinetic boundary for most practical alloys, with the possible exception of iron aluminides³³. However, aluminides can corrode rapidly in high pressure syngas containing HCl³¹.
- 3) The rate of the mixed oxide-sulfide scale growth decreases rapidly with temperature and several commercially available alloys may be acceptable, for some processes, especially at evaporator temperatures (300-450°) where most metal alloy components will be used. However, at superheater temperatures the corrosion rates of commercial alloys may become marginal. Thus, the approach of preventing excessive corrosion in mixed oxidant gases has changed from finding an alloy which will form a thermodynamically stable, impervious, generally pure oxide scale to that of finding alloys forming scales which will grow slow enough to provide commercially acceptable corrosion rates, in a given coal gasification environment. This is mainly a kinetic problem and can be highly dependent on factors other than oxygen and sulfur pressure of the gas composition alone. Perkins³⁴ has made a study of many variables affecting corrosion rates in syngas coolers including the effect of pressure, cyclic operation, deposits, HCl content of syngas, corrosion during downtime, etc. He comes to the conclusion that the effect of many variables is somewhat alloy specific. For instance, elevated pressure increases the corrosion rates of low alloy steel as they are dependent on the H₂S partial pressure, but not those of most stainless steels tested. The combination of high levels of HCl and pressure will result in accelerated attack on aluminide coatings. Cyclic operation generally increases corrosion rates, but deposits and temperature differentials between the alloy and the gas generally do not. However, deposits do have a major effect on corrosion during downtime, especially when they contain carbon and chlorides²⁰. His final conclusion is that isothermal atmospheric pressure corrosion tests are suitable for alloy screening, provided the syngas environment is duplicated as much as possible except for pressure. Thus, he recommends non equilibrium gas compositions containing impurities such as HCl, which are the same as used in commercial equipment under pressure. The gas flow during the test should be high enough to prevent shifts towards equilibrium at the test temperature. However to fully duplicate plant conditions, high pressure, high flow rate tests with cooled

samples, cyclic exposures including periods of downtime and deposits on the samples are required. Such tests are difficult and time consuming and will reproduce corrosive conditions for one gasification process and one coal only. It may, therefore, be difficult to generalize the results of such tests. Carefully controlled exposure tests in actual plants may be preferable.

In this study one of the objectives is to obtain corrosion data for a large number of closely related gas compositions. Therefore, the experimental approach recommended by Perkins for atmospheric pressure tests was selected, rather than high pressure testing.

3

RESEARCH OBJECTIVES

1. To study mixed oxidant corrosion in non equilibrium gas mixtures closely resembling those found in syngas coolers of gasifiers presently ready for commercial deployment.
2. To study the effect of H₂O partial pressure on corrosion rate and scale morphology of Fe-Ni-Cr alloys.
3. To compare corrosion rates of Fe-Ni-Cr alloys with small additions of sulfide formers (V), and oxide formers (Ti, Si, Al).
4. To determine the relation between corrosion products and the rate of corrosion and to identify the most desirable corrosion products, giving the lowest corrosion rates.

4

EXPERIMENTAL PROCEDURES AND CONCEPTS

4.1 GAS COMPOSITION ANALYSIS AND SELECTION

The composition of "raw" syngas entering the syngas coolers is rarely measured before quenching the gas after its passage through the syngas cooler(s). Gas compositions given by coal gasification process engineers are often on a waterfree basis, after desulfurization. "Raw" gas compositions are generally derived from process mass balance calculations and/or calculated back from the gas composition measured after the gas is quenched with water. An extensive compilation of gas compositions was given earlier by Natesan³⁵.

In general, the raw gas composition depends on the feed stock, usually coal, and the gasification process. The H₂S content in the gas is mostly dependent on the sulfur content of the coal, which is largely converted into H₂S under substoichiometric combustion conditions. Dependent on the amount of oxygen and steam used in the process, and the amount of sulfur retained in the ash, the H₂S content in syngas ranges from about 25-45% of the sulfur content of the coal in oxygen blown gasifiers and about half that for air blown gasifiers. The sulfur pressure of the gas is determined by the H₂S/H₂ ratio in the gas. This ratio is about the same for air and oxygen blown gasifiers and is determined mainly by the H₂S content of the gas. However, the H₂S partial pressure of the gas will be twice as high in oxygen blown gasifiers as in air blown gasifiers, when gasifying coals, with the same sulfur content.

The oxygen pressure of the gas depends on its CO₂/CO and H₂O/H₂ ratios. These are dependent on the gasification process which can be roughly divided in the following categories (Table 4.1)

- Entrained slagging gasifiers fueled with dry coal. The gas is characterized by a low CO₂ and H₂O content and thus has a very low PO₂. Steam is frequently added to dry coal fed entrained slagging gasifiers to moderate gasification temperature. Thus, the gas usually contains 1-2% H₂O.
- Entrained slagging gasifiers fueled with coal water slurries. The CO₂ and steam contents of the gas depend on the amount of coal in the slurry and are generally 5-10 times higher than in dry coal fed gasifiers.

Table 4.1
Typical Syngas Compositions (vol %)

Gasifier Type	CO	CO ₂	H ₂	H ₂ O	H ₂ S	CH ₄	N ₂
Oxygen blown gasifiers							
• Entrained, slagging							
• dry fed	62-64	2-4	27-30	0-3	0.2-1.2	tr	1-5
• slurry fed	35-45	10-15	27-30	15-25	0.2-1.2	tr	0-2
• Fluidized bed	30-40	10-15	24-28	11-20	0.2-1.2	3.5	0-2
Air blown gasifiers							
• fluidized bed	15-20	5-8	10-15	5-12	0.1-0.6	2-4	40-50

- Fluidized bed gasifiers. Fluidized bed gasifiers are generally fed with dry coal, but steam is injected to moderate the bed temperature. CO₂/CO and H₂O/H₂ ratios are in the same range as those of slurry fed entrained gasifiers. Because of the lower operating temperature, the gas also contains significant amounts of CH₄.

The descriptions above pertain mainly to oxygen blown gasifiers. CO₂/CO ratios and H₂O/H₂ ratios in equivalent air blown gasifiers are essentially unchanged, but the gas is diluted with 40-55% nitrogen. Thus, the oxygen and sulfur pressure of the gas remains unchanged.

There are several minor impurities in the syngas, most of which probably don't contribute to corrosion. Examples are vaporized metals such as Pb, Zn, As, Sb which are sometimes found in deposits on heat exchanger tubes, COS and other minor sulfur species. The exception is HCl, which is derived from chlorine compounds in the coal. Direct measurements of the HCl content of syngas are not published. From data of boilers fueled by high chlorine coal, it can be concluded that the chlorine in the coal is mostly converted to HCl³⁶ here, as well as under coal gasification conditions. However in boilers the HCl content of the flue gas is greatly diluted by excess air. Thus 0.1% chlorine in the coal will produce 50-80 ppm HCl in the flue gas. Under these conditions only coals containing chlorine in excess of 0.25% are prone to cause corrosion problems. In oxygen blown gasifiers, dilution with oxidant is much less, thus 0.1% chlorine in the coal will result in 200-400 ppm HCl in the syngas.

Calculations show that the gas compositions shown in Table 1 are in equilibrium only at the gasification temperature, usually above 1000°C. Apparently the gas flow through the syngas coolers is rapid enough to freeze in the high temperature equilibrium. This is desirable because massive carbon precipitation would occur if the gas would indeed shift to its low temperature equilibrium and thus make gasification economically unattractive. Heat exchangers in syngas coolers are also at a lower temperature than the surrounding

syngas. Thus, it can be concluded with great certainty that the syngas in contact with metallic alloys will not be in equilibrium in the temperature range of greatest interest 300-600°C. Therefore, non equilibrium gas compositions will be used in this study, even if it will complicate the theoretical interpretation of the data obtained. The main reason for selecting non equilibrium gases is that their oxygen and sulfur partial pressures usually differ considerably, from those of equivalent equilibrated gases³², which may lead to significant differences in corrosivity. This will be demonstrated in the next paragraphs.

To explore the differences in corrosion potential between equilibrium and non equilibrium gas mixtures, two model syngas compositions, representing dry coal and coal-water slurry fed entrained slagging gasifiers were selected (Table 4.2). Equilibrium gas mixtures resulting from these initial gas mixtures were calculated by Norton³⁷ using a modified solgas mix type computer program.

Table 4.2
Model Syngas Compositions (vol %)

	Gas 1	Gas 2
H ₂	32	30
H ₂ O	-	15
CO	64	45
CO ₂	3.8	9.8
H ₂ S	0.2	0.2

The oxygen and sulfur pressures of the non equilibrium gas are not uniquely defined. Approximate sulfur and oxygen pressures can be calculated from the CO₂/CO, H₂O/H₂, and H₂S/H₂ ratios in the gas using a procedure suggested by Perkins³⁸. For instance, the equilibrium oxygen pressure at high temperatures is calculated as follows:



$$K_p = \frac{p_{\text{CO}_2}}{p_{\text{CO}} (p_{\text{O}_2})^{1/2}} \quad (\text{eq. 2})$$

$$\text{Log } p_{\text{O}_2} = 2 \text{ Log } \frac{p_{\text{CO}_2}}{p_{\text{CO}}} - 2 \text{ Log } K_p \quad (\text{eq. 3})$$

where K_p is the equilibrium constant from the Janaf tables³⁹ and $p_{\text{CO}_2}/p_{\text{CO}}$ is the high temperature equilibrium pressure ratio. According to Perkins, the "non equilibrium" oxygen pressure $p_{\text{O}_2}^1$ at a lower temperature is obtained by substituting the equilibrium constant K_p^1 for that temperature in equation (3), while keeping the pressure ratio $p_{\text{CO}_2}/p_{\text{CO}}$ of the gas constant.

For water containing syngas, the non equilibrium p_{O_2} can also be calculated using the H_2/H_2O ratio and the K_p of the reaction $H_2 + \frac{1}{2}O_2 \rightarrow H_2O$. This gives a different value when the gas is not in equilibrium. The plots of $\log K_p$ as a function of $1/T$ are straight lines for the CO_2/CO and H_2O/H_2 equilibria, (Figure 4.1). Thus the p_{O_2} calculated from these equilibria decreases with decreasing temperature as shown in Figure 4.2. In the temperature range of interest, 300-600°C, the equilibrium oxygen pressure is always higher than the non equilibrium oxygen pressure. The difference increases with increasing temperature. For water containing gases, the p_{O_2} calculated from the H_2O/H_2 ratio is higher than that calculated from the CO_2/CO ratio but still lower than the equilibrium oxygen pressure. Thus, the oxygen pressure, and presumably the oxidation potential of the gas is not uniquely defined. It can be argued on kinetic grounds that the oxygen pressure calculated from the H_2O/H_2 ratio is the most likely to determine the corrosivity of the gas as high pressure steam generally is a more aggressive oxidant than CO_2 .

A similar approach is used to calculate the non equilibrium p_{S_2} , using the high temperature equilibrium H_2S/H_2 ratio, but the low temperature K_p of the reaction $H_2 + \frac{1}{2}S_2 \rightarrow H_2S$.

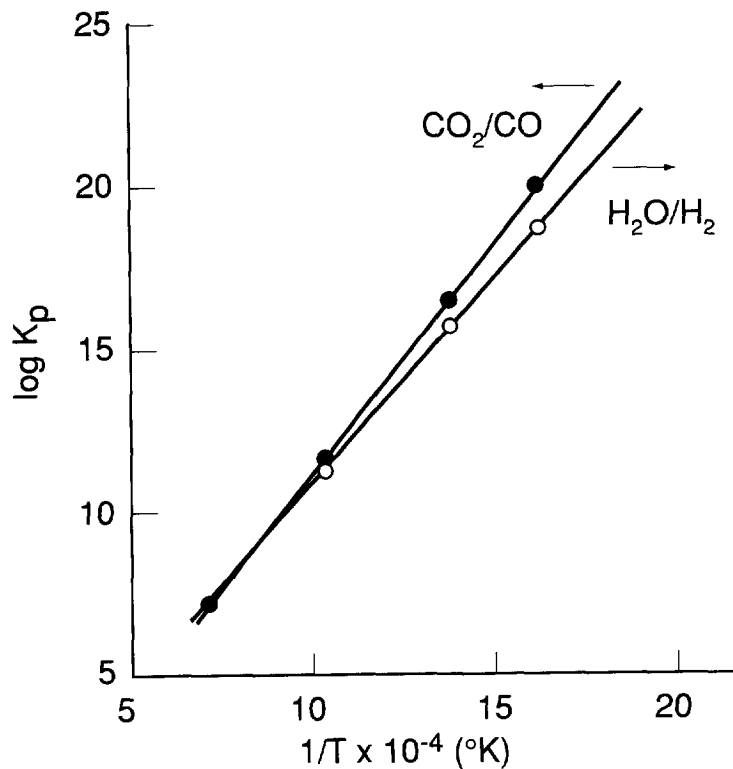


Figure 4.1
Equilibrium Constants of CO_2/CO and H_2O/H_2 Reactions

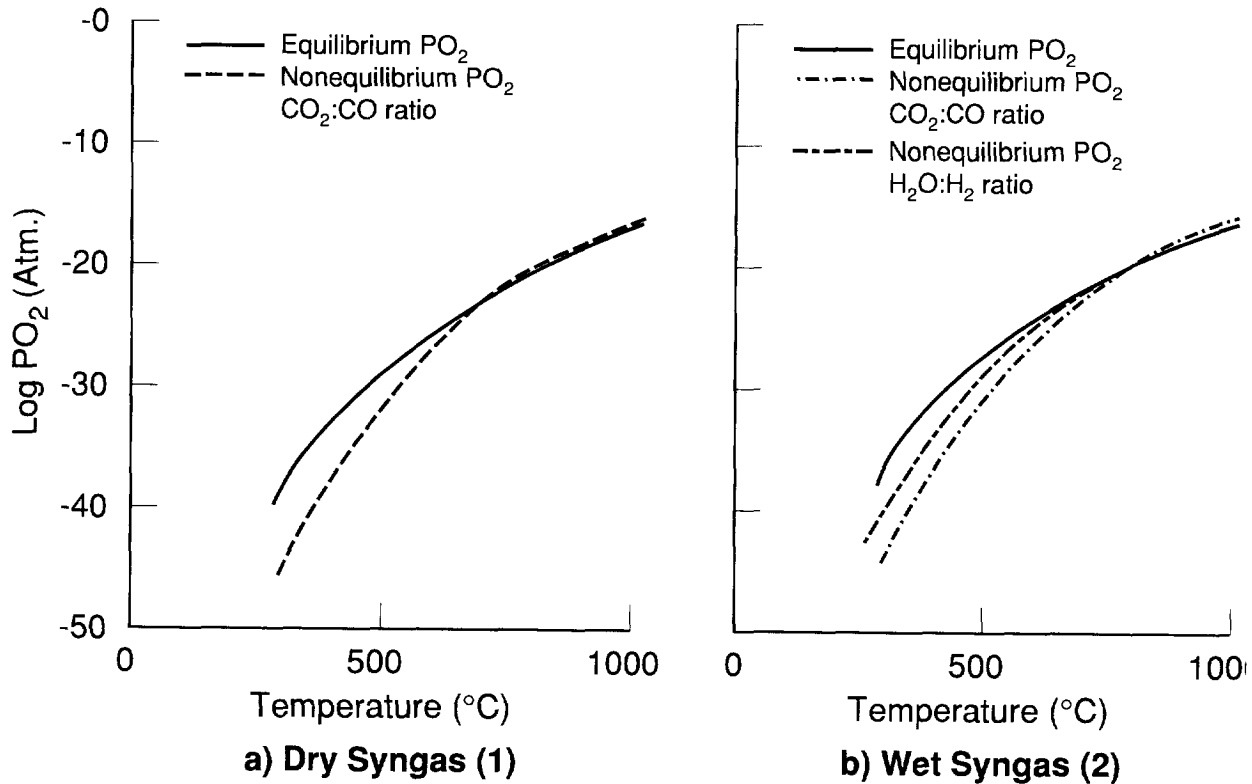


Figure 4.2
Equilibrium and Nonequilibrium Oxygen Pressures of Syngas

The plot of Log K_p from the Janaf tables as an inverse function of T for the H_2S/H_2 equilibrium shows a discontinuity between 700 and 800K (424-525°C) as shown in Figure 4.3. This discontinuity is not possible from a thermodynamic point of view. However, a change in slope at the boiling point of sulfur; 713 K (440°C), is likely. This discrepancy points to an error in the data given in the Janaf tables. In any case, it is likely that the decrease in sulfur pressure with temperature becomes less pronounced at temperatures below 440°C, as is shown in Figure 4.4. The PS_2 calculated from the equilibrium data does not show this decrease, most likely because the computer program used data extrapolated from higher temperatures. The difference in PS_2 of the water containing and water-free gases is relatively small, as the H_2 content of the gas does not change significantly. Thus the PS_2 is mainly dependent on the H_2S content of the gas. A 0.6% difference in H_2S results in about one order of magnitude difference in the non equilibrium PS_2 . The discrepancy in PS_2 at around 440°C will not affect the data presented here, as this study only covers mixed oxidant corrosion at 540°C.

Since the corrosive potential of syngas is believed to be mainly determined by its PO_2 and PS_2 and the PS_2 depends mainly on the H_2S content of the gas, which is constant for a given coal, it is of interest to know how the non equilibrium PO_2 of a syngas changes

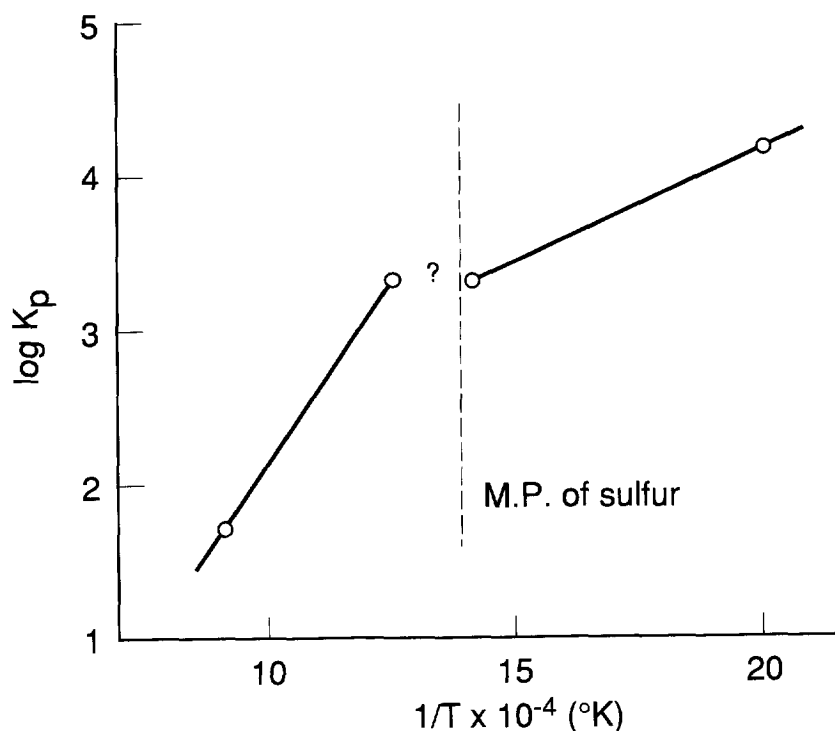


Figure 4.3
Equilibrium Constants of $\text{H}_2\text{S}/\text{H}_2$ Reaction

when its steam content is increased. The result of the calculation is shown in Figure 4.5. It shows that small amounts of steam in nominally dry syngas will sharply raise its PO_2 , while increasing the steam content from 10-15% causes only a small change in PO_2 . This could be of practical interest as nominally water-free syngas from dry coal fed entrained slagging gasifiers generally contains 1-3% steam, which may change its corrosive potential considerably.

Based on the discussion above the main gas compositions selected for this study are those shown in Table 4.3. All gas compositions are non equilibrium to best simulate plant operating conditions. The steam content is varied from 0 to 15%, which covers most of the gas compositions found in entrained and fluid bed gasifiers, with special emphasis on gas compositions with a low water content. Two levels of H_2S were selected 0.2 and 0.8%, which are representative of low and high sulfur coals, respectively. In addition, 400 ppm HCl was added to all compositions. Figure 4.6 shows the location of the gas mixtures on the Cr-O-S phase equilibrium diagram. Two other dry gas compositions were chosen with CO_2/CO ratios, calculated to provide a PO_2 , similar to that of the PO_2 of gases containing 5 and 15% H_2O , respectively, based on the $\text{H}_2\text{O}/\text{H}_2$ ratio.

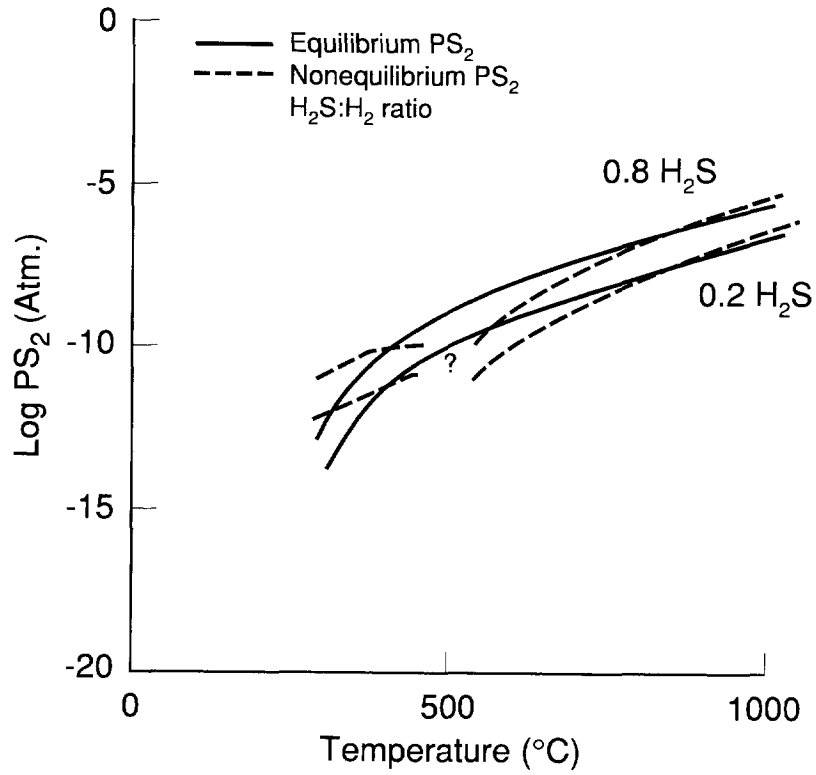


Figure 4.4
Equilibrium and Nonequilibrium Sulfur Pressure of Syngas

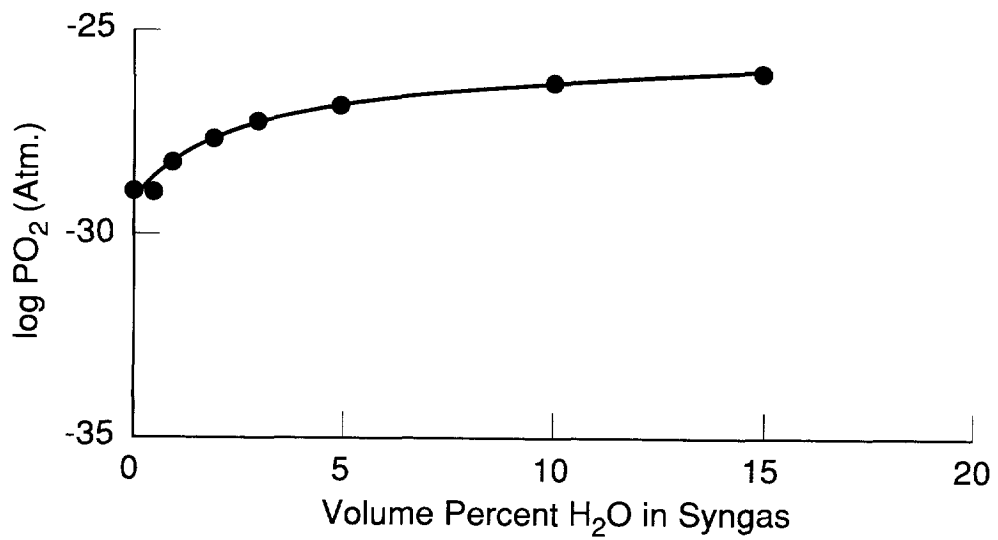


Figure 4.5
Nonequilibrium Oxygen Pressure of Syngas as a Function of Steam Content at 550°C

Table 4.3
Nonequilibrium Gas Compositions Used in This Study (vol %)

	0	1**	2**	3	4**	5	6	7	8*	9*
H ₂ O	0	0	1	2	3	5	10	15	0	0
H ₂	31.1	32	30.2	29.2	28.8	28.2	28.2	30	29.2	30
CO	68	64	64	64	64	60	52	45	23	42
CO ₂	0.1	3.2	4	4	4	6	9	9.2	47	27.2
H ₂ S	0.8	0.8	0.8	0.8	0.8	0.8	0.8	0.8	0.8	0.8
HCl	0.04	0.04	0.04	0.04	0.04	0.04	0.04	0.04	0.04	0.04
Log PO ₂ (550°C)	-32.2	-29	-28.4	-27.8	-27.4	-27	-26.4	-26.0	-26	-27.0

* dry gas mixtures with same PO₂ as wet gas mixtures containing 15 and 5% H₂O, respectively.

** similar gas mixtures with 0.2% H₂S were also studied, gases 1A, 2A and 4A.

Notes: 1. Nonequilibrium PO₂ calculated from H₂O/H₂ equilibrium except in dry gas mixtures
2. Nonequilibrium PS₂ same for all gas mixtures: for 0.8% H₂S Log PS₂ = -9.3,
0.2% H₂S, Log PS₂ = -10.5

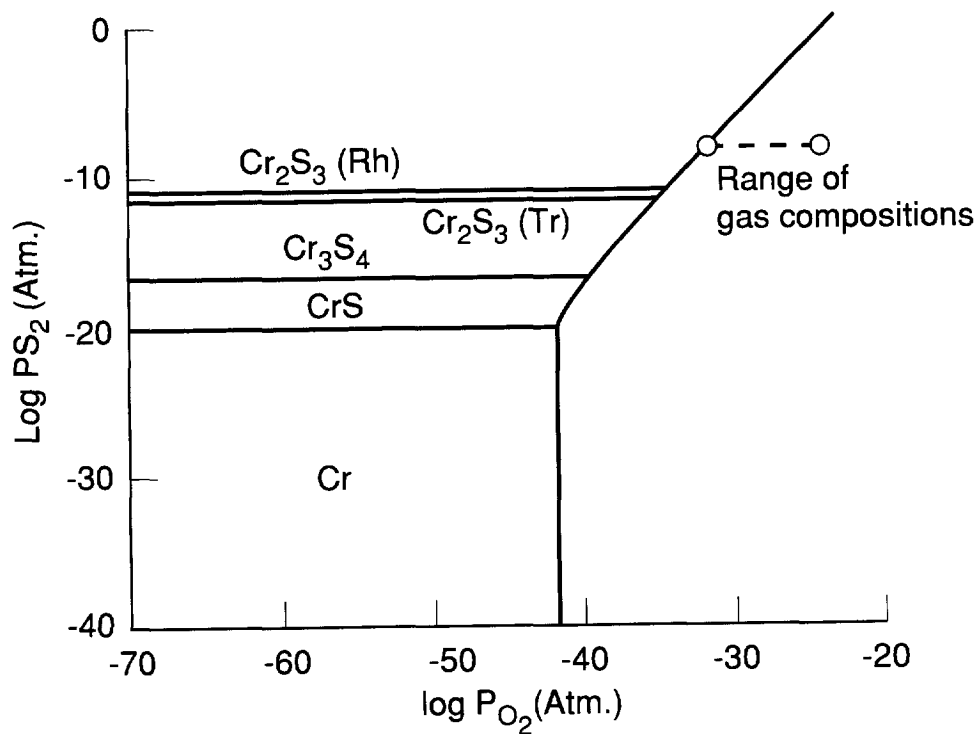


Figure 4.6
Cr-O-S Phase Diagram at 550°C

4.2 ALLOY SELECTION AND PREPARATION

4.2.1 Alloy Selection

To limit the scope of the proposed research, it was decided to study fully austenitic alloys only. To obtain a better understanding of the effect of minor alloying elements, the chromium content of the model alloy was kept constant at 20%. This is not necessarily the optimum chromium content for a commercial alloy for use in coal gasification, but it was feared that the effect of the chromium would obscure the influence of the minor alloying additions, at higher chromium contents. To make the model alloys more similar to commercial alloys 0.3% silicon and 1.0% manganese were added to each alloy, which approximately represents the level of these common impurities in commercial stainless steels.

The following minor alloying elements were selected and added at a nominal 3.25% level:

- **Vanadium.** This element was selected because the V-O-S phase stability diagram⁴⁰ (Figure 4.7) suggests that it should form stable sulfides, most likely V_2S_3 in most of the test gases used in this study. Previous work by Bakker and Perkins⁴¹ has also suggested that vanadium will reduce aqueous corrosion during downtime and may reduce high temperature sulfidation rates, at least in gas mixtures with a high water content.
- **Titanium.** This element was selected because the Ti-O-S phase stability diagram⁴⁰ suggests that it should form TiO_2 in most of the gas mixtures in this study. (Figure 4.8) However, the gas compositions are close to the boundary of the TiS_2 and TiO_2 phase stability fields. Thus, it is likely that both TiS_2 and TiO_2 can form, at least initially, before equilibrium conditions are established. The situation here is very similar to that of chromium (Figure 4.6). Although the phase stability diagram indicates Cr_2O_3 as the most stable phase, chromium sulfides can and will form in gases similar to those proposed in this study^{24,42}.
- **Silicon and Aluminum.** These elements were selected because they are expected to form oxides in all gas composition in this study, as the gas compositions are far away from the oxide/sulfide phase boundaries and probably well to the right of the "kinetic boundary" as defined earlier by Perkins and Natesan^{24,42} (section 2.2).

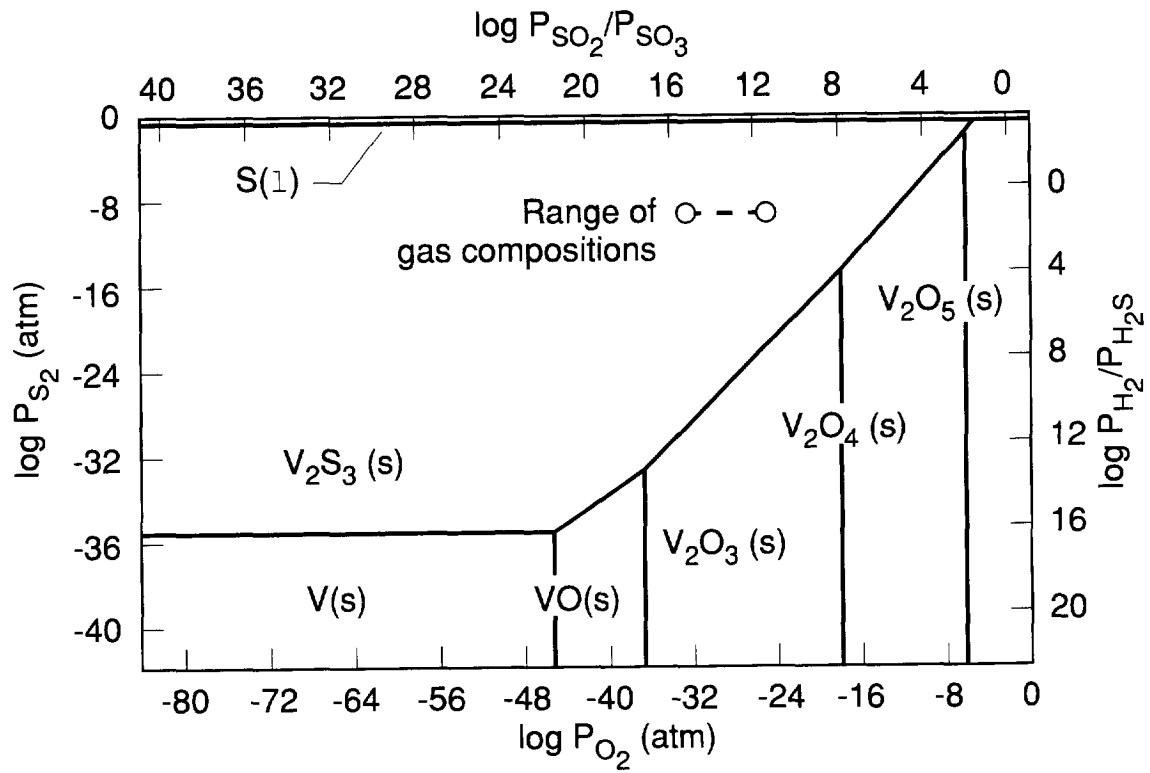


Figure 4.7
Condensed Phase Equilibria for the V-O-S System at 550°C (823°K)

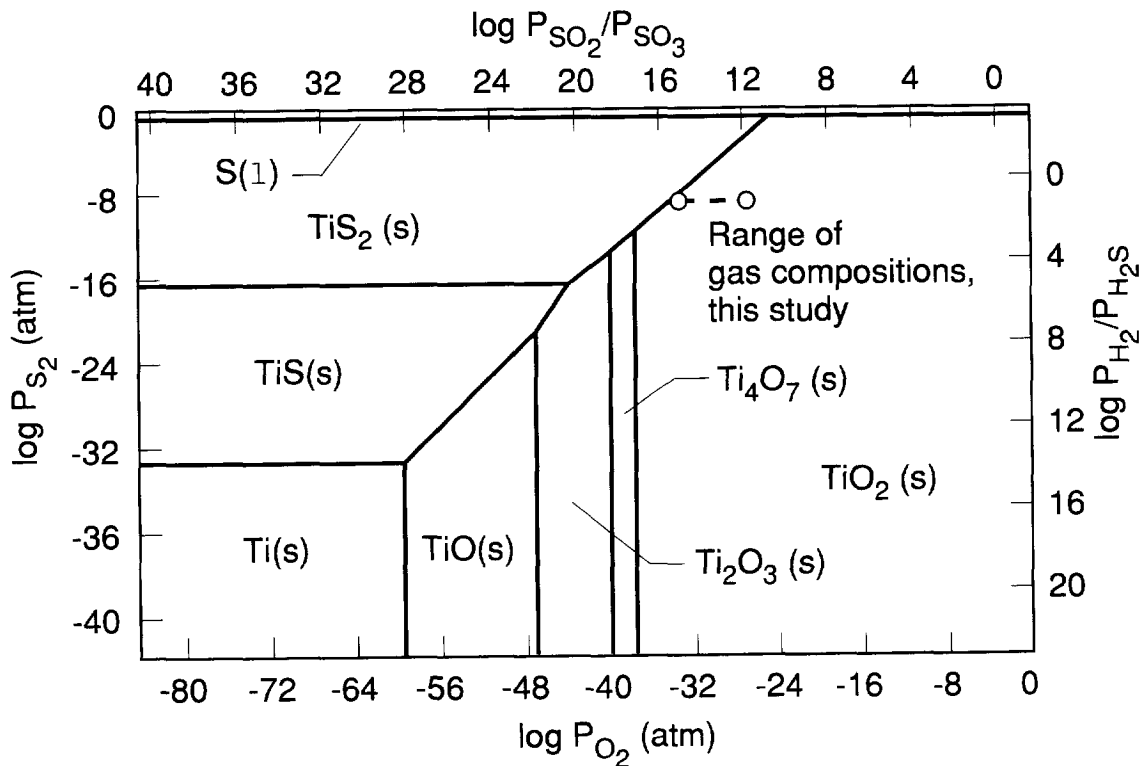


Figure 4.8
Condensed Phase Equilibria for the Ti-O-S System at 550°C (823°K)

The nickel content of the alloys was chosen to be 35%, high enough to ensure a fully austenitic structure even when the strongest ferrite stabilizer is added. This is usually done by plotting the Ni equivalent against the chromium equivalent on a Schaeffler diagram⁴³, i.e

$$\% \text{ Ni eq} = \% (\text{Ni}) + 30 (\% \text{ C}) + 25 (\% \text{ N}) + 0.5 (\% \text{ Mn})$$

$$\% \text{ Cr} = \% (\text{Cr}) + 2\% (\text{Si}) + 5\% (\text{V}) + 5.5 (\% \text{ Al}) + 1.5 (\% \text{ Ti})$$

Since C and N were not deliberately added to the alloy, their content will be assumed to be low enough to be ignored. Since Al is the strongest ferrite stabilizer, the Al containing alloy will be most likely to form ferrite. Its Ni and Cr equivalents are, respectively, 35.5 and 38.5. The diagram (Figure 4.9) indicates that all alloys will be fully austenitic.

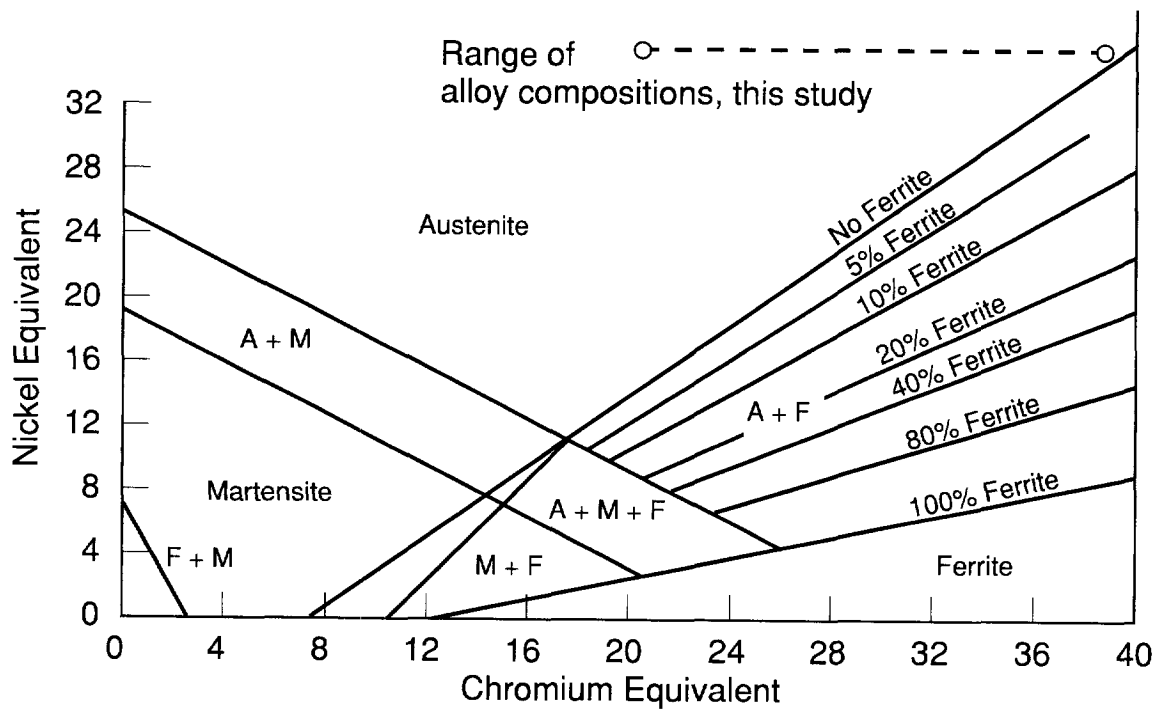


Figure 4.9
Modified Schaeffler Diagram

4.2.2 Alloy Preparation

Melting and Casting

Alloys are melted in a vacuum induction furnace. An initial charge of iron, nickel and chromium is placed directly in a magnesium oxide crucible. The total weight of the charge is approximately 2.5 Kg. The air inside the furnace is evacuated using a rough vacuum pump. The initial charge of iron, nickel and chromium takes approximately twenty minutes to melt. At this time the minor alloying additions are made via a drop 'bucket' mounted just above the crucible. Adding these elements at the last minute minimizes oxidation and results in final chemistry close to target. A graphite rod is used to push the alloys below the molten surface. This final charge is held for two additional minutes and is then poured into a 38 × 38 × 125 mm tall graphite mold. Table 4.4 shows the target and actual composition of the alloys.

Table 4.4
Composition of Experimental Alloys

	Alloy	Ni	Cr	Mo	V	Nb	Ti	Al	Si	Mn	Fe	C
A	Target	35.0	20.5	-	-	-	-	-	0.3	1.0	bal	<0.1
	Actual	34.9	20.8	-	-	-	-	-	0.42	0.21	bal	n/a
B	Target	35.0	20.5	-	3.25	-	-	-	0.3	1.0	bal	<0.1
	Actual	34.5	20.2	-	3.61	-	-	-	0.35	1.16	bal	n/a
C	Target	35.0	20.5	-	-	-	3.25	-	0.3	1.0	bal	<0.1
	Actual	35.3	20.5	-	-	-	3.42	-	0.55	0.76	bal	n/a
D	Target	35.0	20.5	-	-	-	-	-	3.25	1.0	bal	<0.1
	Actual	34.4	20.8	-	-	-	-	-	3.67	0.92	bal	n/a
E	Target	35.0	20.5	-	-	-	-	3.25	0.3	1.0	bal	<0.1
	Actual	34.8	20.4	-	-	-	-	3.37	0.38	0.79	bal	n/a

Heat Treating and Rolling

The 38 × 38 × 125 mm ingot is heated in air to 1030°C then rolled in a mill. Several rolling passes are made, each reducing the thickness by 10-15% until the final thickness is approximately 2.5mm. The ingot is reheated to 1030°C in air between each pass. After the last pass, the plate is heat treated at 1030°C for one hour in air, followed by a water quench.

Early on sample coupons were cut from the 2.5mm thick plate, solution heat treated to 1150°C for ten minutes in argon, and then water quenched. This was performed to insure complete solution of carbides. Later on the samples cut from the plate were inadvertently not solution heat treated. A test was run using alloy A to determine if the lack of solution

heat treatment made a difference in corrosion rate. The test data showed no significant difference in metal recession.

Alloys D and E were fabricated later and did not have the one hour exposure in air to 1030°C. Instead, they were solution heat treated at 1150°C for 10 minutes in argon, followed by a water quench.

The microstructure of each alloy and ASTM grain size number are shown in Figure 4.10.

Sample Preparation

The heat treated and hot rolled plates are machine lapped, flat and parallel, to within 25 μ m. Very small samples relative to the plate size are cut and are therefore flat and parallel to less than 5 μ m.

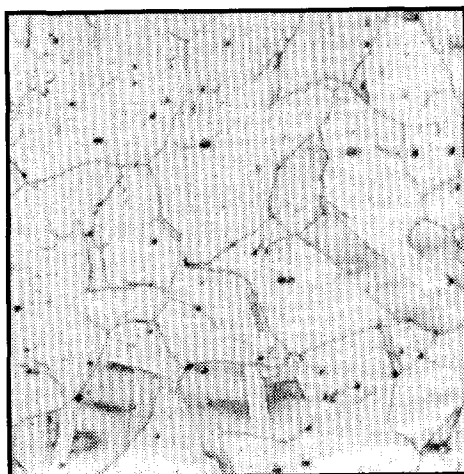
The size of the samples cut is approximately 12.5 \times 9 \times 2.5mm. A small hole is drilled into each sample to accommodate a platinum hanging wire. The cut sample surfaces are lightly ground to 300 grit finish using silicon carbide sanding paper. Digital calipers were used to measure the length and width of each sample. A single ball micrometer was used to measure the thickness of the samples to within 1 micron. Finally each sample was weighed on a Sartorius balance to within 0.0001 grams, after affixing a platinum hanger wire.

4.3 CORROSION TEST PROCEDURES

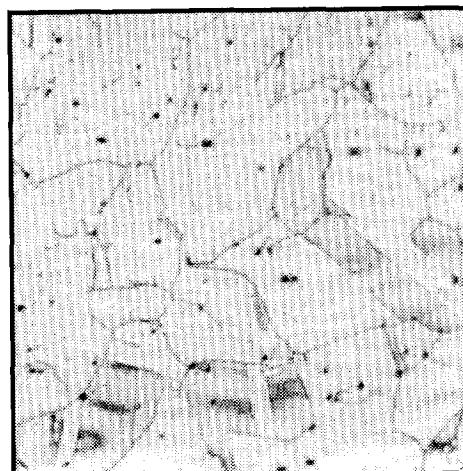
4.3.1 Corrosion Test Furnace Description and Test Procedures

The corrosion furnace is shown schematically in Figure 4.11. The samples are exposed inside a 75 mm diameter alumina tube. The furnace utilizes resistance heating which in turn heats the alumina tube by radiation. A control thermocouple is located just inside the furnace windings. It maintains the furnace temperature to within $\pm 5^\circ\text{C}$. A monitor thermocouple is located in close proximity to the samples. Teflon covers with ethylene-propylene gaskets are used to seal the ends of the alumina tube. The temperature of these covers is maintained above 100°C to prevent condensation. The samples hang on a five-inch long platinum 'tree' which was fabricated from several strands of twisted platinum wire. The tree hangs from a single platinum wire. A thermal gradient exists in the furnace, but was generally kept to less than $\pm 10^\circ\text{C}$ for the alloys studied here.

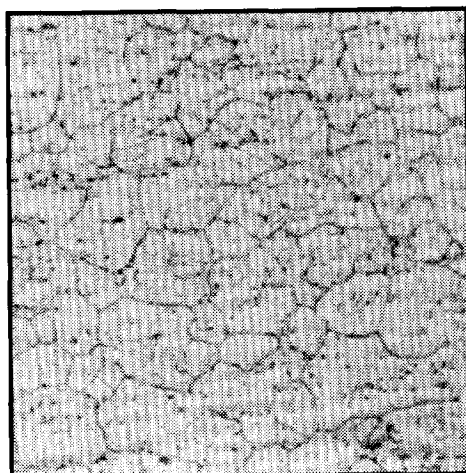
The syngas enters through the bottom Teflon cover having a total flow rate of 1 liter per minute. The gas rises through the vertical tube containing the samples. The syngas exits through the top of the furnace, then passes through a water-cooled glass condensing tube. Condensed water is collected in a plastic reservoir where it is later weighted to calculate



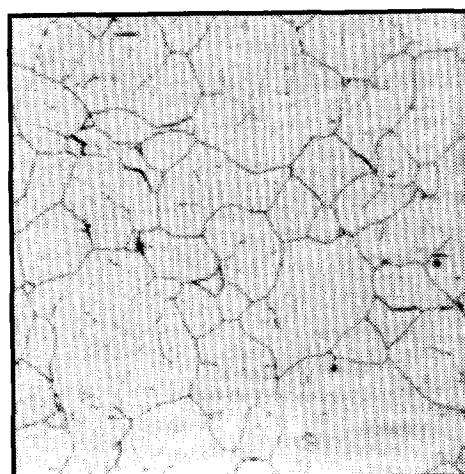
Alloy A) ASTM 2



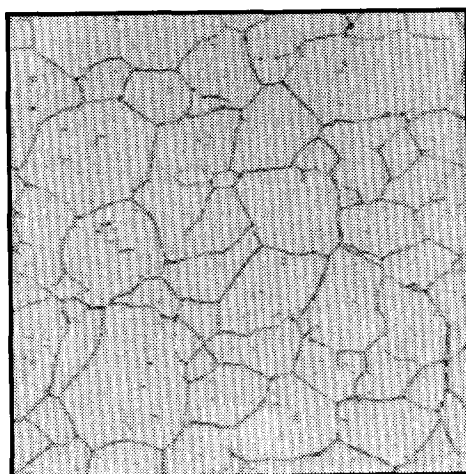
Alloy B) ASTM 2



Alloy C) ASTM 3-4



Alloy D) ASTM 3



Alloy E) ASTM 3

ASTM grain sizes:
2 - 180 μ m
3 - 120-125 μ m
4 - 90 μ m

Figure 4.10
Microstructure of Experimental Alloys (100x)

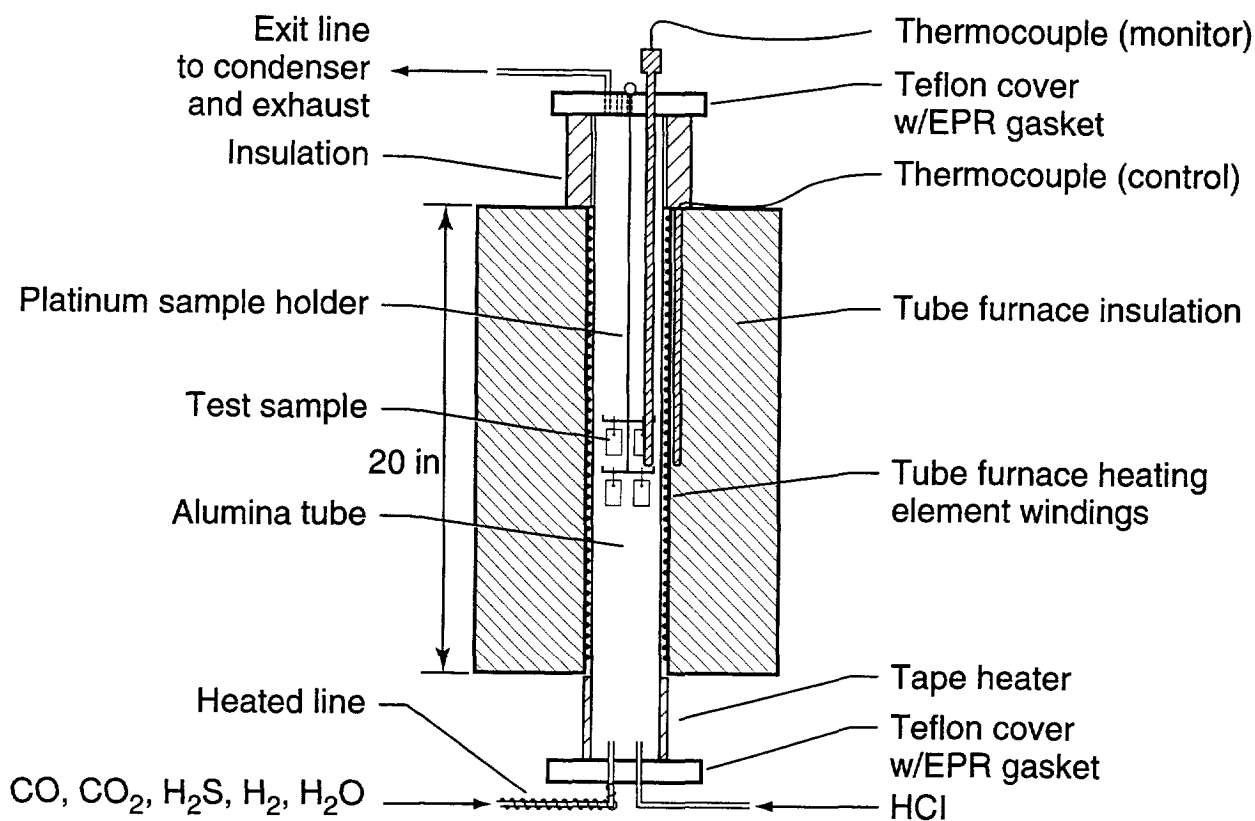


Figure 4.11
Schematic of Corrosion Test Furnace

the average water content of the gas. Water not condensed because of room temperature humidity is carried off by the exit gas. This uncondensed water is taken into account via a mathematical correction factor, based on the percent humidity at ambient temperature. The flow rate of 1000 cc/min. is considerably less than the flow rate in actual gasifiers, but considered fast enough to prevent a shift from the non-equilibrium to the equilibrium gas composition, as indicated by the lack of carbon deposition, which would be the most visible result of a shift to equilibrium³⁸.

Prior to startup the furnace is purged with argon or nitrogen. Syngas is admitted to the furnace about 10 minutes before turning on the heat. Heat up rate is approximately 14°C/min., thus allowing the furnace to reach 550°C in about 40 minutes. At the end of each corrosion test, the syngas is shut off and the furnace is purged with argon or nitrogen during cool down. The cool down rate is about 2°C/min.

4.3.2 Gas Flow Control

Ball-float rotameters with needle valves are used to control the flow rates of the various gases. Each rotameter is calibrated by flowing the gas from the rotameter into the bottom of a glass column of known volume that has a film of soap across the cross section. The

amount of time it takes the soap film to rise through the known volume is measured. A flow rate is then calculated.

The carbon monoxide, carbon dioxide, and hydrogen sulfide/hydrogen mixture combine together via a manifold immediately after flowing through their respective rotameters. The hydrogen gas can be switched to pick up moisture and then is tied into this line closer to the furnace. The hydrogen chloride/hydrogen mixture flows in it's own Teflon line directly to the bottom of the test vessel. A schematic diagram showing this gas flow configuration is shown in Figure 4.12.

As the gas in each supply cylinder is consumed, the pressure indicated on the cylinder's regulator drops accordingly. The amount of gas that should be consumed each day is calculated based on the internal volume of the cylinder. This corresponds to a specific drop in pressure that can be read directly from the cylinder regulator. Daily readings of the pressure regulators on each cylinder of gas are documented to ensure that the correct amount of gas is being consumed.

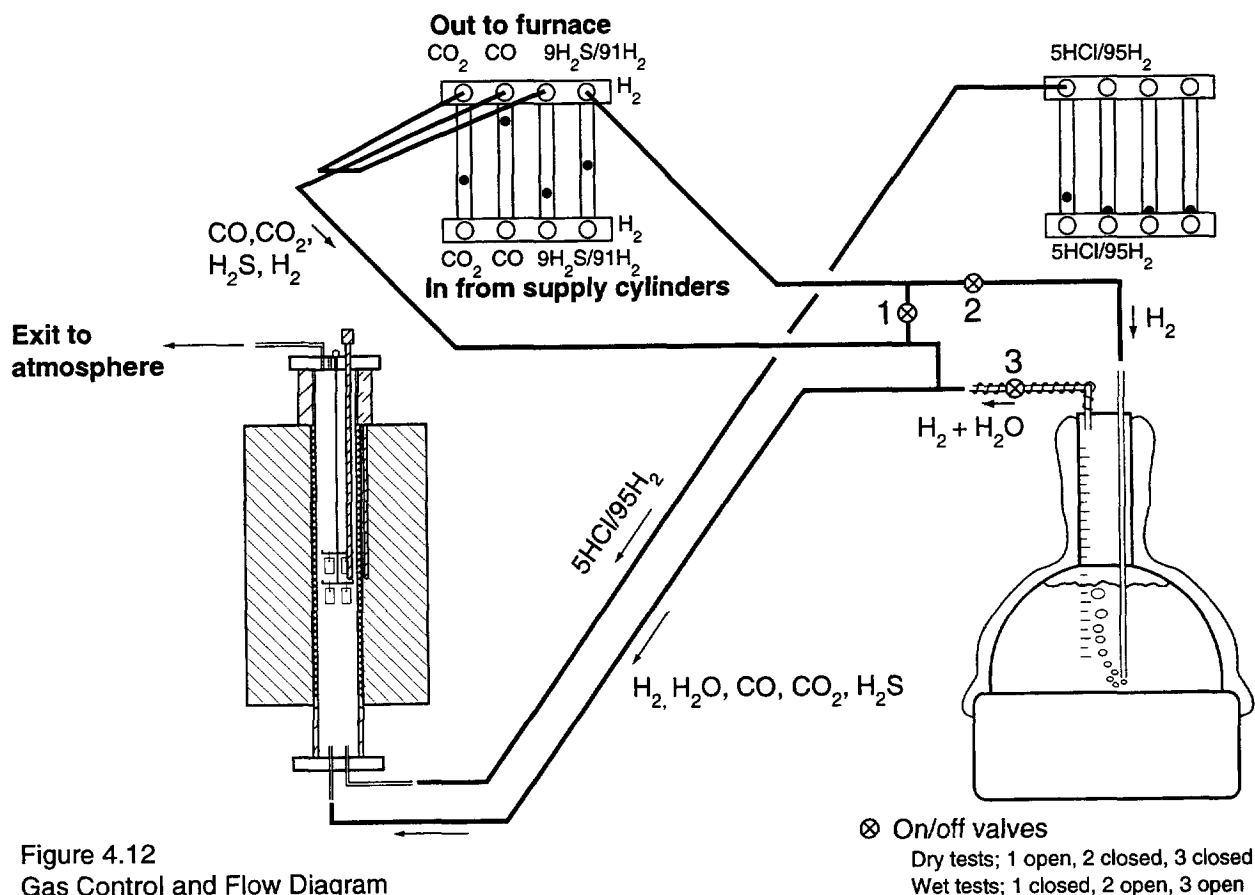


Figure 4.12
 Gas Control and Flow Diagram

4.3.3 Water Addition Procedure and Control

In tests where water is part of the gas composition, hydrogen gas is diverted to a water addition system before it is mixed with the remaining gases. This water addition system is shown schematically in Figure 4.13. The hydrogen is passed to the bottom of a glass boiling flask via a stainless steel tube. As the hydrogen exits into the water it picks up an amount of moisture that is dependent on the water temperature. The hydrogen/water vapor rises in the column of the boiling flask. It is the temperature at the top of the column, where the outlet tube exits, which ultimately determines how much water vapor will enter the test vessel. This temperature is controlled using a thermistor probe coupled to a proportional controller. The thermistor probe is mounted at the same vertical height as the outlet tube and controls the glass flask heater. The exiting hydrogen/water vapor mixture passes into a stainless steel tube that is heated to a greater temperature than the column temperature to prevent condensation.

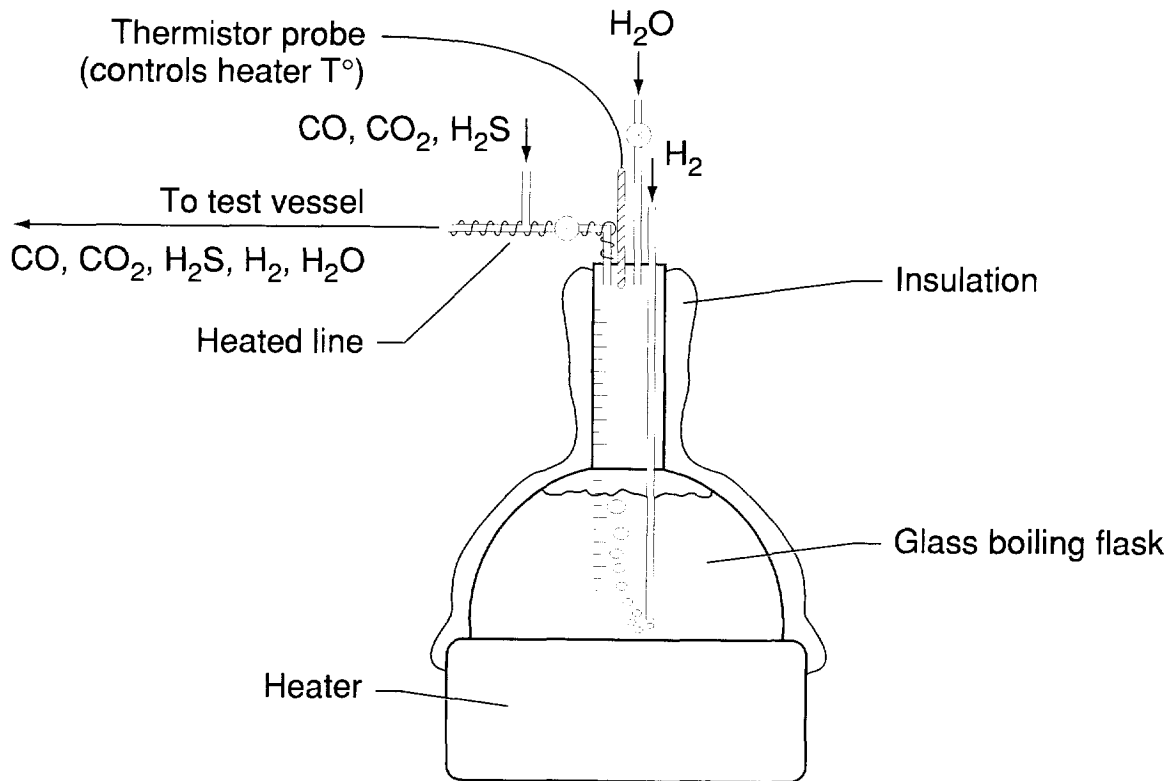


Figure 4.13
Schematic of Water Addition System

The set point temperature of the thermistor probe is determined using data from published steam tables, as shown in Table 4.5. The following is an example of how the temperature of the water in the flask is determined in order to achieve 2% water vapor:

Conditions:

Hydrogen Flow Rate = 210cc/min.

Total Flow Rate = 1000cc/min.

Need 20cc/min. Water Vapor to achieve 2% water in gas mixture

44°C water has a vapor pressure of = 68.26 mm Hg and thus contains

$68.26 \text{ mm Hg} \times \frac{1\text{atm}}{760\text{mmHg}} = 0.0898 \text{ atm}$ 'Saturated Steam'. This results in

$$\frac{0.0898\text{atm}}{(1\text{atm} - 0.0898\text{atm})} = 0.0987 \text{ 'Steam Pick-Up' per cc H}_2$$

In a Test Where the H₂ Flow Rate is 210cc/min.:

$$\begin{aligned} \text{Total Steam Pick-up} &= 210 \text{ cc H}_2 \times \frac{0.0987\text{ccSteam}}{\text{ccH}_2} \\ &= 20.7 \text{ cc Steam} \end{aligned}$$

$$\frac{20.7\text{ccSteam}}{1000\text{ccSyngas}^*} \times 100 = 2.07\% \text{ Steam}$$

*includes steam

The multiplication factor has been calculated for each temperature in Table 4.5. Any hydrogen flow rate used in a test is simply multiplied by various 'steam pick-up' multiplication factors until the desired quantity of steam results. The corresponding temperature of that multiplication factor is then used as the set-point temperature. The percent steam in the gas mixture has been calculated for a range of temperatures for a hydrogen flow rate of 210 cc/min. These data have been plotted in Figure 4.14.

Table 4.5
Water Vapor Pressure as a Function of Temperature

Temp. (°C)	Vapor P° (mmHg)	% Saturated Steam	Steam Pick-up/ cc H ₂
20	17.54	2.31	0.024
25	23.76	3.13	0.032
30	31.82	4.19	0.044
35	42.18	5.55	0.059
40	55.32	7.28	0.079
45	71.88	9.46	0.105
50	92.51	12.17	0.139
55	118.04	15.53	0.184
60	149.38	19.66	0.245
65	187.54	24.68	0.328
70	233.7	30.8	0.44
75	289.1	38.0	0.61
80	355.1	46.7	0.88
85	433.6	56.9	1.31
90	525.8	69.2	2.24
95	633.9	83.4	5.03

Water is added to the boiling flask daily. Calibrated markings on the boiling flask allow the amount of water consumed to be measured. This measurement is used as the basic control for steam additions. The temperature of the water is adjusted to stay as close as possible to the desired steam content. As shown in Figure 4.14, the steam pickup changes only slowly with temperature at low temperatures, but quite rapidly closer to the boiling point of water. Thus, there will be more variability in gases with water contents above 10%. Fortunately here the oxygen pressure of the gas does not change much as a function of water content as shown previously in Figure 4.5.

The daily water consumption is finally checked against the total amount of water condensed at the end of each test. Generally, the two measurements are within 10%. Usually the amount of water condensed at the exit was somewhat higher than that going into the furnace.

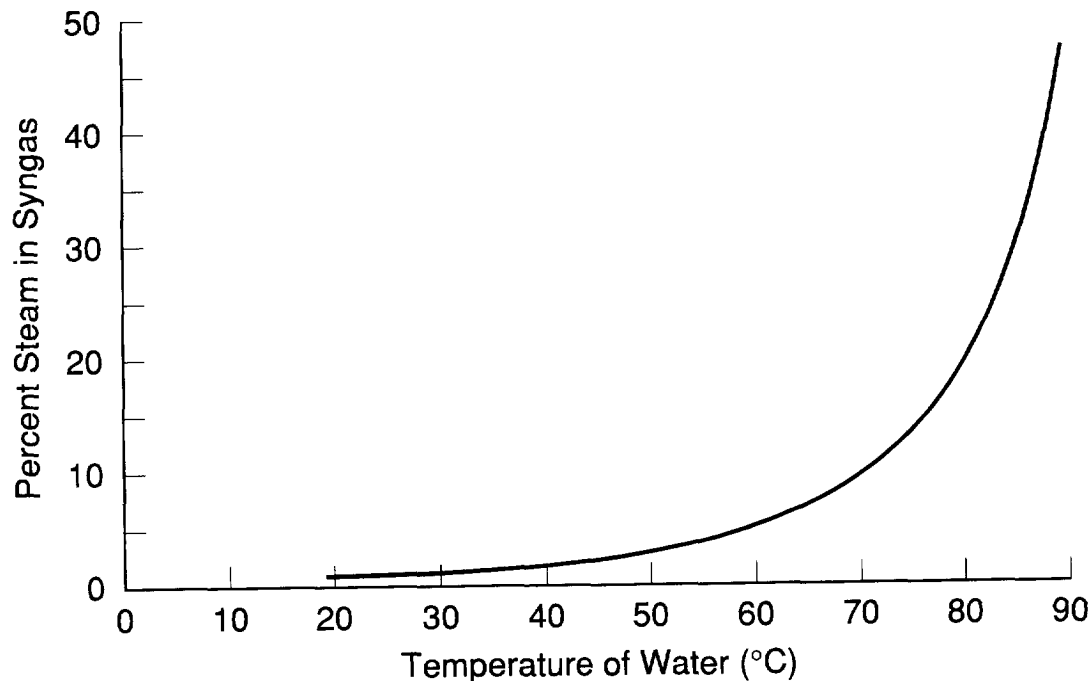


Figure 4.14
Steam Addition vs. Temperature at Hydrogen Flow Rate of 210 cc/min. Total Gas Flow = 1000 cc/min.

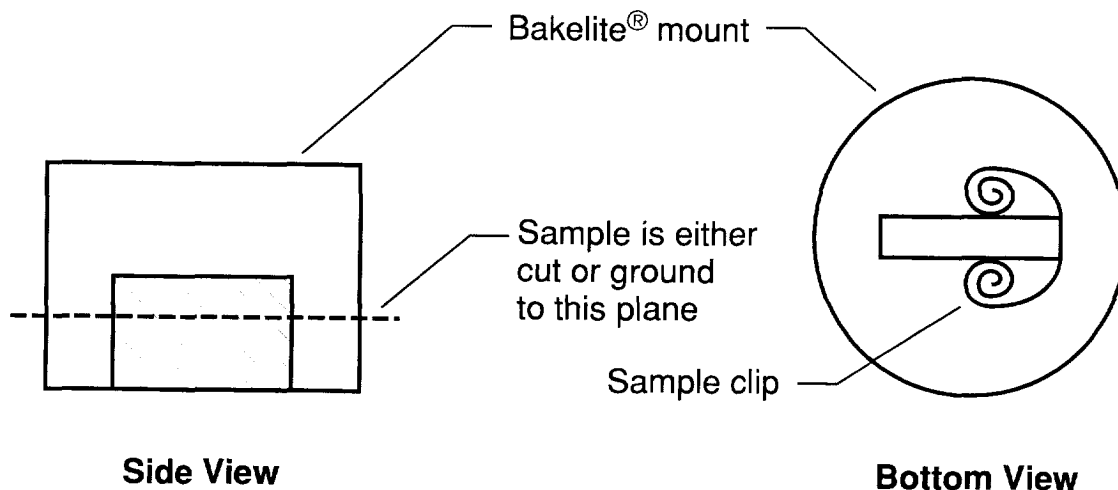
4.4 ANALYTICAL PROCEDURES

4.4.1 Sample Preparation and Optical Microscopy

After exposure to the syngas, the samples are once again weighed on the Sartorius balance. They are then observed using a 'wide-field' light microscope at ~30X. The external appearance of the samples is recorded. The weight gain/cm² is calculated. However, partial spalling usually occurs. This makes the use of weight changes as a means to calculate corrosion losses unreliable, except for very short exposures.

All samples are subsequently mounted for more detailed microscopic analysis and measurement of metal recession. The metallographic mounting procedure is given below:

1. Each sample is individually mounted on edge in a once-inch diameter die. A stainless steel sample clip is used to keep the mount perpendicular to the base of the die. This minimizes error in subsequent recession measurements. Bakelite is used as the mounting material.
2. The mounted sample is either ground in half, or, cut in half with a silicon carbide cut-off wheel. This is illustrated schematically in Figure 4.15.



Note: Sample clip is left out of side view drawing for clarity

Figure 4.15
Schematic Diagram of Sample in Metallographic Mount

3. The sample is then hand ground using silicon carbide grinding paper in the sequence of 180 grit, 320 grit and 600 grit. Care is taken to keep the sample flat and parallel.
4. An automated polishing wheel is used with one-micron diamond paste and a nylon cloth to remove the deformation from the grinding procedure.
5. Final polishing occurs in two steps:
 - a. Automated polishing wheel with a polishing slurry containing cerium oxide and a blend of other metallic oxides. This is used with a 1% solution of sodium hydroxide in distilled water to prevent aqueous corrosion and pitting during polishing. The polishing cloth is made of hard cotton to ensure sample flatness.
 - b. Automated polishing wheel with a micro-cloth is used briefly to remove any remaining fine scratches.
6. The sample is then cleaned, dried and ready for microscopic examination.

An optical microscope is used to study the general features of the corrosion scale and its morphology. One optical photomicrograph is taken to illustrate the typical scale appearance usually at 500-1000 magnification. Since it is difficult to maintain focus on all parts of the scale, 2 photographs are quite often taken and spliced together later. Optical microscopy is also used to measure the metal recession in two ways. A

microscope from a microhardness tester with a measuring scale is used to determine the remaining sound metal of each sample in the middle one half of the cross section in three different fields. First, the deepest penetration on the top edge is located, then that of the bottom edge and the distance between the two is measured (Figure 4.16). The measurements from the three locations, which are usually very close, are averaged, subtracted from the thickness of the original samples and divided in two to determine the total metal lost during the test exposure. The direct measurement of remaining sound metal works very well when the loss is relatively large ($>10\text{-}20\mu\text{m}$), provided the samples are mounted exactly perpendicular and cut at a 90° angle. To do this, the sample clip was found indispensable.

In addition to the sound metal loss, the thickness of the inward growing scale, is also measured and recorded. For samples with high corrosion losses, the sound metal loss measurement is generally larger than that of the scale thickness, indicating some scale spallation. For samples with low corrosion rates, the two measurements usually agree quite well. Occasionally the thickness of the inward growing scale is larger than the sound metal loss possibly indicating a slight error in sample mounting and cutting. In all cases, the largest measurement is considered the most correct one, since errors in the techniques used will result in lower measurements. Figure 4.17 shows an optical photomicrograph of a corroded alloy and indicates how the scale thickness is measured. In this study we will call the inward growing scale "topotactical" and the outward growing scale "epitactical". This usage is derived from previous studies of oxidation of boiler steels by hot water or steam, where both inward and outward growing magnetite scales are present⁴⁴.

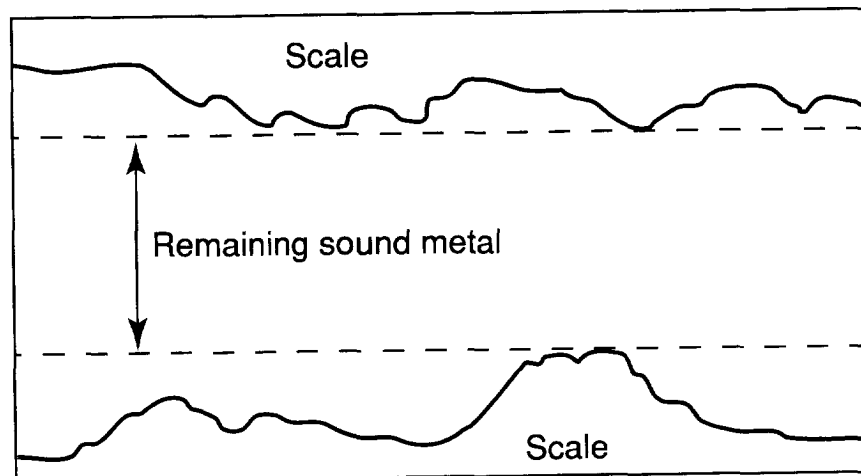


Figure 4.16
Measurement of Remaining Sound Metal

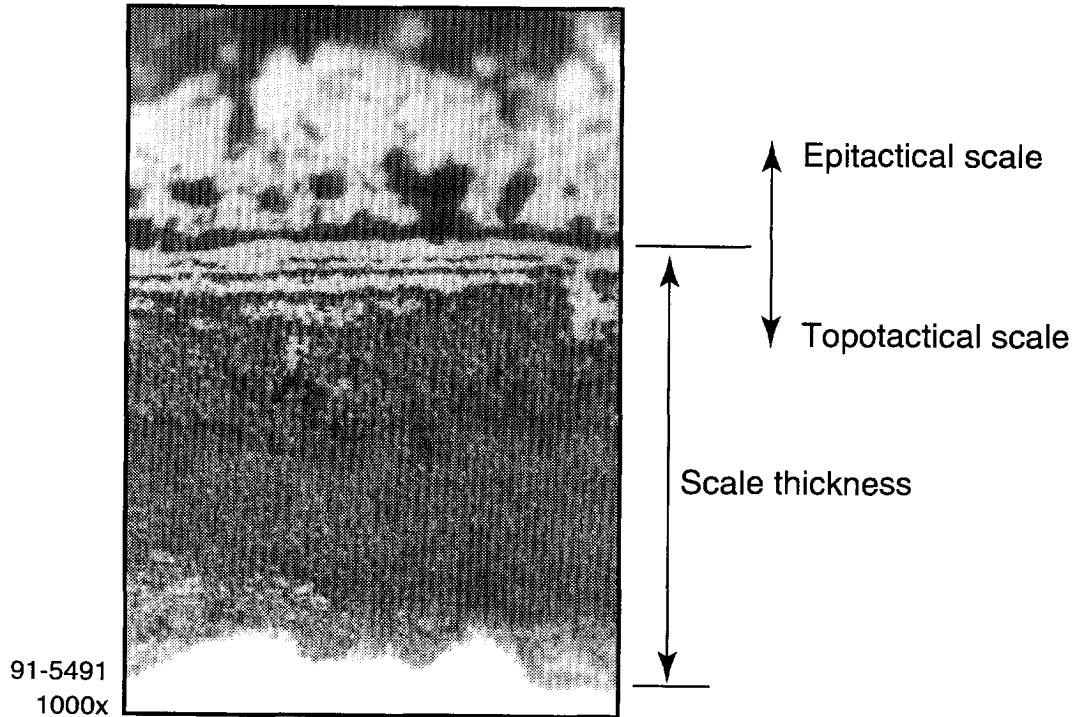


Figure 4.17
Measurement of Thickness of Topotactical Scale On Alloy A

Measurements on duplicate samples in the same corrosion run indicate that the reproducibility of the measurements is quite good as variations were generally less than $\pm 5 \mu\text{m}$ using samples showing 40-200 μm total corrosion. Reproducibility between duplicate runs was somewhat less, especially for alloys with high corrosion losses. However, the relative corrosion resistance of the alloys remained the same, in duplicate tests. Potential reasons for run to run variability are:

- 1) Variations in temperature and temperature gradients within the furnace
- 2) Small variations in moisture content
- 3) Random changes in initial nucleation of corrosion products; especially of alloys with low corrosion resistance.

In general, it is concluded that the accuracy of individual measurements is probably in the range of $\pm 10\%$, except for alloys with very high corrosion losses. This level of accuracy is considered sufficient to track trends of corrosion behavior as a function of gas composition and time.

4.4.2 SEM/EDS/WDS Analysis

The main objectives of the SEM analysis are as follow:

- (1) To determine the spatial distribution of the major alloying elements in the scale.
- (2) To determine the mineral composition of the scale in key areas.
- (3) To detect changes in alloy composition near the scale/metal interface.

Prior experience and initial experiments indicated that the composition of the scale is quite variable, thus requiring a large number of measurements to fully characterize the scale composition. It is, therefore, necessary to use a rapid method to determine the approximate chemical composition of the scales at various distances from the scale/metal interface. Scanning electron microscopy, equipped with EDS or WDS microanalyzers is the most applicable technique to meet the objective stated above. W.D.S. (wave length dispersive spectroscopy) will provide the most accurate chemical analyses, however, it is time-consuming and needs frequent recalibration, at least with the available equipment, a Jeol JXA-840A SEM, equipped with a KEVEX 8000, computerized EDS/WDS microanalyzer. Fortunately, the capability to obtain reliable semiquantitative analyses using energy dispersive spectroscopy (EDS) has greatly improved recently. Thin windows and improved detectors make it possible to obtain better peak separation, even for elements with low atomic numbers such as oxygen. X-ray spectrum deconvolution software makes it potentially possible to obtain meaningful chemical analyses for all elements of interest, except carbon, provided they are present at levels above 1% and major peaks don't overlap completely. This level of precision is considered adequate for the purpose of this study, since the main interest is in determining which mineral species - oxides, sulfides, metals - are present, not their exact chemical composition.

The possibility of using EDS to carry out semiquantitative analyses and to determine its precision and accuracy was explored by analyzing several standards, such as: Cr_2O_3 , FeO , Fe_2O_3 , Al_2O_3 , FeS_2 , SiO_2 and orthoclase ($\text{K}_2\text{O}\cdot\text{Al}_2\text{O}_3\cdot 6\text{SiO}_2$). Initial experiments indicated that the exact analysis of each standard can be readily obtained by EDS, by adjusting an instrument parameter called the "Window Thickness Correction Factor" (W.T.C.), which ranges from 0.7 to 1.7. The W.T.C. needed to match the EDS analysis with the known composition of the standard is different for each standard as shown in Table 4.5. However, it was found that a WTC in the 1.4-1.5 range gives EDS analyses of all standards with a precision of equal to or better than $\pm 7.5\%$ of the absolute value (Table 4.6). Duplicate measurements taken consecutively showed good agreement generally $\pm 2.5\%$ and did not vary as a function of the area analyzed. A somewhat larger variation was shown when the standards were measured on different days, but generally the precision remained with $\pm 5\%$. This is considered sufficiently precise for the purpose of this study.

Table 4.6
Semiquantitative EDS Analysis of Standards

Material	At%							Window thickness factor
	Cr	Fe	Al	O	S	Si	K	
Cr₂O₃								
Chemical analysis	<u>40</u>			<u>60</u>				
EDS analysis 1 ¹	40			60				1.49
2 ²	41			59				1.49
3 ³	38			62				1.49
4	41			59				1.40
5	43			57				1.30
Fe₂O₃								
Chemical analysis		<u>40</u>		<u>60</u>				
EDS analysis		42		58				1.49
FeO								
Chemical analysis		<u>50</u>		<u>50</u>				
EDS analysis		53		47				1.49
		54		46				1.40
Al₂O₃								
Chemical analysis			<u>40</u>	<u>60</u>				
EDS analysis			38	62				1.49
			38.5	61.5				1.40
			39	61				1.30
			40	60				1.20
FeS₂								
Chemical analysis			<u>33.33</u>	<u>66.66</u>				
EDS analysis			33.35	66.65				1.40
SiO₂								
Chemical analysis				<u>66.6</u>		<u>33.3</u>		
EDS analysis				65.5		34.5		
Orthoclase								
Chemical analysis			<u>7.6</u>	<u>61.5</u>		<u>23</u>	<u>7.6</u>	
EDS analysis			7.6	61.4		23	8	1.49

- (1) Large area
 (2) 1 micron spot
 (3) repeat 2 weeks later

From the elemental analysis provided by the EDS microanalyzer, the approximate composition of the scale can be deduced, by considering the thermodynamic stability fields of the various possible minerals, in comparison with the gas composition. Information from Figures 4.6-4.8, 4.18 and literature data³⁸ indicates that the probability of forming oxides in the gas composition range studied will decrease in the following order: Al_2O_3 , SiO_2 , TiO_2 , Cr_2O_3 , V_2O_3 -FeO, MnO-NiO. The probability of forming sulfides will increase in the same order. In this ranking FeS and V_2S_3 are considered equally likely to form. However, short term corrosion experiments using metal powders indicated that the kinetics of FeS formation are much faster than those of V_2S_3 formation. Previous studies³¹ also strongly suggested the presence of vanadium oxide instead of sulfide in gases containing 15-20% H_2O . TiO_2 is considered a more stable oxide than Cr_2O_3 , because the $\text{TiO}_2/\text{TiS}_2$ phase boundary is located slightly to the left of that of $\text{Cr}_2\text{S}_3/\text{Cr}_2\text{O}_3$ in the M.O.S. stability diagrams. Short term exposure of mixed Ti - Cr powders also indicated that in gas compositions close to the $\text{Cr}_2\text{O}_3/\text{Cr}_2\text{S}_3$ boundary, Cr sulfides and Ti oxides were formed.

Following the stability ranking of the various oxides and sulfides, their stoichiometry must be considered. As a first approach, the compound which is indicated as stable in the M.O.S. stability diagram is used to calculate the mineral composition, i.e. $\text{Fe}(\text{Ni}, \text{Mn})\text{S}$, Cr_2O_3 , V_2S_3 or V_2O_3 , TiO_2 , SiO_2 and Al_2O_3 . In many cases this satisfactorily accounts for all the elements present, especially considering the level of accuracy of the E.D.S. analysis. X-ray diffraction studies, discussed later indicate that some of the compounds present usually form solid solutions or mixed compounds. Thus Ni and Mn, which are generally present in small amounts, are considered to be present in solid solution in FeS. FeO and Cr_2O_3 are considered to form the spinel FeCr_2O_4 . Similarly, FeS and Cr_2S_3 are combined to the sulfur spinel equivalent FeCr_2S_4 , which is frequently identified by X-ray diffraction.

In many analyses, especially on samples exposed to gases with very low oxygen pressures, not enough oxygen and sulfur are present to combine with the metallic elements at the stoichiometry considered stable in the corrosive gas used. It is considered likely that the gas composition will change on its passage through the scale and many become depleted in sulfur or oxygen or both²⁴. Under these circumstances, compounds with lower oxygen and sulfur content are more likely to be present, i.e., CrS or Cr_3S_4 instead of Cr_2S_3 . Cr_2O_3 itself is quite stable, but the literature mentions the possibility of oxygen depleted nonstoichiometric Cr_2O_3 , Cr_3O_4 and even CrO ^{26, 45}. V and Ti can also form a large number of suboxides with a high metal content, i.e. Ti_3O , TiO , V_2O , VO , etc.^{46,47}. Considering the possible valencies of the metallic elements present, the following classification of scale compositions is suggested:

- **S + O > 50-55 At%**. Oxides and sulfides mostly present at stoichiometry compatible with initial gas composition.

- **S + O \approx 40-50 at%.** Reduced oxides and sulfides predominate, some metallic species possible.
- **S + O < 40 at%.** Metallic species are likely to be present in the scale in addition to reduced oxides and sulfides.

Examination of the phase diagrams indicates that Fe and Ni are the most likely to occur as metals as the stability field of Fe and Ni is much larger than that of Cr, Ti, V, Si and Al. Only a relatively small decrease in sulfur pressure, and no change in oxygen pressure is needed to make Fe and Ni the stable phases. All other alloying elements need significant shifts in both P_{O_2} and P_{S_2} before the metal becomes the stable phase. Figure 4.18 illustrates this for Fe, Ni and Cr at 622°C using data from Ref. 48. The stability fields of V, Ti, and Al are even smaller than those of Cr. The relatively size of the metal stability fields does not change much with decreasing temperature, but shift to lower P_{O_2} and P_{S_2} values. Table 4.7 gives examples of mineral phase compositions calculated for the three groups.

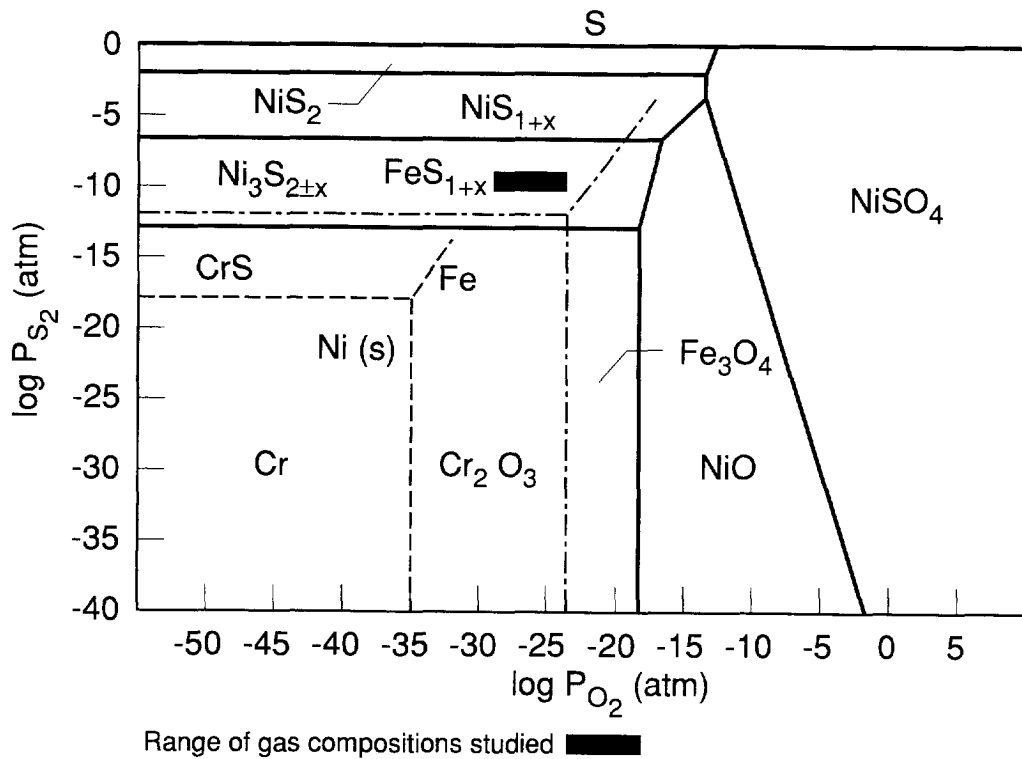


Figure 4.18
Phase Stability Fields of Cr, Fe and Ni at 622°C

Table 4.7
Probable Mineral Composition of Scale Calculated from EDS Analysis (At%)

S + O > 55						S + O = 40-50				S + O < 40			
EDS Analysis		Mineral Composition				EDS Analysis		Mineral Composition		EDS Analysis		Mineral Composition	
		Simple		Combined									
O	22	TiO ₂	18	TiO ₂	18	O	15	SiO _{2-x}	24	O	32	SiO ₂	21
Si	1	SiO ₂	3	SiO ₂	3	Si	9	CrS _{1-x}	37	Si	7	Cr _x O _y	36?
S	39	Cr ₂ O ₃	14	Cr ₂ O ₃	14	S	33	FeS _{1-x}	33	S	2	FeS	4
Ti	6	Cr ₂ S ₃	38	FeCr ₂ S ₄	54	Cr	21			Cr	21	Fe	30
Cr	21	Fe(Mn)S _{1-x}				Fe	19	Ni S _{1-x}	6	Fe	32	Ni	6
			27									Cr	3?
Mn	1			Cr ₂ S ₃	11	Ni	3			Ni	6		
Fe	10												

The above system worked well for all alloys studied, except alloys containing vanadium. Here the measured oxygen and sulfur content was never much higher than 40% even in scales far away from the metal interface, which may be expected to be fully converted. To investigate this problem, samples of V metal and V₂O₅ were analyzed. Under standard conditions, with the instrument calibrated using the copper and aluminum K and L lines, the analysis of the V₂O₅ sample did not show any oxygen. Recalibration of the instrument using the vanadium, K and L lines resulted in a correct analysis for V₂O₅, but completely erroneous analyses for the other oxides. The probable reason for this behavior is that the major L line for vanadium is very close to the K line of oxygen as shown in Figure 4.19. Figure 4.20 shows a similar spectrum for a scale containing Cr, Fe and Ni oxides and sulfides, indicating much less overlap. Apparently the deconvolution software calculates the oxygen content of the sample incorrectly when V is present.

Efforts to develop an empirical correlation between observed and actual oxygen content using mixtures of FeO and vanadium or Ferro vanadium were unsuccessful, partially because of oxidation of the V samples, partially because the mounting medium contained oxygen. The possibility of measuring the oxygen content separately using W.D.S. (wavelength dispersive spectroscopy) was finally investigated and proved successful, or at least gave a more credible total oxidant content. However even for WDS, the separation between the oxygen K peak and the vanadium L peak is marginal for accurate analyses. Table 4.8 shows the results obtained on scales from samples exposed to gases containing 1 and 10% H₂O, respectively. In both cases, the O + S content of the scale indicated that the S and O compounds approach the expected stoichiometry. A scale from the Ti containing alloy was also analyzed both ways, to show that the differences between

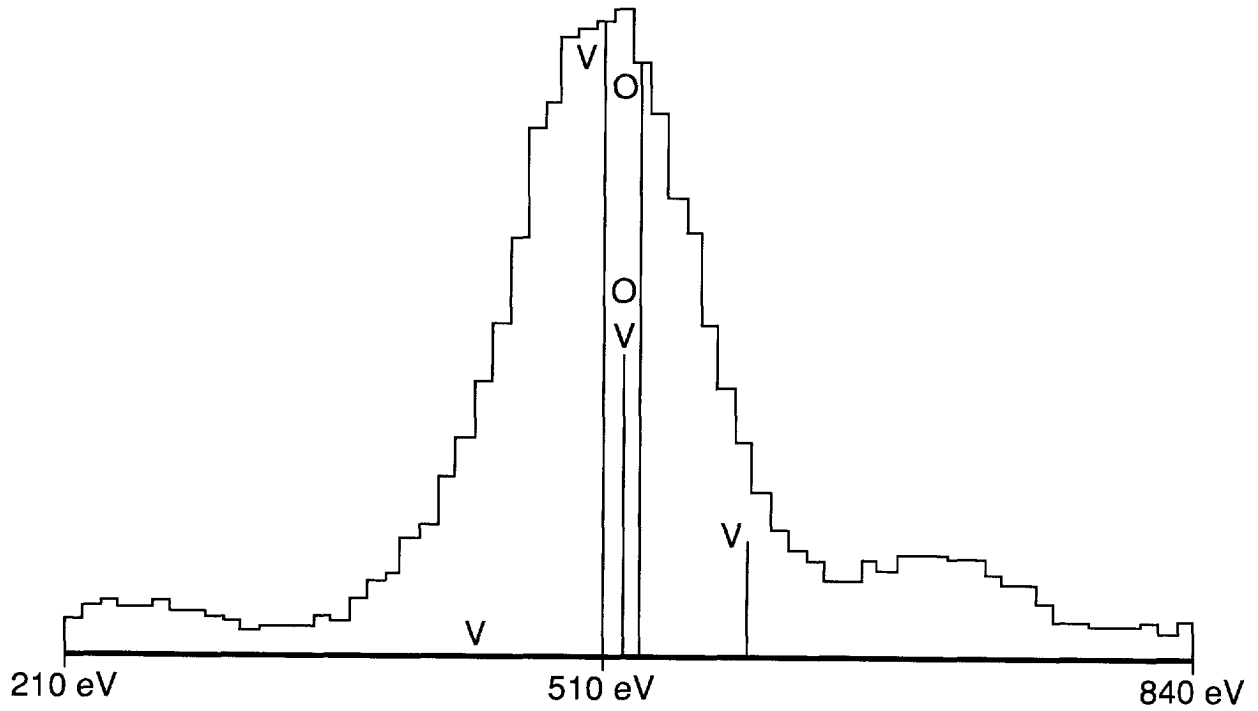


Figure 4.19
EDS Spectrum for V_2O_5 Near K Line of Oxygen, Showing Oxygen K Lines and Vanadium L Lines

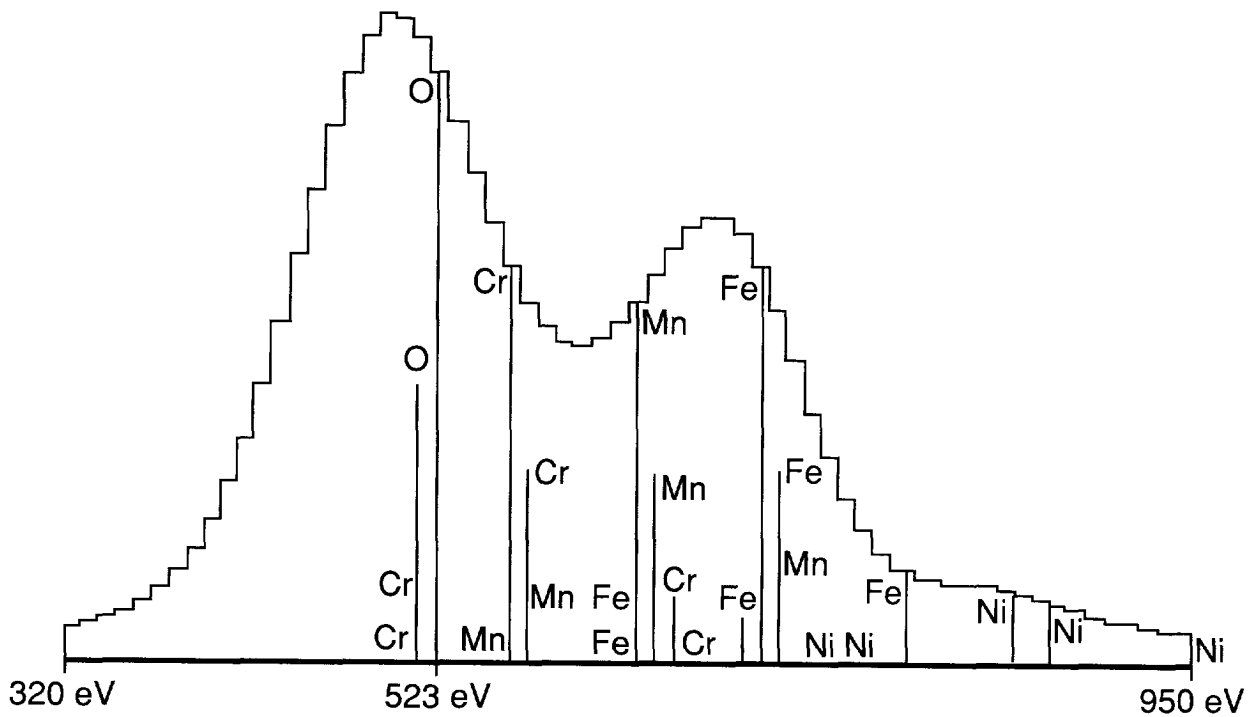


Figure 4.20
EDS Spectrum for Cr, Fe, Ni, O, S Scale Near K Line of Oxygen, Showing Oxygen K Lines and L Lines of Cr, Fe, Mn and Ni

WDS and EDS are small here and is included in Table 4.8. Thus, it was decided to determine the scale composition by EDS for all alloys, except those containing vanadium. For V containing alloys, WDS is used to measure the oxygen content of the scale separately.

Table 4.8
Oxygen Content Scales of Measured by EDS and WDS

Mount No. H ₂ O in gas	921102 1%		930064 10%		93066 10%	
	EDS	WDS*	EDS	WDS*	EDS	WDS*
O	23	31	29	45	47	47
Si	1	1	1	1	1	1
S	21	20	8	8	5	5
V	6	5	6	5	-	-
Cr	35	30	35	27	27	27
Mn	1	-	1	-	1	1
Fe	11	9	17	13	13	13
Ni	2	4	2	2	1	1
Ti	-	-	-	-	3	4

*Oxygen by WDS, remainder by EDS.

4.4.3 X-Ray Diffraction

It was originally thought that the penetration of standard X-ray diffraction equipment was such that it would easily penetrate scales 10-50 microns deep. Efforts were, therefore, made to locate a low angle X-ray diffraction apparatus to reduce the depth of penetration. A suitable instrument was located at the Stanford University. Preliminary experiments were done on a corroded sample of AISI 310 stainless steel (25Cr-20Ni bal Fe).^{*} The apparatus used was specially designed for thin film texture, strain and phase characterization, but could also be used for high angle reflection diffractometry, similar to the widely used Bragg-Brentano diffractometer⁴⁹. The SS 310 sample had a scale about 100 microns thick containing Fe, Cr, Ni, O and S, with sulfide rich phases concentrated near the surface of the scale. Results of the tests were unexpected in that the X-ray diffraction pattern did not change with changes in incident angle, i.e. depth of penetration. At all angles the same pattern was obtained, which showed that FeCr₂S₄ was the major mineral present. It was, therefore, suspected that the penetration of the

* Dr. Bain of Stanford University conducted the experiments.

X-rays even at 90° incident angle was less than originally expected. X-ray absorption by the elements present in the scale was, therefore, calculated using both the standard Cu K α radiation used here and Mo K α radiation⁵⁰. X-ray absorption is governed by an exponential decay law, and the fraction of intensity, I/I_0 , transmitted through a thickness of material, x , is given by:

$$\frac{I}{I_0} = \exp(-\mu x)$$

where μ is the absorption coefficient which is wavelength dependent. The quantity, μ , is given by the product of the mass absorption coefficient, μ/ρ , and the density of the material, ρ , two intrinsic properties. Table 4.9 lists these values for Fe, Cr, S, and O at the Cu K α and Mo K α wavelengths.

Table 4.9
Mass Absorption Coefficients and Densities for Some of the Elements Considered in This Study

Element	ρ (gm/cm ³)	μ/ρ (cm ² /gm)	
		Mo Ka (.711Å)	Cu Ka (1.542Å)
Cr	7.19	29.25	252.3
Fe	7.87	37.74	304.4
S	2.09	9.625	92.53
O	-	1.147	11.03

Table 4.10 shows the penetration depths which would be achieved for these elemental materials as well as some typical corrosion phases at the two common x-ray wavelengths and as a function of incident angle. The penetration depths in Table 4.9 are the depths at which an atomic plane would be illuminated by an incident beam which was reduced in intensity by a factor of e . It is a characteristic distance and represents the approximate depth from which diffraction will be seen. In all cases for Cu K α radiation, the penetration depth is much less than 100 μ m, the corrosion product thickness. The high background is due to fluorescence from the Cr and the Fe. It is clear from the table that the penetration depth of the scale is maximum 15 μ m, with Cu K α radiation.

Unfortunately, a Mo K α radiation source was not available. Attempts to reduce the thickness of the sample by polishing were unsuccessful due to surface roughness and polishing difficulties.

Another attempt to use X-ray diffraction was made using a new X-ray diffraction apparatus at the Palo Alto laboratories of Lockheed Missile and Space Company. This apparatus, a Siemens Model D5000, was capable of low and high angle X-ray diffractometry. The samples studied, were from alloy B, containing 20%Cr - 35Ni and

Table 4.10

Penetration Depth for Different Corrosion Products. The 1/e Depth is Defined as the Depth at Which the Planes are Illuminated by a Beam Reduced in Intensity by a Factor of e. There is Additional Reduction of the Diffracted Beam by Another Amount Dependent on the Exit Angle.

Phase	Fe	Cr	FeCr ₂ S ₄	FeO	FeS
ρ	7.72	7.19	3.83	5.65	4.85
μ/ρ (Cu K α)	304.4	252.3	168.4	131.7	145.2
μ/ρ (Mo K α)	37.74	29.25	19.25	15.25	16.10
Incident Angle, α	Cu K α 1/e Penetration Depth (microns)				
10°	0.74	0.96	2.69	2.33	2.47
20°	1.46	1.89	5.30	4.59	4.86
30°	2.13	2.76	7.74	6.72	7.11
40°	2.74	3.55	9.95	8.63	9.13
50°	3.26	4.22	11.86	10.29	10.89
60°	3.69	4.78	13.14	11.63	12.31
70°	4.00	5.18	14.55	12.62	13.35
80°	4.19	5.43	15.25	13.23	13.99
90°	4.26	5.52	15.49	13.43	14.21
Incident Angle, α	Mo K α 1/e Penetration Depth (microns)				
10°	5.96	8.26	23.53	20.20	22.25
20°	11.74	16.27	46.34	39.80	43.83
30°	17.16	23.79	67.74	58.18	64.07
40°	22.07	30.58	87.09	74.79	82.37
50°	26.30	36.44	103.78	89.13	98.17
60°	29.73	41.20	117.33	100.76	110.98
70°	32.26	44.70	127.31	109.34	120.42
80°	33.81	46.85	133.42	114.59	126.20
90°	37.33	47.57	135.48	116.35	128.15

3.25%V, bal Fe. The thickness of the scale of the first sample 91.1282 varied from 7-12 microns. Semiquantitative EDS analysis indicated the presence of Cr, Fe, V, O and S in the scale near the metal surface. The thickness of the scale on the second sample 91.0722 was 30-40 μm . EDS analysis indicated the presence of Fe Cr₂ S₄ in the upper part of the scale and FeS, Cr₂ O₃ and V₂ S₃ or V₂ O₃ in the lower part of the scale.

The resulting XRD patterns are shown in Figure 4.21 and 4.22, respectively. They are very complex, with many overlapping lines. Further complications are the presence of peak shifts, because the sample surface was not exactly in the focal plane of the X-ray machine. Preferred orientation is also possible. However, the presence of many overlapping peaks is the greatest barrier to the interpretation of the pattern. Both patterns indicate that FeCr_2S_4 is probably the predominant species while FeS_{1+x} , Cr_2O_3 , FeCr_2O_4 , and Cr_2S_3 are most likely present. There are also diffraction lines, which correspond with the pattern of the underlying alloy, especially in sample 91.1282 having the thinner scale. Unfortunately, these lines overlap with those of FeCr_2S_4 . No indications of V compounds were found.

A final attempt to make use of XRD was the study of reaction products of 50Cr-50Ti, 50Cr-50V and 50Fe-50V pressed pellets to determine which oxides and/or sulfides would form after short term (15hr) exposures. X-ray diffraction patterns were again very complex with overlapping peaks. The sample with 50% Fe powder showed mainly various iron sulfides, which apparently grew fast enough to obscure all other species, including Fe and V metal and V sulfides or oxides. The chromium containing mixtures did not show chromium metal, but only chromium sulfides Cr_2S_3 and possibly Cr_3S_4 , indicating that the chrome sulfides were thick enough ($> 10\text{-}20\ \mu\text{m}$) to mask chromium

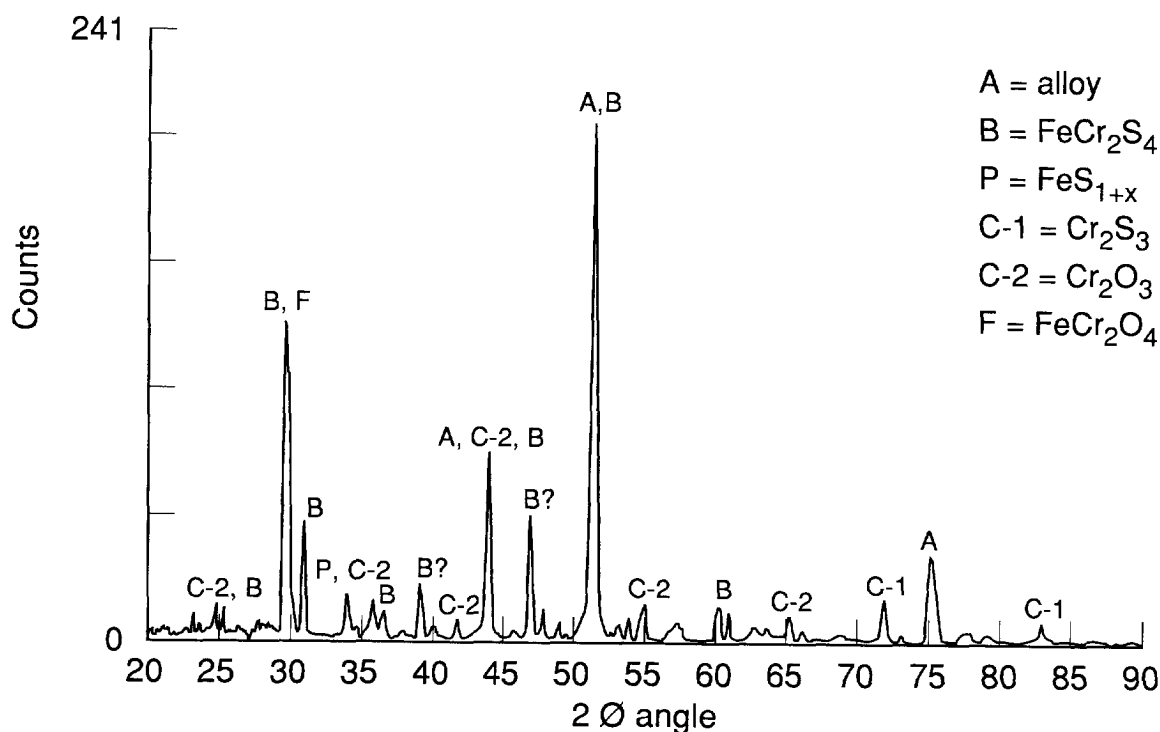


Figure 4.21
 XRD Analysis of Scale on Sample 92-1282, Scale Thickness 7-12 μm

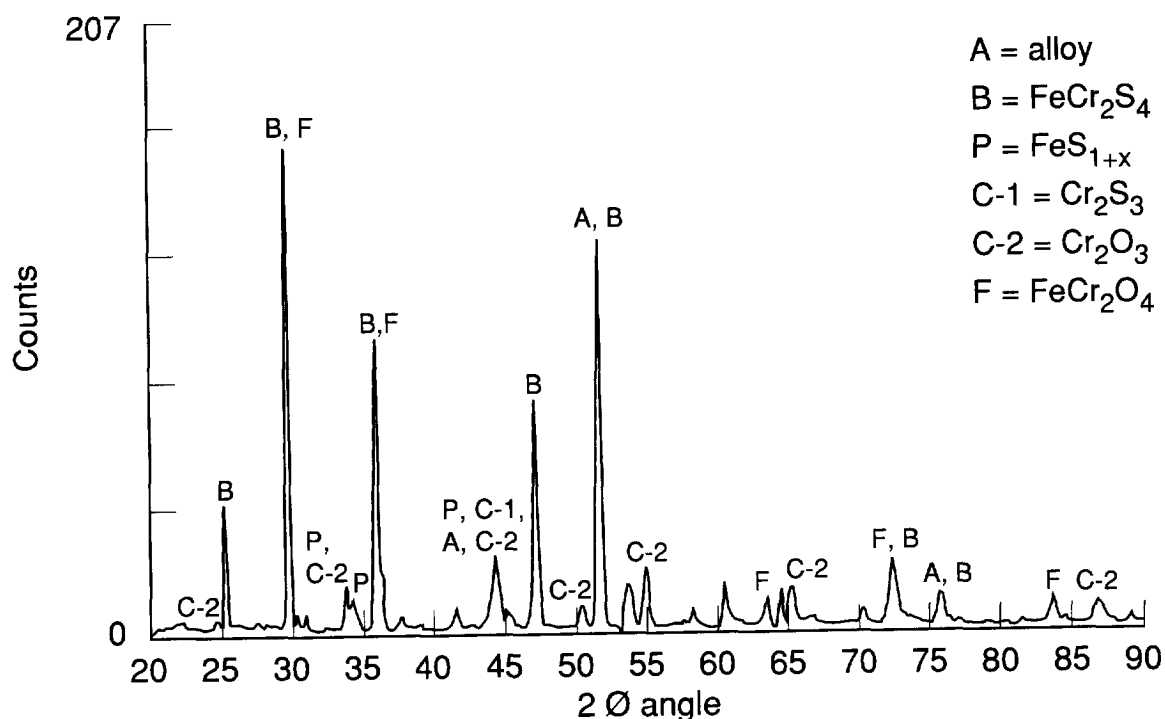


Figure 4.22
 XRD Analysis of Scale on Sample 91-0722, Scale Thickness 30-40 μm

[Figures 4.23 and 4.24]. V and Ti metals were detected, together with patterns for V_3S_4 and TiO_2 , respectively. However in both cases similar information can be obtained by EDS analysis, as shown below.

Figure 4.25A shows a BSE image of the 50Cr-50Ti mixture after 15 hr. exposure in gas 1, Table 4.3. The acicular crystals are mainly chromium sulfide, while the coarse grains consist mainly of titanium and oxygen. Table 4.11 gives the EDS chemical analyses. The chromium rich crystals consists mainly of Cr_2S_3 with a lesser, but significant amount of Cr_2O_3 . The Ti rich grains consists of titanium oxide with a 3/2 O/Ti ratio. This may indicate that the electron beam penetrated the thin TiO_2 scale into the metal or that the scale consisted of Ti_2O_3 . Figure 4.25B shows a BSE image of the 50Cr-50V mixture after exposure. The chrome sulfides were similar here to those in the Ti containing sample, but contained a little less oxygen. The scale on the vanadium rich particles contained both sulfur and oxygen and had an excess V, which probably indicates scale penetration by the electron beam. The V used in this sample was partially oxidized prior to the experiment. Thus, V oxides may have only partially converted to V sulfides. In general, the quantitative EDS analysis provides more useful information than XRD analysis.

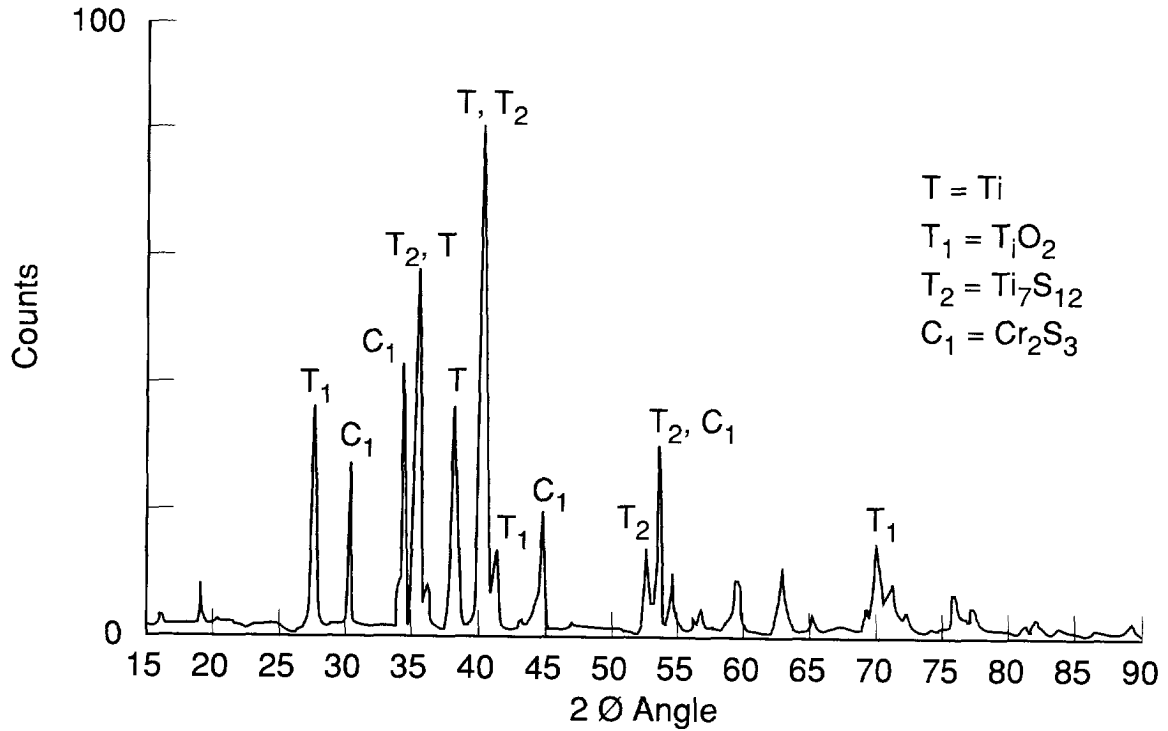


Figure 4.23
XRD Analysis of 50 Cr-50 Ti Mixture After 15 Hours Exposure to Gas 1

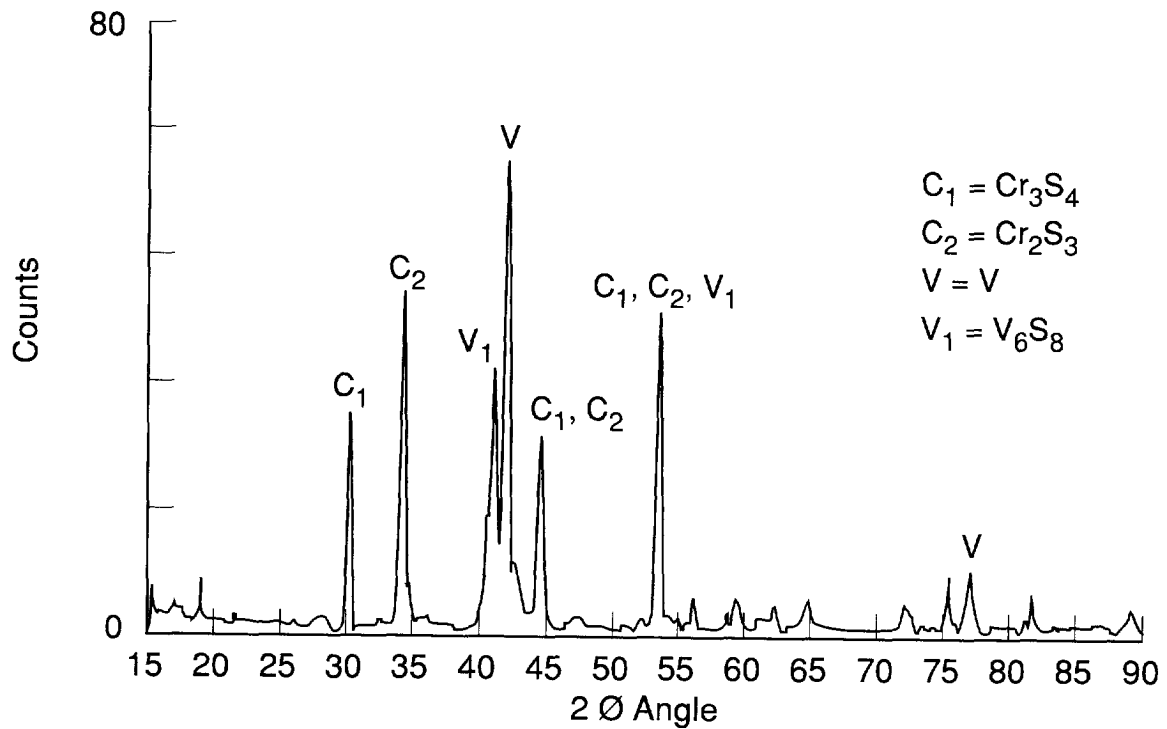
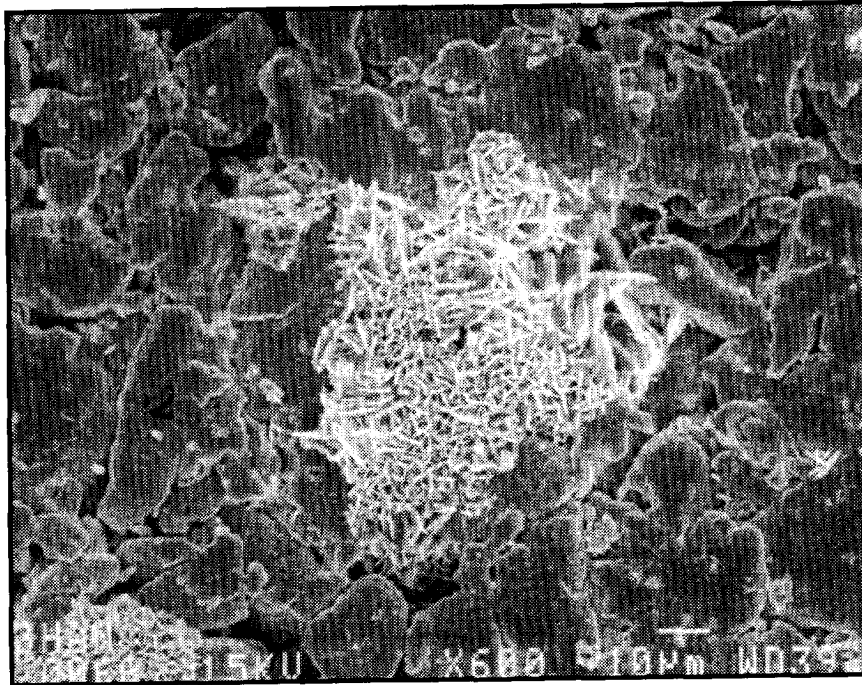
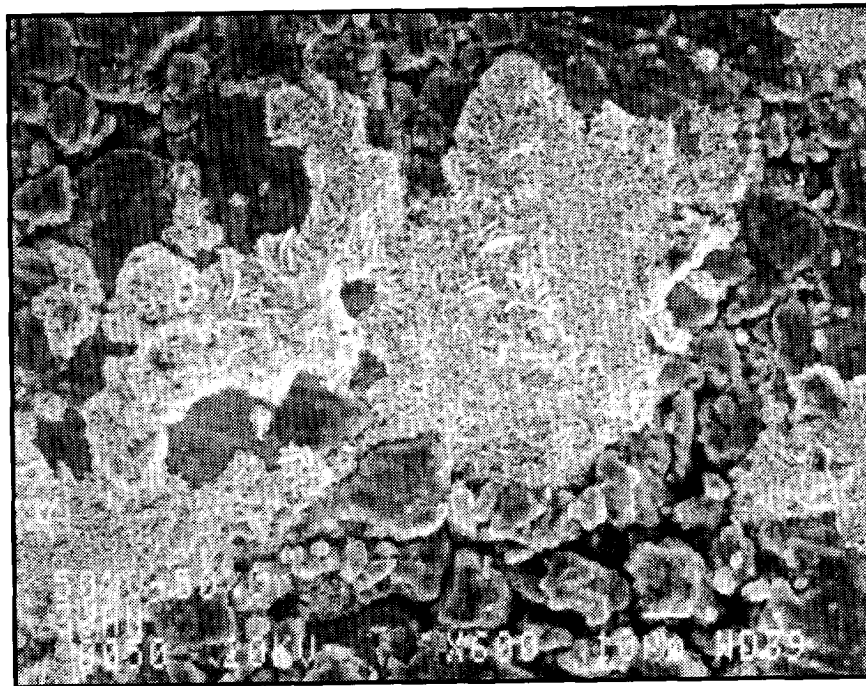


Figure 4.24
XRD Analysis of 50 Cr-50 V Mixture After 15 Hours Exposure to Gas 1



a) 50 Ti - 50 Cr



b) 50 V - 50 Cr

Figure 4.25
Granular Ti-Cr and V-Cr Mixture After 15 Hours Exposure to Gas 1, 0% H₂O

Another factor which diminishes the usefulness of X-ray diffraction is the existence, at least in the files used for computerized phase identification, of a myriad of Fe, Cr, Ti, V and other sulfides and oxides, as well as mixed oxides and sulfides, i.e., Cr_2S_3 , Cr_3S_4 , Cr_5S_6 , CrS , Cr_2O_3 , CrO , $\text{Cr}_2\text{Ti}_6\text{O}_{15}$, CrVO_4 , etc. This makes the already complex XRD pattern very difficult to analyze.

Table 4.11
Chemical Composition of Scales on Ti-Cr and V-Cr Mixtures After 15 hr exposure to Gas 1

A. 50Cr-50Ti mixture

Cr rich crystallites				Ti rich particles			
EDS analysis at %		probable composition at %		EDS analysis at %		probable composition at %	
O	14	Cr_2S_3	77	O	62	TiO_2	93
S	42	Cr_2O_3	23			Ti	7
Cr	42			Ti	38		

B. 50Cr-50V mixture

Cr rich crystallites				V rich particles			
EDS analysis at %		probable composition at %		EDS analysis at %		probable composition at %	
O	6	Cr_2S_3	90	O	12	VO	24?
S	54	Cr_2O_3	10	S	22	VS	44?
Cr	40			V	64	V	32

In summary, X-ray diffraction analysis is of limited value, due to the presence of many overlapping peaks. It is mainly useful for the analysis of the outer part of the scale, due to penetration depth limitations, when using $\text{Cu K}\alpha$ radiation. However, FeCr_2S_4 was clearly established as a major scale component. For the above reasons, XRD was not used widely in this study.

5

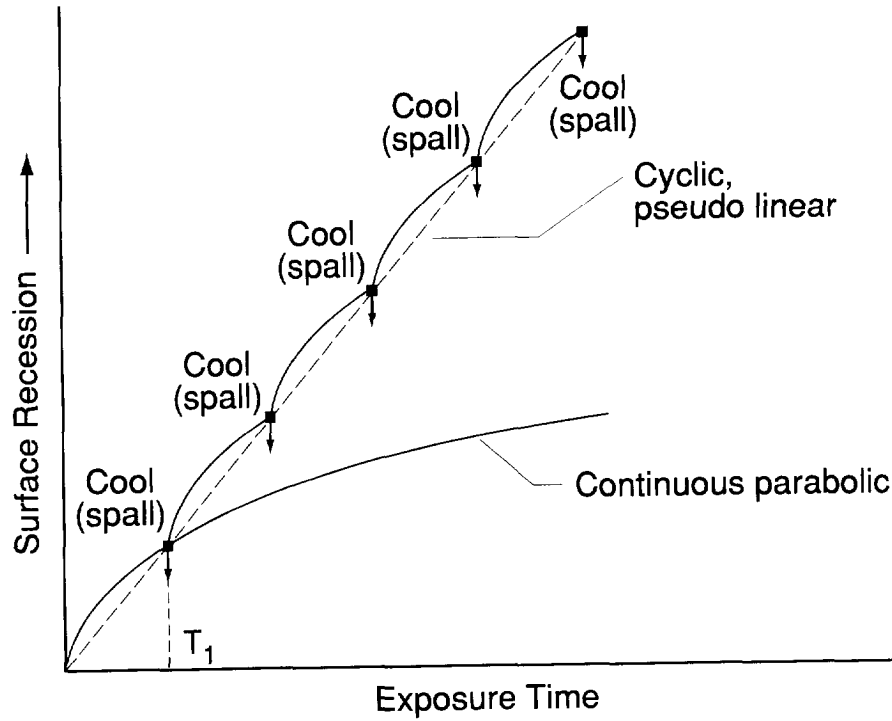
RESULTS

5.1 CORROSION KINETICS IN WATER FREE GAS MIXTURES

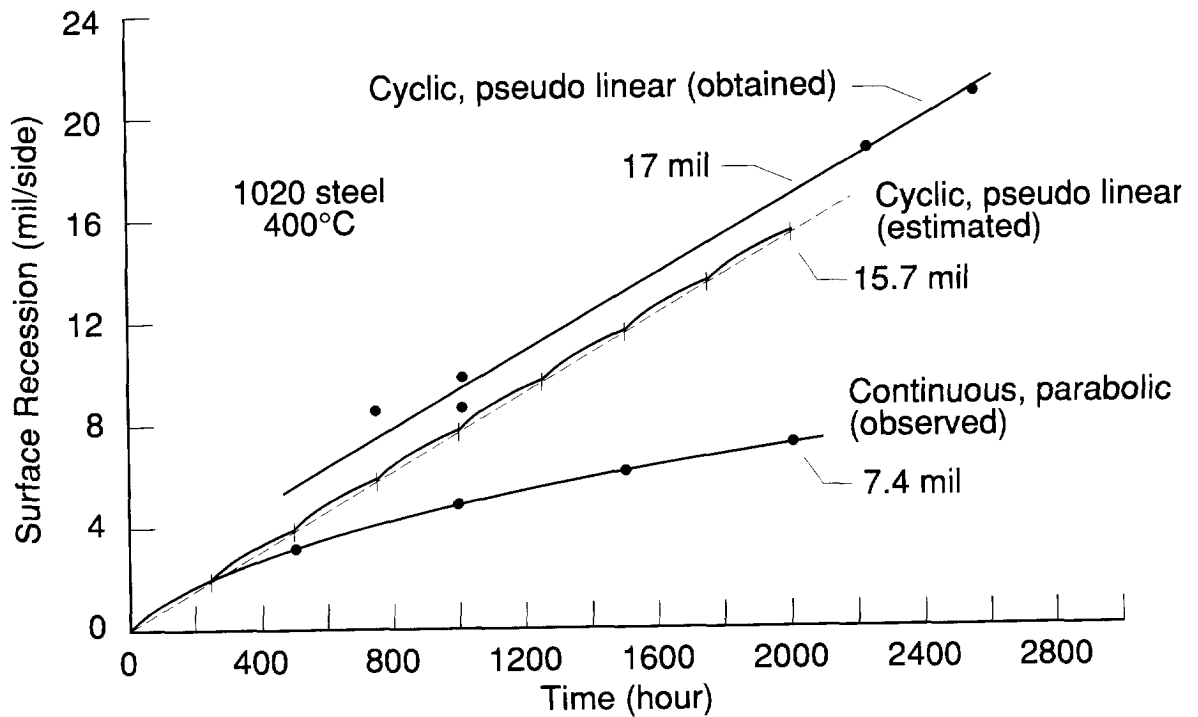
The corrosion rate or rate of sound metal loss is generally the only result of corrosion studies of interest to design engineers, plant operators and other users of materials technology. Although the corrosion loss of specimens exposed in laboratory corrosion studies can be readily determined, extrapolation of the results to predict long term performance in the plant environment is difficult and usually not possible, unless at least some plant exposure data are available for comparison.

Previous mixed oxidant corrosion studies using gas mixtures containing at least 15% steam, indicated that the best agreement with corrosion data from plants was obtained by running cyclic tests in which the specimens were periodically cooled to room temperature to simulate a plant shutdown. Figure 2.4 showed results of 1000 hr laboratory corrosion tests^{17, 38} on low alloy steels which were conducted in 4,250 hour intervals, in syngas containing 14% H₂O in comparison with plant data. This procedure resulted in apparently linear corrosion kinetics. Perkins⁵¹ showed later that the actual corrosion rate of low alloy steels in mixed oxidants is parabolic. Thus, isothermal tests result in relatively low corrosion rates, which do not correspond with plant experience. The sulfur rich scale on low alloy steels is brittle, does not adhere well and tends to spall off. This leads to a pseudo linear corrosion rate, in which the rate is dependent not only on the actual scale growth, but more importantly on the frequency of thermal cycling. This is illustrated in Figure 5.1⁵¹. Austenitic stainless steels in the same tests were generally not subject to spalling on thermal cycling in syngas containing 15% H₂O. Scale growth was slow enough to yield low corrosion rates even when extrapolated linearly at least at temperatures up to 500°C^{38, 52}.

With this background in mind, the first corrosion tests in water free syngas [gas composition 1 in Table 4.3] were carried out cyclically. Total exposure time was 600 hr run in 3,200 hr segments. Corrosion losses observed were very high when compared with similar tests in syngas containing about 15% steam, generally 5-10 times higher. A few corrosion loss data on a model alloy and some commercial alloys are given in Table 5.1.



a) Proposed model



b) Experimental Verification of Model

Figure 5.1
Accelerated Sulfidation of Low Alloy Steel by Thermal Cycling

Table 5.1
Corrosion Loss and Linear Corrosion Rates of Some Alloys After 600 hr. Cyclical Exposure in Dry Syngas, 0.8% H₂S

Alloy	Composition wt%	Corrosion Loss μm	Linear Corrosion Rate mm/yr
B	20Cr-35Ni-3V	71	1.0
800	20Cr-31Ni-Al,Ti	146	2.1
310	25Cr-20Ni	92	1.4

Metallurgists involved with the development of dry coal fed gasifiers have suggested that linearly extrapolated corrosion rates from cyclic corrosion tests are considerably higher than those experienced in service⁵³. Data presented in reference 53 indicate roughly parabolic reaction kinetics, at least in laboratory corrosion studies. Unfortunately, the authors so far have not published results from alloys exposed in service.

Based on these considerations, it was decided to run only continuous corrosion tests in this study. 600 hr was selected as the standard exposure time. This is somewhat shorter than in previous studies³⁸, where 1000 hr. minimum exposures were standard, using syngas with a high steam content. Because of the higher corrosion rates in gas mixtures without steam, a decrease in exposure time was considered justified, especially since a large number of tests were needed to accomplish the research goals of this study. Prior to the start of the main study, a small number of tests were carried out with different exposure times, to obtain some information on corrosion kinetics and to make sure that corrosion mechanisms did not change significantly with time. Exposure times of 150, 600 and 1350 hrs. were selected. At these intervals, the metal recession will approximately double, if the corrosion kinetics are parabolic. Two sets of experiments were run, one with 0.8% H₂S on the gas, the other with 0.2% H₂S in the gas. Metal recession data are given in Table 5.2. A straightforward plot of metal recession vs. time is given in Figure 5.2A. It can be seen that in most cases the metal recession rate decreases with increased exposure time. However the corrosion rate of alloys A and B exposed to the gas with 0.8% H₂S appears close to linear. In general, the initial rate of scale growth is smaller in the more sulfidizing gas with 0.8% H₂S. This is especially marked in the titanium containing alloy C.

To determine the corrosion rate laws for the various alloys and exposure conditions, the data were replotted on log-log paper in Figure 5.2B. A straight line was drawn through the three data points for each alloy. This gave a reasonable fit for all alloys except alloy C exposed to gas 1 (0.8% H₂S). Here the corrosion loss after 600 hrs. exposure was

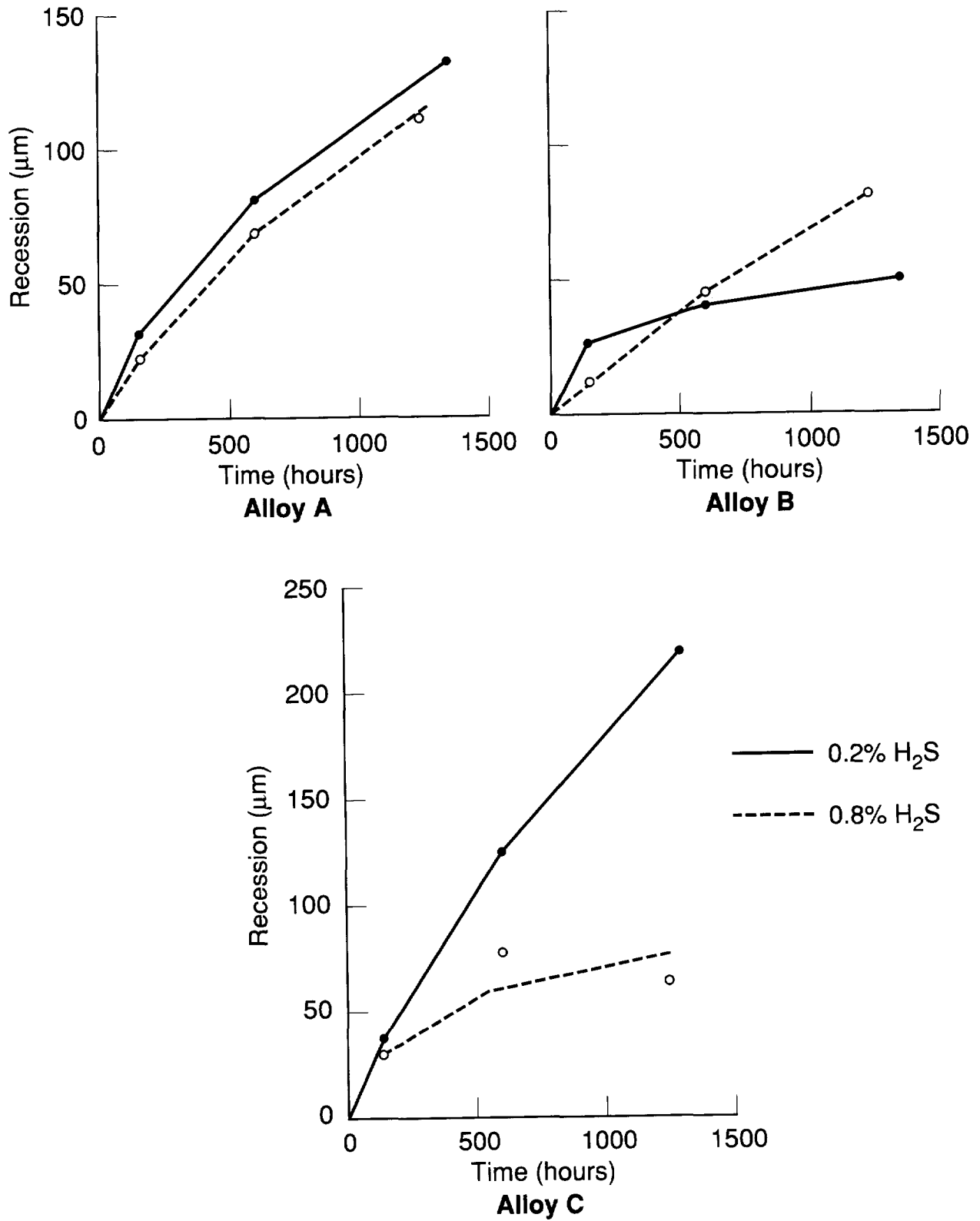


Figure 5.2A
Corrosion Loss As a Function of Time

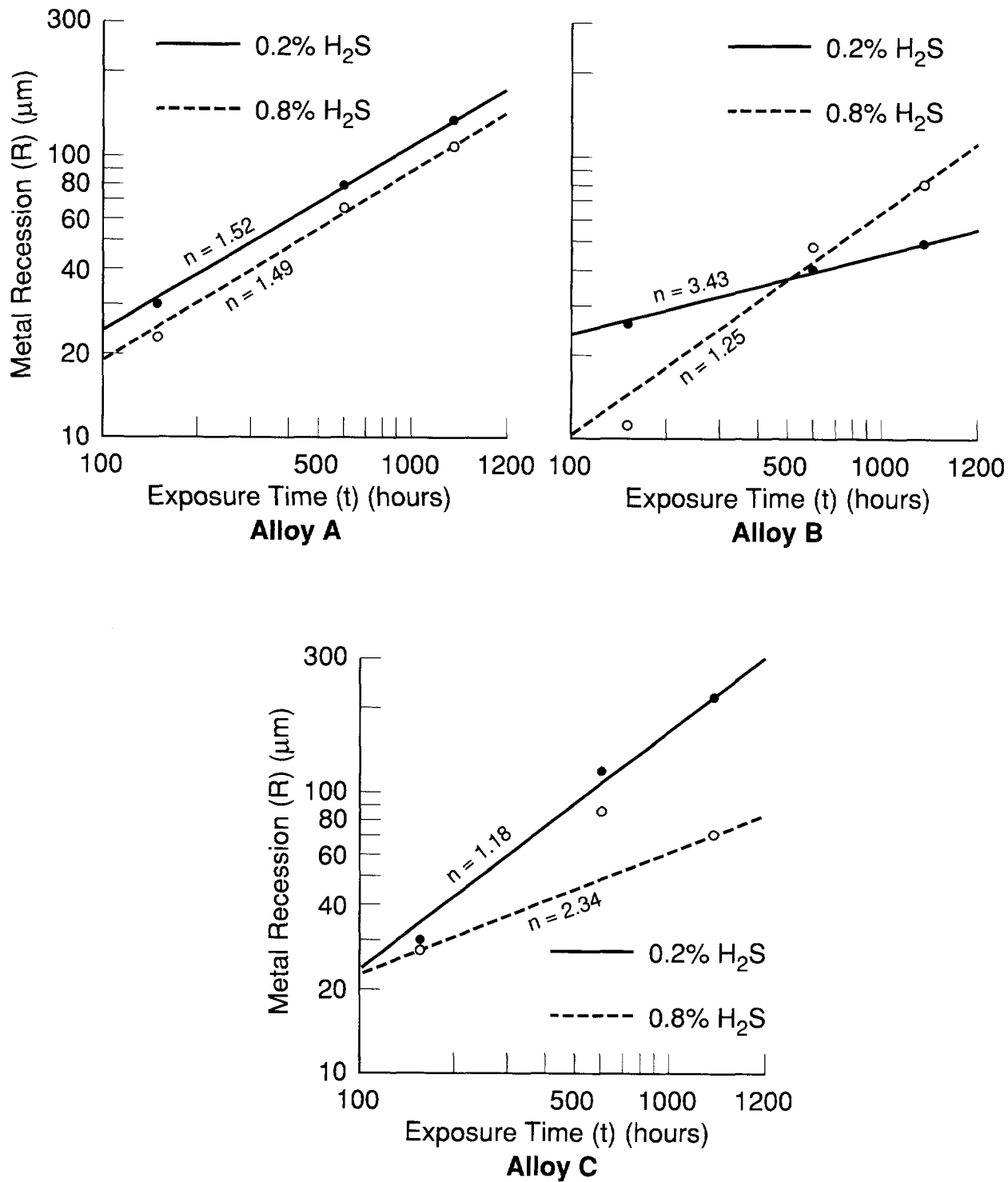


Figure 5.2B
Corrosion Loss As a Function of Time, Log-Log Plot

Table 5.2
Metal Recession (μm) After Continuous Corrosion Tests 550°C Gas 1

A. 0.2% H₂S

Alloy	150 hrs.	600 hrs.	1350 hrs.
A	30*	80	134
B	25*	40	49
C	30*	120*	217

B. 0.8% H₂S

A	23*	66	110
B	11*	47	80
C	27	87	70

* metal recession from scale thickness, all other measurements direct.

ignored, because the scale composition and morphology after 600 hrs. exposure is completely different from that after the 150 and 1350 hrs. exposures (see page 5.15-16). The slope of the straight line, thus obtained, indicates the corrosion rate law:

$$R^n = Kt$$

$$n = \frac{\text{Log}t_2 - \text{Log}t_1}{\text{Log}R_2 - \text{Log}R_1}$$

R = corrosion loss (μm), t = exposure time (hrs), K = rate constant, n = corrosion rate exponent, n = 1, when the rate law is linear, n = 2, when the rate law is parabolic, etc.

Figure 5.2B indicates that alloy C in gas 1A (0.2% H₂S) and alloy B in gas 1 (0.8% H₂S) show nearly linear corrosion kinetics. The rate law governing the corrosion rate of alloy A is about halfway between linear and parabolic in both gases, while the corrosion kinetics of alloy B in gas 1A and alloy C in gas 1 are clearly subparabolic. Annual corrosion rates can be estimated from the log-log plots by extrapolating the straight line to 8700 hrs. exposure and are shown in Table 5.3 together with annual corrosion rates obtained by extrapolating the 1350 hr. data assuming linear kinetics. The latter are still considerably higher for the alloys which exhibit a rate exponent close to 1.

To analyze the results in terms of parabolic corrosion kinetics, the data have been replotted in Figure 5.3 as a function of the square root of time. Here linear plots indicate parabolic kinetics. Parabolic corrosion kinetics usually indicate that the corrosion rate is controlled by diffusion through a protective scale. This is not likely to be the case in complex gas mixtures, where oxides and sulfides can form simultaneously. However

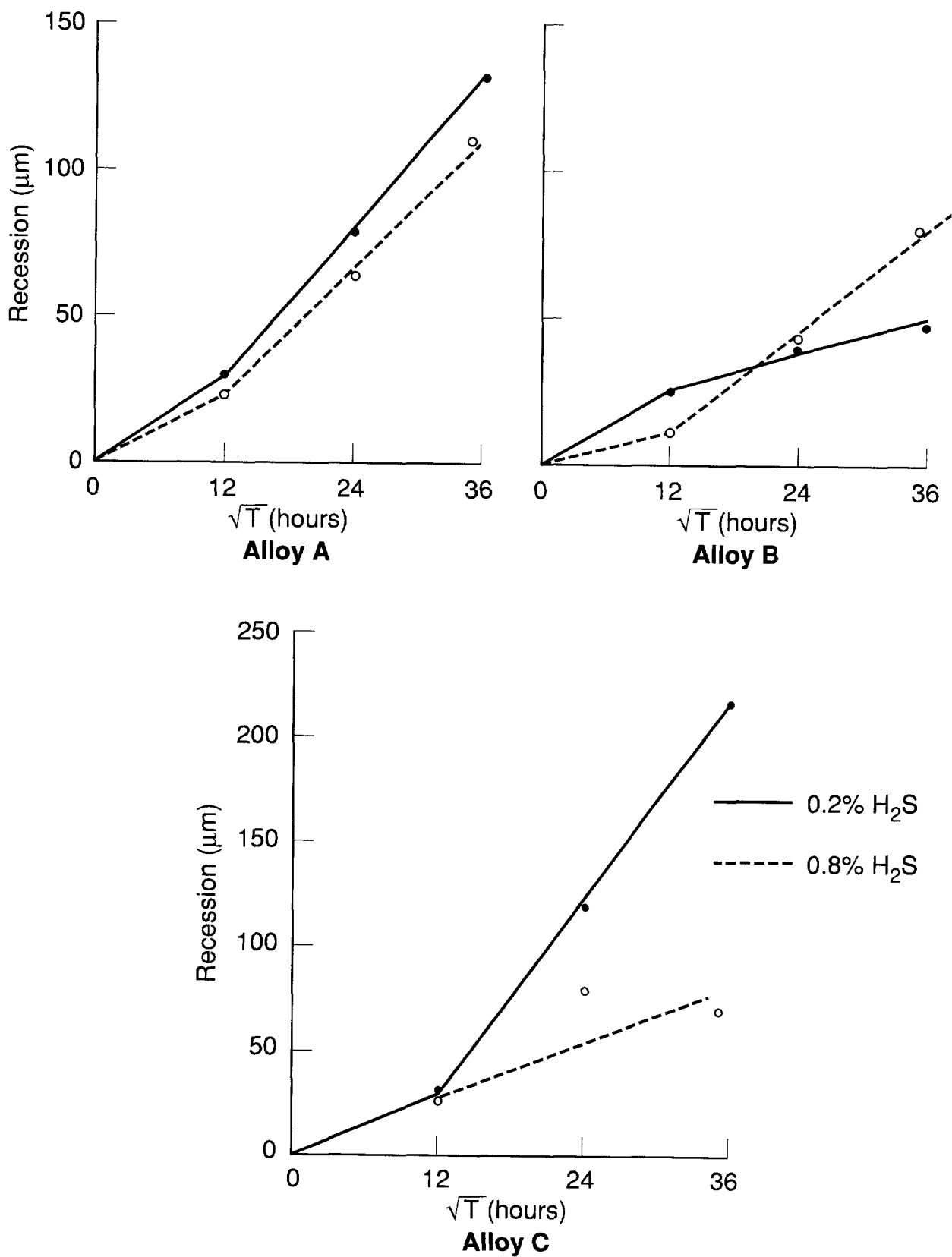


Figure 5.3
Corrosion Loss as a Function of \sqrt{T}

Figure 5.3 indicates that an interpretation of the data in terms of parabolic kinetics is possible for exposures between 150 and 1350 hrs., again with the exception of the 600 hr. data point of alloy C in gas 1. Approximate parabolic corrosion constants were calculated and are also shown in Table 5.3. Annual corrosion rates calculated from parabolic constants are generally somewhat lower than those derived from the log-log plots.

Table 5.3
Approximate Parabolic Corrosion Constants and Corrosion Rates

Alloy		$K_p (\mu\text{m})^2/\text{hr}$	Parabolic Corrosion rate mm/yr	Corrosion rate from Log-Log plot mm/yr	Linear Corrosion rate (mm/yr.*)
A	1**	17	0.4	0.44	0.9
	2***	11	0.3	0.4	0.8
B	1	1	0.1	0.08	0.3
	2	6	0.2	0.14	0.6
C	1	60	0.7	0.9	1.4
	2	5	0.2	0.12	0.5

* Linearly extrapolated from longest exposure.

** 0.2% H_2S gas

*** 0.8% H_2S gas

In general it can be concluded that the data presented here do not support the hypothesis that corrosion kinetics are parabolic, even in isothermal tests, where scale spallation is minimal. The corrosion rate exponent appears to be quite variable depending on gas and alloy composition. Thus the most practical approach is to extrapolate linear log-log plots of corrosion rate as a function of time. This does not assume a particular corrosion mechanism and gives annual corrosion rates some what higher than predicted from parabolic corrosion kinetics. They are therefore more conservative. It should finally be stressed here that only a few data points were available for extrapolation. Therefore the predicted annual corrosion rates are not very accurate. More data points and longer exposure times are needed to improve accuracy and to define the governing rate laws more clearly.

5.2 EFFECT OF OXYGEN PRESSURE ON CORROSION

Previous studies at relatively high oxygen pressures have indicated the presence of a "kinetic boundary" separating a region of slow stable oxide scale growth, with parabolic growth kinetics, from a less stable regime; where both oxide and sulfide growth are possible. Unfortunately, syngas compositions from commercial gasification processes fall in the latter region. Here the effect of oxygen pressure on corrosion is less obvious, although most researchers tend to believe that corrosion rates will increase with

decreasing oxygen pressure or PO_2/PS_2 ratio⁵³. The presence of non equilibrium instead of equilibrated gas mixtures further complicates the situation since the oxygen pressure is not uniquely defined and partial shifts to equilibrium may occur at the metal surface or during diffusion of the gas species through the scale. It was, therefore, considered of interest to study the effect of oxygen pressure on corrosion rates, at a constant sulfur pressure, in an area of the M-S-O stability diagram where FeS and Cr_2O_3 or Cr_2S_3 are the thermodynamically stable phases. Steam was the main variable used to modify the oxygen pressure. This was done in part because the oxygen pressure of a typical gas mixture calculated from the H_2/H_2O ratio is generally higher than that calculated from the CO/CO_2 ratio. Additional reasons are that the water content in commercial syngas is quite variable and dependent on the gasification process. A few water free gas compositions based on the CO/CO_2 ratio were also used to determine, if the corrosion kinetics are solely dependent on the PO_2 or also dependent on the type of oxidant at the same nominal PO_2 . Finally a few tests were made with a PS_2 about one order of magnitude less than that in the main test sequence. All tests were carried out for 600 hrs without interruptions. Gas compositions are given in Table 4.3, corrosion loss data in Table 5.4.

Table 5.4
Corrosion Loss in 600 hrs Laboratory Tests at 540°C (μm)

Gas	0	1	2	3	4	5	9	6	7	8	1A	2A	4A	
% H_2O	0	0	1.2	2	2.9	5.1	0	9.8	15.1	0	0	1	3	
CO_2/CO	0.0015	0.062					0.64			2.1	0.062			
-Log PO_2	32.2	29	28.4	27.8	27.4	27	27	26.4	26	26	29	28.4	27.4	
-Log PS_2	←—————						9.3	—————→				←	10.5	→
Alloy														
A	50	66	155	177	343	193	170	126	46	114	80	353	180	
B	30	47	110	202	200	148	120	107	38	95	40	224	120	
C	50	87	87	77	154	147	90	95	40	20	120	97	120	
D	30	33	30	3	-	-	-	-	5	-	-	4	1	
E	40	77	40	7	-	-	-	-	4	-	-	7	7	

5.2.1 Corrosion as a Function of Steam Content of Syngas

Seven tests were carried out with gases having a steam content varying from zero to 15.1%, giving a variation of Log PO_2 from 26-29, based on the H_2O/H_2 ratio of the gases. Figure 5.4 shows that corrosion rates do not decrease with increasing oxygen pressure as might be expected. The corrosion loss of alloy A, the baseline Fe-Ni-Cr alloy increases sharply with increasing steam content of the gas up to 3% steam. Thereafter the corrosion

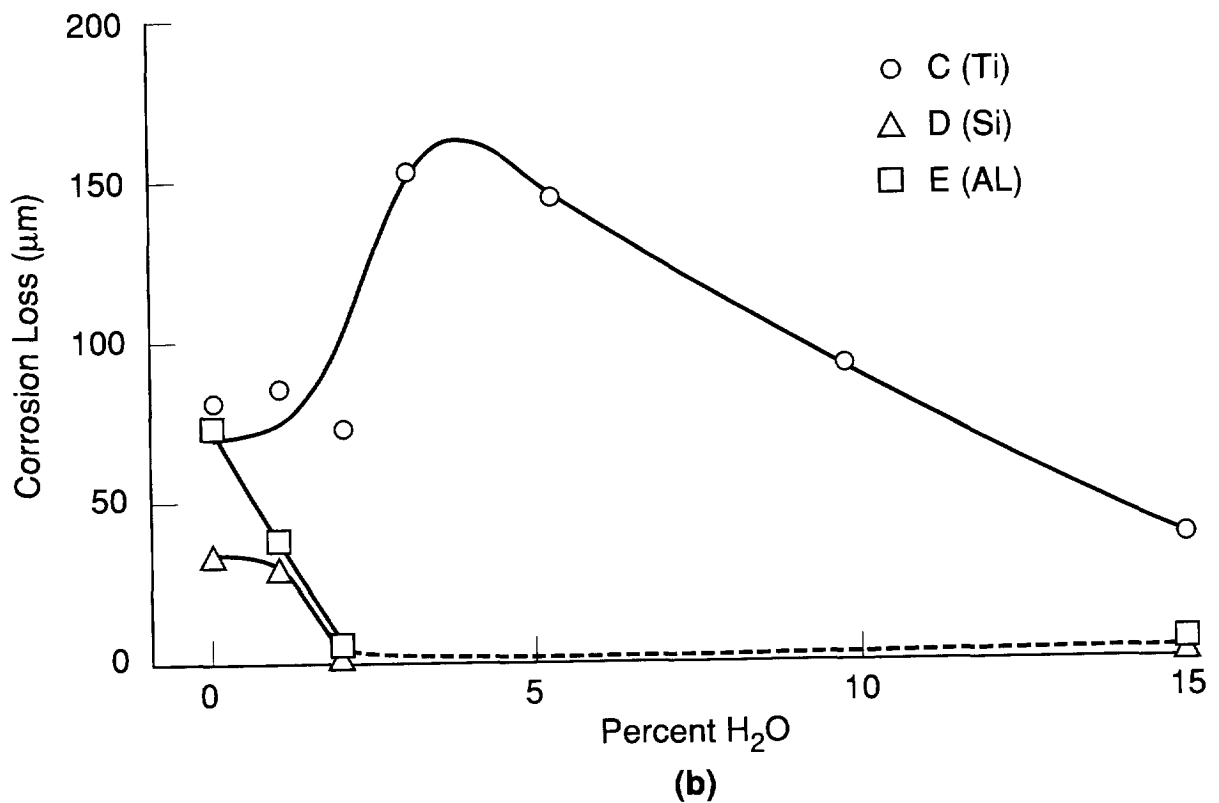
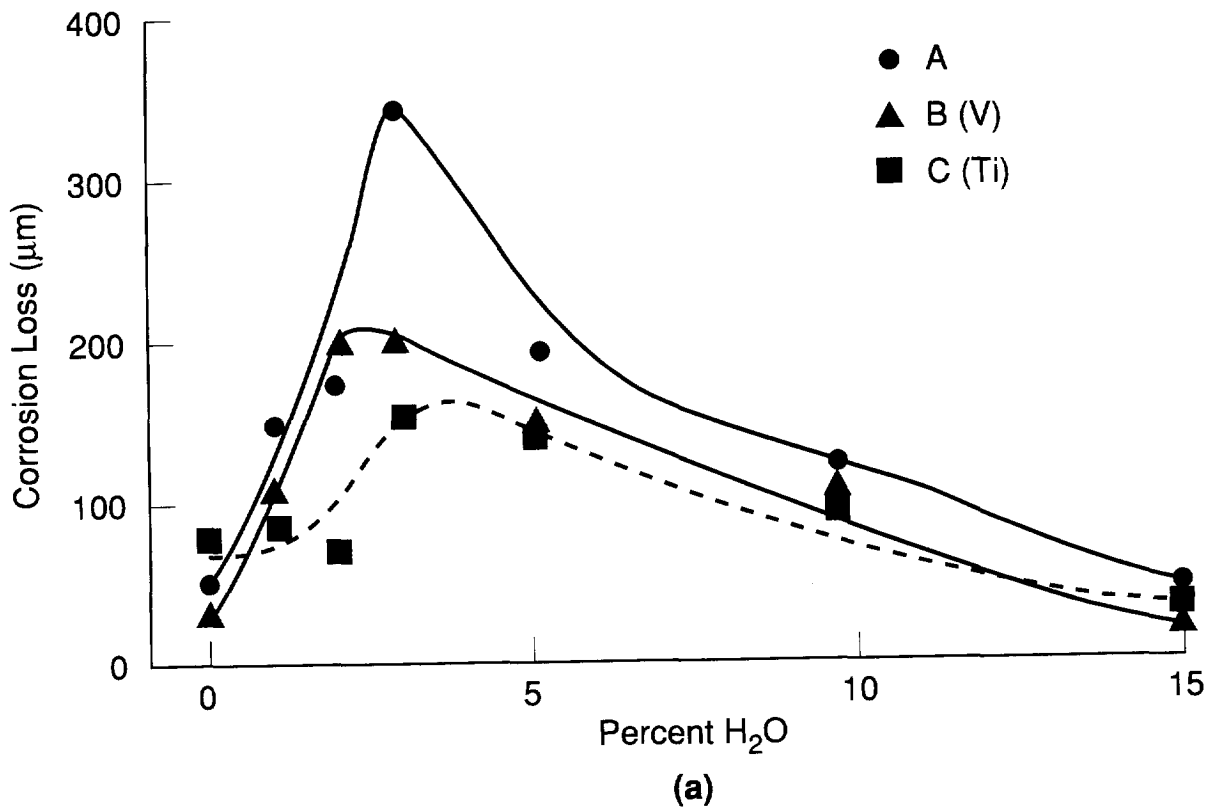


Figure 5.4
Corrosion As a Function of H₂O Content of Syngas (0.8% H₂S)

loss decreases with increasing H₂O content, although at this point the oxygen pressure increases only slowly with increasing water content. Alloys B and C containing V and Ti, respectively, follow the same trend with maximum corrosion losses when the syngas contains 2-5% steam.

The shape of the curves appears to indicate that the maximum corrosion loss of the V containing alloy occurs at a lower water content than that of the Ti containing alloy. Alloys containing Si and Al behave differently. Their corrosion losses are moderately high at low water contents, but drop to less than 10 μm when the water content reaches 2% (Figure 5.4B). This suggests the existence of a relatively sharp "kinetic boundary" as defined by Natesan²⁷ and Perkins²⁴.

5.2.2 Corrosion as a Function of the CO₂/CO Ratio of the Gas

The composition of the steam containing gases was such that the oxygen pressure derived from the H₂O/H₂ ratio was always higher than that calculated from the CO₂/CO ratio (see Section 4.1). It was argued previously (Section 4.1) that the oxygen pressure derived from the H₂O/H₂ ratio is most likely to determine the corrosivity of the gas. However, it was decided to study a few water free gas mixtures as well for the following reasons.

1. to create gases with a very low PO₂.
2. to study the effect of oxidant on corrosion loss at the same PO₂.

Only a few corrosion tests were performed, because dry gas mixtures are of theoretical interest only, as they do not occur in practical gasifiers. Figure 5.5 shows the results plotted in the same format as the results on the water containing gases.

The corrosion test at the extremely low CO₂/CO ratio indicates that corrosion loss does not increase, when the gas becomes less oxidizing and, therefore, more sulfidizing. Most alloys show a decrease in corrosion rate with decreasing PO₂ while the corrosion loss of alloy D does not change. At the highest CO₂/CO ratio, the corrosion loss of the base line alloy (A) and the V containing alloy is much higher than in the equivalent water containing gas, while that of the Ti containing alloy was somewhat lower. Si and Al containing alloys were not tested here. At the intermediate CO₂/CO ratio the corrosion losses in both water-free and water-containing gases is high and somewhat variable. The limited data presented here clearly indicate that the type of oxidant used can affect the corrosion loss, at least in the non equilibrium gases used here.

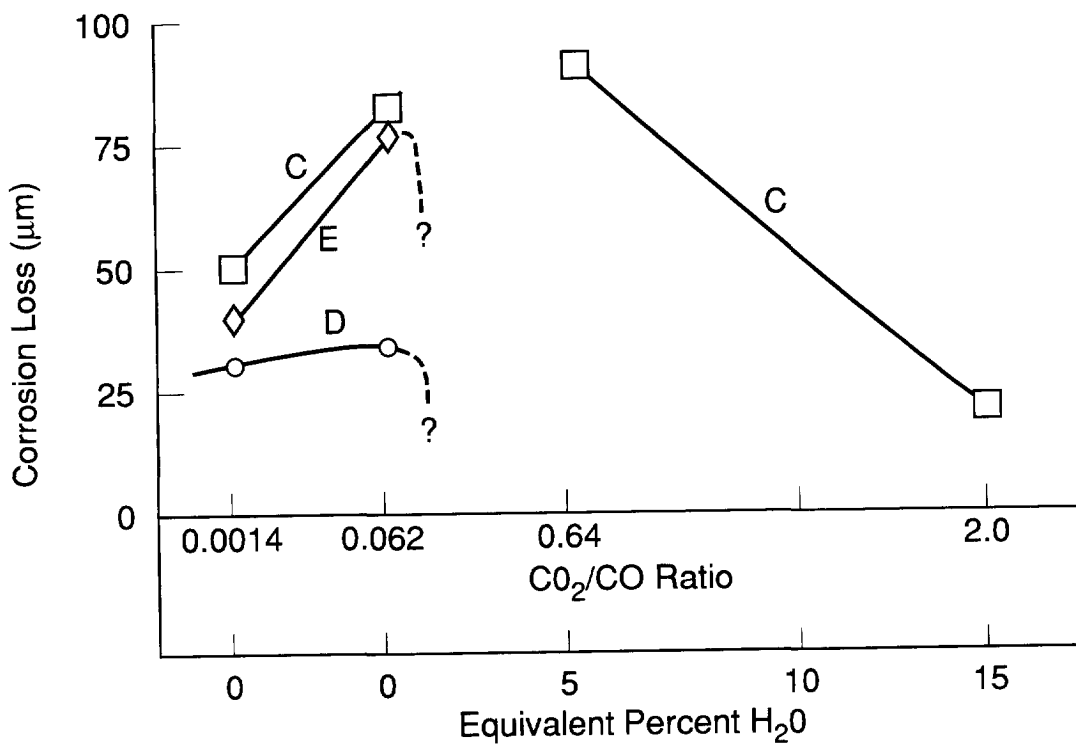
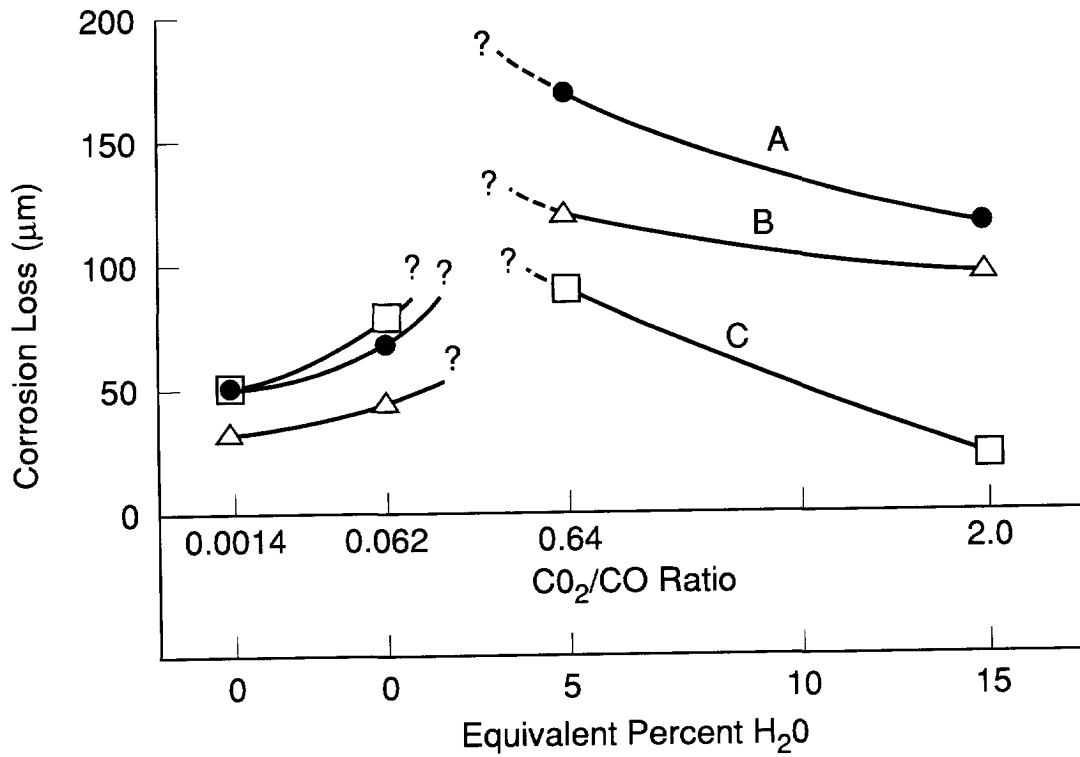


Figure 5.5
Corrosion As a Function of CO₂/CO Ratio of Syngas (0.8% H₂S, 0% H₂O)

5.2.3 Corrosion in Gases Containing 0.2% H₂S

A few tests were run with syngas containing 0.2% H₂S instead of 0.8% H₂S. The steam content of the gases were 0, 1 and 3% respectively. The PS₂/PO₂ ratio of the above gases is the same as that of gases containing 0.8% H₂S and 2, 3 and 15% H₂O respectively. Thus if the PS₂/PO₂ ratio of the gas is a factor controlling the corrosion rate, metal losses should be similar. Results are given in Table 5.4, gas composition 1A, 2A and 4A, and are plotted in Figure 5.6 for alloys A, B and C. Alloys D (Si) and E (Al) have very low corrosion losses after exposure for both gases containing 1 and 3% H₂O as expected from PO₂/PS₂ considerations. Alloys A and B have a maximum corrosion loss in syngas with 1% water, which is close to that found in syngas containing 0.8% H₂S and 3% H₂O. However the corrosion found in the water free gas is much lower than that in syngas containing 0.8% H₂S and 2% H₂O, while the corrosion loss in the syngas as containing 3% H₂O and 0.2 H₂S is much higher than that in syngas containing 0.8% H₂S and 15% H₂O. Thus it can be concluded that the correlation with the PS₂/PO₂ ratio is qualitative at best. There appears to be no major effect of the steam content in syngas containing 0.2% H₂S for alloy C, containing Ti. Here the corrosion loss is relatively high in all three gases, but does not peak in the gas containing 1% H₂O.

5.3 SCALE ANALYSIS

Scales formed during exposure to reducing gases are generally complex and consists of several layers. They are difficult to describe using simple parameters such as oxygen or sulfur content. Correlations between scale thickness and composition are not obvious or consistent. In this section we will, therefore, concentrate mainly on describing the morphology and mineralogical composition of the scale and how it changes when exposure time or exposure conditions are changed. No attempt will be made at this point to determine the reasons for changes in scale composition or correlation of scale composition with corrosion losses. To organize the large amount of data to be presented, this section is divided in the following subsections:

- 5.3.1 General description of typical scale, comparison between optical and SEM photomicrographs.
- 5.3.2 Effect of exposure time on scale development.
- 5.3.3 Effect of changes in steam content in the gas mixture.
- 5.3.4 Effect of changes in CO/CO₂ ratio in steam-free gases.
- 5.3.5 Effect of different H₂S levels (0.2% H₂S vs 0.8% H₂S).

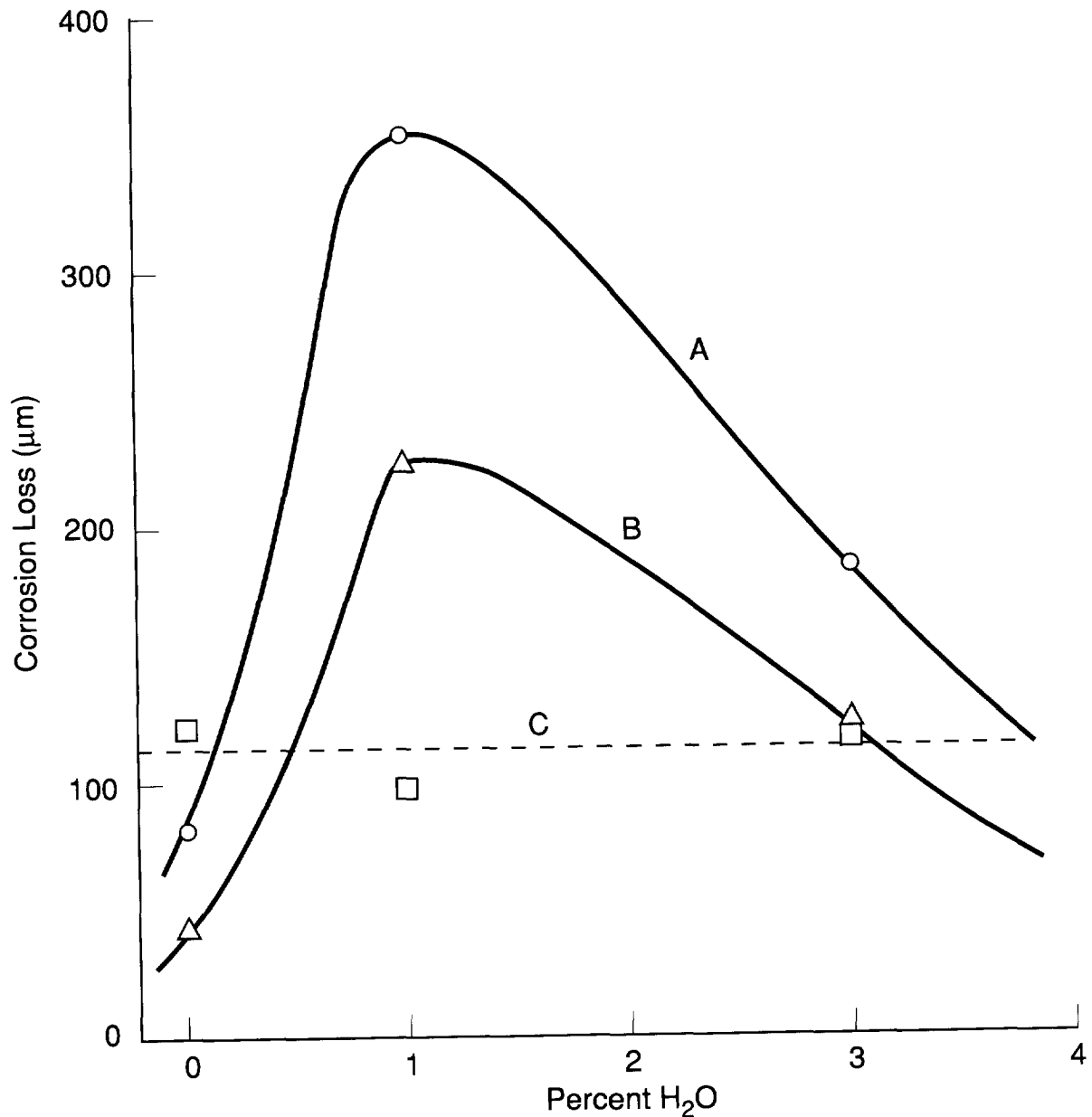


Figure 5.6
Corrosion As a Function of H₂O Content in Syngas (0.2% H₂S)

In all subsections scale development on the base alloy will be discussed first, followed by a description of the effect of the various alloying elements. Table 5.5, 5.6, and 5.7 show which specimens were selected for evaluation, since it was not possible to analyze all specimen exposed.

Table 5.5
Scale Analysis. Effect of Exposure Time. Test Matrix.

Alloy	A		B		C		D		E	
H ₂ S	0.2	0.8	0.2	0.8	0.2	0.8	0.2	0.8	0.2	0.8
Time (hrs)										
1.5		x						x		
15		x						x		x
150		x				x				
600	x	x		x		x		x		x
1350		x	x		x					
1224		x		x		x				

Table 5.6
Scale Analysis. Effect of Oxidants. Test Matrix

Alloy		A	B	C	D	E
%H ₂ O	CO/CO ₂ ratio					
	0.0015	x	x	x	x	
	0.062	x		x	x	x
1		x	x		x	x
2			x	x	x	x
3		x				
5	0.04			x		
10		x	x	x		
15	2.1	x		x		

Table 5.7
Scale Analysis. Effect of H₂S Content. (0.2H₂S). Test Matrix

Alloy		A	B	C	D	E
%H ₂ O	CO/CO ₂ ratio					
0	0.062	x	x	x		
1		x	x	x	x	x
3		x	x	x		

5.3.1 General Description of Typical Scale

Figure 5.7A shows an optical photomicrograph of Alloy A after 1350 hrs. exposure to gas 1A in Table 4.3 (0% H₂O 0.2% H₂S). This scale is considered fairly typical after a long term exposure (≥ 600 hrs.). The original alloy surface is clearly visible. The outward growing (epitactical) scale is generally porous and has detached from the inward growing (topotactical) scale. The epitactical scale consist of a very porous crystalline outer layer (A), which according to SEM/EDS analysis, consists of (Fe, Ni) S. Generally, the Fe content of the scale is significantly higher than the Ni content, but considerable variation occurs. Closer to the original alloy surface (B), the epitactical scale is more dense and continuous and generally contains a small amount of Cr in addition to Fe, Ni and S. The chromium content generally increases towards the bottom of the scale and the Ni content decreases. This is usually indicated by a lower reflectivity.

The top layer of the inward growing (topotactical) scale (C) has frequently a higher reflectivity than remainder of the topotactical scale and usually consists mainly of FeCr₂S₄ spinel. It is not always clear whether this layer is epitactical or topotactical. Oxygen is either absent or present in minor amounts only. The remainder of the topotactical scale (D) has a low reflectivity and frequently has a granular, and sometimes a banded appearance. It generally consists of oxides and sulfides. In some environments, it may contain areas, deficient of oxidants (O and S). The oxygen content of this zone generally increases with increasing oxygen partial pressure in the gas. Frequently, sulfides and oxides are not homogeneously distributed. For alloys containing minor alloying additions (V, Ti, Si, Al), this alloying addition is present only in the topotactical scale. The Ni content of the topotactical scale is generally low. The scale/metal interface is generally irregular, and can show pronounced pitting, with minor intergranular corrosion or precipitation of oxides and sulfides. The alloy just below the scale (E) frequently contains less Cr and more Ni than the original alloy.

The above is only a very general description of the scale formation in non equilibrium highly, reducing gases. The many variations caused by changes in time, gas composition and alloy composition will be described in detail in the following sections. Readers not interested in microscopic details, may want to skip to Section 6, where the results will be summarized and correlated with corrosion loss data.

5.3.2 Effect of Exposure Time on Scale Development. Gas 1, 0% H₂O, 0.8% H₂S, 540°C.

A. Base alloy (A) 20Cr-35Ni-0.35, 1.0 Mn bal Fe.

Samples of the alloy were exposed for 1.5, 15, 150, 600 and 1224 hrs. Each run was carried out continuously without interruptions. The sample exposed for 1.5 hrs had a weight gain of only 2.4 mg/cm², indicating a very thin scale. It was, therefore, not sectioned; the

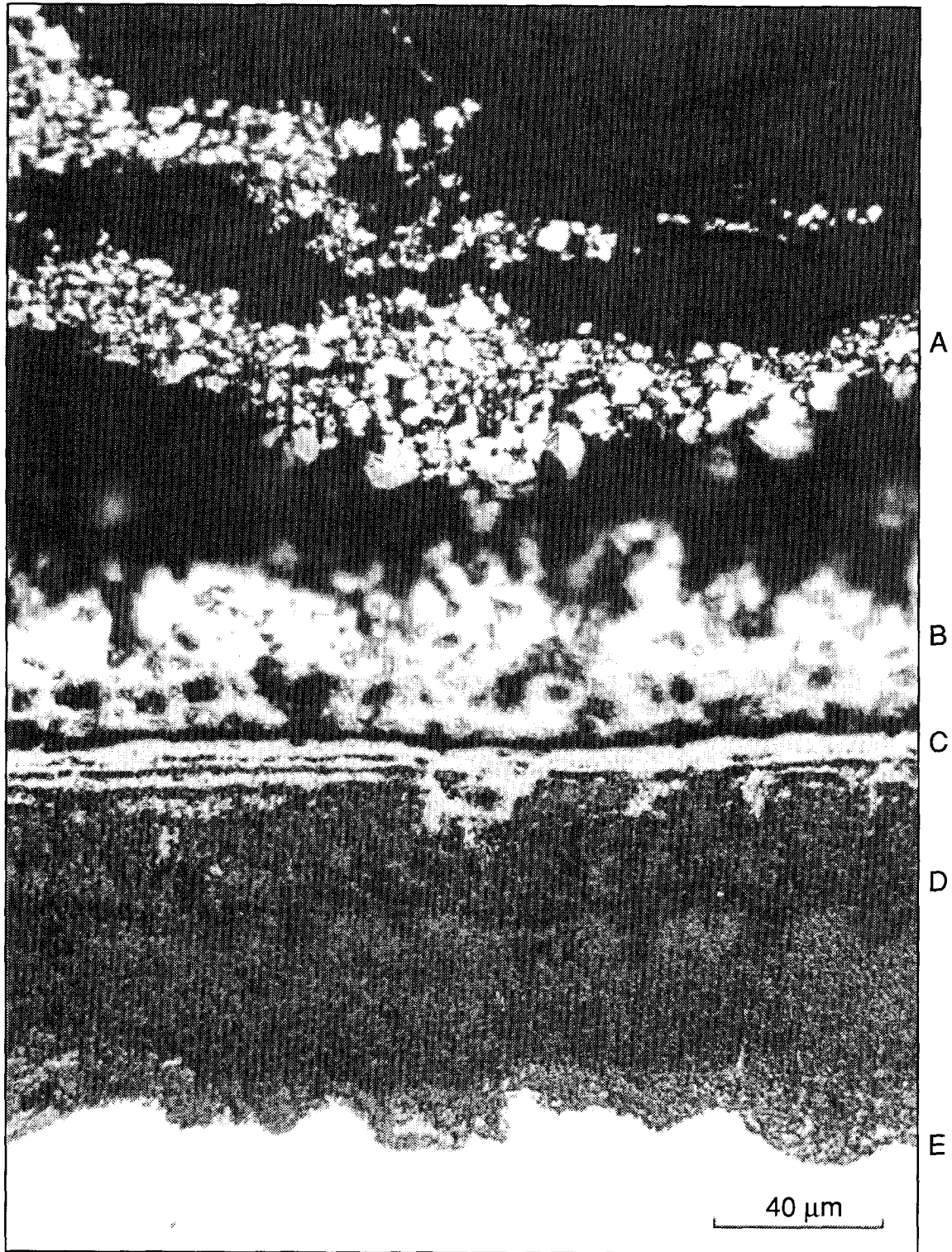


Figure 5.7
Optical Photomicrograph of Scale on Alloy A, 1350 hr Exposure, Gas 1A

corroded surface was examined directly by SEM/EDS. Two layers of scale were visible an outer/partially spalled layer and an inner seemingly adherent layer. Both layers were finely crystalline and similar in appearance to the scale formed on alloy D, which contains 3% Si (Figure 5.19). The chemical composition of the two scale layers is given in Table 5.8. The E.D.S. analysis provided is not as accurate as those from flat polished sections. Both scales consist mainly of iron and nickel sulfides, with only a minor amount of oxide present. Nickel appears to be the fastest outward diffusing element followed by Fe and Cr.

Table 5.8
Scale Composition on Alloy A. 1.5 hrs Exposure, Gas 1, 540°C (at%)

Scale Area	O	S	Fe	Ni	Cr
outer	11	35	17	37	<1
inner	2	46	40	7	5

After 15 hrs exposure a well defined corrosion scale was present on the alloy as shown in Figure 5.8. The scale consists of two layers, an outer slightly brighter layer and an inner layer, separate by an irregular interface. The inner layer is cracked. Quantitative EDS analysis indicates that the inner layer consist of stoichiometric FeCr_2S_4 and contains no oxygen. The outer layer was analyzed qualitatively only and consisted of FeNi sulfides.

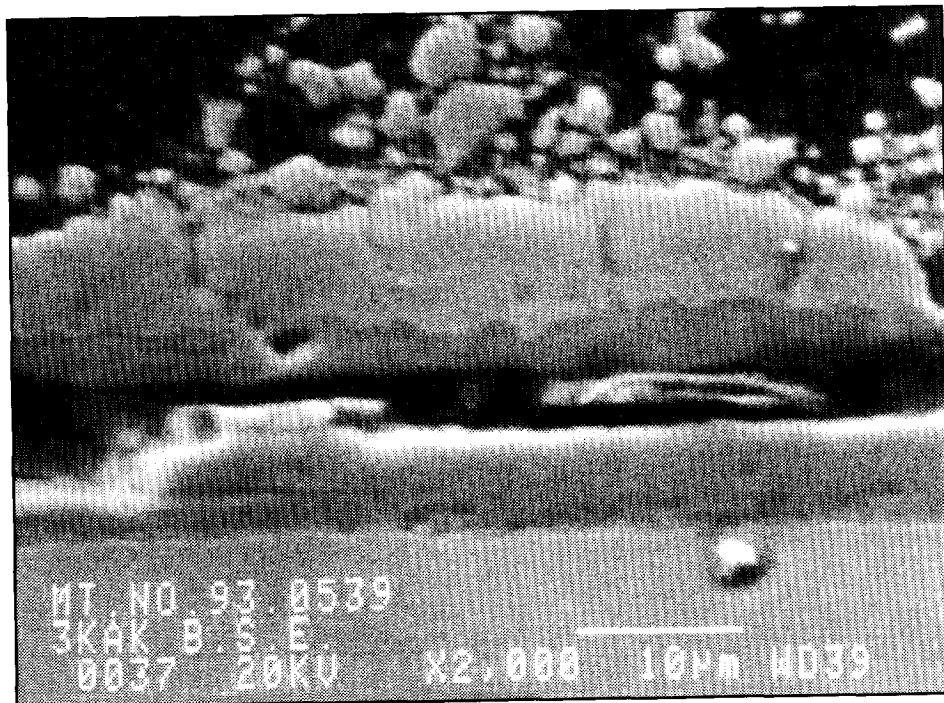


Figure 5.8
Back Scattered Electron (BSE) Image of Scale on Alloy A, 15 hr Exposure, Gas 1, 540°C

After 150 hrs exposure a more complex scale is present, as shown in Figure 5.9. Quantitative EDS analyses were made of the various elements in the scale and are presented in Table 5.9

Table 5.9
Scale Composition on Alloy A. 150 hrs Exposure, Gas 1, 540°C (at %)

Scale Area	O	Si	S	Cr	Fe	Ni
1	21	1	18	30	29	1
2	24	2	28	41	4	>0.5
3	<0.5	<0.5	55	30	14	<1
4	0	<0.5	50	10	29	11
5	1	<0.5	45	<0.5	28	25

Note: Scale areas are shown on BSE image. Fig. 5.9.

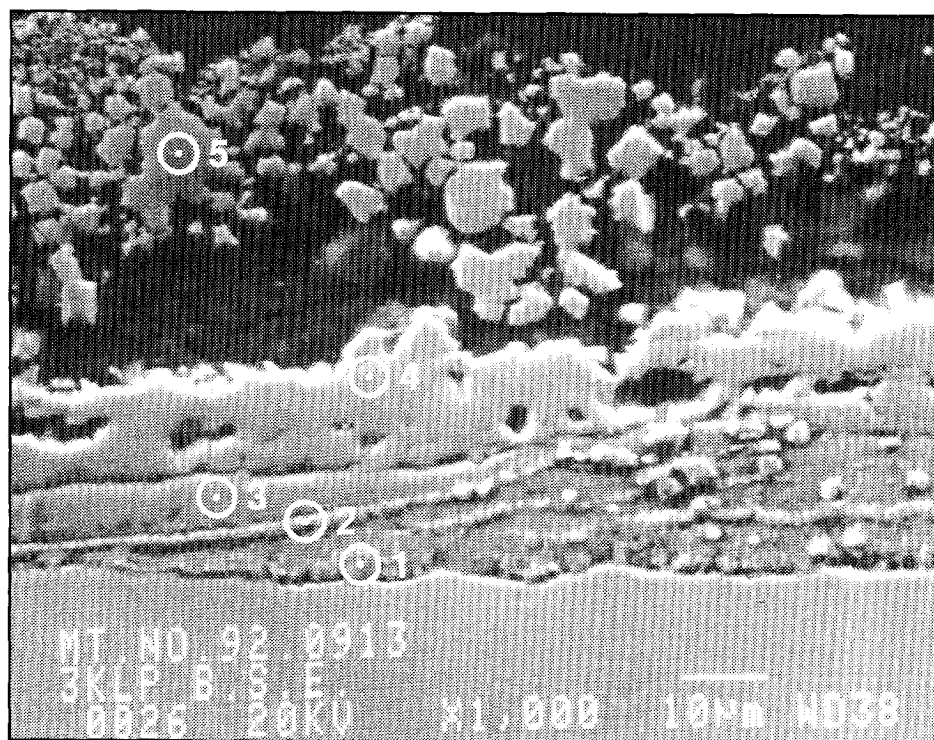


Figure 5.9
BSE Image of Scale on Alloy A, 150 hr Exposure, Gas 1, 540°C

The granular layer close to the metal surface (1) appears to be incompletely oxidized as the S+O content of this part of the scale is less than 40%, indicating that as much as 20% metallic material may be present in the scale. This part of the scale also contains more fully converted bands (2), consisting mainly of substoichiometric Fe and Cr oxides and sulfides. Apparently this layer is formed under a stoichiometric FeCr_2S_4 layer (exact stoichiometry of FeCr_2S_4 is Fe 14at%, Cr 28at%, S 57at%), represented by 3. On top of the FeCr_2S_4 layer FeNi sulfides are predominant, initially with some chromium present (4). The loose crystalline outer scale consist of slightly substoichiometric FeNi sulfide. In general, the Ni content of the scale increases away from the scale metal/interface.

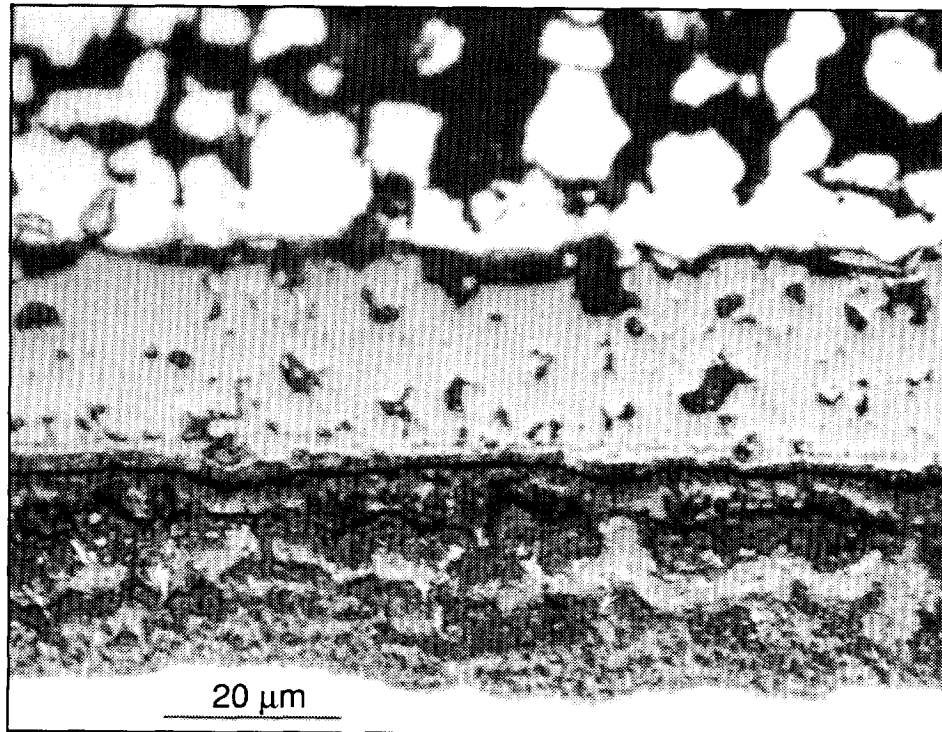
The scale development after 600 hr exposure is shown in Figure 5.10. Figure 5.10A shows an optical photomicrograph while Figure 5.10B shows a BSE image of the topotactical scale. The optical photomicrograph shows the standard scale development with an epitactical scale consisting of Ni rich Fe sulfide on the outside and Cr containing Fe sulfide near the topotactical scale. The topotactical scale is in-homogeneous with sulfide and oxide rich areas. Quantitative EDS analyses are shown in Table 5.10 below.

Table 5.10
Composition of Topotactical Scale on Alloy A. 600 hr Exposure, Gas 1, 540°C (at%)

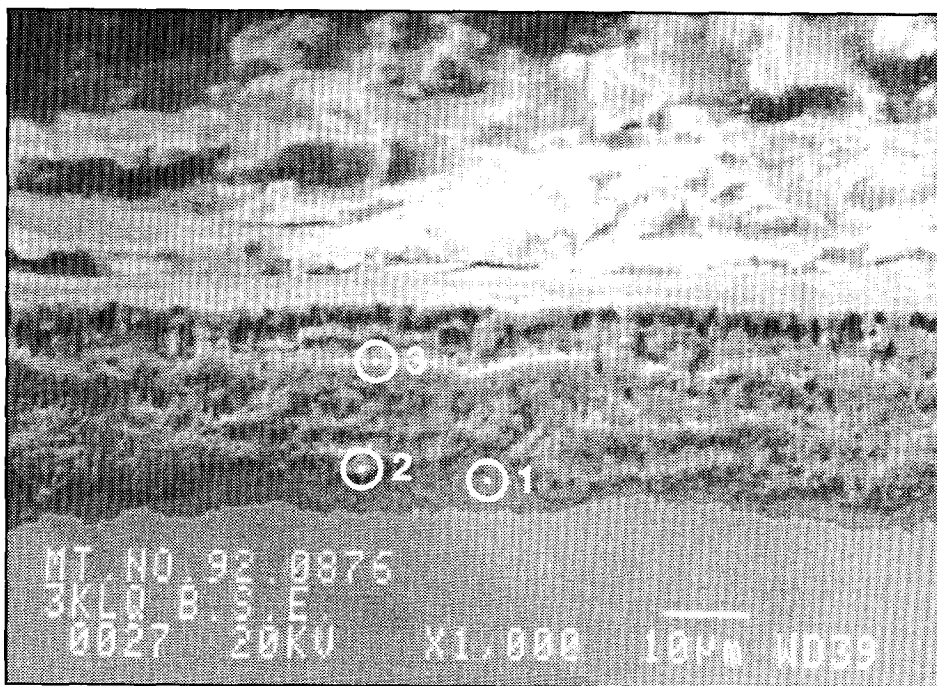
Scale Designation	1	2	3
O	9	49	35
Si	1	<1	1
S	44	3	12
Cr	33	44	45
Fe	13	3	5
Ni	<1	<1	1
Mn	<1	1	1

The scale near the scale/alloy interface consists mainly of FeCr_2S_4 with minor amounts of chromium oxide (1). A small discrete crystallite was mainly CrO_y with a O/Cr ratio of 1.1, i.e., highly reduced (2). The small amounts of Fe and S present are probably from the surrounding scale as the crystallite size was close to the beam width of the SEM ($\pm 1\mu\text{m}^2$). The upper scale consists of oxygen and sulfur rich bands. Area 3 gives an analysis of an oxygen rich band, which is somewhat oxidant deficient and consists mainly of chromium oxides and iron sulfides.

After 1224 hrs exposure the topotactical scale is still inhomogeneous as shown in Figure 5.11. Table 5.11 gives EDS analyses of selected areas. Near the metal/scale interface the scale consists of a sulfur rich matrix (1), with Cr_xO_y precipitates (2) with an O/Cr ratio of 1.4, i.e., close to stoichiometric Cr_2O_3 . Further away from the metal/scale



(a)
Optical Photomicrograph



(b)
BSE Image of Topotactical Scale

Figure 5.10
Photomicrographs of Scale on Alloy A, 600 hr Exposure, Gas 1, 540°C

interface, the scale generally has a high sulfur content and probably consist mainly of FeCr_2S_4 with a minor, but significant amount of oxygen (3). Most likely some of the sulfur in the thiospinel is replaced by oxygen here.

Table 5.11

Composition of Topotactical Scale on Alloy A. 1224 hr Exposure, Gas 1, 540°C

Scale Designation	1	2	3
O	25	56	16
Si	1	<0.5	1
S	34	2	38
Cr	29	40	31
Fe	11	1	14
Ni	<0.5	0	<0.5
Mn	<0.5	1	<0.5

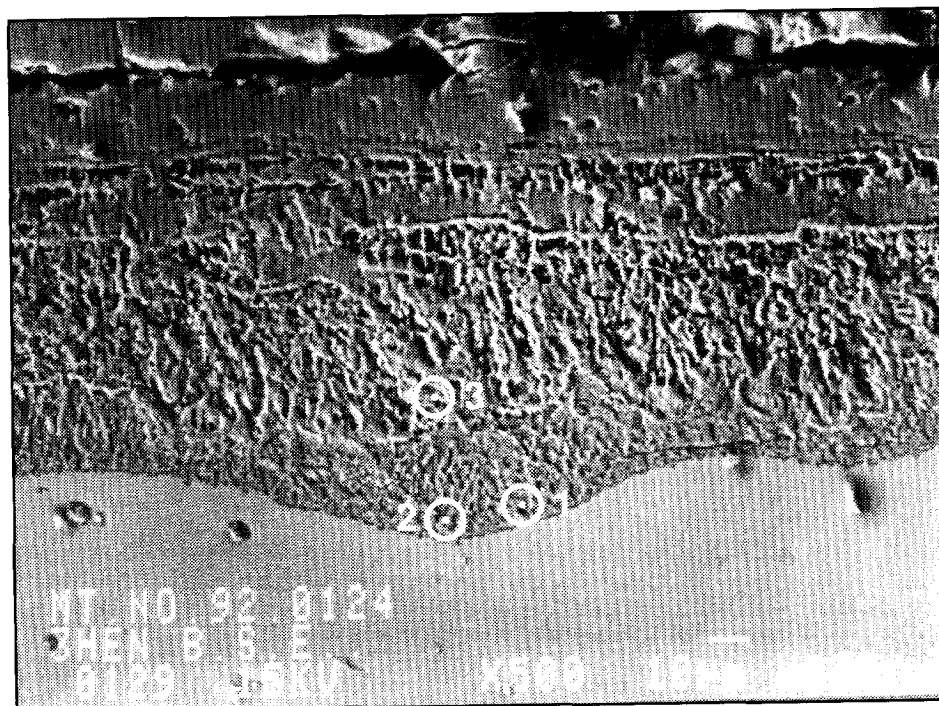


Figure 5.11

BSE Image of Scale on Alloy A, 1224 hr Exposure, Gas 1, 540°C

B. Alloy B, 20Cr-35Ni - 3.25V - 1Mn 0.3 Si, bal Fe

The scale developed on this alloy after 15 hrs exposure is shown in Figure 5.12. The scale has spalled away from the alloy and consists of three layers. the top layer A consists of Fe Ni sulfides. Analyses of the middle and bottom layers are given in Table 5.12.

Table 5.12
Composition of Scale on Alloy B. 15 hr Exposure, Gas 1, 540°C (at%)

Scale Area	O	Si	S	V	Cr	Mn	Fe	Ni
1	1	2	52	18	19	<.5	3	5
2	1	<.5	56	<.5	29	1	13	<.5

The thin layer adjacent to the alloy (1) consist mainly of $(Cr, V)_yS_x$ with a S/m ratio of 1.4, i.e. halfway between M_2S_3 and M_3S_4 . The iron and Ni may be present in metallic form as indicated by the mottled appearance of the layer. The middle layer (2) is stoichiometric $FeCr_2S_4$ with very little V. The top layer of the alloy contains some S, C and O in addition to the main alloying elements. The analysis described above indicates an epitactical scale consisting of a FeNiS outer layer and a $FeCr_2S_4$ inner layer. Under the epitactical scale is an almost completely converted precipitation zone enriched in vanadium.

The scale developed after 600 hrs is shown in Figure 5.13. The topotactical scale is inhomogeneous. The scale/alloy interface is irregular. Precipitates are visible in the alloy surface. WDS/EDS analyses of the scale are given in Table 5.13.

Table 5.13
Composition of Scale on Alloy B After 600 hr Exposure, Gas 1, 540°C (at%)

Scale Area	O	Si	S	V	Cr	Mn	Fe	Ni
1	6	1	53	4	22	2	10	2
2	29	<.5	28	6	29	<.5	5	1
3	32	<1	13	4	30	<.5	16	3
4	30	1	9	4	24	<.5	26	4

The lack of oxidants in areas 3 and 4 indicate the presence of metallics, most likely Fe and some Ni in the "scale" near the alloy/scale interface.

After 1224 hr exposure a topotactical scale, about 60 μ m thick is present. The scale is quite inhomogeneous as shown on Figure 5.14A. Therefore, elemental maps of the topotactical scale were prepared also, which are shown in Figure 5.14B. The epitactical scale consists

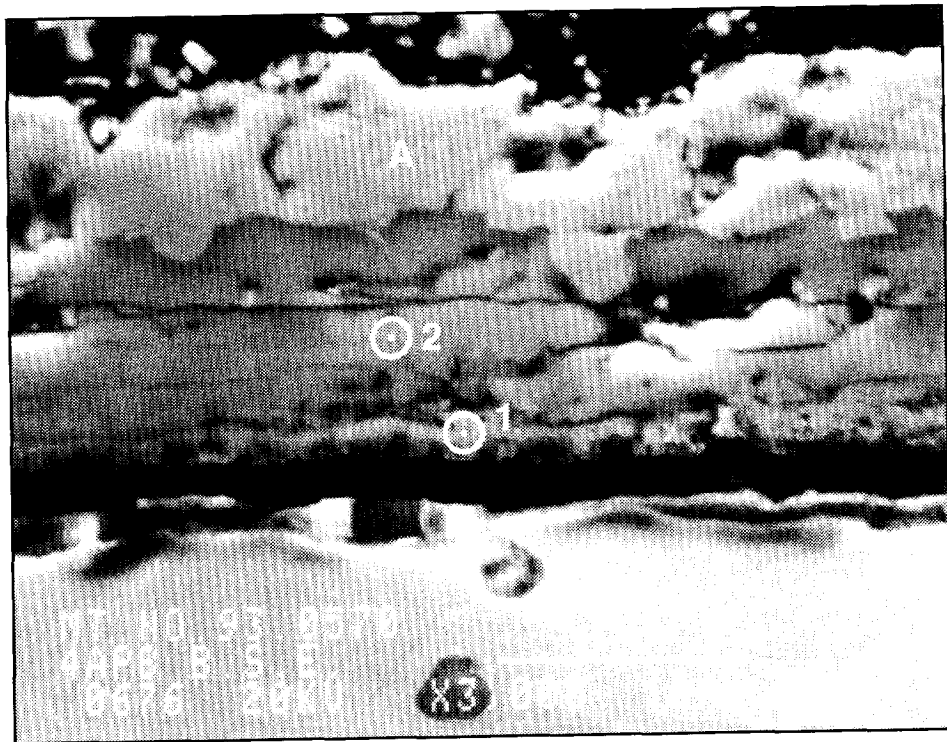


Figure 5.12
BSE Image of Scale on Alloy B, 15 hr Exposure, Gas 1, 540°C

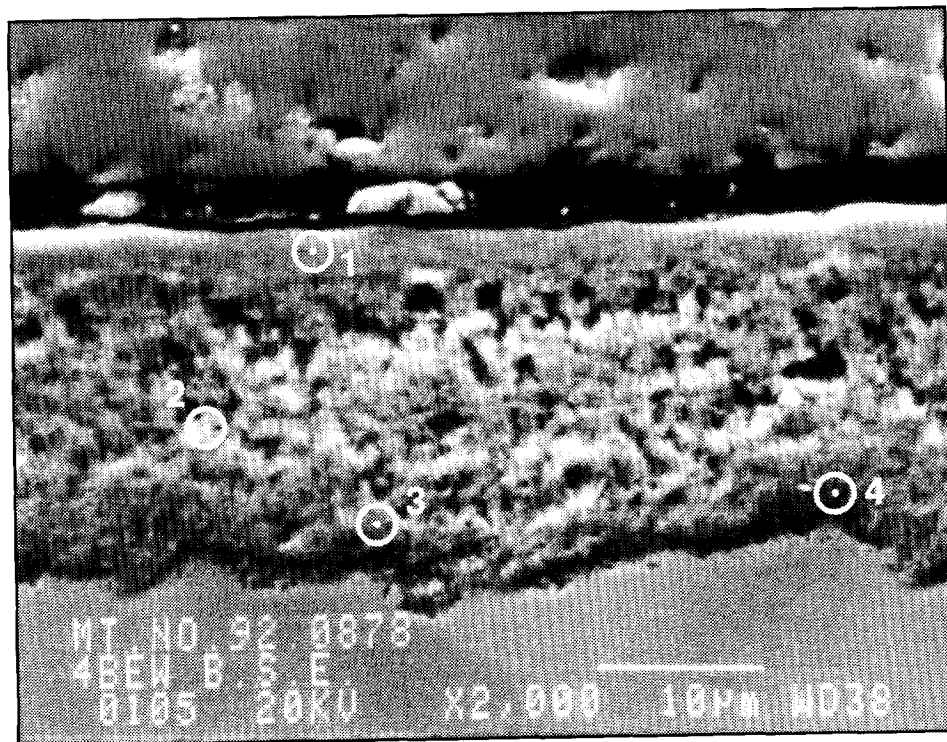
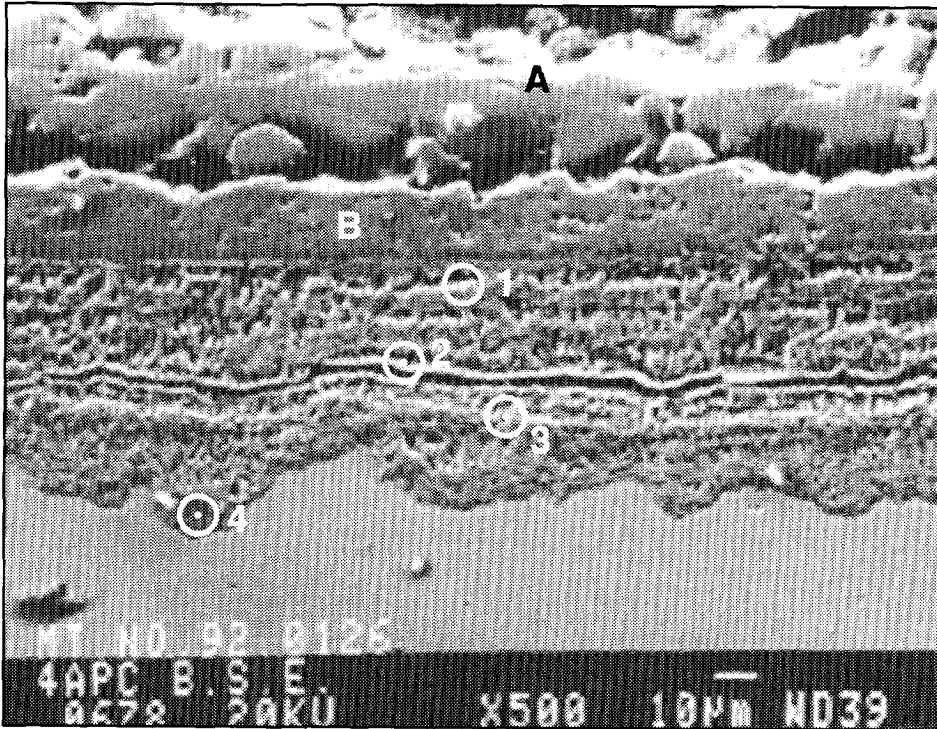
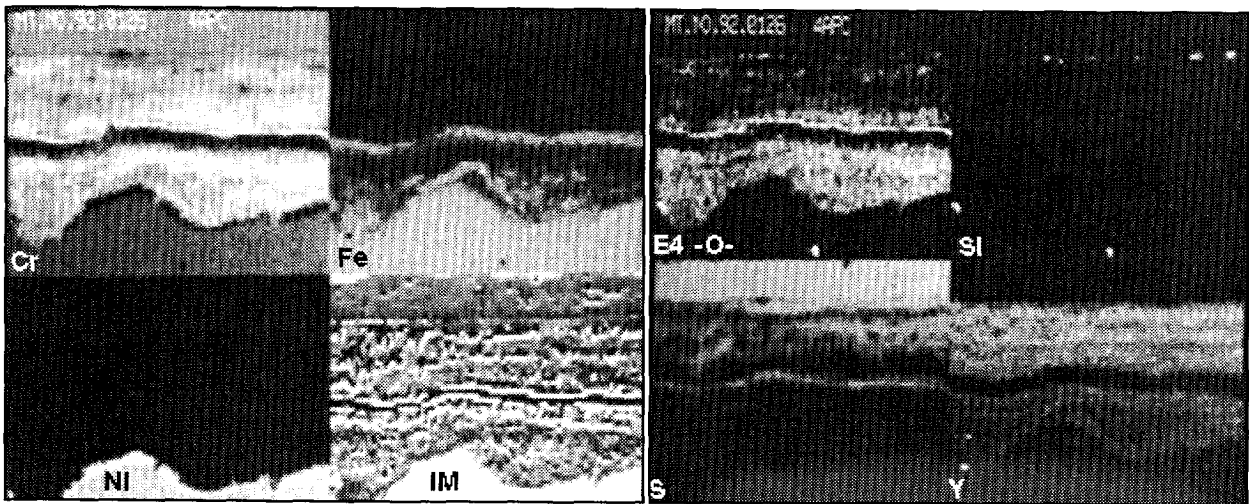


Figure 5.13
BSE Image of Scale on Alloy B, 600 hr Exposure, Gas 1, 540°C



(a)
BSE Image



(b)
Elemental Maps

Figure 5.14
Photomicrographs of Scale on Alloy B, 1224 hr Exposure, Gas 1, 540°C

of a layer of FeCr_2S_4 below a FeNiS layer. Quantitative EDS/WDS analyses of selected areas in the topotactical scale are given in Table 5.14.

Table 5.14
Composition of Scale on Alloy B. 1224 hrs Exposure, Gas 1, 540°C (at%)

Scale Area	O	Si	S	V	Cr	Mn	Fe	Ni
1	7	2	34	15	3.5	<5	6	1
2	44	1	14	6	24	0	9	1
3	2	<.5	50	1	25	1	20	1
4	24	1	6	4	23	1	34	5

There appears to be a partially converted V rich layer on the top of the topotactical scale as well as at the scale alloy interface.

C. Alloy C, 20Cr-35Ni-3Ti, 0.3Si, 1.0 Mn, bal Fe

After 15 hrs exposure the scale developed on this alloy was similar to that on the base alloy, except for a very thin Ti rich subscale at the scale alloy interface. Figure 5.15 shows the SEM/BSE age, while Table 5.15 gives quantitative EDS analyses of the lower scale. The loose top scale consists of (Fe, Ni) S similar to the base alloy.

Table 5.15
Scale Composition on Alloy C, 15 hrs Exposure, Gas 1, 540°C (at%)

Scale Designation	O	Si	S	Ti	Cr	Fe	Ni	Mn
1	6	<0.5	51	<1	27	14	<1	1
2	6	3	37	20	10	5	20	1

The main scale (1) consists of slightly oxidized FeCr_2S_4 without Ti while the "subscale" consists mainly of Ti, Cr and Fe sulfides (2), minor amounts of SiO_2 and a significant amount of unreacted metal.

The scale developed after 150 hrs exposure is shown in Figure 5.16, and is inhomogeneous. This is confirmed by the scale analyses in Table 5.16. The thick top layer was not analyzed quantitatively, but showed the EDS spectrum of FeCr_2S_4 . The topotactical scale consists of alternating layers of partially and more fully converted layers. The partially converted layers contain significant amounts of Fe.

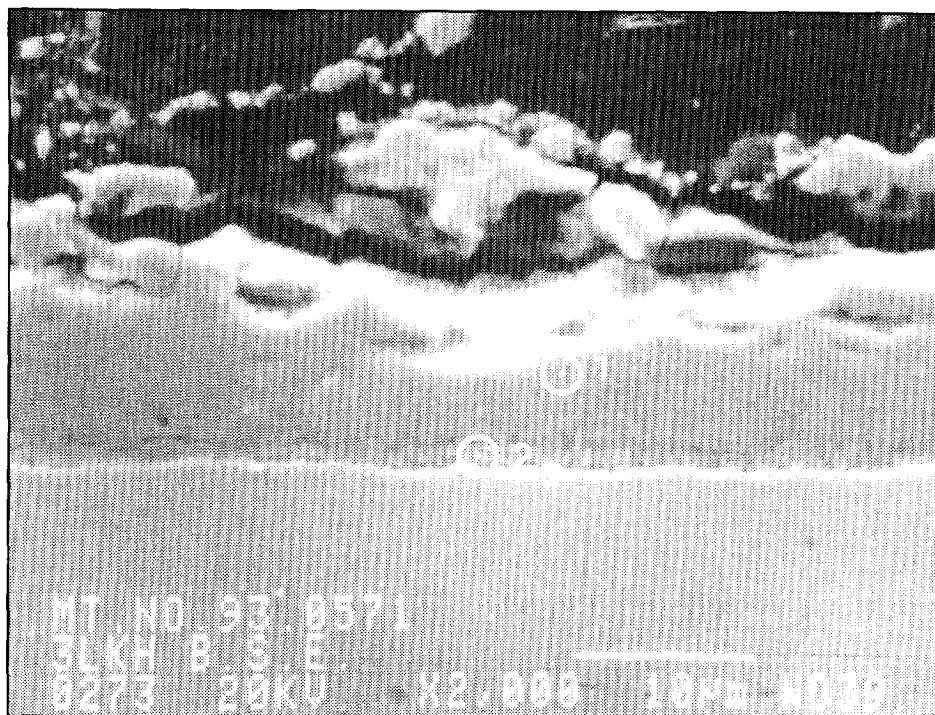


Figure 5.15
BSE Image of Scale on Alloy C, 15 hr Exposure, Gas 1, 540°C

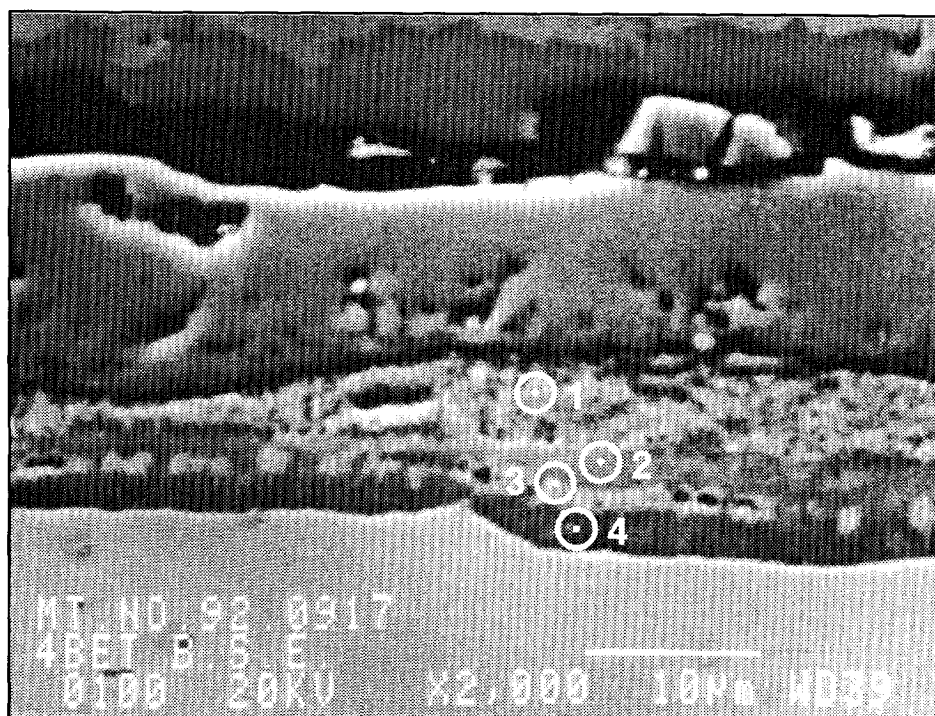


Figure 5.16
BSE Image of Scale on Alloy C, 150 hr Exposure, Gas 1, 540°C

Table 5.16
Composition of Scale on Alloy C, 150 hrs Exposure, Gas 1, 540°C (at%)

Scale Area	O	Si	S	Ti	Cr	Mn	Fe	Ni
1	6	<1	22	1	16	<.5	48	6
2	18	2	29	7	37	<1	6	<.5
3	25	1	7.5	6	19	<.5	38	4
4	19	1	32	7	35	<1	4	<.5

After 600 hrs a very homogeneous topotactical scale is covered with a more porous epitactical scale, which as usual consists of FeNi sulfides, Figure 5.17. There are no partially converted scale areas. The scale composition is (at%): O 43, Si 1, S 13, Ti 4, Cr 30, Fe 7 and Mn 1. Therefore, scale consists mainly of Ti and Cr oxides with lesser amounts of Cr and Fe sulfides.

Figure 5.18 shows the scale present at the surface of alloy C after 1224 hrs exposure. Here the scale is inhomogeneous again, similar to that after 150 hr exposure. Table 5.17 shows the EDS analyses of the various scale features.

Table 5.17
Composition of Topotactical Scale on Alloy C, 1224 hr Exposure, Gas 1, 540°C (at%)

Scale Designation	O	Si	S	Ti	Cr	Fe	Ni	Mn
1	20	1	32	5	33	8	1	<0.5
2	24	1	6	3	27	30	8	1
3	21	1	34	7	30	<0.5	<0.5	

The analyses given in Table 5.17, indicate that the scale near the alloy (1) is sulfur rich and probably consists mainly of Cr and Fe sulfides with minor, but significant amounts of Ti and Cr oxides. Within this region, there are significant areas, deficient in oxidants (2), which most likely contain Fe and Ni in metallic form together with some Ti and Cr oxide and minor amounts of sulfides. The scale further away from the alloy surface is fully converted and is similar to that near the alloy surface (3).

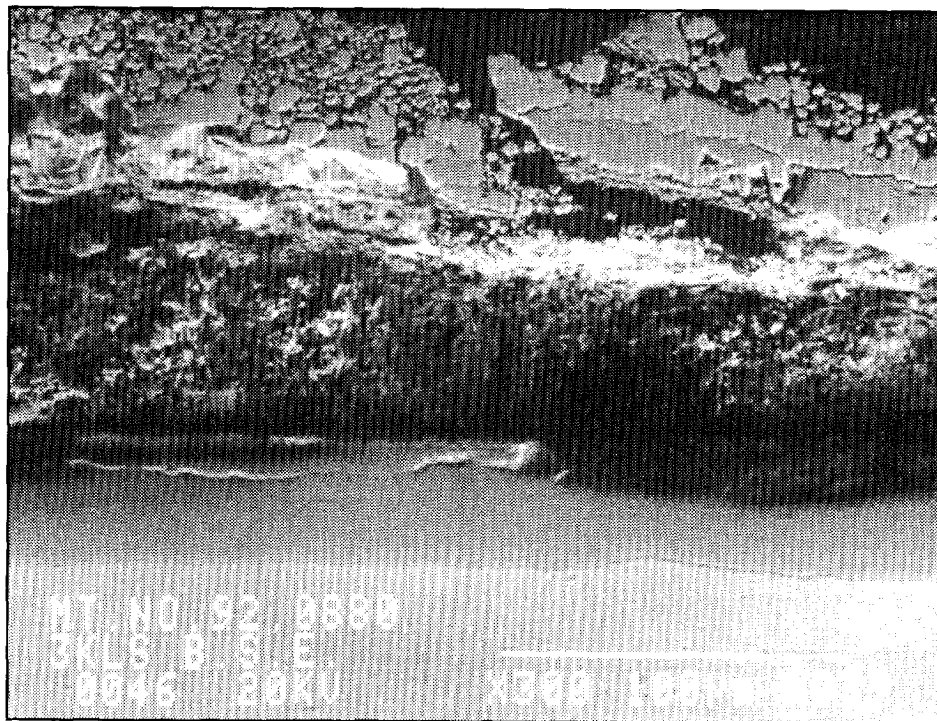


Figure 5.17
BSE Image of Scale on Alloy C, 600 hr Exposure, Gas 1, 540°C

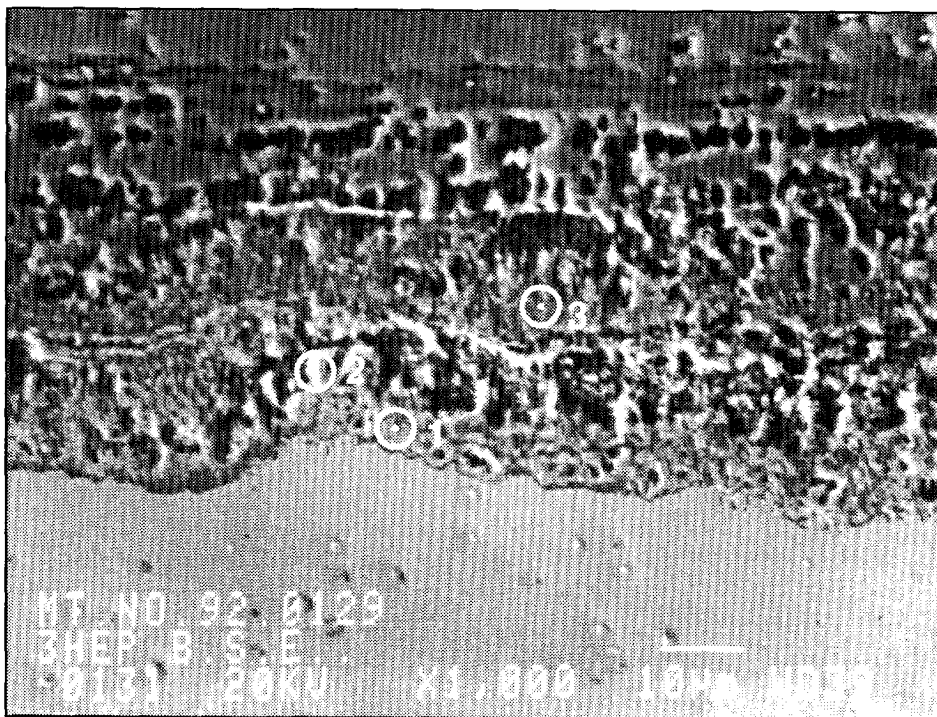


Figure 5.18
BSE Image of Scale on Alloy C, 1224 hr Exposure, Gas 1, 540°C

D. Alloy D, 20Cr-35Ni-3Si 1Mn 0.3S bal Fe

The appearance of the corroded alloy surface after 1.5 hr exposure is shown in Figure 5.19. EDS analysis showed little difference between the composition of the nodules and the scale. Both consist of Fe, Ni sulfides, but do not contain silicon.

After 15 hrs the scale has already become very complex as shown in Figure 5.20A. Quantitative EDS analyses of the various layers are given in Table 5.18 below.

Table 5.18
Scale Composition on Alloy D, 15 hr Exposure, Gas 1, 540°C (at%)

Scale Designation	O	Si	S	Cr	Fe	Ni	Mn
1	11	15	27	19	10	19	<1
2	2	14	23	11	6	43	<1
3	3	1	54	28	13	<1	1
4	1	<1	49	5	27	17	<1

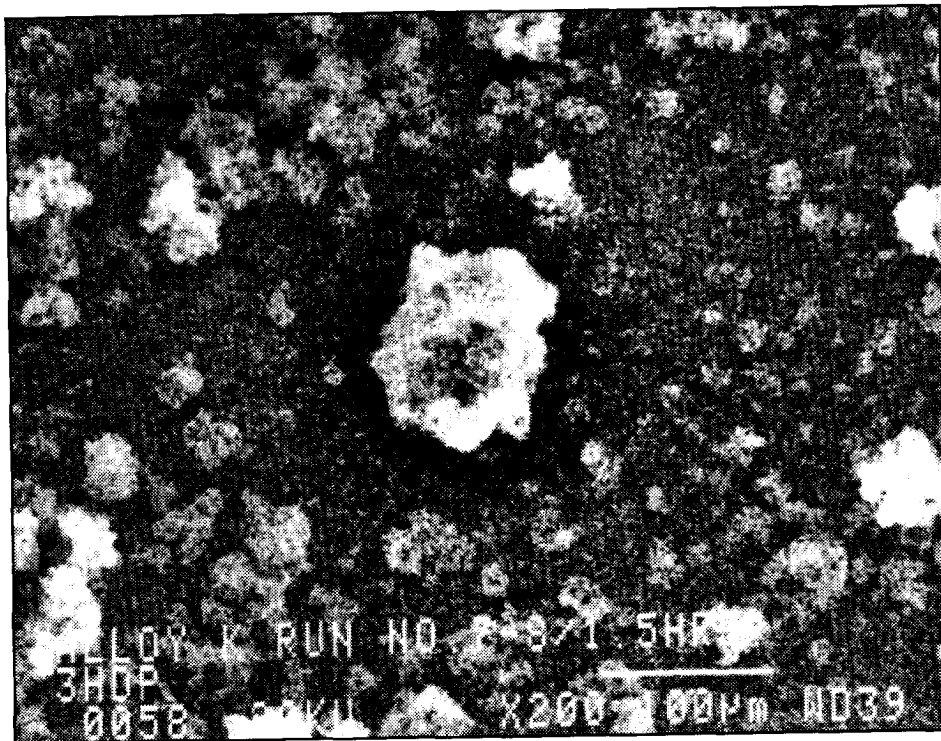


Figure 5.19
 BSE Image of Corroded Surface on Alloy D, 1.5 hr Exposure, Gas 1, 540°C

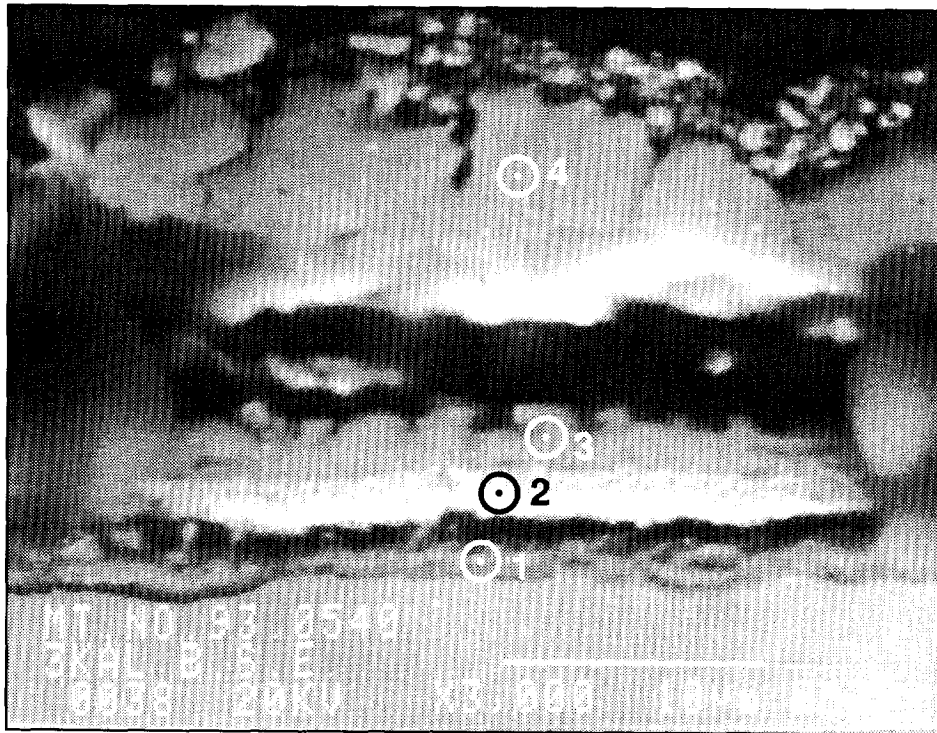
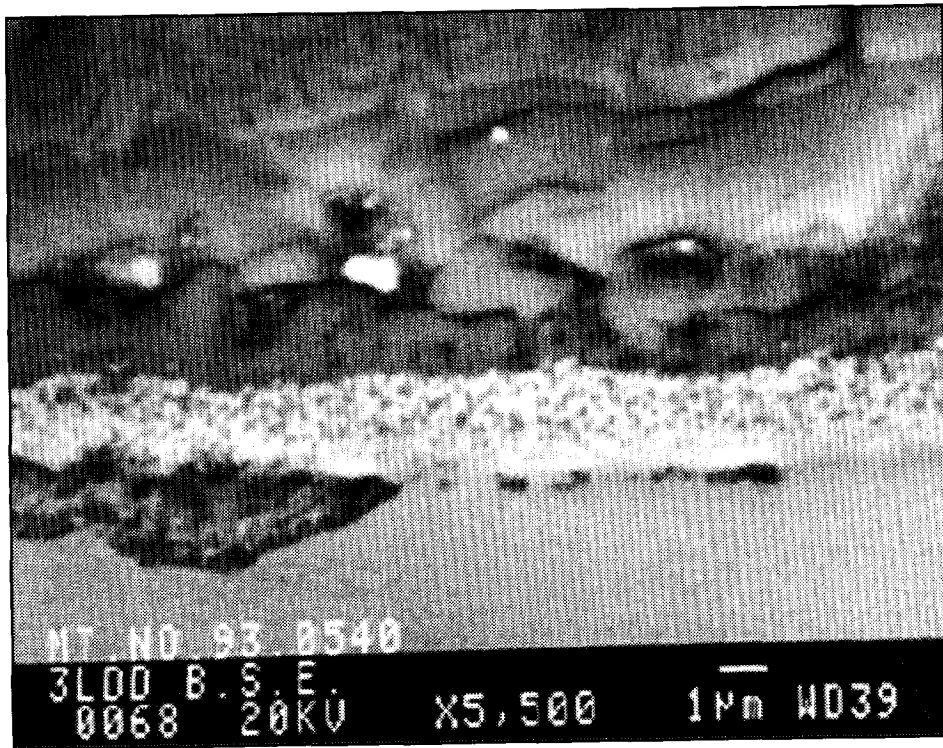


Figure 5.20a
BSE Image of Scale on Alloy D, 15 hr Exposure, Gas 1, 540°C

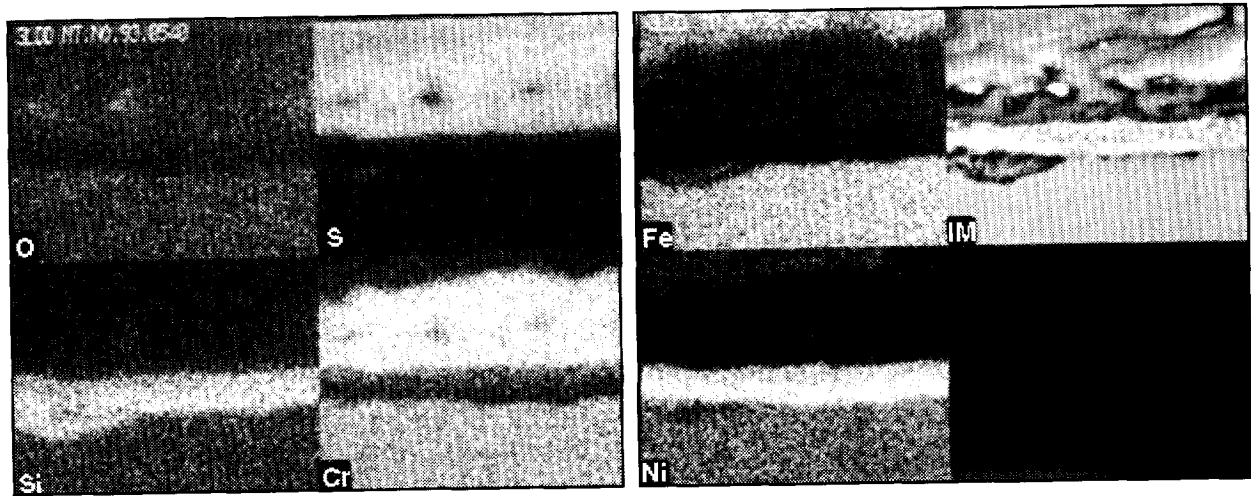
The layer adjacent to the alloy (1) is deficient in oxidants, but sulfide rich. Layer 2 is even more oxidant deficient and appears to consist mainly of a Ni rich alloy with sulfide precipitates. Si is enriched in both layers, but not enough oxygen is present to support the presence of SiO_2 . Only about half of the available Si in layer 1 can possibly be present as SiO_2 . On top of the Ni rich layer a near stoichiometric FeCr_2S_4 layer (3) is present which is silicon poor. The outer scale consists again of FeNi sulfides (4), with a minor amount of Cr.

To further study the elemental distribution in the scale; elemental maps of the scale were prepared and are shown in Figure 5.20B. The elemental maps reinforce the impression that sulfidation/oxidation occurred below a Ni rich alloy layer depleted in Cr and Fe. The silicon enrichment of layers 1 and 2 is also clearly shown.

After 600 hrs the scale thickness has increased considerably and exhibits a banded structure as shown in Figure 5.21. Table 5.19 gives the corresponding EDS analysis of the topotactical scale.



(a)
BSE Image of Scale



(b)
Elemental Maps

Figure 5.20b
Elemental Maps of Scale on Alloy D, 15 hr Exposure, Gas 1, 540°C

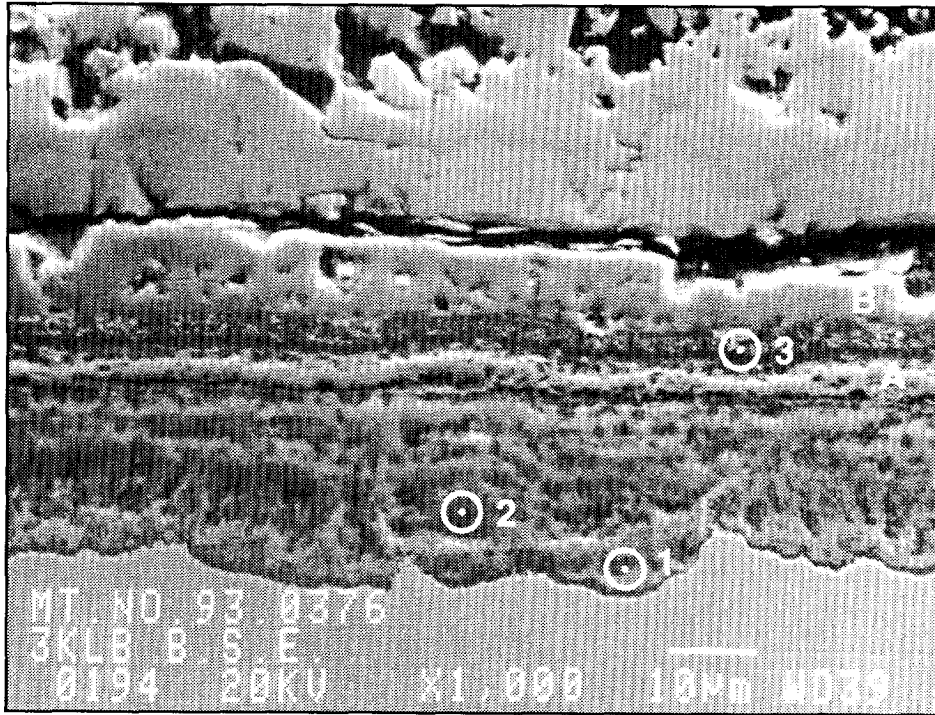


Figure 5.21
BSE Image of Scale on Alloy D, 600 hr Exposure, Gas 1, 540°C

Table 5.19
Composition of Topotactical Scale on Alloy D, 600 hr, Gas 1, 540°C (at%)

Scale Designation	O	Si	S	Cr	Fe	Ni	Mn
1	41	9	2	<9	16	2	1
2	42	8	15	30	4	<1	1
3	27	21	23	11	5	13	1

The dense layer on top of the topotactical scale again consist of FeCr_2S_4 (A) and FeNi sulfides (B). The composition of the topotactical scale suggest the initial formation of an SiO_2 rich layer at the alloy /scale interface (3), which was not protective enough to prevent ingress of oxygen and sulfur into the alloy. This resulted in an oxygen rich inward growing scale which is frequently deficient in oxidants.

E. Alloy E, 20Cr-35Ni-3Al-1Mn 0.3Si bal Fe

The scale formed after 15 hrs exposure is shown in Figure 5.22. A significant epitactical scale, consisting of (Fe, Ni) S is already present (A). Below the epitactical scale is a

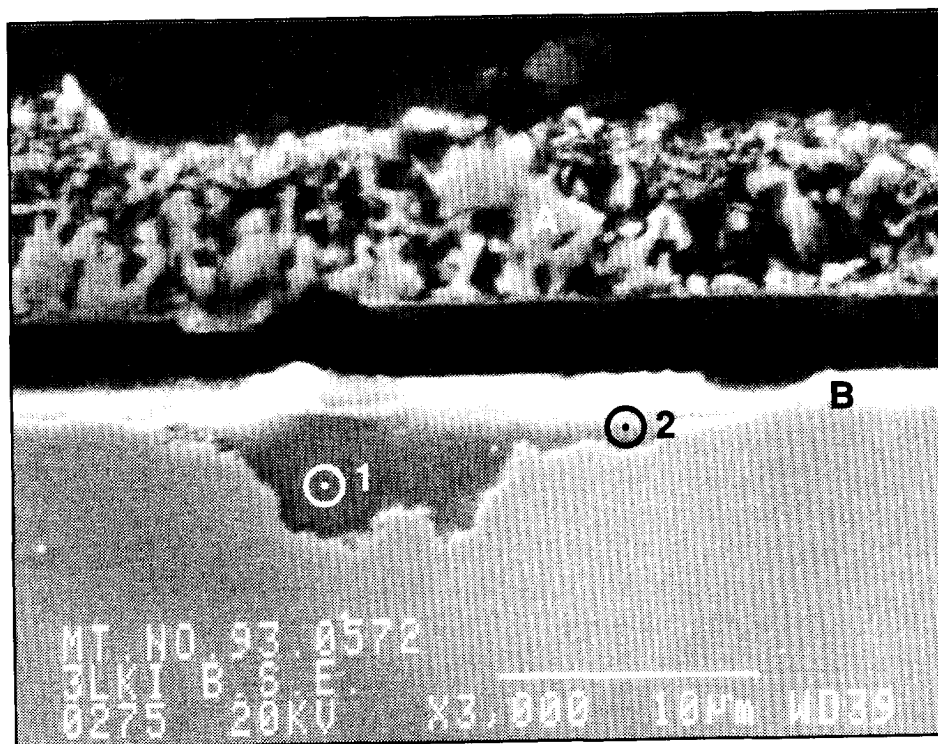


Figure 5.22
BSE Image of Scale on Alloy E, 15 hr Exposure, Gas 1, 540°C

partially spalled layer (B) consisting of FeCrNi sulfides. Pitting attack of the alloy occurs below this layer. Analyses of the corrodants in the pits are shown in Table 5.20.

Table 5.20
Scale Composition on Alloy E, 15 hr Exposure, Gas 1, 540°C (at%)

Scale Designation	O	Al	Si	S	Cr	Mn	Fe	Ni
1	26	10	1	20	25	1	12	5
2	26	7	1	14	24	1	17	9

The EDS analysis indicates a mixture of Al and Cr oxides with Fe and Ni sulfides. The O+S content of the scale is rather low, especially that of area 2. Thus, the oxides and sulfides are probably nonstoichiometric and some unreacted Fe and Ni may be present in area 2, close to the alloy scale interface.

After 600 hrs a relatively thick topotactical scale (55-65µm) has developed. An epitactical Fe, NiS scale is also present, but is not shown in Figure 5.23. The EDS analysis of two selected areas is shown in Table 5.21, below.

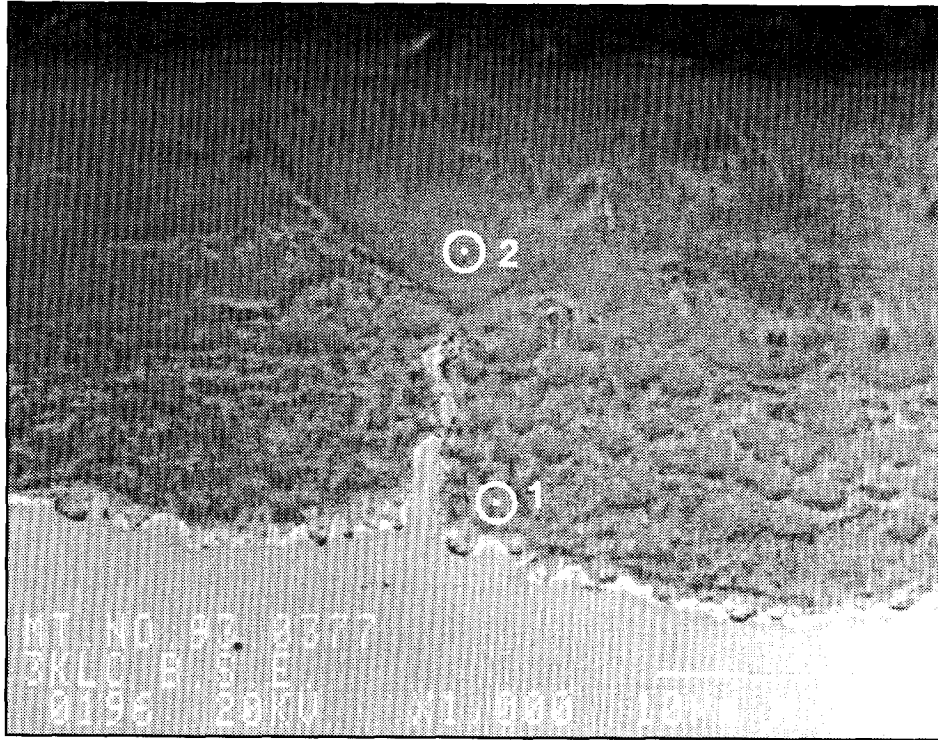


Figure 5.23
BSE Image of Scale on Alloy E, 600 hr Exposure, Gas 1, 540°C

Table 5.21
Scale Composition on Alloy E, 600 hrs Exposure, Gas 1, 540°C (at%)

Scale Designation	O	Al	Si	S	Cr	Mn	Fe	Ni
1	38	9	1	17	27	1	6	<0.5
2	26	10	1	27	26	2	6	1

The scale analyses indicate that the scale composition is close to stoichiometric after 600 hrs exposure, and consists of a mixture of sulfides and oxides. The sulfur content of the scale increases away from the alloy/scale interface.

F. Short Term (15 hr) Exposures in Syngas 4 (3% H_2O , 0.8% H_2S)

Adding 3% steam to the dry syngas composition 1, leads to a dramatic increase in corrosion loss for alloys A, B, and C, and an equally dramatic decrease in corrosion rate for alloys D and E. To better understand the reasons why, 15 hr exposure tests were done

in addition to the 600 hr tests, described in the next section. The following results were obtained:

Alloy A. After 15 hr exposure a relatively uniform topotactical scale has formed on the alloy with an average thickness of about 20 μm (Figure 5.24). The composition of the topotactical layer is as follows (at%) O 26, Si 1, S 22, Cr 39, Mn <0.5, Fe 12, Ni <0.5. This is quite different from the initial scale formed on alloy A in the dry gas, which consisted of FeCr_2S_4 without oxygen. A more detailed analysis indicated that the top of the topotactical scale is more sulfur rich and corresponds to an oxygen containing sulfur spinel $\text{FeCr}_2[\text{S}(\text{O})_4]$. The epitactical scale consists of the usual Fe, Ni, sulfides.

Alloy B. The topotactical scale on alloy B is considerably thinner and richer in sulfur than that on alloy A (Figure 5.25). EDS analyses indicate that the oxygen content of the scale decreases towards the metal scale interface as shown in Table 5.22, below.

Table 5.22
Composition of Topotactical Scale on Alloy B, 15 hrs, Gas 4, 540°C (at%)

Area Analyzed	O	Si	S	V	Cr	Mn	Fe	Ni
1	22	1	33	7	32	<.5	3	1
2	6	<.5	47	8	32	<.5	4	1

Qualitative analyses were made of the spalled, largely epitactical scale. Area A consisted mainly of FeCr_2S_4 , with some V and Ni, while Area B consisted of the usual Fe, Ni sulfides.

Alloy C. The topotactical scale on alloy C is fine grained, homogeneous and about 10 μm thick (Figure 5.26). A thin subscale appears to be present below it. A thin layer of FeCr_2S_4 (A) forms the base of the epitactical scale. Both top layers of the epitactical scale consist of Fe, Ni sulfide (B). Analyses of the topotactical scale are given in Table 5.23.

Table 5.23
Composition of Topotactical Scale on Alloy C, 15 hrs, Gas 4, 540°C (at%)

Area Analyzed	O	Si	S	Ti	Cr	Mn	Fe	Ni
1	40	1	11	5	30	1	12	1
2	11	1	3	3	22	<.5	32	26

The oxygen content of the main topotactical scale is higher than that of the scale on alloys A and B. The thin layer separating the scale from the alloy, appears to consist mainly of alloy with some oxide precipitates.

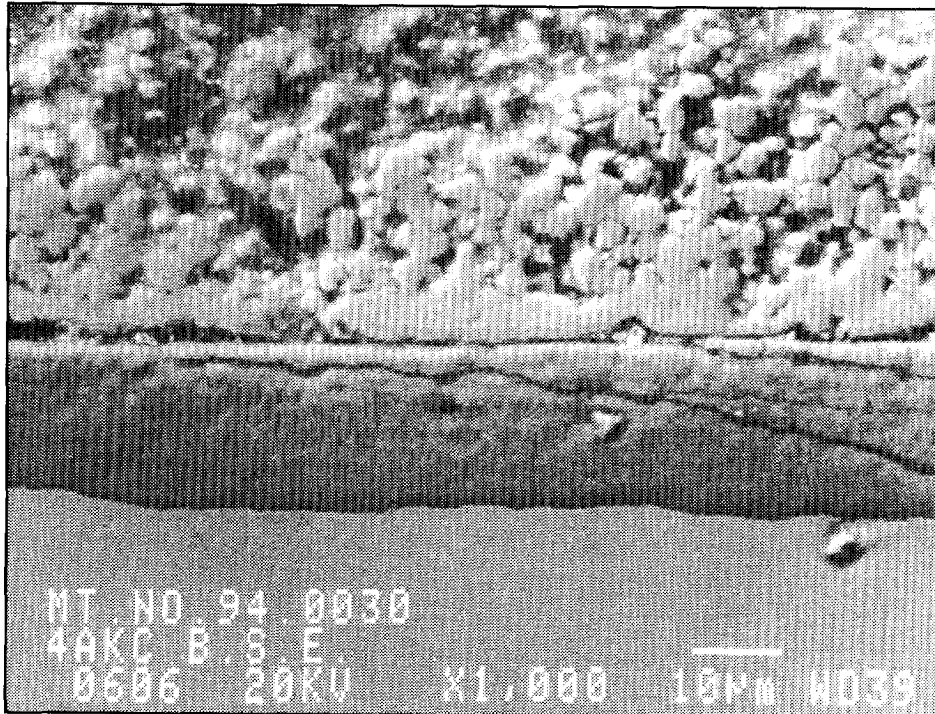


Figure 5.24
BSE Image of Scale on Alloy A, 15 hr Exposure, Gas 4, 540°C

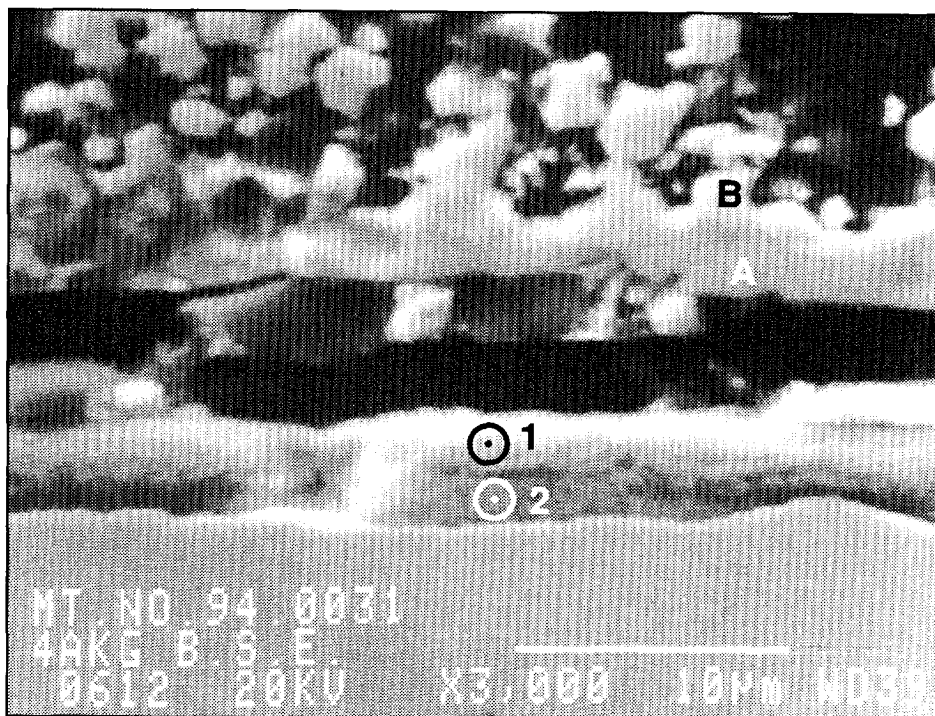


Figure 5.25
BSE Image of Scale on Alloy B, 15 hr Exposure, Gas 4, 540°C

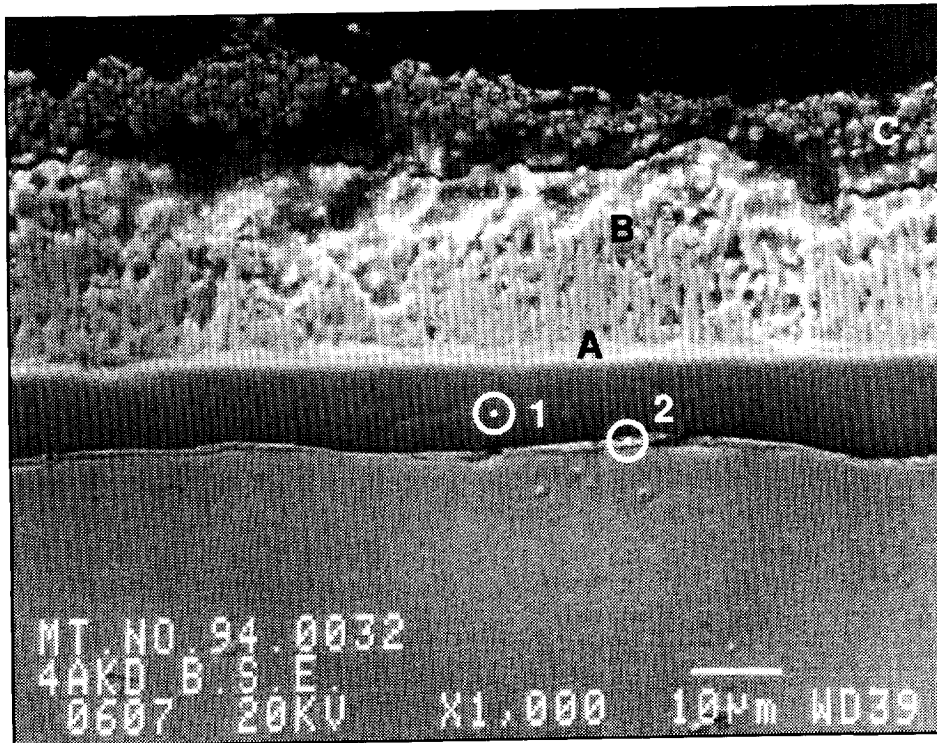


Figure 5.26
BSE Image of Scale on Alloy C, 15 hr Exposure, Gas 4, 540°C

Alloys D and E. Scales on alloys D and E were very thin. Only the Si containing alloy D was analyzed in detail. Figure 5.27 indicates that the topotactical scale is largely absent. The surface of the alloy appears to contain precipitates, with occasional small pits. EDS analyses of designated areas are shown in Table 5.24.

Table 5.24

Composition of Scale/Alloy Interface on Alloy D, 15 hrs, Gas 4, 540°C (at %)

Area Analyzed	O	Si	S	Cr	Mn	Fe	Ni
1	24	7	16	17	1	19	15
2	20	8	12	17	1	20	22
3	9	1	44	12	<1	20	12

The surface of the alloy contains oxide and sulfide precipitates and is enriched in silicon presumably as SiO_2 (1,2). The bottom of the spalled scale consist of Fe, Ni, Cr sulfides (3). The bright crystals on top contain Fe and Ni sulfides only.

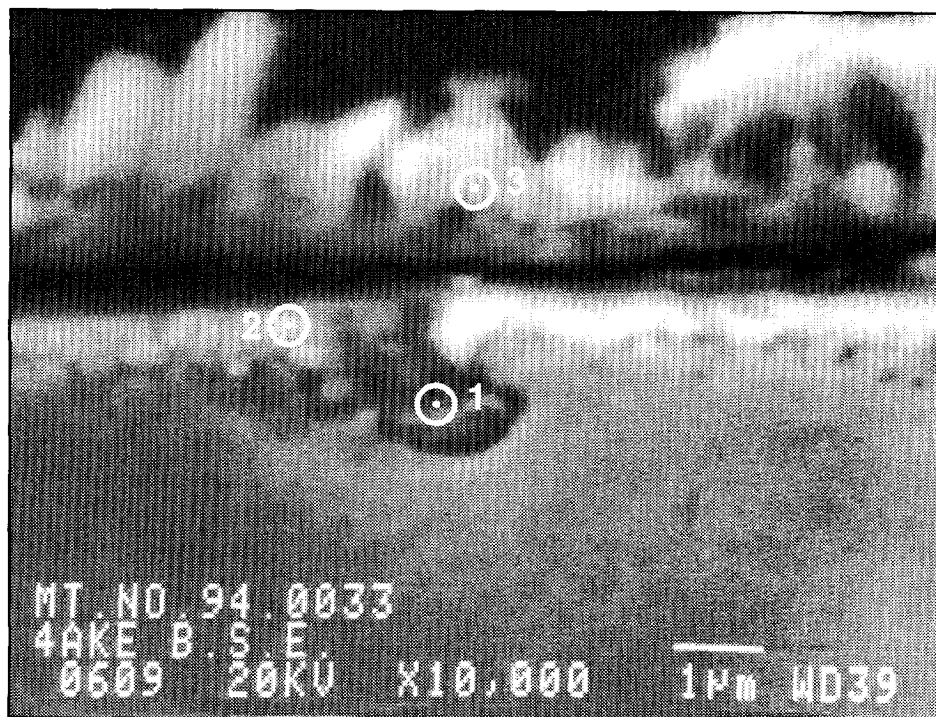


Figure 5.27
BSE Image of Scale on Alloy D, 15 hr Exposure, Gas 4, 540°C

5.3.3 Effect of Variation in Steam Content on Scale Development, 600 hr Exposure; 0.8% H₂S, 540°C

A. Base Alloy (A)

Scale development in the water free gas 1 (Table 4.3) was described in Section 5.3.2. The scale in direct contact with the alloy consisted mainly of FeCr₂S₄, while oxygen enrichment of the scale was noted away from the scale/metal interface. Adding 1% H₂O to the gas mixture considerably increased the corrosion rate, as shown previously in Figure 5.1. The topotactical scale is shown in Figure 5.28. Pertinent scale analyses are given in Table 5.25, below.

Table 5.25
Composition of Topotactical Scale on Alloy A, 600 hrs Exposure, 540°C, Gas 2 (at %)

Scale Designation	O	Si	S	Cr	Mn	Fe	Ni
1	25	1	27	32	0	13	<0.5
2	48	1	6	37	<.5	6	2
3	23	2	39	23	0	10	1

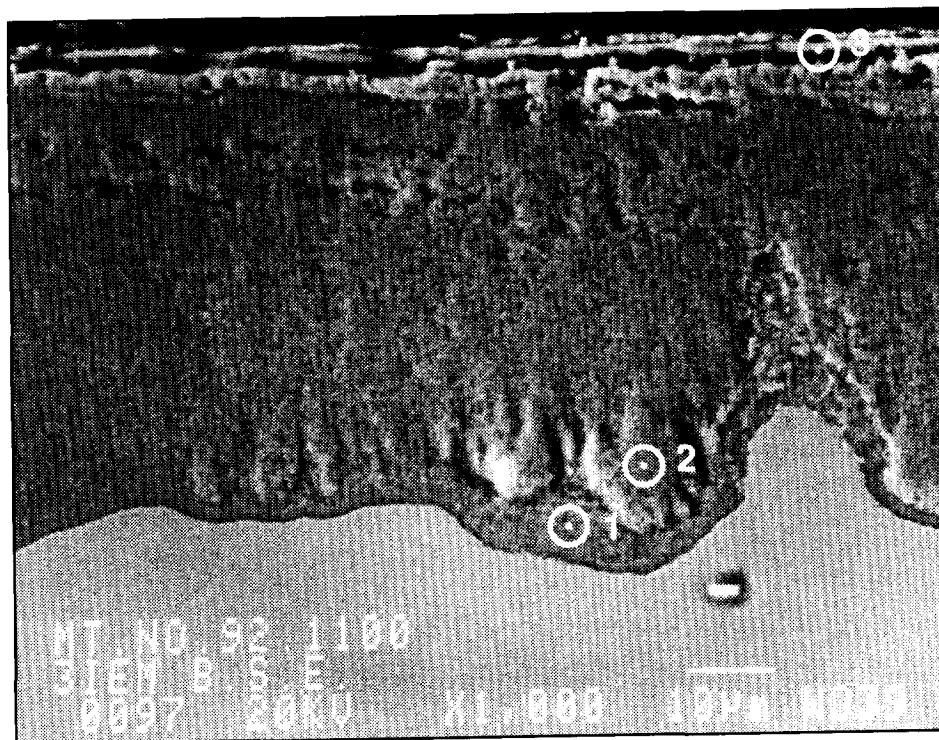
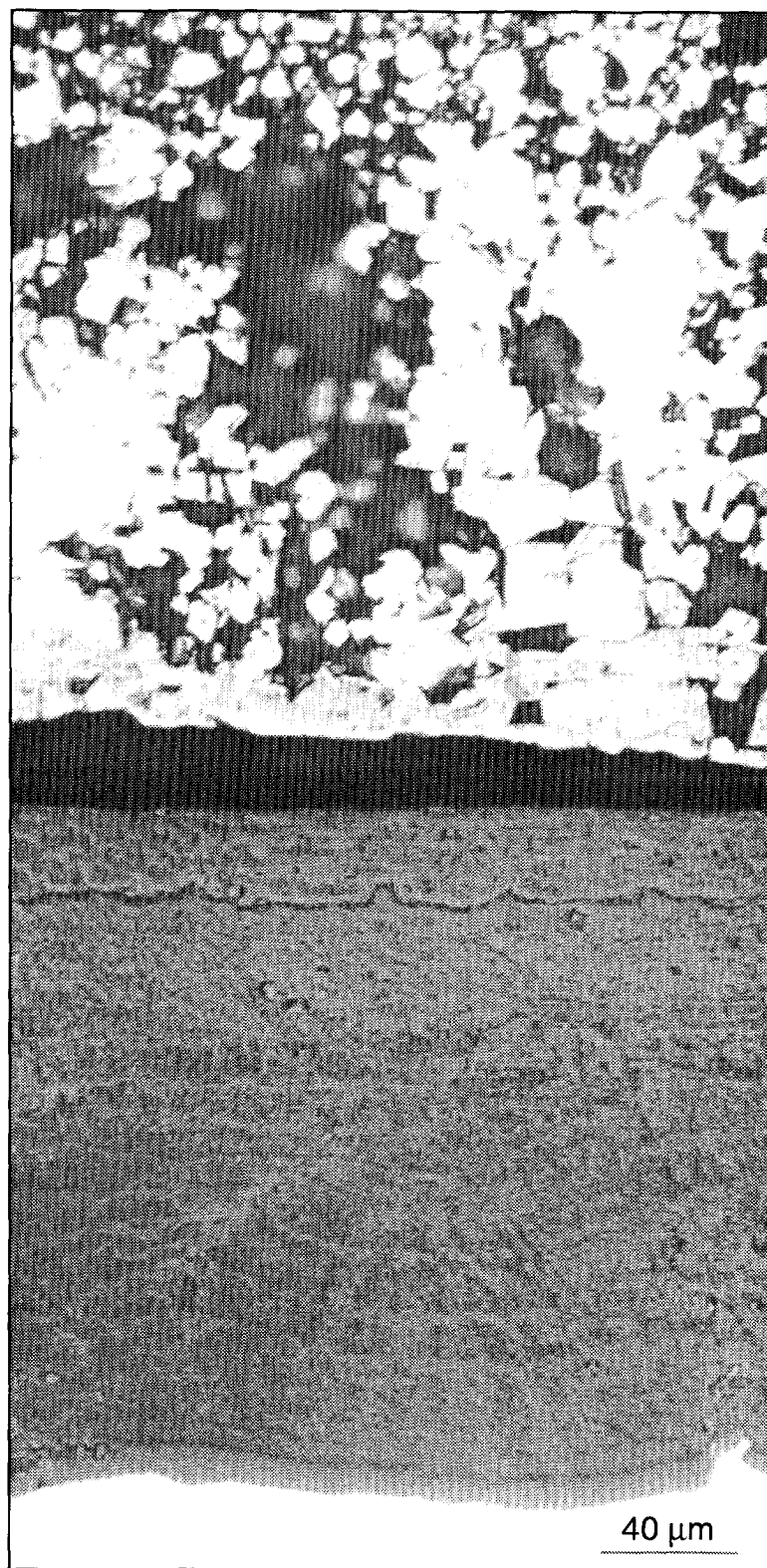


Figure 5.28
BSE Image of Scale on Alloy A, 600 hr Exposure, Gas 2, 540°C

The scale in contact with the alloy (1) contains considerably more oxygen than that on the sample exposed to the water free gas. The sulfur rich scale originally formed appears to oxidize away from the scale alloy interface as indicated by composition 2. Here the scale consists mainly of Cr_2O_3 with minor amounts of Fe(Ni) sulfide. The scale alloy interface is irregular. The scale in areas of minimum corrosion is sulfur rich. At the top of the topotactical scale is a sulfur rich layer (3), containing a considerable amount of oxygen. It probably is equivalent to the FeCr_2S_4 spinel layer present in scales exposed to the water free gas, but is now partially oxidized to $\text{FeCr}_2(\text{S}, \text{O})_4$.

Increasing the water content of the gas to 3%, causes another significant increase in corrosion rate [Fig. 5.29]. The optical photomicrograph of Figure 5.29A shows a fairly homogeneous scale with a banded structure, which is not immediately evident from the B.S.E. image shown in Figure 5.29B, which has a coarsely crystalline appearance. Selective EDS analyses, given in Table 5.26 still show an increase in oxygen content away from the scale metal interface, but the oxygen content of the scale at the alloy interface is now considerably higher than the sulfur content (1). Thus, generally more oxidizing conditions have resulted in a significant increase in corrosion rate.



Optical Photomicrograph

Figure 5.29a
Photomicrographs of Scale on Alloy A, 600 hr Exposure, Gas 4, 540°C

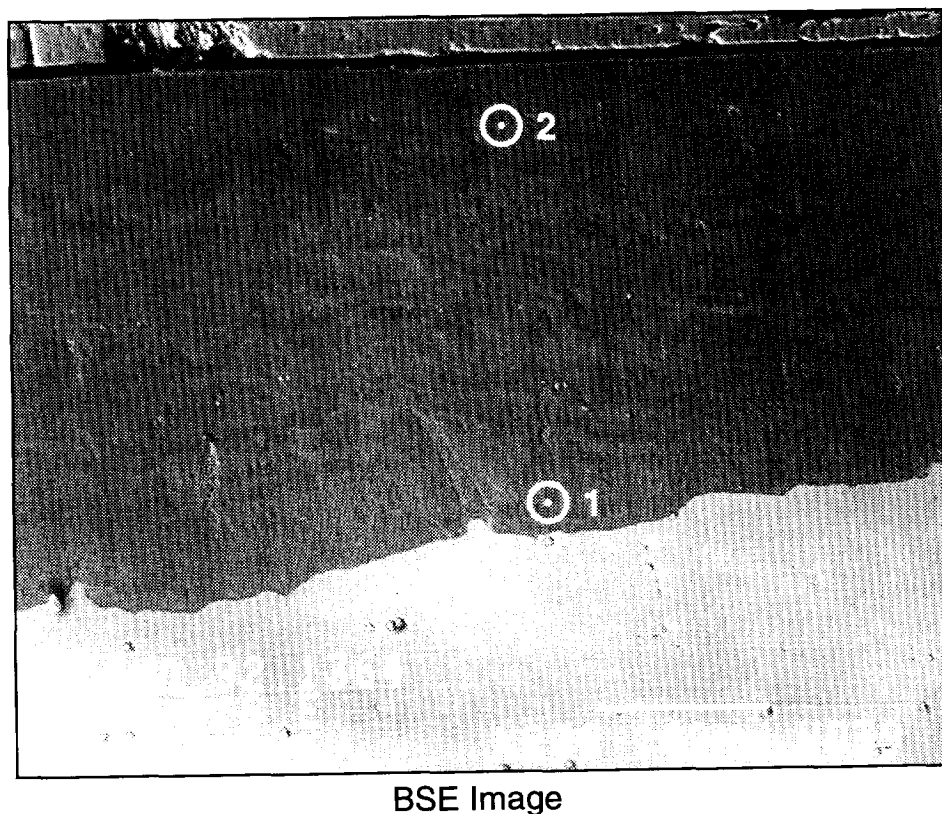


Figure 5.29b
Photomicrograph of Scale on Alloy A, 600 hr Exposure, Gas 4, 540°C

Table 5.26
Composition of Topotactical Scale on Alloy A, 600 hr Exposure, Gas 4, 540°C (at %)

Scale Designation	O	Si	S	Cr	Mn	Fe	Ni
1	35	1	19	29	<.5	15	<.5
2	45	1	10	30	<.5	13	2

When the water content of the gas is raised to 5-10%, the corrosion rate declines considerably, but is still significant. The scale is now fairly homogeneous as shown in Figure 5.30. EDS analyses show that the difference in sulfur content between the top and the bottom of the topotactical scale has largely disappeared. A typical scale composition is (at%) O 45, Si 1, S 7, Cr 28, Mn <0.5, Fe 15, Ni 3. There is very little difference between the composition of the scales formed in the two gases, although the difference in corrosion rate is considerable. The chemical analysis shown above suggests that the scale consists mainly of $\text{Fe}(\text{Ni})\text{Cr}_2\text{O}_4$ with some oxygen replaced by sulfur.

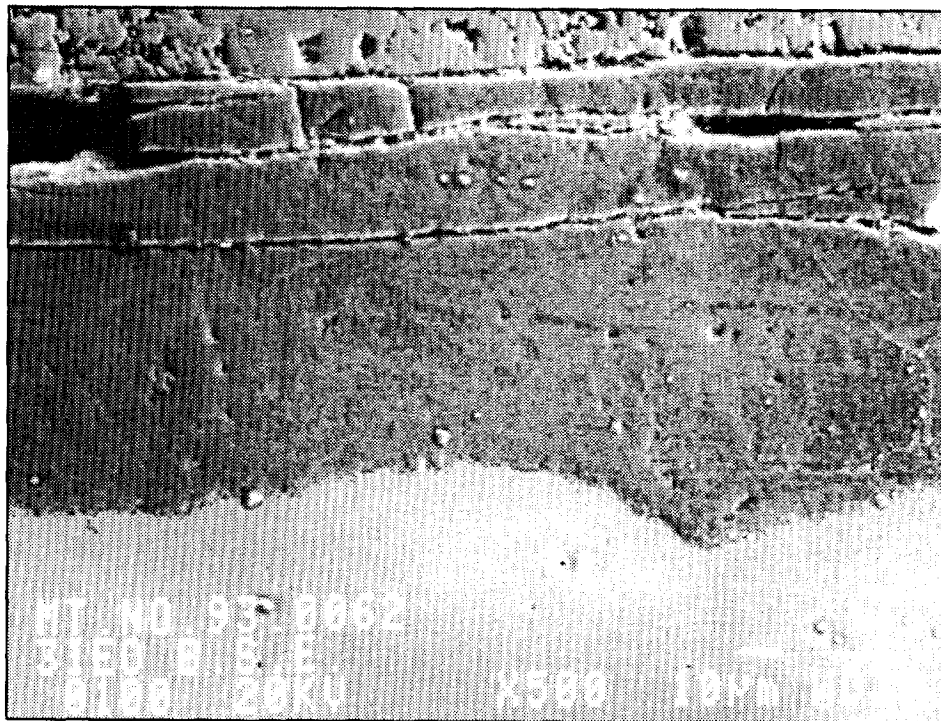


Figure 5.30
BSE Image of Scale on Alloy A, 600 hr Exposure, Gas 6, 540°C

Increasing the water content of the gas to 15% further decreases the corrosion loss and also makes the corrosion front irregular as is shown in the optical photomicrograph of Figure 5.31. EDS analysis of the topotactical scale shows that its composition is very similar to that after exposure to the gas with 10% water. The epitactical scale was also analyzed and consisted of $(\text{Fe}, \text{Ni}) \text{S}_{1-x}$ with about 44% at%S and equal amounts of Fe and Ni.

B. Alloy B Containing 3.25%V

Adding 1% H_2O to the dry syngas significantly increases the overall corrosion rate and also makes the corrosion front extremely irregular as shown in Figure 5.32. Table 5.27 shows quantitative EDS/WDS analyses of selected areas.

To further clarify the scale composition elemental maps of the scale alloy interface were obtained (Figure 5.33). These confirm that areas of deep penetration are relatively rich in oxides, while areas of slow scale growth are rich in sulfides.

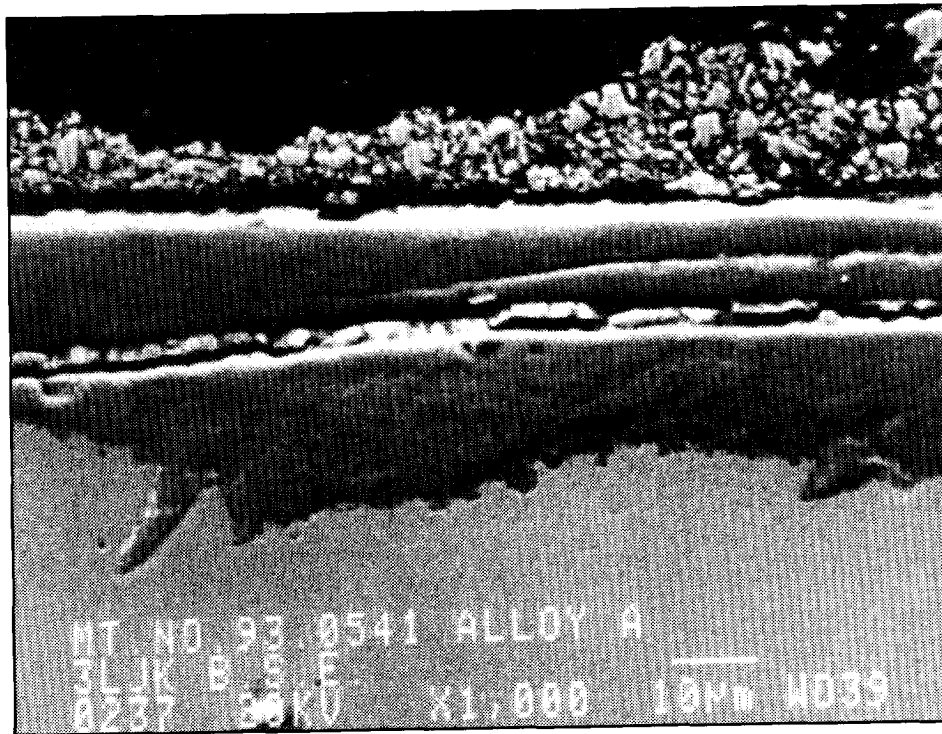
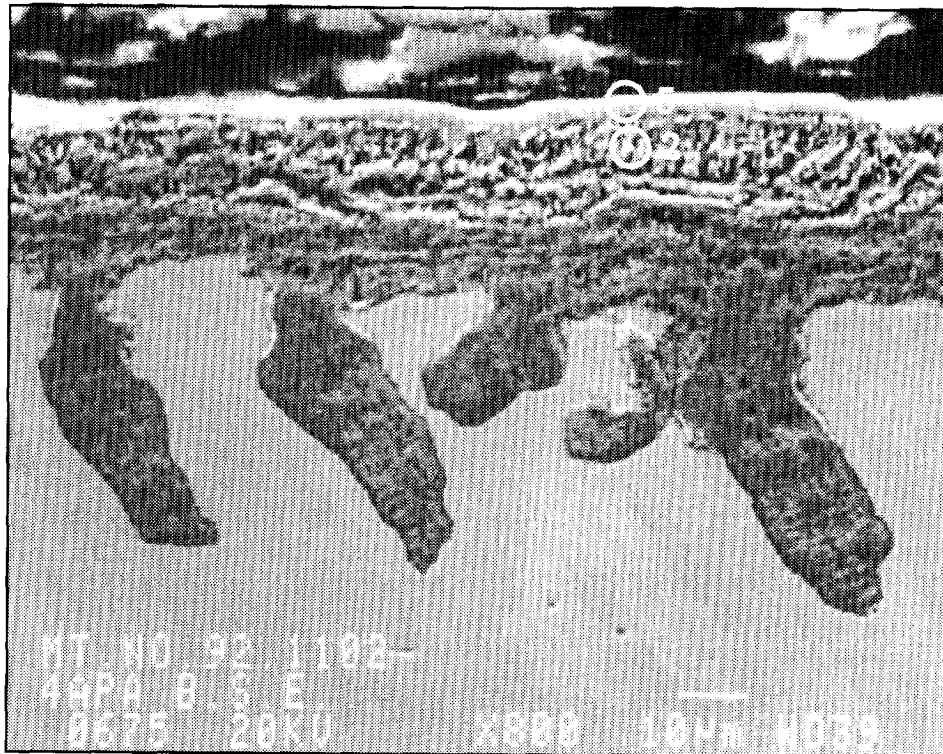


Figure 5.31
BSE Image of Scale on Alloy A, 600 hr Exposure, Gas 7, 540°C

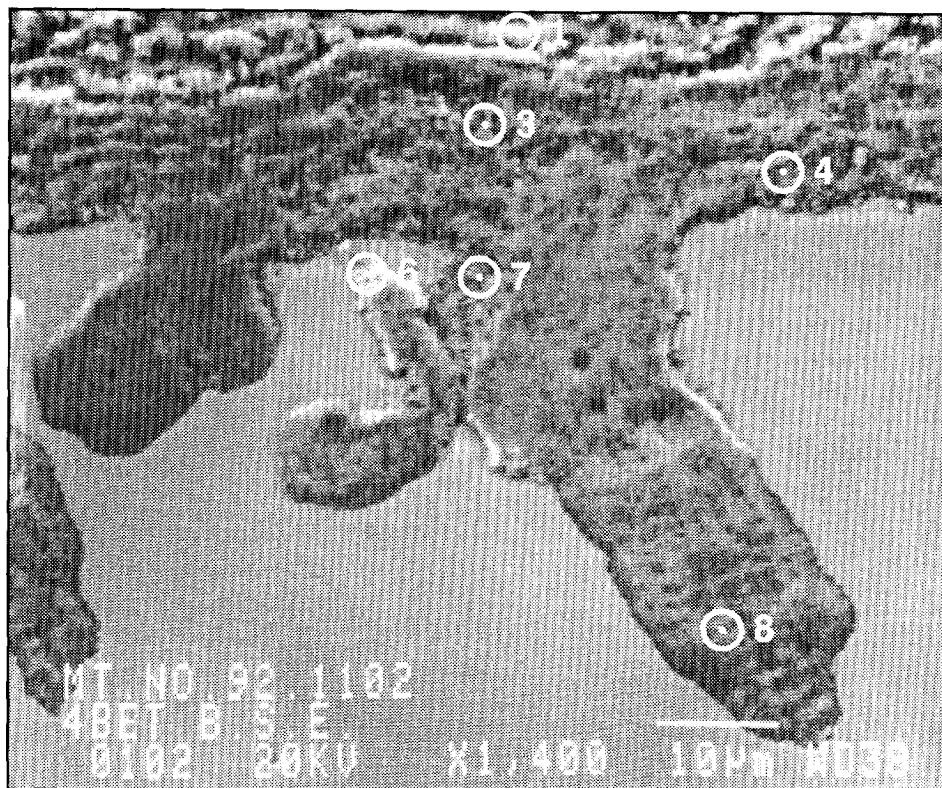
Table 5.27
Composition of Topotactical Scales on Alloy B, 600 hr, Gas 2, 540°C (at %)

Scale Area	O	Si	S	V	Cr	Mn	Fe	Ni
1	3	<.5	48	1	8	<.5	33	5
2	29	1	28	7	27	1	6	2
3	31	1	20	5	30	<.5	9	4
4	37	<1	19	5	28	<1	8	2
5	4	3	46	5	21	2	15	4
6	2	<1	12	3	10	0	26	46
7	27	<.5	29	4	26	<1	9	2
8	36	<.1	18	5	26	<1	10	2

When the water content of the gas is raised to 3%, the overall corrosion rate increases significantly. The scale/alloy interface is still irregular, but less so than after exposure to the gas with 1% H₂O. Elemental maps indicate areas of high sulfur content alternating



(a)

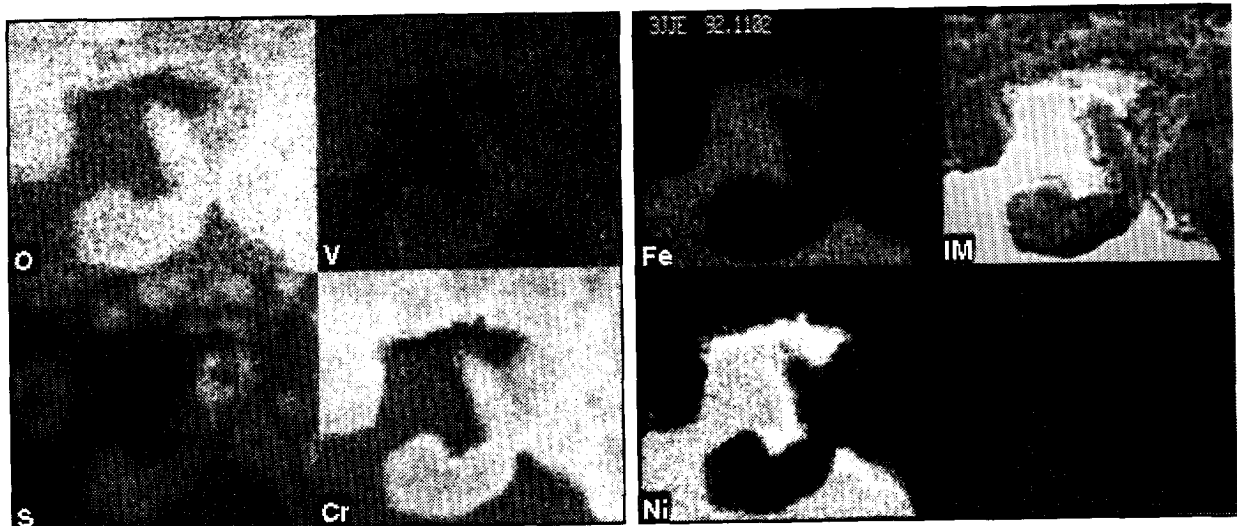


(b)

Figure 5.32
BSE Image of Scale on Alloy B, 600 hr Exposure, Gas 2, 540°C



(a)
BSE Image of Scale



(b)
Elemental Maps

Figure 5.33
Elemental Maps of Scale on Alloy B, 600 hr Exposure, Gas 2, 540°C

with areas of high oxygen content. At the scale/alloy interface the oxygen content is generally high (Figure 5.34). Quantitative EDS analyses of specific areas are given in Table 5.28 below.

Table 5.28
Composition of Topotactical Scales on Alloy B, 600 hr Exposure, Gas 4, 540°C (at %)

Scale Area	O	Si	S	V	Cr	Mn	Fe	Ni
1	31	<1	17	5	28	2	14	2
2	50	1	6	3	28	1	8	1

The detailed scale analyses show a relatively high oxygen content, even in high sulfur areas. The scale in contact with the alloy consist mainly of Cr_2O_3 and FeS .

The scale formed after exposure to a gas containing 10% water is fine grained and seemingly homogeneous (Figure 5.35). The corrosion rate is less than after exposure to the gas with 3% H_2O , but still quite high. The epitactical scale consists only of porous FeNi sulfides. A few quantitative EDS/WDS analyses are given in Table 5.29. They confirm that the scale composition is quite uniform.

Table 5.29
Composition of Topotactical Scale on Alloy B, 600 hrs, Gas 6, 540°C (at%)

Scale Area	O	Si	S	V	Cr	Mn	Fe	Ni
1	44	1	8	5	27	<.5	13	2
2	43	1	9	5	28	<.5	12	2

Increasing the steam content of the gas to 15% further decreased the corrosion rate. The alloy/scale interface has also become irregular, with some areas showing very low corrosion losses. Figure 5.36 shows the scale morphology, while Table 5.30 gives selective EDS/WDS analyses. The composition of the scale is similar to that after the exposure to gas with 10% H_2O . Near the scale/alloy interface the sulfur content of the scale is low.

Table 5.30
Scale Composition on Alloy B, 600 hrs, Gas 7, 540°C (at%)

Scale Area	O	Si	S	V	Cr	Mn	Fe	Ni
1	41	<.5	14	4	23	1	14	3
2	45	<1	8	5	30	1	8	2
3	46	<1	3	6	34	1	6	3

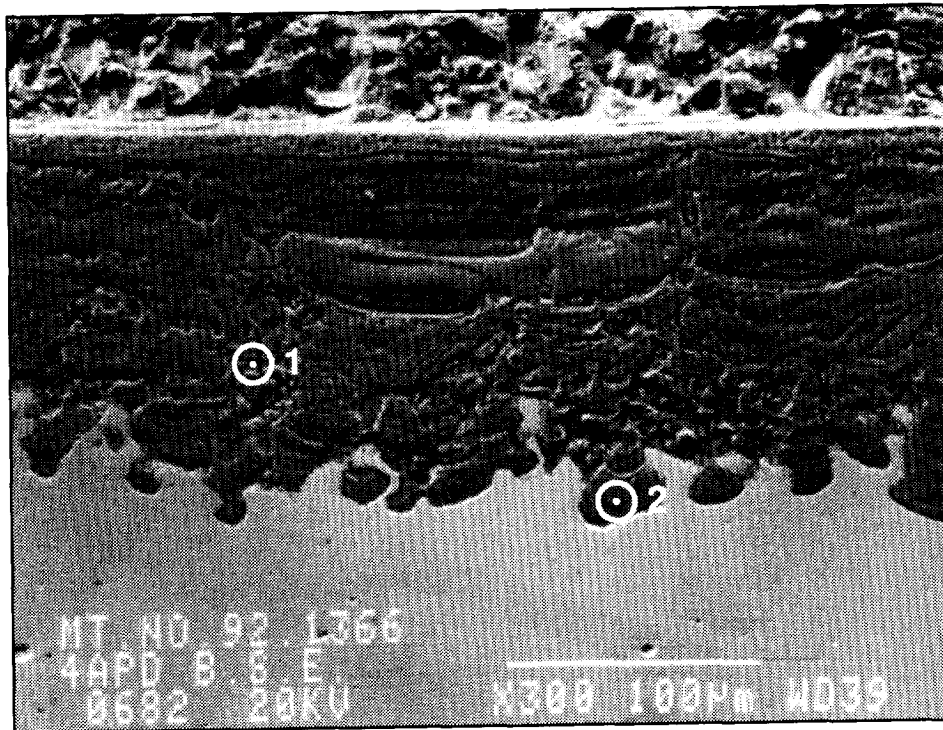


Figure 5.34
BSE Image of Scale on Alloy B, 600 hr Exposure, Gas 4, 540°C

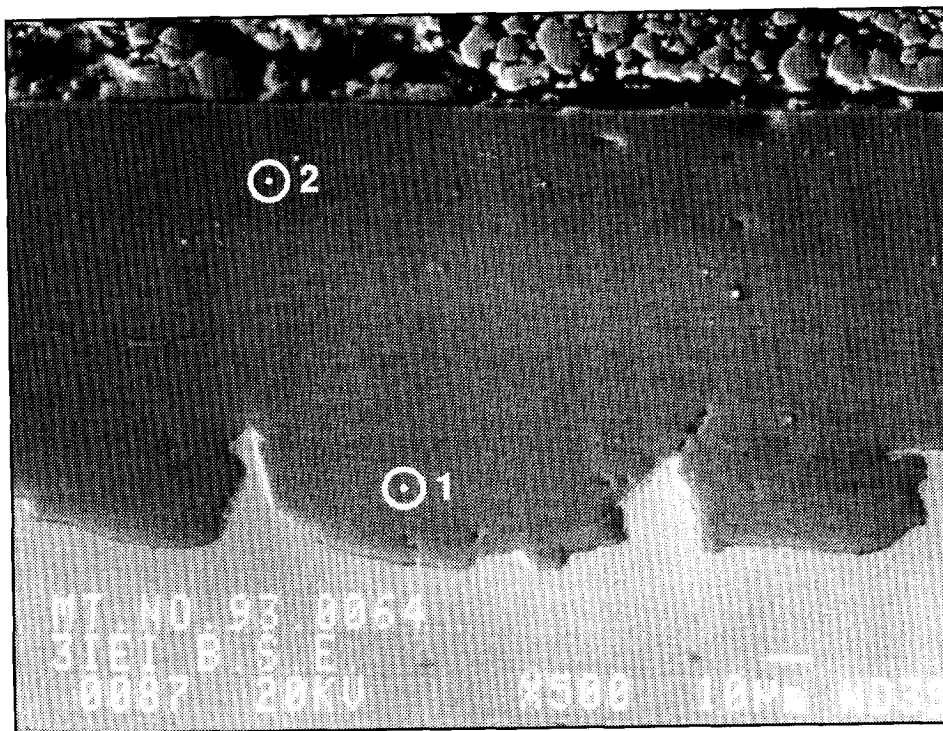


Figure 5.35
BSE Image of Scale on Alloy B, 600 hr Exposure, Gas 6, 540°C

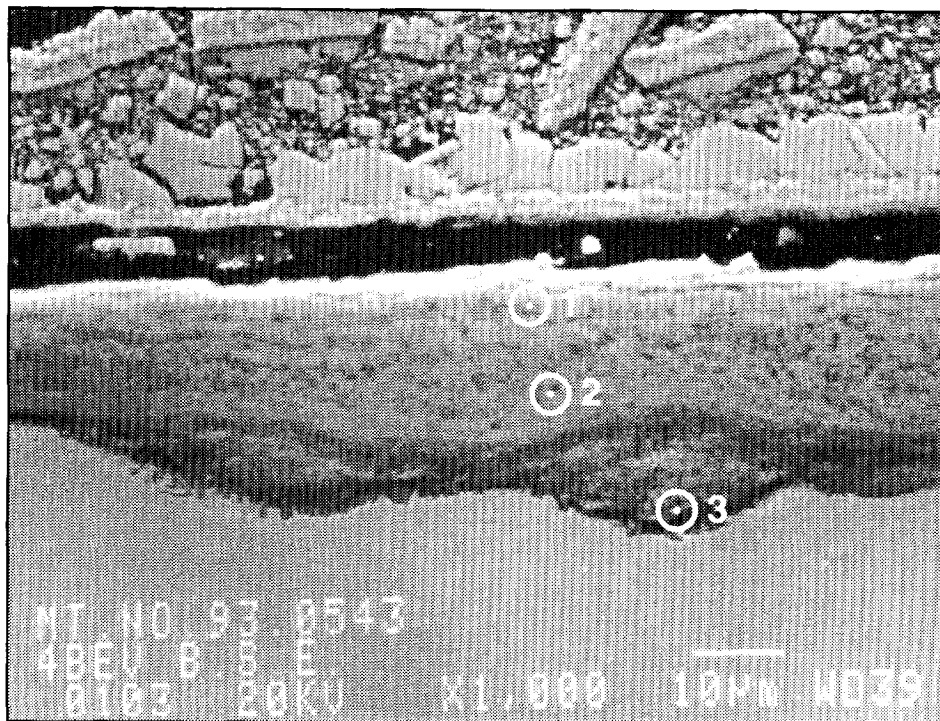


Figure 5.36
BSE Image of Scale on Alloy B, 600 hr Exposure, Gas 7, 540°C

C. Alloy C Containing 3.25%Ti

Adding 1% water to the dry gas of Section 5.3.2 does not increase the corrosion rate of the alloy significantly (Figure 5.37) and also does not significantly change the topotactical scale composition, which consists mainly of Cr and Ti oxide and iron sulfide. The morphological features shown in Figure 5.37 do not correspond with changes in scale composition. Increasing the water content to 2% still does not cause major changes in corrosion rate or scale composition (Table 5.31), if anything, the sulfur content of the scale is somewhat higher here than after exposure to gases with a lower water content.

Table 5.31

Typical Composition of Topotactical Scale on Alloy C After Exposure to Gases Containing 0, 1, 2, 3, 10 and 15% H₂O, 600 hrs, 540°C, (at%)

Steam (vol%)	O	Si	S	Ti	Cr	Mn	Fe	Ni
0	43	1	13	4	30	1	7	<0.5
1	41	1	13	4	30	1	9	1
2	37	1	15	4.5	32	1	9	<0.5
3	39	1	15	4	31	1	9	<0.5
10	49	1	5	4	27	1	12	1
15	48	1	6	5	28	1	10	1

When the water content of the gas is raised to 3%, the corrosion rate increases significantly, but the scale composition is again largely unchanged as is shown in Table 5.31.

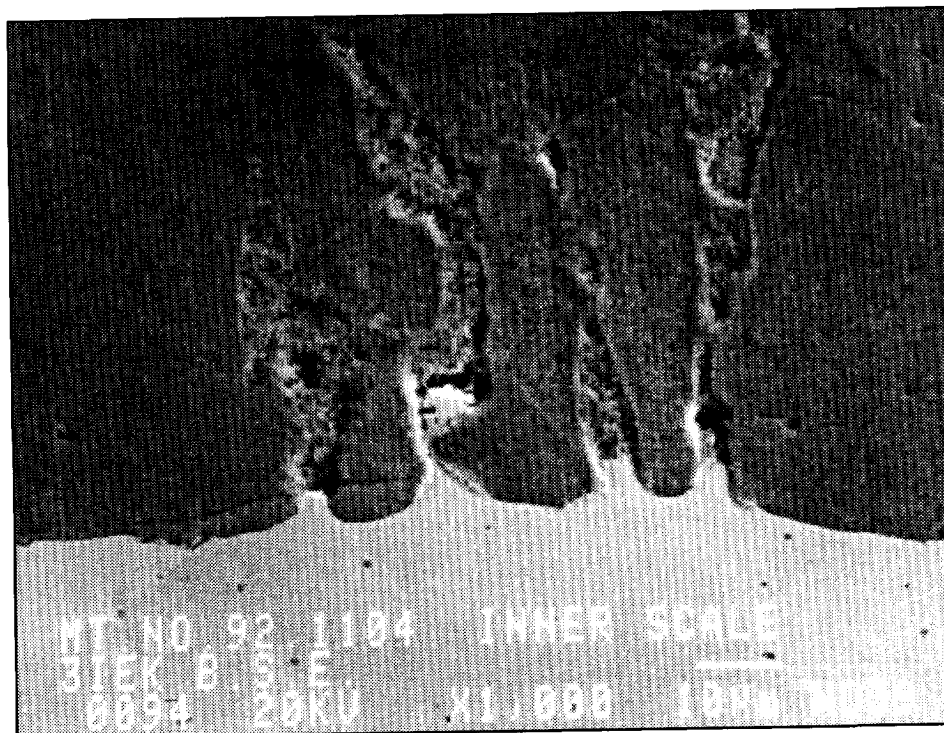


Figure 5.37
BSE Image of Scale on Alloy C, 600 hr Exposure, Gas 2, 540°C

A significant increase in oxygen content occurs when the steam content is raised to 10%, corresponding with a drop in corrosion rate. Raising the steam content to 15% further decreases the corrosion rate, but does not change the scale composition. The scale/metal interface does also become irregular as shown in Figure 5.38. In general, the overall scale composition is fairly close to that of an FeCr_2O_4 spinel in which part of the Fe is replaced by TiO and to a lesser extent by Ni and Mn and part of the oxygen is replaced by sulfur.

D. Alloy D

Adding 1% water to the water free gas of Section 5.3.2 does not significantly change the scale thickness after 600 hr exposure. The scale morphology and composition is also similar, although somewhat finer grained as shown in Figure 5.39A and Table 5.32.

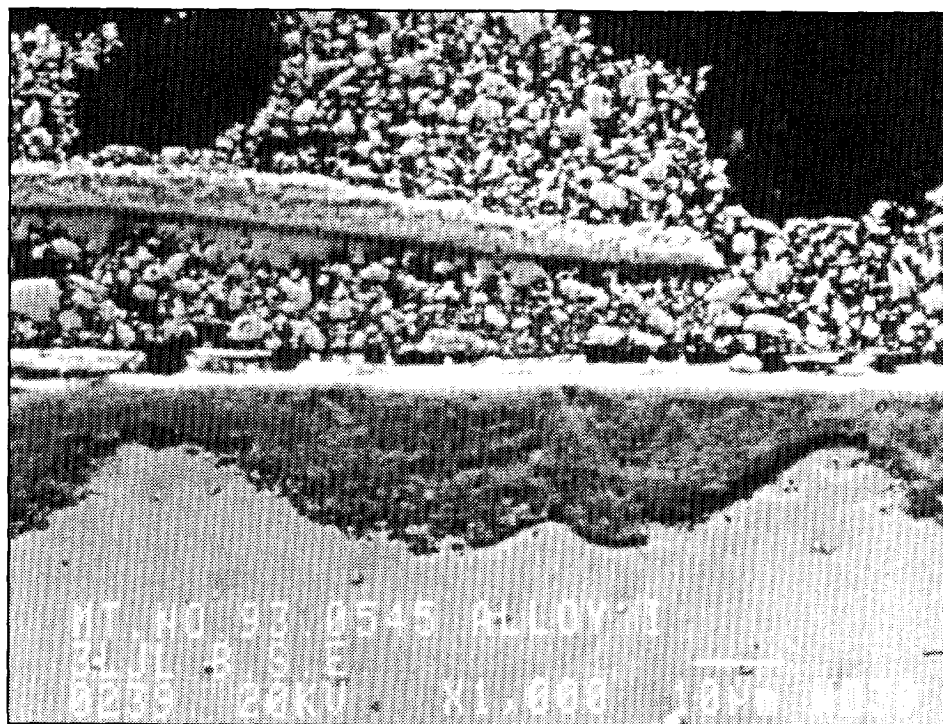


Figure 5.38
BSE Image of Scale on Alloy C, 600 hr Exposure, Gas 7, 540°C

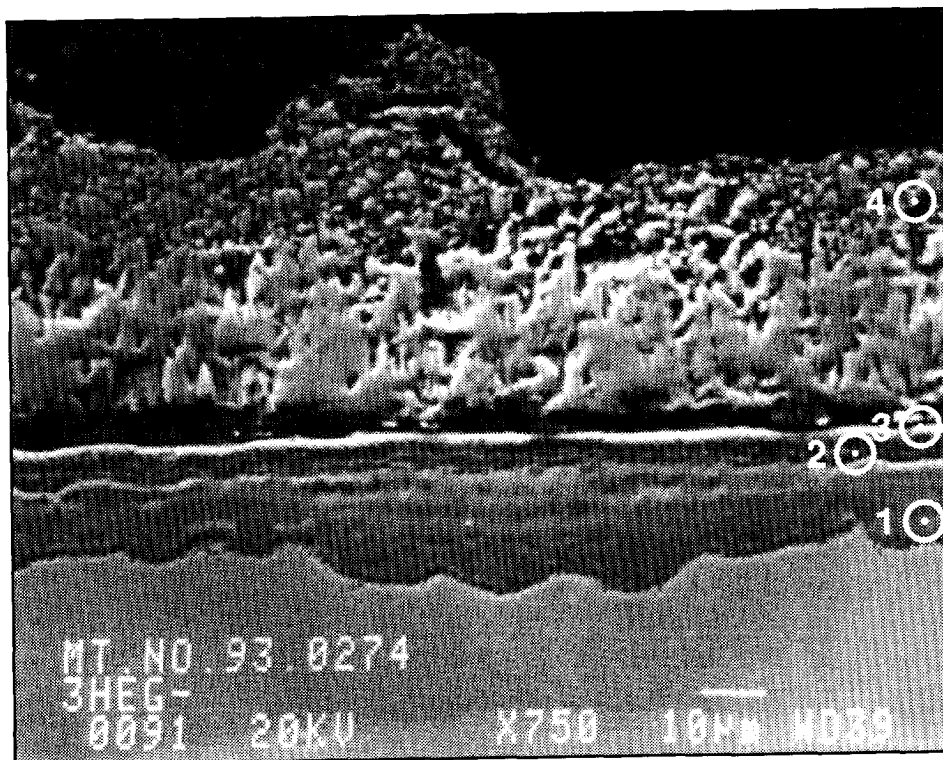
Table 5.32
Composition of Scales on Alloy D, 600 hr Exposure, Gas 2, 540°C (at%)

Scale Area	O	Si	S	Cr	Mn	Fe	Ni
1	42	8	16	28	1	4	<.5
2	30	17	27	11	0.5	6	7
3	11	7	44	24	1	11	2
4*	0	0	48	0	0	24	28

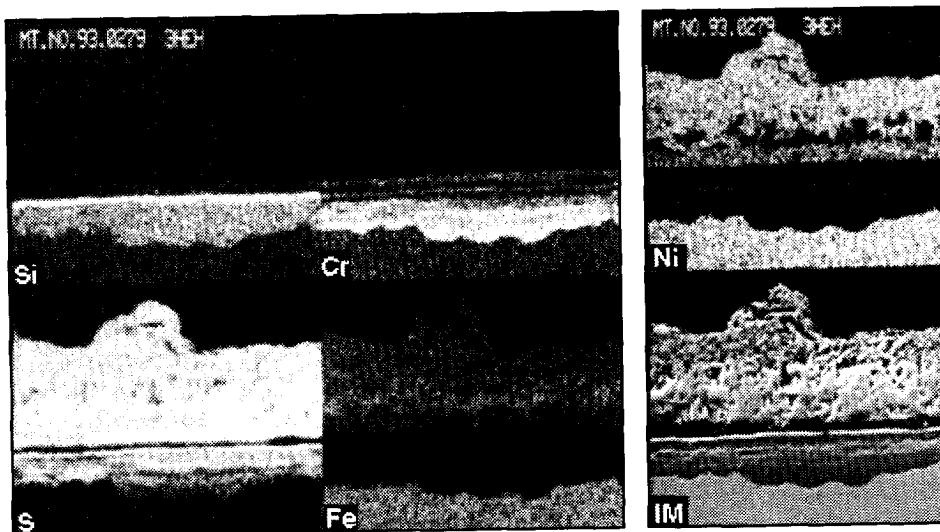
*epitactical

In both cases, a SiO_2 rich layer (2) did form on the alloy which was not fully protective, but allowed oxidation and sulfidation of the alloy below it. Even so, the corrosion rate is considerably less than that of the base alloy. The silicon rich layer on top of the epitactical scale is also clearly shown in the elemental maps of Figure 5.39B.

Increasing the water content to 2% resulted in a dramatic drop in the scale thickness to less than $5\ \mu\text{m}$. However, all typical scale features are still present (i.e., an epitactical scale consisting mainly of porous FeNiS crystallites and a dense epitactical scale consisting of



(a)
BSE Image of Scale



(b)
Elemental Maps

Figure 5.39
Photomicrographs of Scale on Alloy D, 600 hr Exposure, Gas 2, 540°C

an oxygen rich outer layer and a sulfur rich inner layer as shown in Figure 5.40, and Table 5.33.

Table 5.33
Composition of Topotactical Scale on Alloy D, 600 hr Exposure, Gas 3, 540°C (at%)

Scale Area	O	Si	S	Cr	Mn	Fe	Ni
1	47	9	11	22	1	7	2
2	24	10	29	23	1	10	2

The scales still contain a considerable amount of sulfur and cannot be considered "protective" oxide scales in the classical sense. Line scans with an Auger electron analyzer were used to determine the presence or absence of a thin protective SiO₂ layer. Figure 5.41 shows that no sulfur free oxide layer was observed.

The corrosion rate of alloy D remained negligible when the steam content of the gas was raised to 15%. The optical photomicrograph shows some interesting features indicating scale spallation (Figure 5.42A). Figure 5.42B shows the corresponding BSE image and Table 5.34 gives EDS analyses of significant scale features.

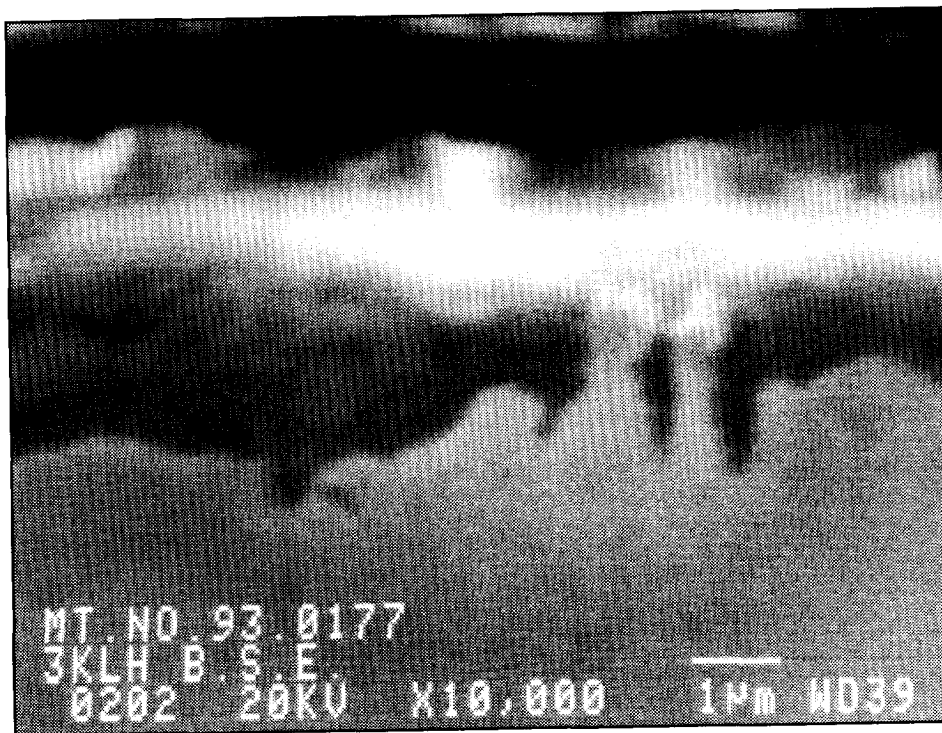
Table 5.34
Composition of Scale on Alloy D, 600 hr Exposure, Gas 7, 540°C (at%)

Scale Area	O	Si	S	Cr	Mn	Fe	Ni
1	27	9	22	9	<.5	17	15
2	45	8	10	21	<.5	8	5
3	32	<.5	16	20	1	20	9

The topotactical scale has roughly the same composition as that formed during the exposure to the gas containing 2% steam (1,2). The "spalled" scale is basically free of silicon and consist of a mixture of FeNiCr oxides and sulfides (3). The dense nodule below the "spalled" scale is FeNiS. There is again no clear evidence of a protective SiO₂ rich scale.



(a)



(b)

Figure 5.40
BSE Image of Scale on Alloy D, 600 hr Exposure, Gas 3, 540°C

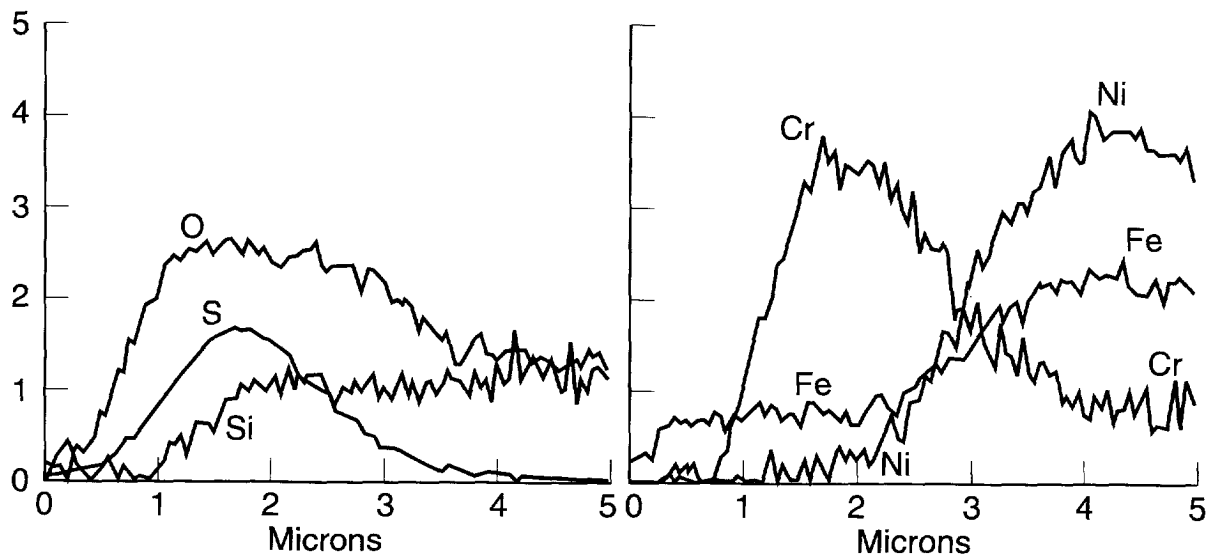
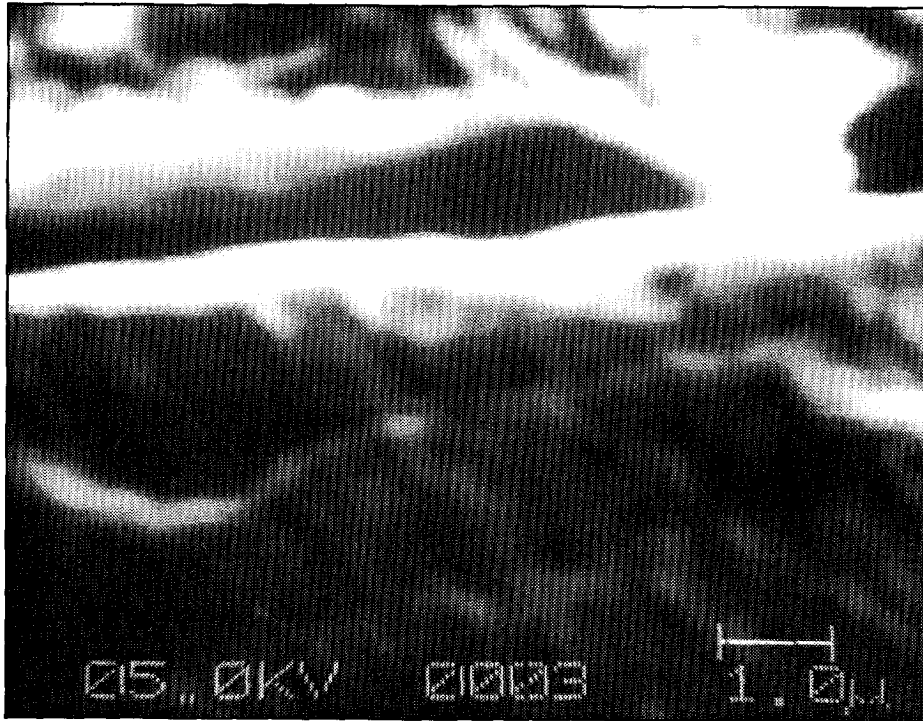


Figure 5.41
Line Scans by Auger Spectroscopy Across Scale-Metal Interface of Alloy D, 600 hr Exposure, Gas 3, 540°C

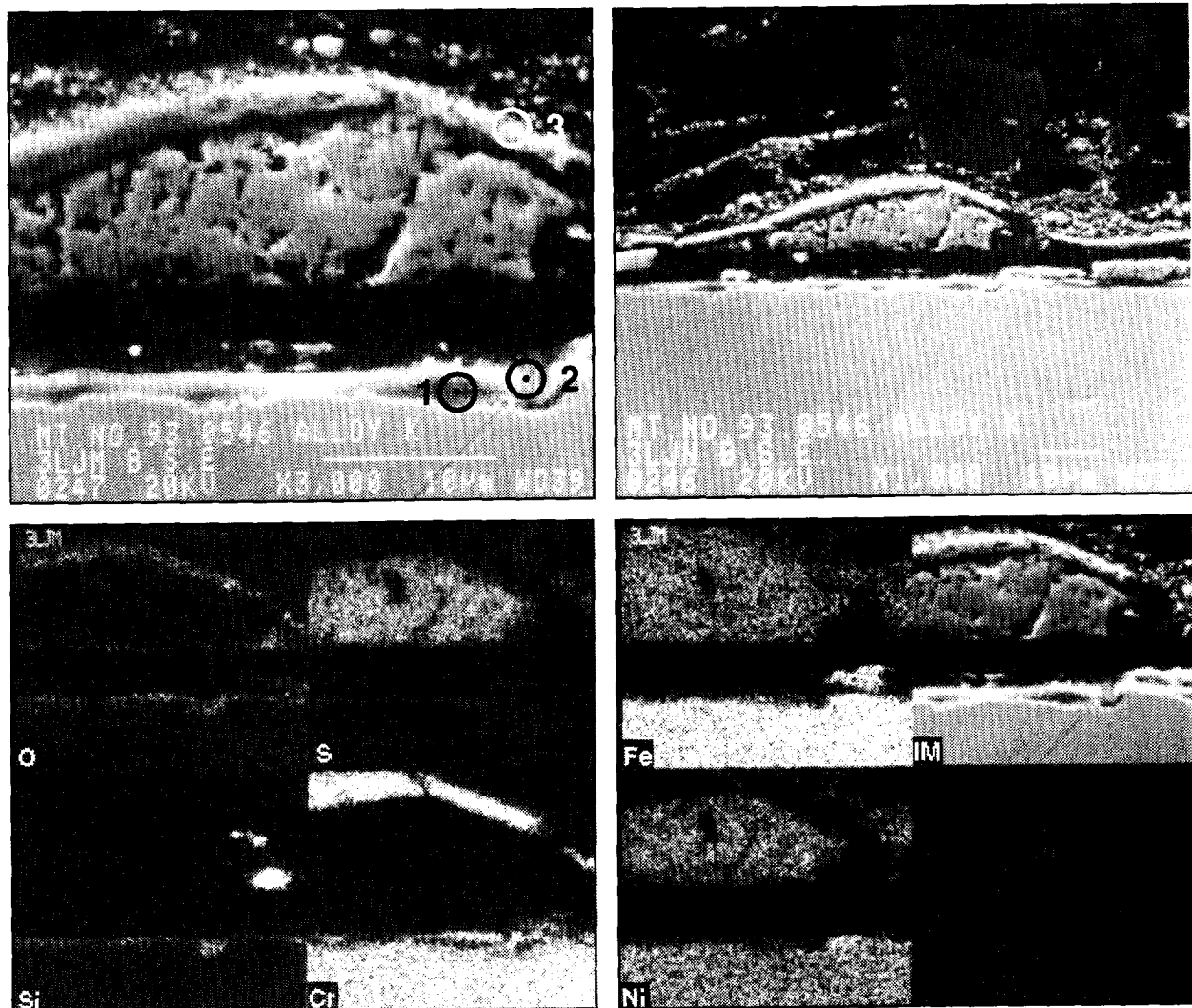


Figure 5.42
Photomicrographs of Scale on Alloy D, 600 hr Exposure, Gas 7, 540°C

A detailed study was made of the surface layer of the alloy to determine the types and quantities of submicroscopic precipitates. Figure 5.43 shows a high magnification BSE image, indicating the center points of the spot EDS analyses, having a diameter of about $1 \mu\text{m}^2$. Results are shown in Table 5.35.

Table 5.35
Composition of Alloy Surface Layer, Alloy D, 600 hrs, Gas 7 (at%)

Scale Area	O	Si	S	Cr	Mn	Fe	Ni
1	37	10	10	15	<.5	16	11
2	13	7	3	18	<.5	32	26

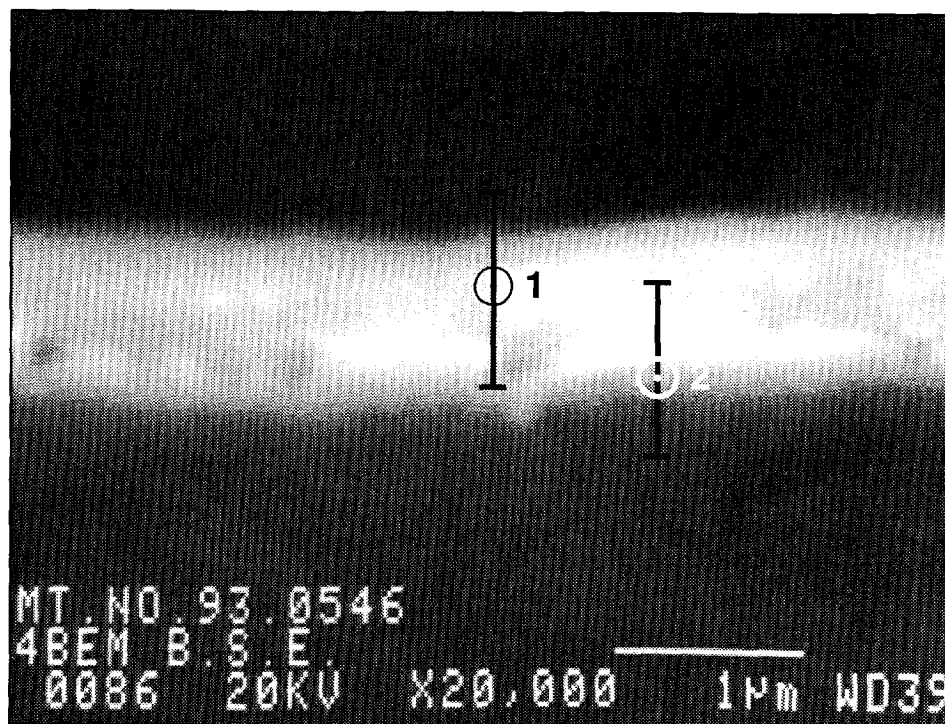


Figure 5.43
BSE Image of Scale and Alloy Surface on Alloy D, 600 hr Exposure, Gas 7, 540°C

These analyses suggest the presence of a precipitation zone containing 20-30 at % SiO_2 , below a scale containing Cr + Si oxides, Cr, Fe, Ni sulfides and probably unreacted Fe, Ni.

E. Alloy E

Adding 1% steam to the water free gas composition described in Section 5.3.2 decreased the corrosion rate significantly as shown previously in Figure 5.1. The EDS analyses of Table 5.36, below, show an increase in the oxygen content of the scale near the alloy interface [Figure 5.44], but otherwise little change.

Table 5.36
Scale Composition on Alloy E, 600 hr Exposure, Gas 2, 540°C (at%)

Scale Area	O	Al	Si	S	Cr	Mn	Fe	Ni
1	45	10	1	12	28	1	4	<.5
2	28	9	1	26	16	1	15	4

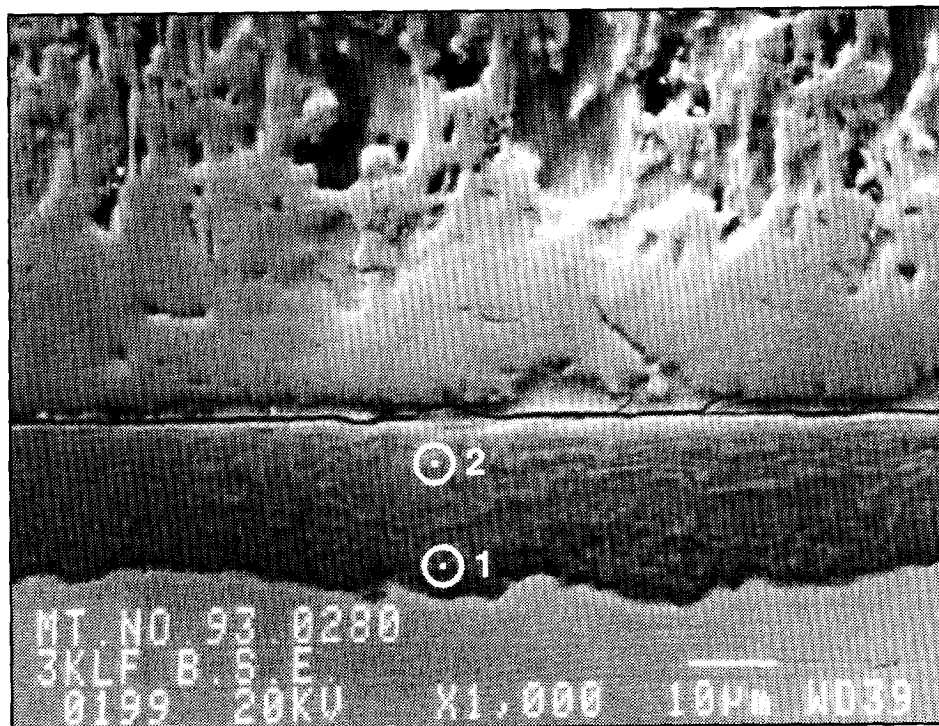


Figure 5.44
BSE Image of Scale on Alloy E, 600 hr Exposure, Gas 2, 540°C

A dramatic decrease in corrosion rate occurs when the steam content of the gas is raised to 2%, similar to that occurring with alloy D. Efforts were again made to find the mythical protective oxide layer. Figure 5.45 shows a high magnification BSE image of the scale and Table 5.37 the corresponding scale analyses.

Table 5.37
Scale Composition on Alloy E, 600 hrs, Gas 3, 540°C (at%)

Scale Area	O	Al	Si	S	Cr	Mn	Fe	Ni
1	16	10	1	2	20	1	27	22
2	47	10	1	8	27	1	6	1
3	18	9	1	30	22	1	15	3

The thin "subscale" (1) appear to be an altered alloy layer with Al_2O_3 precipitates. The scale closest to the alloy (2) has a relatively high oxygen content, but has about the same sulfur content, associated with significantly higher corrosion rates in the base alloy A.

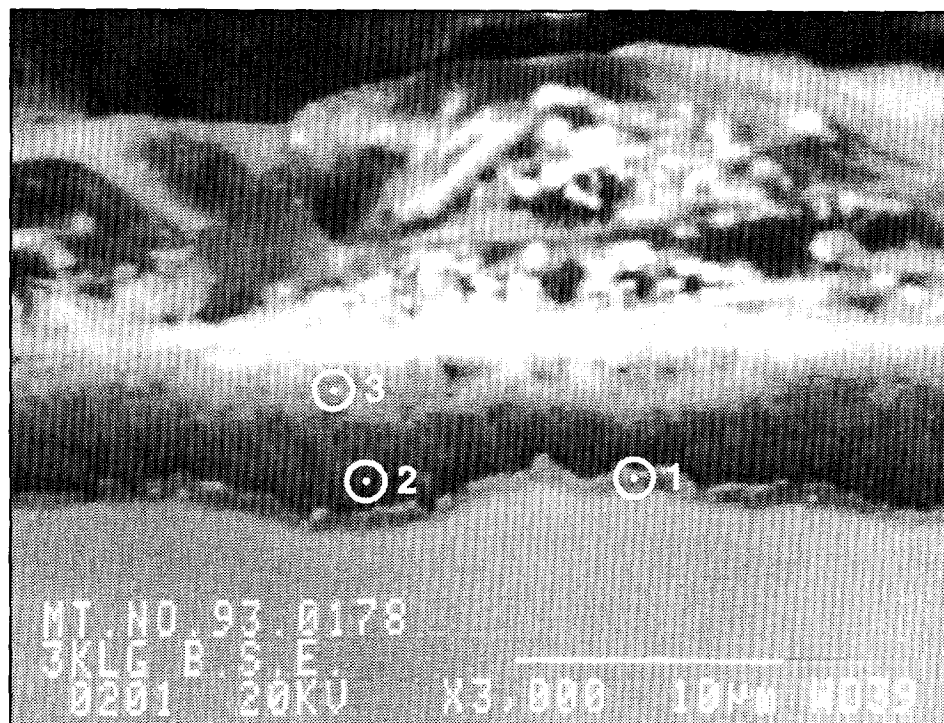


Figure 5.45
BSE Image of Scale on Alloy E, 600 hr Exposure, Gas 3, 540°C

When the water content of the gas is raised to 15% the scale becomes very thin and difficult to analyze. The BSE image, together with elemental maps, indicate pockets of aluminum rich scale covered with CrFe oxides and sulfides (Figure 5.46). No continuous Al_2O_3 rich scale is indicated. Quantitative EDS spot analyses indicate that Al_2O_3 occurs mainly as precipitates in the alloy just below the (Cr, Fe, S) scale.

5.3.4 Effect of Changes in the CO/CO_2 Ratio in Steam Free Gases

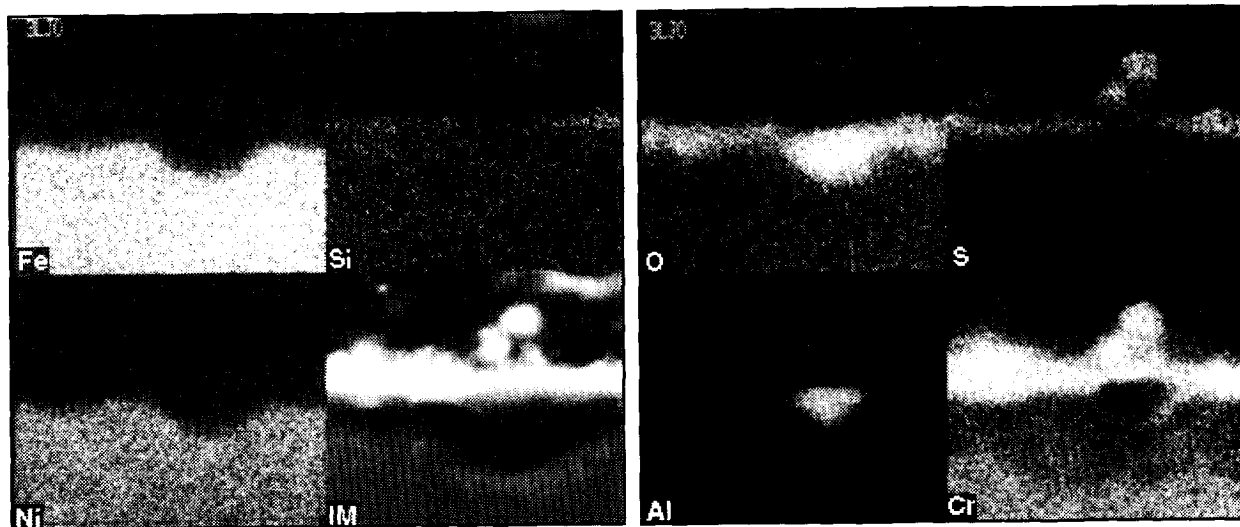
From a strictly thermodynamic point of view, a steam free gas with a CO_2/CO ratio, giving the same oxygen pressure as that of a syngas containing steam, should have the same corrosive effect, unless kinetic factors predominate. A water free gas with a very low CO_2/CO ratio was also used to test the effect of a very low oxygen pressure on scale formation and corrosion loss.

Changing the CO_2/CO ratio from 4/64 to 0.1/68 reduces the PO_2 of syngas by 3 orders of magnitude as discussed previously in Section 4.1. The corrosion losses of 4 alloys decreased with decreasing PO_2 while that of alloy D remained unchanged, as shown previously in Figure 5.2. Figure 5.47A shows the scale formed on standard alloy A. The



(a)

BSE Image of Scale



(b)

Elemental Maps

Figure 5.46
Photomicrographs of Scale on Alloy E, 600 hr Exposure, Gas 7, 540°C

EDS analysis of the topotactical scale indicates the following composition (at%): O 12, Si <0.5, S 19, Cr 41, Mn 1, Fe 19 and Ni 7. Since the Cr+S content is only 31%, it must be assumed that the apparent "scale" has a high content of metal, possibly as high as 25-35%. The inward growing scale is covered with a dense FeCr_2S_4 layer below a porous layer of FeNiS, as shown in the optical photomicrograph of Figure 5.47B.

Addition of 3.25V to the alloy reduces the corrosion loss somewhat (alloy B). The BSE image in Figure 5.48 shows a two layered topotactical scale under the usual FeCr_2S_4 and FeNiS layers. The composition of the two layers is given in Table 5.38.

Table 5.38
Scale Composition on Alloy B, 600 hrs, Gas 0, 540°C (at%)

Scale Area	O	Si	S	V	Cr	Mn	Fe	Ni
1	27	<1	12	5	29	<.5	23	3
2	30	<1	22	7	30	<.5	9	2

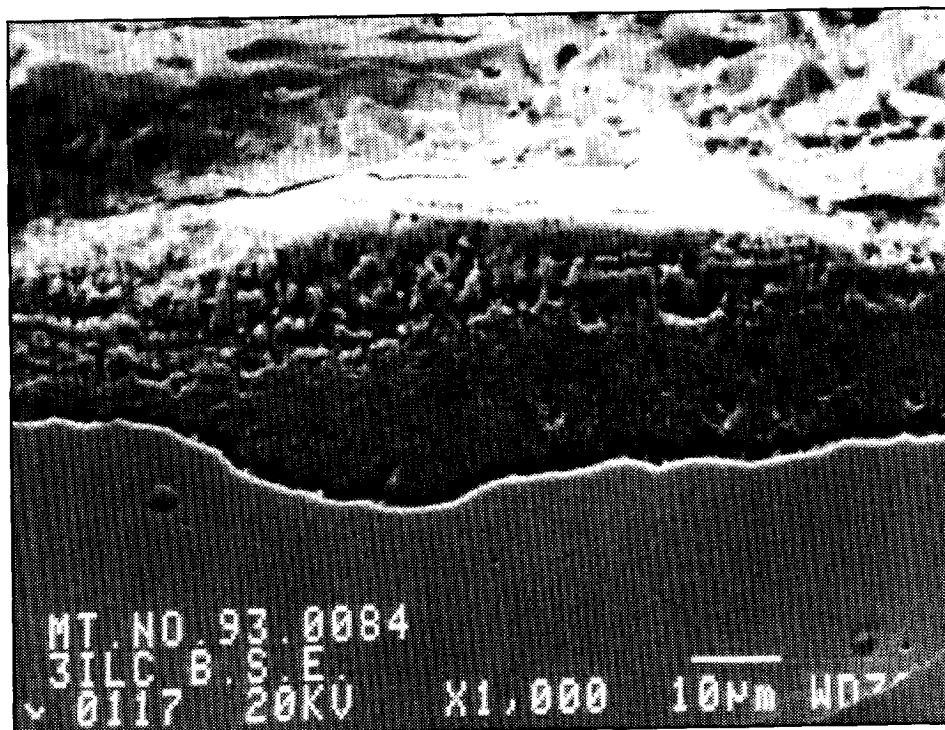
The data indicate an oxidant deficient layer at the scale/metal interface, with a fully converted sulfur rich top layer.

Addition of 3.25% Ti (alloy C) to the base alloy does change the corrosion rate significantly, and produces an inward growing scale with a different morphology, very similar to that on alloy C after 1224 hrs exposure in gas 1. Figure 5.49 shows the microstructure of the topotactical scale, while Table 5.39 gives EDS analyses of selected areas.

Table 5.39
Scale Compositions on Alloy C, 600 hrs Exposure, Gas 0, 540°C (at%)

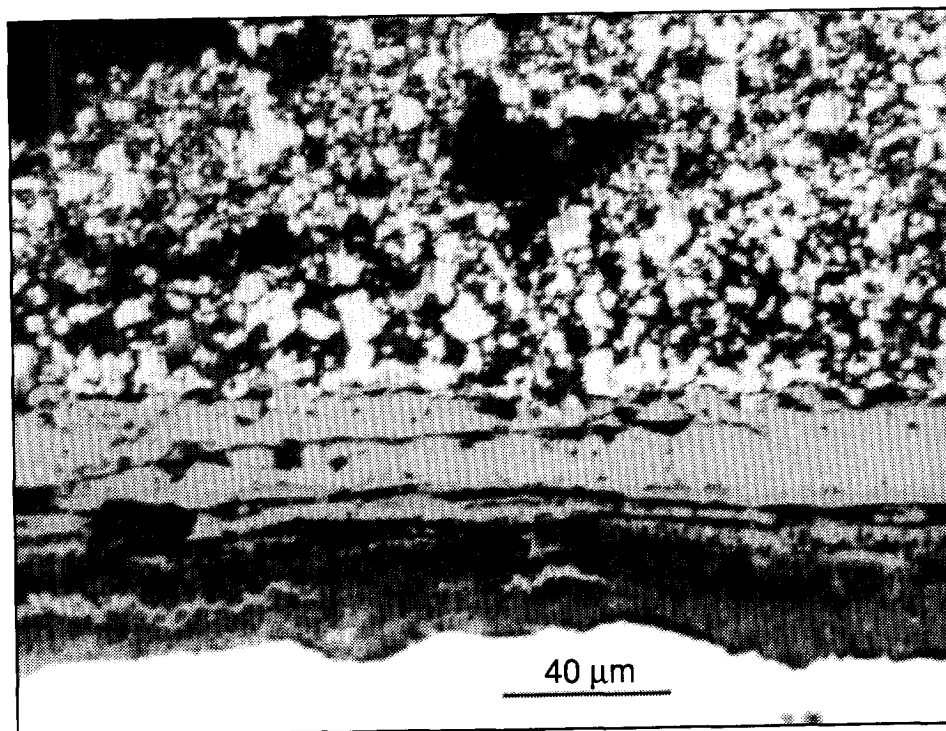
Scale Area	O	Si	S	Ti	Cr	Mn	Fe	Ni
1	22	1	1	9	26	<.5	37	4
2	47	1	1	5	29	<.5	15	1
3	22	1	39	6	21	1	10	<.5

Most of the topotactical "scale" is deficient in oxygen and sulfur. Within the "scale" are oxide rich inclusions. The sulfur content of the penetrated area is remarkably low (1, 2), except near the top, where a near stoichiometric sulfide-oxide scale is present (3).



(a)

BSE Image of Topotactical Scale



(b)

Optical Photomicrograph

Figure 5.47
Photomicrographs of Scale on Alloy A, 600 hr Exposure, Gas 0, 540°C

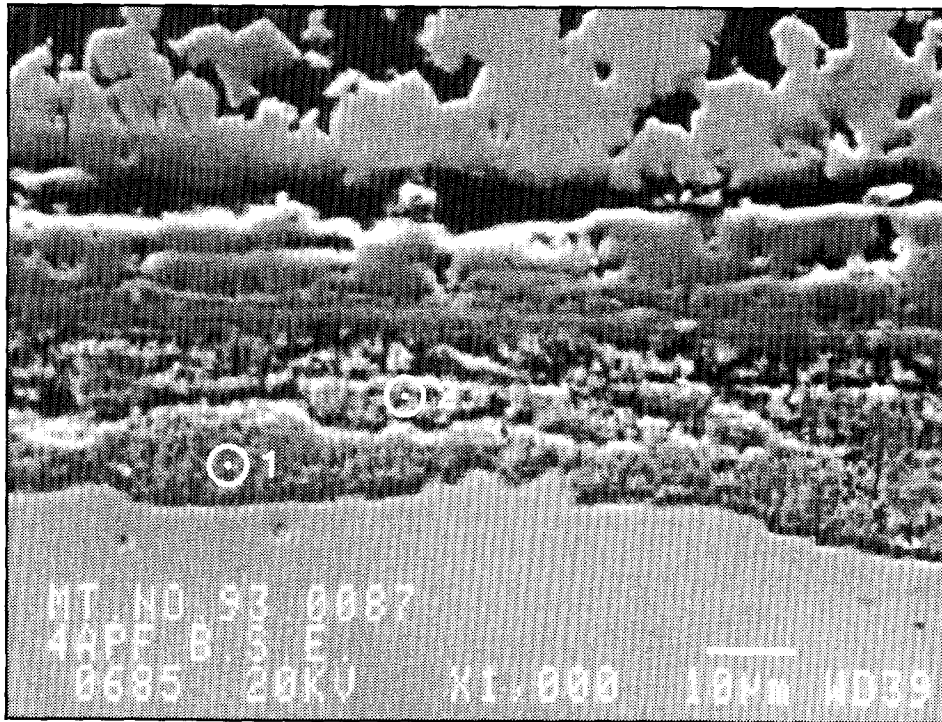


Figure 5.48
BSE Image of Scale on Alloy B, 600 hr Exposure, Gas 0, 540°C

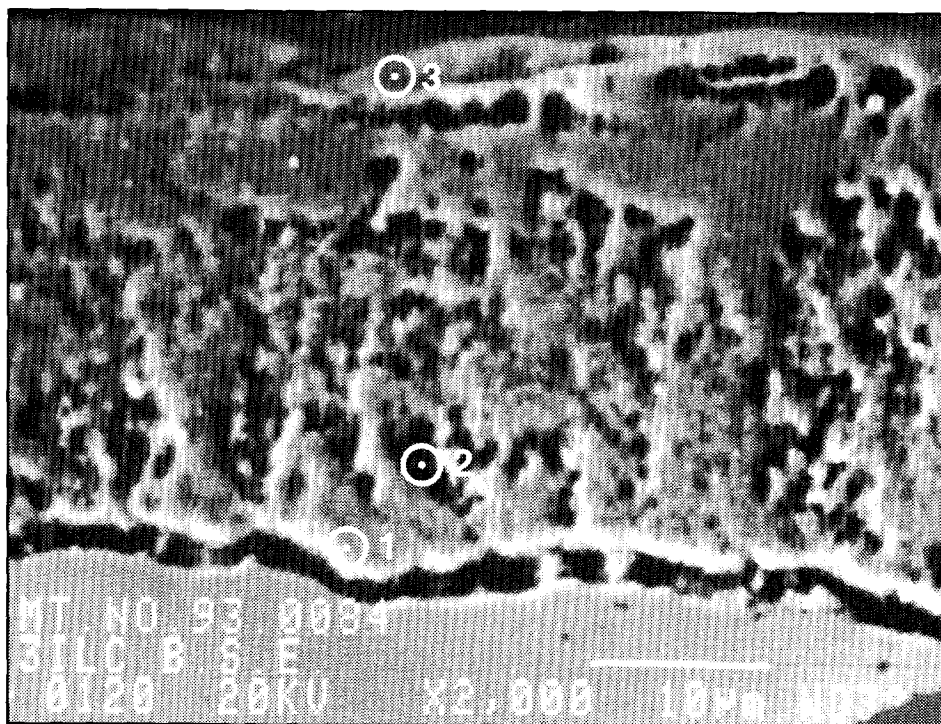


Figure 5.49
BSE Image of Scale on Alloy C, 600 hr Exposure, Gas 0, 540°C

The scale on alloy D, containing silicon is shown in Figure 5.50. Table 5.40 shows the composition of the topotactical scale. Similar to Alloy B, an oxidant deficient low sulfur layer (1) is present, below a more fully converted top layer (2).

Table 5.40
Scale Compositions on Alloy D, 600 hrs Exposure, Gas 0, 540°C (at%)

Scale Area	O	Si	S	Cr	Mn	Fe	Ni
1	32	7	2	21	<.5	32	6
2	15	9	33	21	<.5	18	3

The bright bands in the topotactical scale consist of chrome rich sulfide with some silicon. The massive bright crystals on top of the scale are iron nickel sulfides.

A water free syngas with a CO_2/CO ratio of 0.64 has the same nominal PO_2 as a syngas containing 5% H_2O (gas 8). Corrosion rates in both gases were about the same in both gases for alloys A and B, but the corrosion rate of Alloy C was considerably lower in the dry gas. Topotactical scales after exposure to both gases were therefore analyzed.

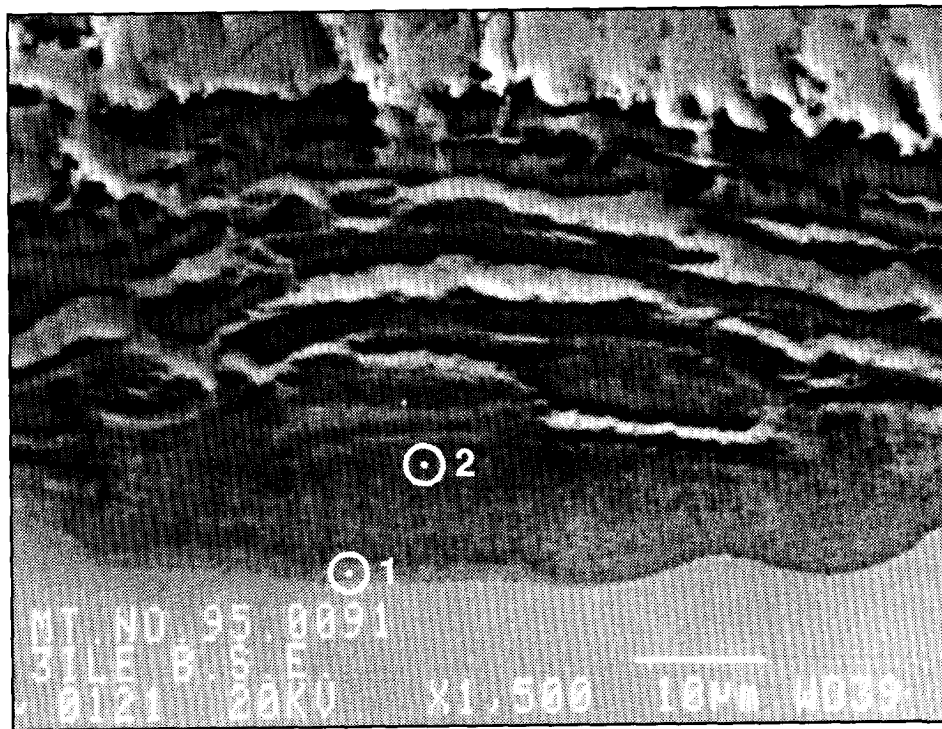


Figure 5.50
BSE Image of Scale on Alloy D, 600 hr Exposure, Gas 0, 540°C

Figure 5.51 shows a considerable difference in scale morphology, but scale analyses given in Table 5.41 are similar.

Table 5.41

Typical Composition of Topotactical Scales on Alloy C After 600 hr Exposure to Syngas with a PO_2 of 10^{-27} at $540^\circ C$

Gas	Scale Area	O	Si	S	Ti	Cr	Mn	Fe	Ni
5 5% H ₂ O	1	45	<1	8	4	28	1	11	2
	2	49	<1	4	4	34	1	4	2
9 CO ₂ /CO 0.64	1	49	1	6	4	26	1	11	1
	2	46	1	10	4	24	<1	11	3

A water free syngas with a CO₂/CO ratio of 2, has the same partial pressure of oxygen as a syngas with a H₂O/H₂ ratio of 0.5, containing 15% H₂O. The results of a 600 hr corrosion test with the latter gas were described in section 5.3.3 (gas 7, 15% H₂O).

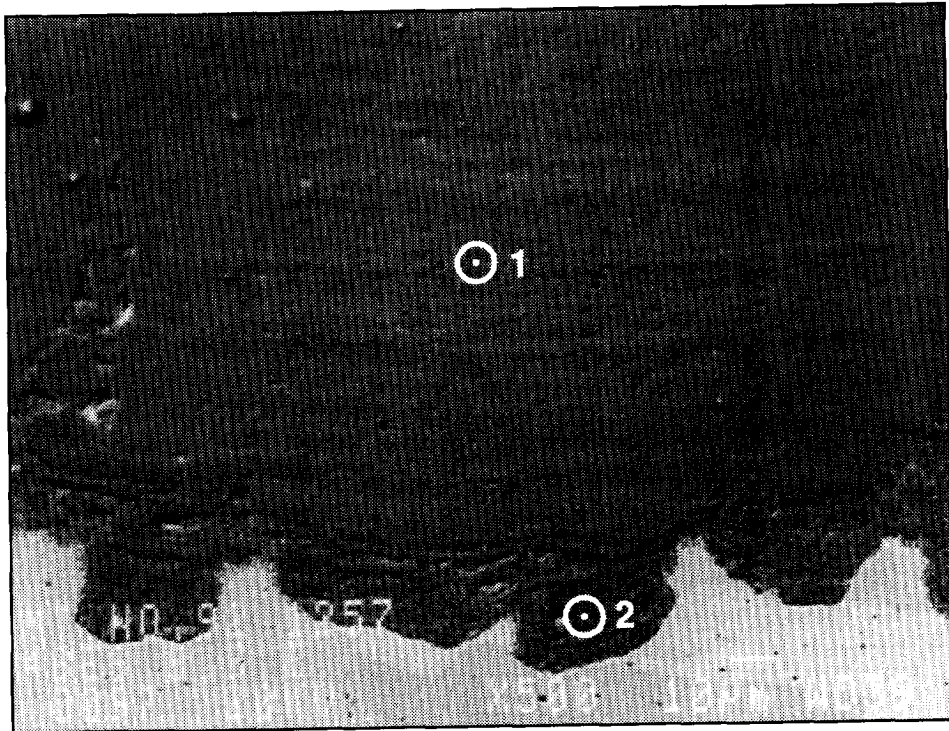
Corrosion rates in the water free gas with the same PO_2 were considerably higher than in the water containing gas for alloys A and B, but lower for alloy C. The BSE images of alloys A and C are shown in Figure 5.52, while the typical scale compositions are given in Table 5.42.

Table 5.42

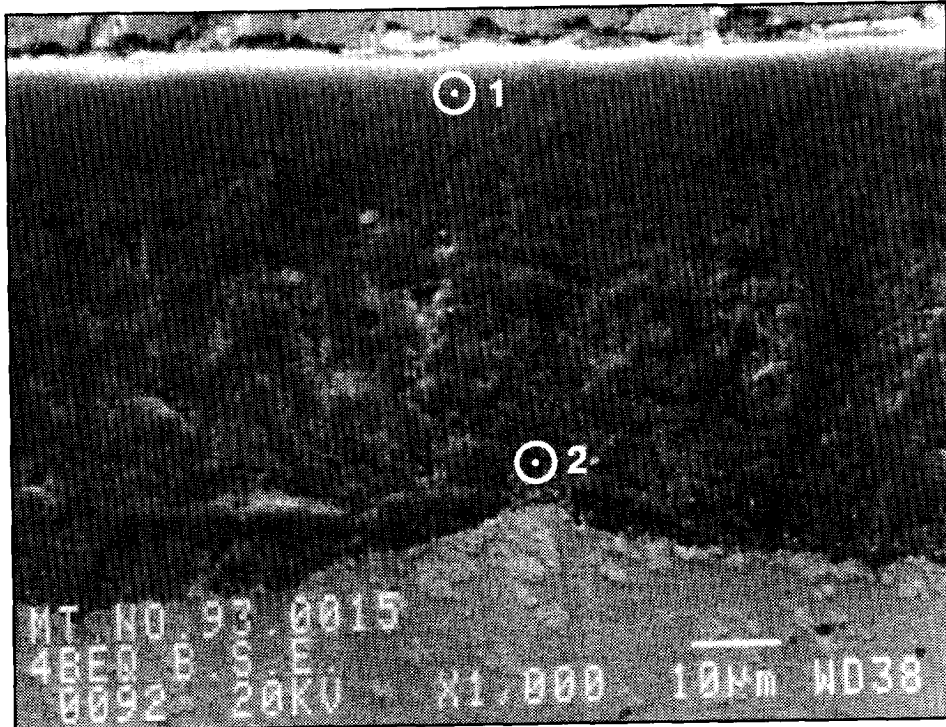
Typical Compositions of Topotactical Scale on Alloys A and C after 600 hr Exposure to Syngas with a PO_2 of 10^{-26} at $540^\circ C$ (at %)

Alloy	Gas	Scale Area	O	Si	S	Ti	Cr	Mn	Fe	Ni
A	7 15% H ₂ O	1	43	1	6	–	30	1	15	3
A	8 CO ₂ /CO=2	1	42	1	7	–	31	<.5	15	3
C	7 5% H ₂ O	1	48	1	6	5	28	1	10	1
C	8 CO ₂ /CO=2	1	47	1	5	5	28	1	11	2
		2	54	1	3	4	32	1	6	1

The composition of the scale on alloy A is the same in both gases, despite a significant difference in corrosion loss. The average composition of the scale on alloy C is also similar. However in the steam free gas a layer with a higher Cr₂O₃ and a lower FeS content was present at the scale/metal interface, which may explain the lower corrosion rate in this case.

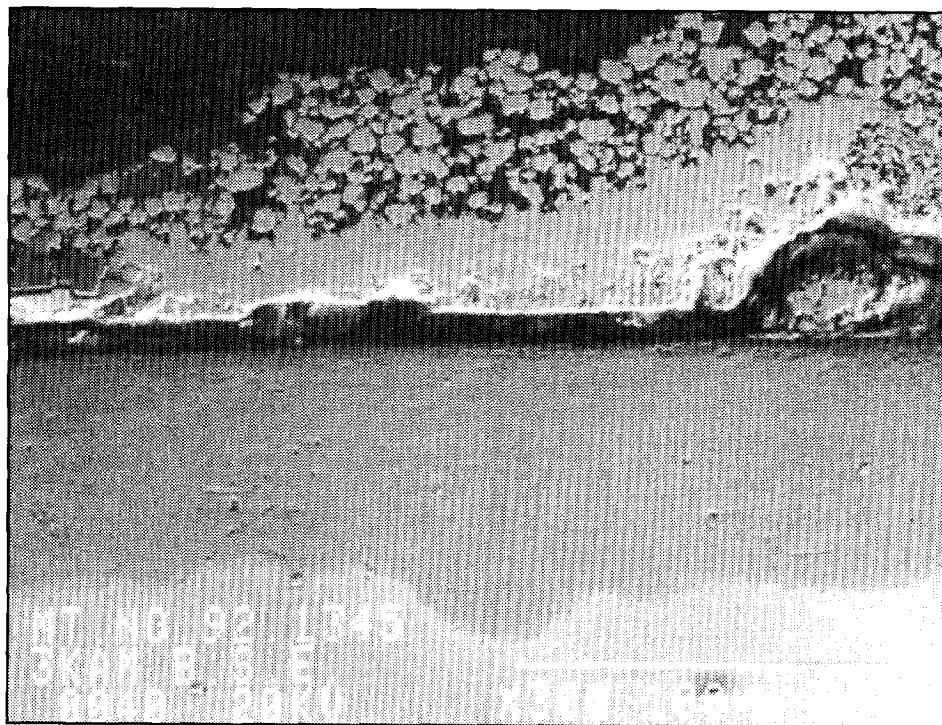


(a)
600 hr, Gas 5, 540°C (5% H₂O)

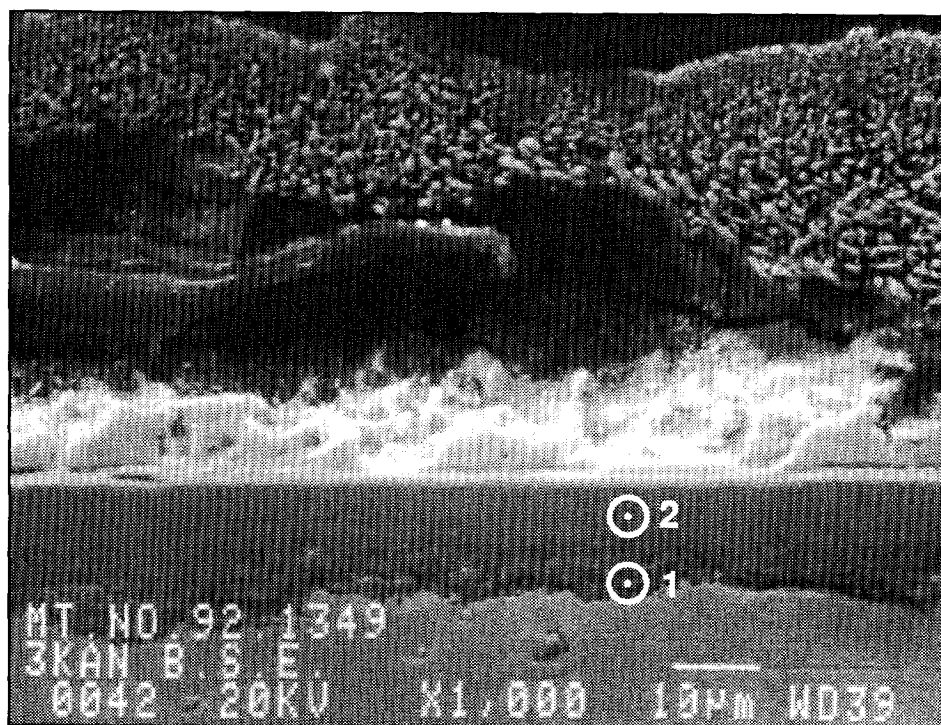


(b)
600 hr, Gas 9, 540°C (CO₂/CO = 0.64)

Figure 5.51
BSE Image of Scale on Alloy C



(a)
Alloy A



(b)
Alloy C

Figure 5.52
BSE Image of Scale on Alloys A and C, 600 hr Exposure, Gas 8, 540°C

5.3.5 Effect of H₂S Content in Syngas

All corrosion tests described up till now used syngas containing 0.8% H₂S, which is representative of syngas produced by coals containing 2-3% sulfur. A limited number of tests were also carried out with similar syngas compositions containing 0.2 H₂S. Corrosion measurements in Sections 5.1 and 5.2 showed generally higher corrosion losses for alloys A, B and C at 0.2% H₂S than at 0.8% H₂S, at low steam contents (0-1%), but lower corrosion rates in gases containing 3% steam. Selective scale analyses were made to discover the root causes of the differences observed.

Alloy A. The scale developed after 600 hrs exposure to dry syngas 1A is shown in Figure 5.53A. Scale analyses are given in Table 5 below.

Table 5.43

Composition of Topotactical Scale on Alloy A, 600 hrs, 540°C, Gas 1A (0.2% H₂S) at %

Scale Area	O	Si	S	Cr	Mn	Fe	Ni
1	32	1	24	32	<.5	11	<.5
2	30	1	2	32	<.5	29	5

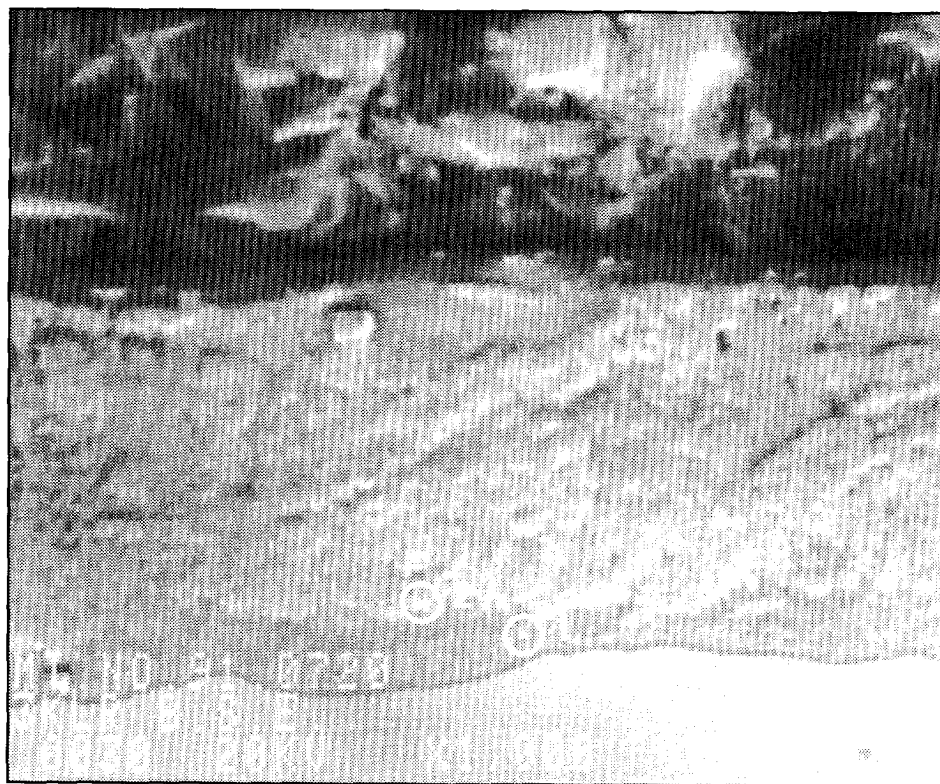
Area 2 is clearly oxidant deficient while the underlying area 1 is not. This is also shown in Figure 5.53B, which gives the distribution of the major elements. Qualitative analyses indicated that the small crystallite near the top of the topotactical scale is Cr₂O₃, while the surrounding scale consists mainly of Fe Cr₂S₄.

After 1224 hrs the scale/alloy interface is irregular (Figure 5.54). EDS analyses given in Table 5.44 indicates that the oxygen content of the scale in the fast corroding areas is higher.

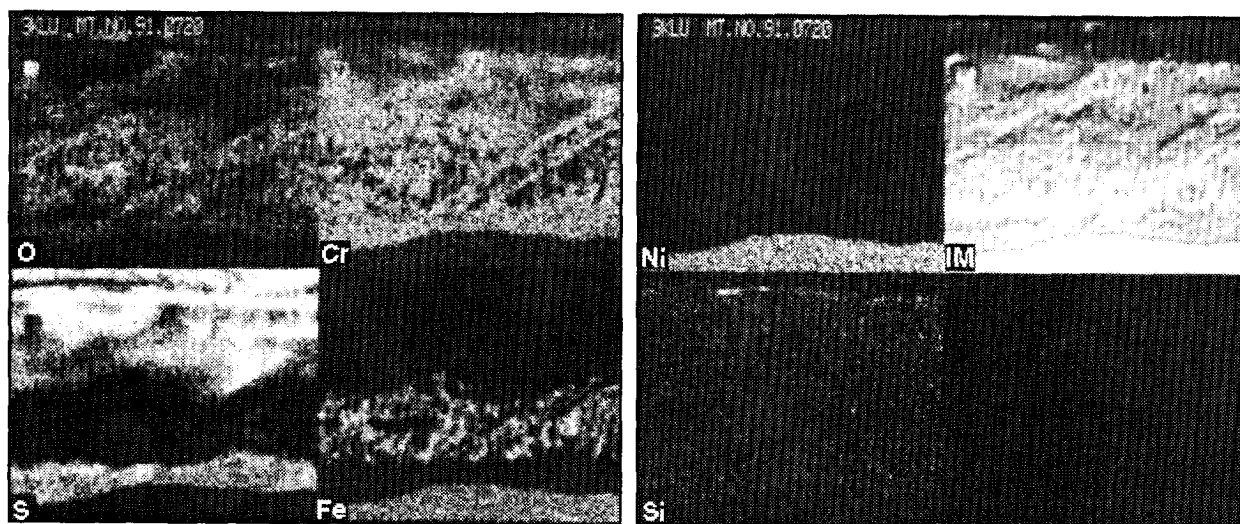
Table 5.44

Composition of Topotactical Scale on Alloy A, 1350 hrs, 540°C, Gas 1A (at %)

Scale Area	O	Si	S	Cr	Mn	Fe	Ni
1	34	1	24	30	<.5	10	<.5
2	40	1	14	28	<.5	16	2



(a)
BSE Image of Scale



(b)
Elemental Maps

Figure 5.53
Photomicrographs of Scale on Alloy A, 600 hr Exposure, Gas 1A, 540°C

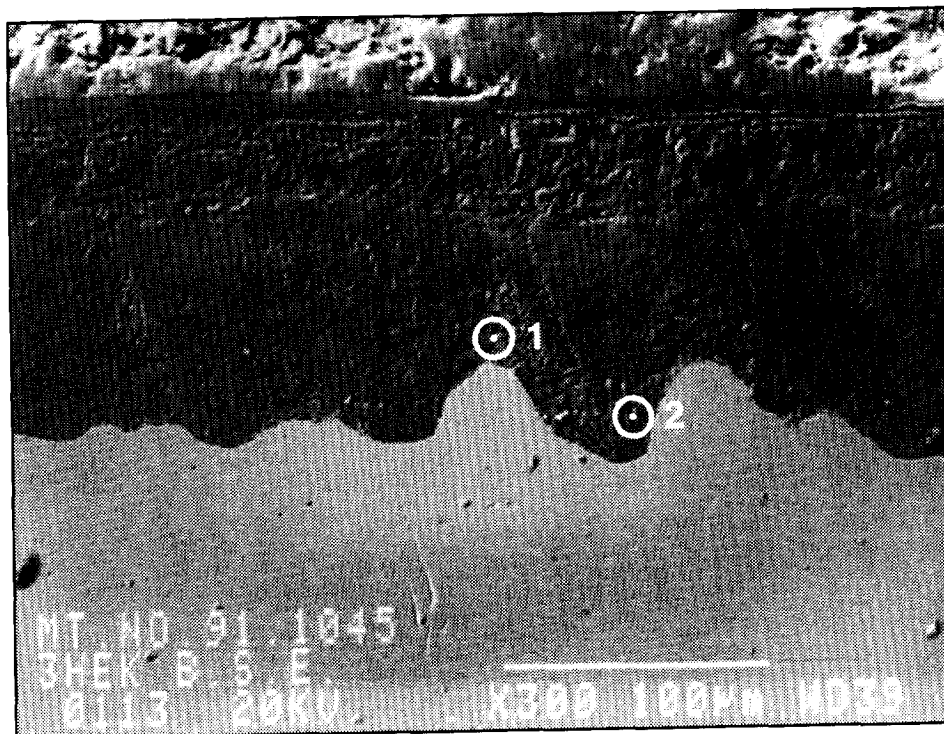


Figure 5.54
BSE Image of Scale on Alloy A, 1350 hr Exposure, Gas 1A, 540°C

Addition of only 1% H₂O to the dry syngas containing 0.2% H₂S, increases the corrosion rate more than 4 fold. The BSE image in Figure 5.55 indicates a relatively homogeneous scale with a slightly irregular alloy/scale interface. Quantitative EDS analyses show that the oxide content of the scales is high in the fastest growing areas of the scale (Table 5.45).

Table 5.45
Composition of Scale on Alloy A, 600 hrs, 540°C, Gas 2A (at %)

Scale Area	O	Si	S	Cr	Mn	Fe	Ni
1	43	1	11	29	<.5	10	5
2	39	1	17	21	<.5	19	1
3	46	1	7	28	<.5	15	2

Increasing the water content of the gas to 3%, significantly decreases the corrosion loss. It also makes the alloy/scale interface extremely irregular, as shown in Figure 5.56. The scale analyses given in Table 5.46 indicate that the fastest growing scale areas contain less sulfur. The Fe/S ratio suggests that significant amounts of FeO are present in the scale in addition to Fe (Ni) S.

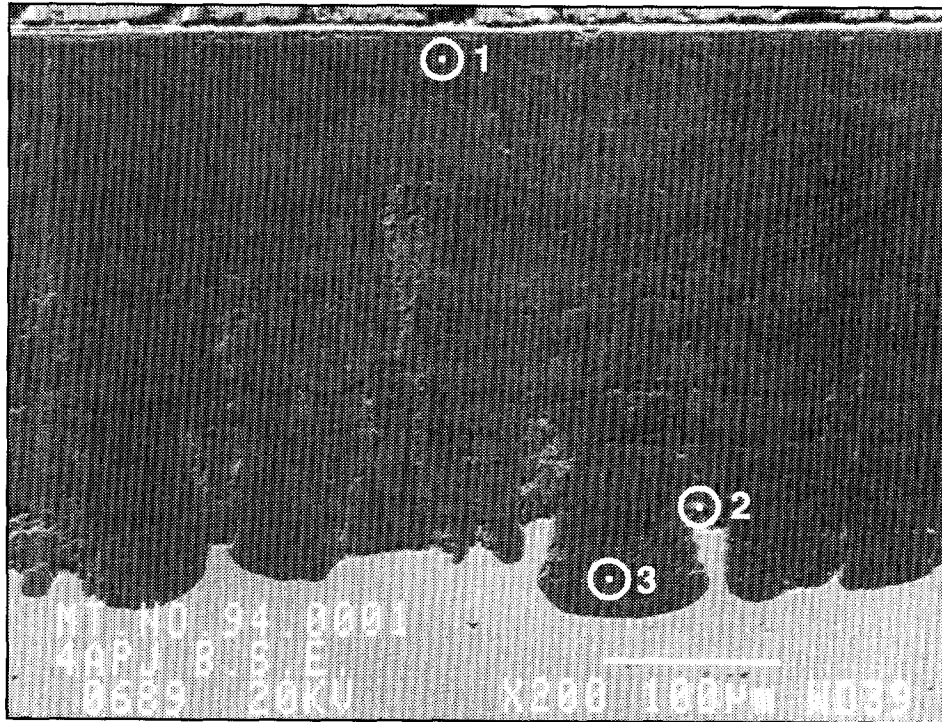


Figure 5.55
BSE Image of Scale on Alloy A, 600 hr Exposure, Gas 2A, 540°C

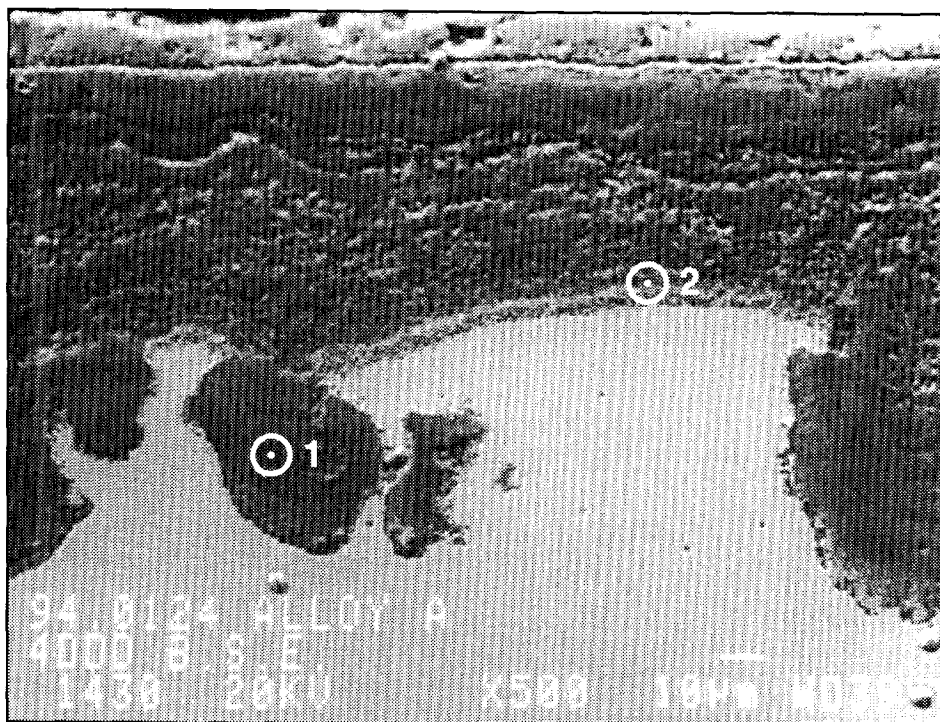


Figure 5.56
BSE Image of Scale on Alloy A, 600 hr Exposure, Gas 4A, 540°C

Table 5.46
Composition of Scale on Alloy A, 600 hrs, 540°C, Gas 4A (at %)

Scale Area	O	Si	S	Cr	Mn	Fe	Ni
1	44	<1	6	32	<1	16	1
2	42	<1	10	29	<.5	16	2

Alloy B. After 1350 hrs exposure to gas 1A, the topotactical scale is about 40 μm thick, indicating a moderate corrosion rate as shown in Figure 5.57. The epitactical scale again consists of a $\text{Fe Cr}_2 \text{S}_4$ layer below a Fe, (Ni) S layer. The topotactical layer is inhomogeneous. Many precipitates are visible in the alloy surface. Quantitative EDS analyses are shown in Table 5.47 below.

Table 5.47
Scale and Alloy Composition of Alloy B, 1350 hrs, 540°C, Gas 1A (at %)

Scale Area	O	Si	S	V	Cr	Mn	Fe	Ni
1	40	1	17	6	27	<.5	6	3
2	39	1	3	4	27	<.5	18	6
3	33	1	1	4	22	<.5	31	7
4	1	<.5	12	3	10	<.5	31	43

The smooth area above the granular scale is similar to the bottom layer of the epitactical scale and consists of $\text{Fe Cr}_2 \text{S}_4$. Below the layer oxides are predominant. In most areas metallic remnants, most likely Fe are present. Thus the topotactical "scale" is in fact a heavily penetrated alloy surface layer.

Adding 1% H_2O to the dry syngas again increases the corrosion rate about four fold. The BSE image of Figure 5.58 shows a relatively inhomogeneous scale, with an irregular scale/alloy interface. Quantitative EDS/WDS analyses are given in Table 5.48 below.

Table 5.48
Composition of Scale on Alloy B, 600 hrs, 540°C, Gas 2A (at %)

Scale Area	O	Si	S	V	Cr	Mn	Fe	Ni
1	34	<.5	20	3	24	1	14	3
2	49	2	11	7	22	<1	3	6
3	43	<1	11	4	29	1	8	2
4	45	<1	9	5	29	1	8	2

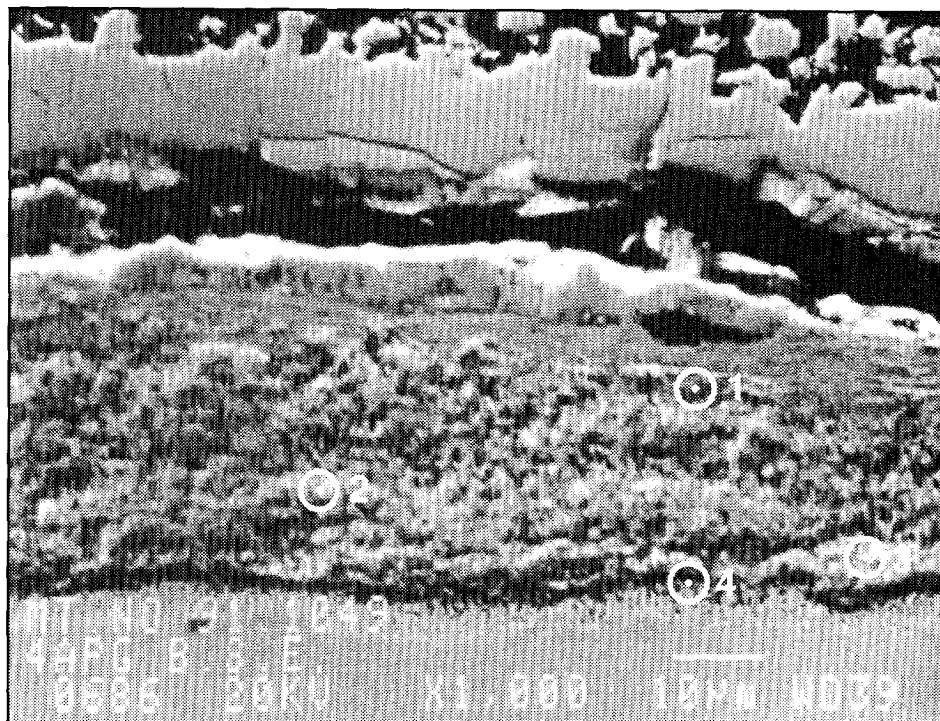


Figure 5.57
BSE Image of Scale on Alloy B, 1350 hr Exposure, Gas 1A, 540°C

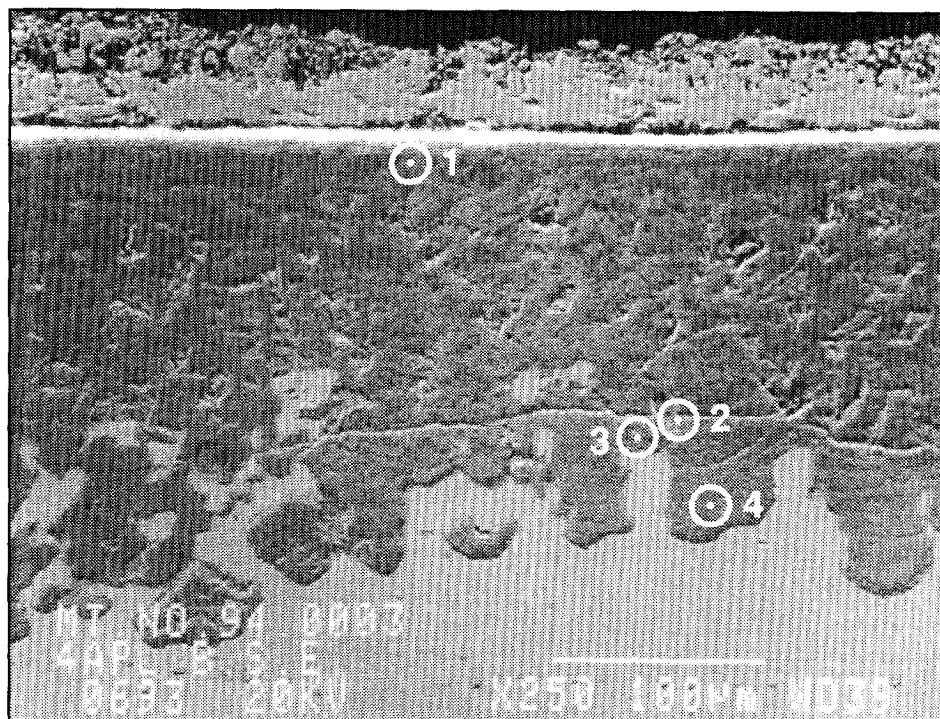


Figure 5.58
BSE Image of Scale on Alloy B, 600 hr Exposure, Gas 2A, 540°C

Apart from some sulfur enrichment at the top, the scale composition is quite uniform and oxygen rich.

An increase of the water content to 3% again reduces the corrosion loss and results in an extremely irregular alloy/scale interface, with a pitted appearance (Figure 5.59). WDS/EDS analyses, given in Table 5.49, again show a lower sulfur content in pitted areas, where maximum scale growth occurred. In general the sulfur content of the scale is higher here than in the scale on alloy A. Between the topotactical scale and the epitactical scale, consisting of Fe (Ni) sulfides, a thin high sulfur layer is present, which also contains a significant amount of Ni.

Table 5.49
Composition of Scale on Alloy B, 600 hrs, 540°C, Gas 4A (at %)

Scale Area	O	Si	S	V	Cr	Mn	Fe	Ni
1	42	<1	9	5	31	2	8	3
2	30	<.5	23	4	22	1	17	3
3	30	<1	23	3	20	<.5	13	11

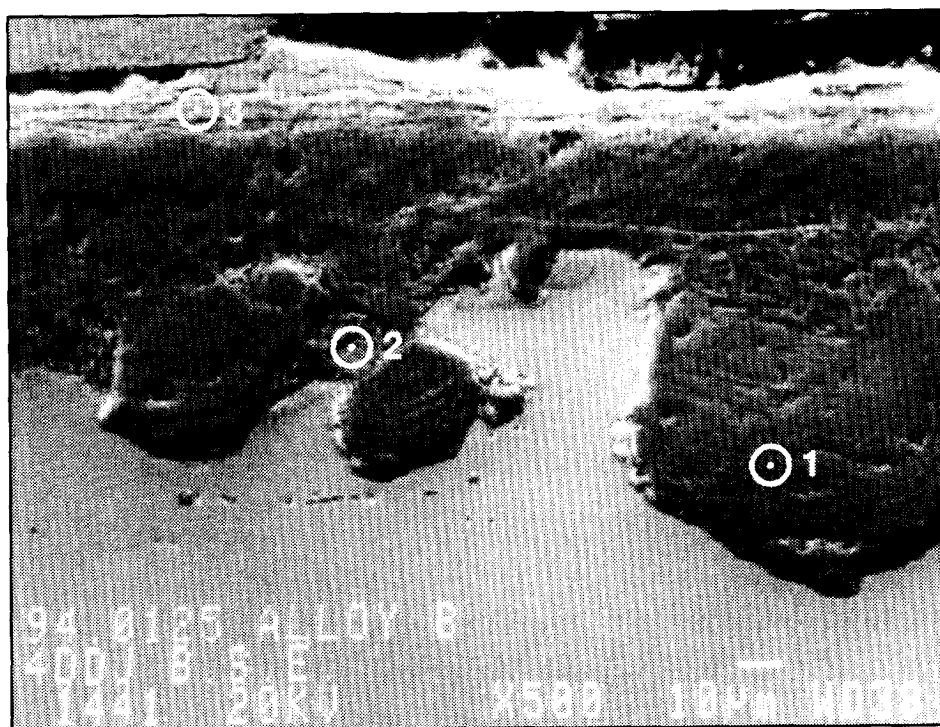


Figure 5.59
BSE Image of Scale on Alloy B, 600 hr Exposure, Gas 4A, 540°C

Alloy C. After 600 hrs exposure to gas 1A, the topotactical scale on alloy C is quite dense, but severely cracked in many areas. The scale/alloy interface is irregular as shown in Figure 5.60. The average topotactical scale analysis is as follows (at %) O 45, Si 1, S 11, Ti 5, Cr 30, Mn <0.5, Fe 8, Ni 1.

After 1350 hrs the scale/alloy interface is still irregular as shown in Figure 5.61, which shows the BSE images as well as elemental distribution maps. Detailed quantitative EDS analysis were made of the indicated areas and of the alloy immediately below the scale. Results are shown in Table 5.50 below:

Table 5.50

Composition of Topotactical Scale on Alloy C, 1350 hrs, 540°C, Gas 1A (at %)

Scale/Alloy Area	O	Si	S	Ti	Cr	Mn	Fe	Ni
1 alloy	3	<.5	5	1	8	<.5	28	53
2 scale	18	1	36	4	29	1	11	2
3 alloy	4	1	0	3	22	1	38	31
4 scale	36	1	18	4	31	1	8	2

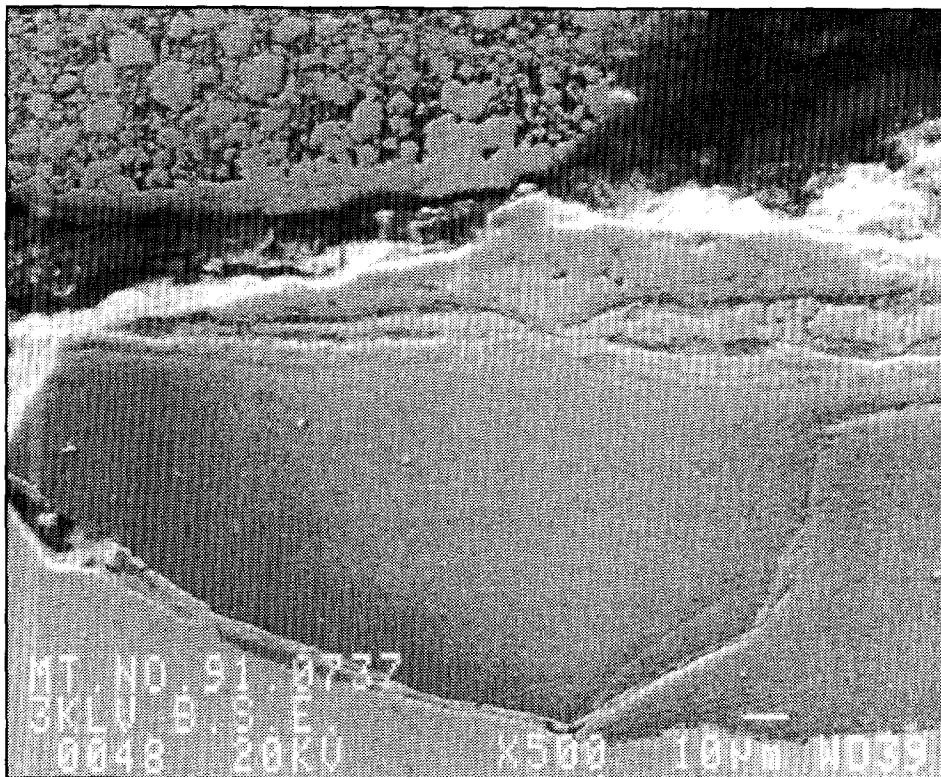


Figure 5.60

BSE Image of Scale on Alloy B, 600 hr Exposure, Gas 1A, 540°C

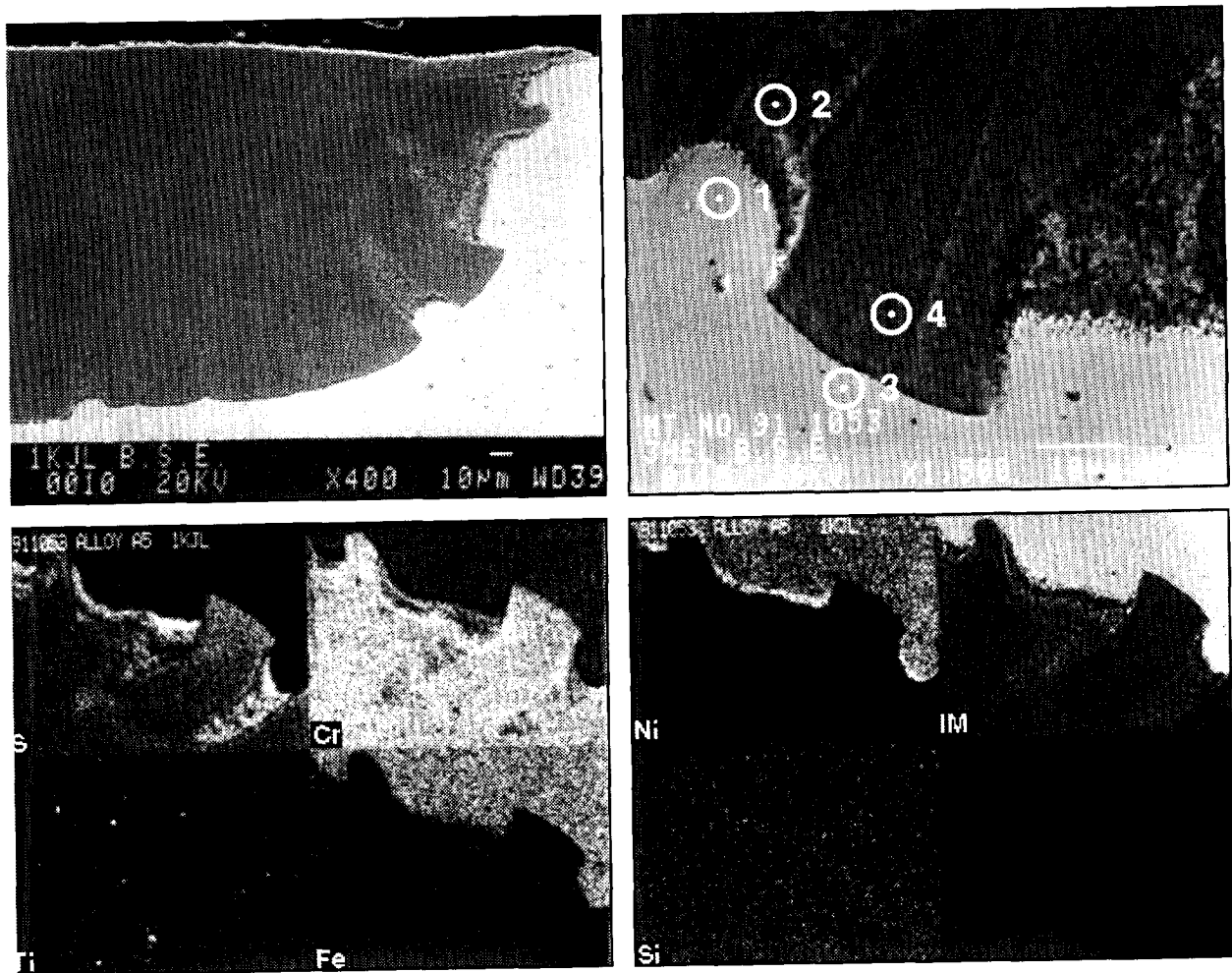


Figure 5.61
BSE Image and Elemental Maps of Scale on Alloy C, 1350 hr Exposure, Gas 1A, 540°C

Again the scale above the faster corroding areas is enriched in oxygen. The difference between areas of slow corrosion and fast corrosion is more pronounced here. The alloy below the fast corroding areas is similar to the original alloy, while Cr and Ti depletion and Ni enrichment occur below the slow corroding areas.

In contrast to alloys A and B, the addition of 1% H₂O to dry syngas does not result in an increase in corrosion rate. The growth rate of the topotactical scale still varies greatly, giving rise to a pitting type of attack, similar to that observed in the water free syngas (Figure 5.62). Quantitative EDS analysis shown in Table 5.51 show that the oxygen content of the topotactical scale in pits is somewhat higher and the sulfur content somewhat lower (1, 2). On top of the topotactical scale is a thin partially converted alloy layer, and a layer with a high sulfur and titanium content (3, 4).

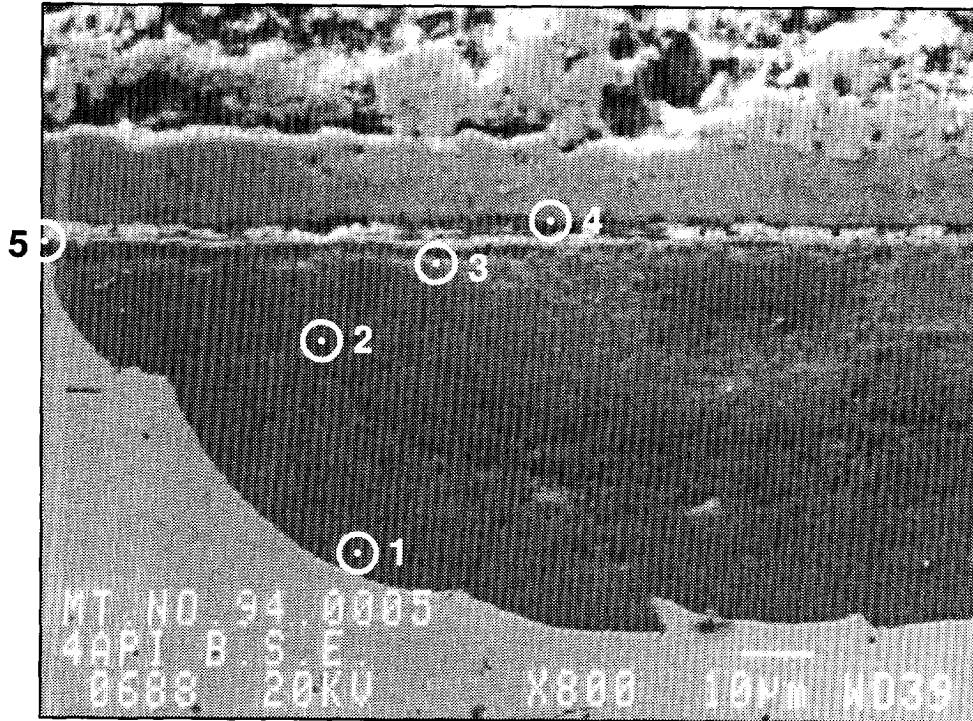


Figure 5.62
BSE Image of Scale on Alloy C, 600 hr Exposure, Gas 2A, 540°C

Table 5.51
Scale Composition on Alloy C, 600 hrs, 540°C, Gas 2A (at %)

Scale Area	O	Si	S	Ti	Cr	Mn	Fe	Ni
1	44	1	10	4	30	<1	8	2
2	41	1	10	4	32	<1	9	1
3	27	3	4	9	21	<1	24	13
4	31	2	28	14	16	<1	8	1
5	32	<1	23	4	31	<1	7	<1

The thin topotactical scale outside the pits has a significantly higher sulfur content (5). A continuous dense, probably epitactical $\text{Fe Cr}_2 \text{S}_4$ layer is present on top of the topotactical scale. The outer scale consists of Fe (Ni) S crystals.

When the water content of the gas is increased, the maximum corrosion loss increases slightly, but the scale/alloy interface becomes again very irregular. Thus the local corrosion rate varies significantly (Figure 5.63). Table 5.52 indicates that the scale has a

high oxygen content and a low sulfur content (1). A Ti rich particle in the scale contained even less sulfur (2). Sulfur enrichment was detected at the scale/alloy interface (3).

Table 5.52
Composition of Scale on Alloy C, 600 hrs, 540°C, Gas 4A (at %)

Scale Area	O	Si	S	Ti	Cr	Mn	Fe	Ni
1	50	<1	6	4	30	<1	7	2
2	49	<.5	4	22	9	0	7	10
3	22	<1	17	10	18	<.5	15	16

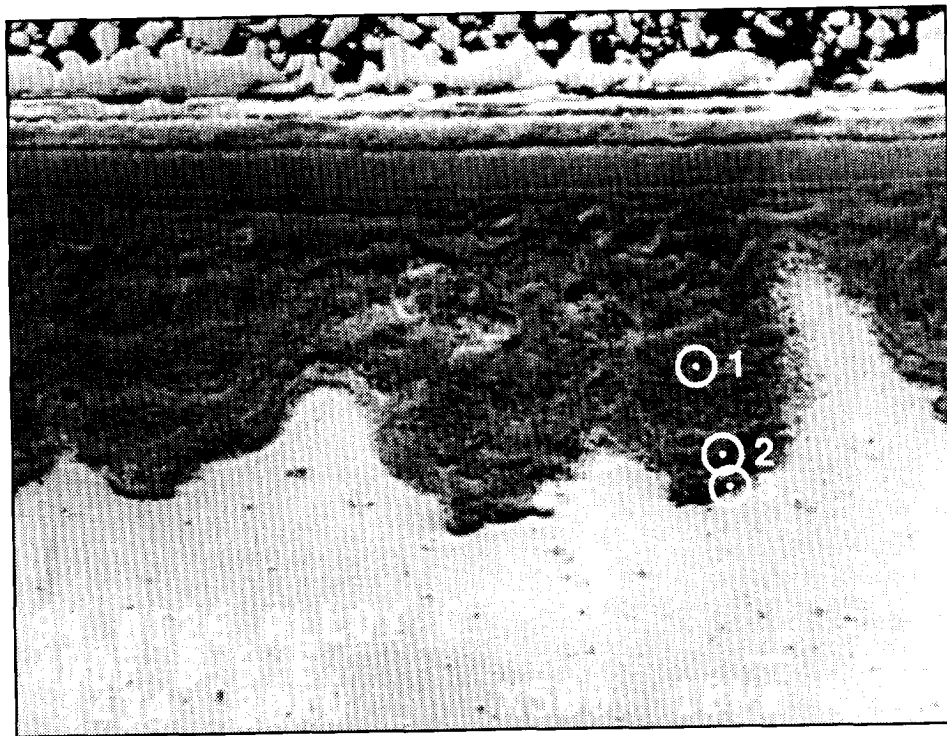


Figure 5.63
 BSE Image of Scale on Alloy C, 600 hr Exposure, Gas 4A, 540°C

Alloy D. Alloy D containing silicon was not exposed in the dry syngas containing 0.2 H₂S. In the syngas containing 1% H₂O alloy D develops a thin seemingly protective scale as shown in Figure 5.64. EDS analyses are given in Table 5.53.

Table 5.53

Composition of Scale on Alloy D, 600 hrs, 540°C, Gas 2A (at %)

Scale Area	O	Si	S	Cr	Mn	Fe	Ni
1	49	9	7	26	1	6	2
2	24	10	27	9	<1	17	13
3	45	9	16	24	<1	6	<1
4	26	12	27	25	<1	9	1

The thin epitactical scale consists of loose Fe (Ni) S crystals. No FeCr₂S₄ layer was detected. Increasing the water content to 3% did not change the corrosion loss significantly. Therefore no SEM analysis of the scale was done.

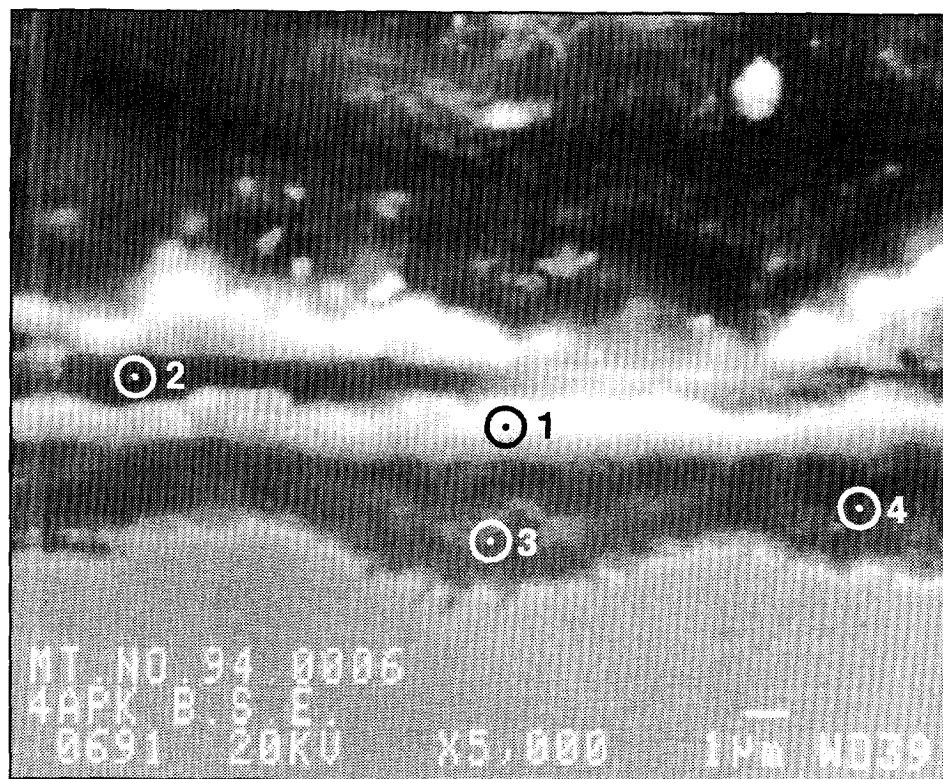


Figure 5.64
BSE Image of Scale on Alloy D, 600 hr Exposure, Gas 2A, 540°C

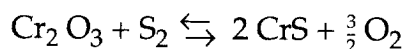
6

INTERPRETATION AND DISCUSSION

6.1 IDENTIFICATION OF CORROSION MECHANISMS

6.1.1 Corrosion as a Function of PS_2 and PO_2

Most previous studies on mixed oxidant corrosion have been done at relatively high temperatures. Here acceptable corrosion rates will occur only when a protective oxide scale can form in gases with a PO_2/PS_2 ratio above a "kinetic boundary", as discussed previously in Section 2.2. Corrosion in gases, where a stable oxide film did not form was considered unacceptably high and corrosion phenomena under such conditions have not been studied widely. An exception is the work by R.C. John et al.⁵³ He discussed corrosion rates in gases in which both sulfides and oxides can form in terms of competition between "slow growing" oxides and "fast growing" sulfides. Thus the corrosion rates are considered to be related to the equilibrium constant of the following reaction.



From this equation it is deduced that the parabolic corrosion rate constant is a power function of the $PS_2/PO_2^{2/3}$ ratio:

$$K_p \sim \alpha \left[\frac{PS_2}{(PO_2)^{3/2}} \right]^x$$

The above expression indicates that the corrosion rate will increase with increasing PS_2 and/or decreasing PO_2 . Our data do not support the presence of parabolic corrosion kinetics for all alloys and gas compositions nor the monotonic increase of corrosion rate with increasing PS_2/PO_2 ratio. However it is possible to plot all data as a function of the non equilibrium PS_2/PO_2 ratio to determine possible trends. Therefore the corrosion loss after 600 hr exposure was plotted as a function of $\text{Log } PS_2/PO_2$ for all three data sets (dry and wet gases with 0.2 and 0.8% H_2S). Results are shown in Figure 6.1 for alloys A and B and Figure 6.2 for alloys C, D and E.

The behavior of Si and Al containing alloys D and E is relatively straight forward. The corrosion losses appear solely dependent on the PS_2/PO_2 ratio and are not affected by the oxygen bearing species or the amount of H_2S present. When the $\text{Log } PS_2/PO_2$ is 19 or higher, the corrosion losses of both alloys are relatively high, 30-70 μm loss in 600 hrs.

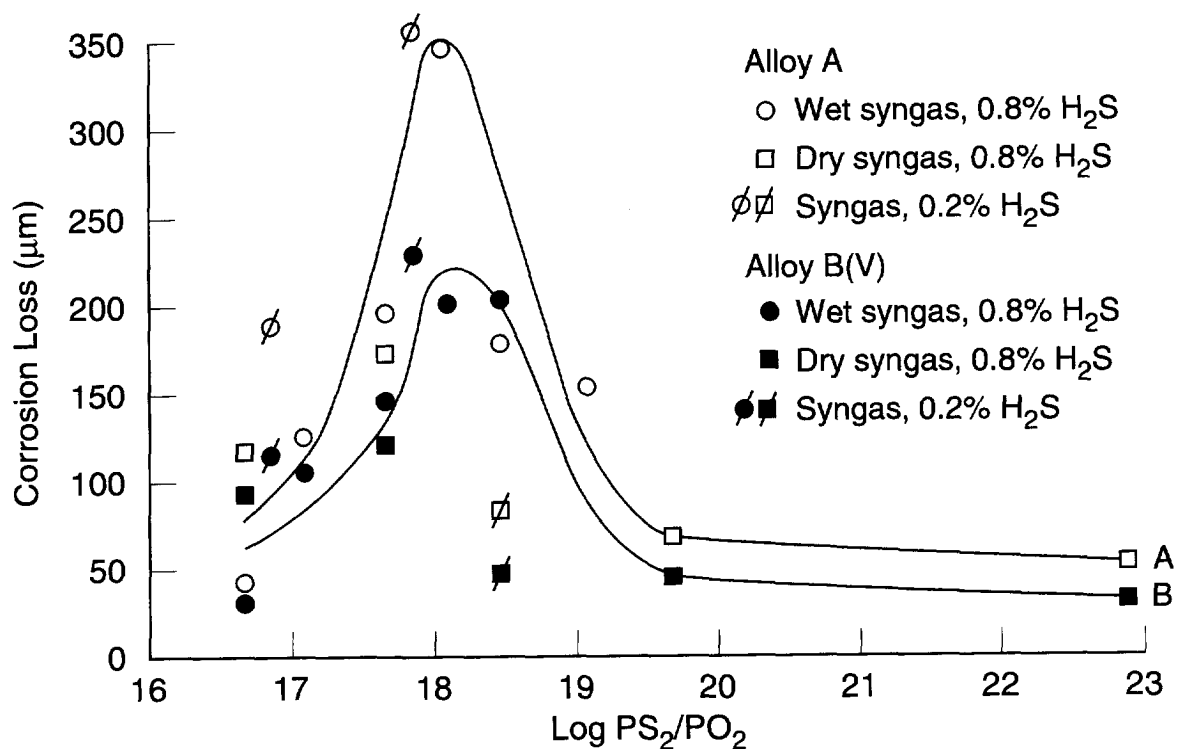


Figure 6.1
Corrosion Loss as a Function of Log PS₂/PO₂

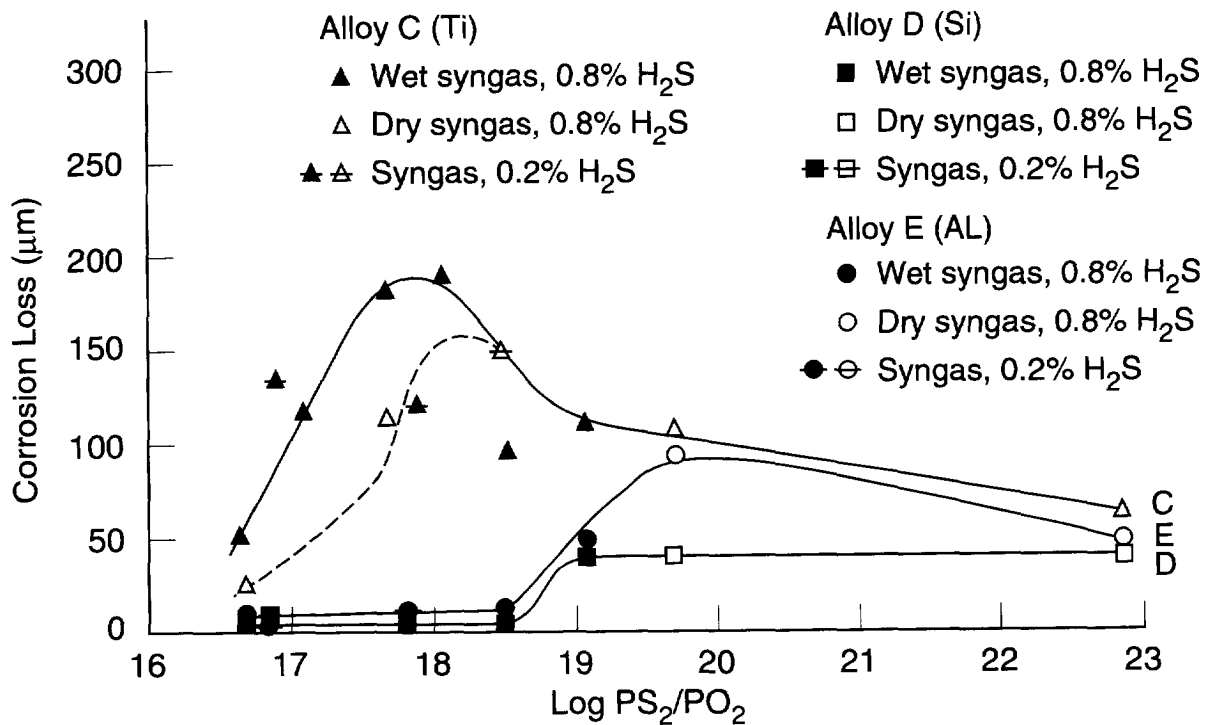


Figure 6.2
Corrosion Loss as a Function of Log PS₂/PO₂

When the $\log PS_2/PO_2$ falls below 18.5, corrosion losses are negligible. This behavior suggests the presence of a "kinetic boundary" below which little or no corrosion occurs. However, microscopic evidence, to be discussed in detail in Section 6.1.3 indicates that this decrease in corrosion rate is not due to the formation of a protective oxide rich scale in the classical sense.

The behavior of alloys A, B and C is considerably more complex. The actual corrosion rate depends not only on the PS_2/PO_2 ratio, but is also influenced by the form of the oxidant (H_2O or CO_2) and the amount of H_2S present. This results in considerable scatter in the data, especially at lower PS_2/PO_2 ratios. However, for all three alloys the corrosion loss increases with decreasing PS_2/PO_2 ratio down to $\log PS_2/PO_2 \approx 18$. Thereafter the corrosion losses decrease, when the PS_2/PO_2 ratio is further decreased. The corrosion loss peaks for all alloys at a $\log PS_2/PO_2$ between 17.5 and 18.5.

The sharp maximum in corrosion loss is most pronounced for the base alloy A, which has a corrosion loss of about 350 μm , in syngas containing 0.8% H_2S and 3% H_2O as well as in syngas containing 1% H_2O and 0.2% H_2S [Figure 5.4, 5.6, 6.1]. The $\log PS_2/PO_2$ of both gases is about 18. This corrosion loss indicates a yearly corrosion rate of 5 mm/yr when extrapolated linearly and in excess of 1 mm/yr when assuming parabolic corrosion kinetics. The high loss after 600 hrs exposure suggest strongly that linear corrosion kinetics are likely.

The effect of oxidant species is variable. In gas mixtures with a high PS_2/PO_2 ratio, dry gas mixtures show significantly less corrosion than gas mixtures containing steam, as shown by a comparison of corrosion losses in gas 2, containing 2% H_2O and 0.8% H_2S and gas 1A, containing 0% H_2O and 0.2% H_2S . The $\log PS_2/PO_2$ of both gases is 18.5. However, the equivalent water free gas produces a significantly higher corrosion loss in gases with a low PS_2/PO_2 ratio ($\log PS_2/PO_2 < 17.5$).

Alloy B, containing 3.25% V, a sulfide former, behaves very similar to the base alloy, except that the peak corrosion loss, at $\log PS_2/PO_2 \approx 18$, is considerably less, 200 μm [Figure 6.1].

Alloy C, containing 3.25% Ti, a weak oxide former, shows a somewhat different corrosion pattern [Figure 6.2]. For gases containing 0.8% H_2S there still is a maximum in the corrosion loss although it is broader and flatter. Water free gases have higher corrosion rates at high PS_2/PO_2 ratios and lower corrosion rates at low PS_2/PO_2 ratios, the exact opposite of alloy A. No maximum corrosion rate is observed in gases containing 0.2% H_2S ; here the corrosion loss remains at about 100 μm , when the $\log PS_2/PO_2$ ranges from 16.9 to 18.5 [Figures 5.6, 6.2].

In general it can be concluded that the correlation between the corrosion loss and purely thermodynamic parameters of the gas mixtures is relatively weak, especially for alloys, with a high corrosion rate. Kinetic factors caused by differences in partial pressure of H₂S and different forms of oxidants play a significant role in the corrosion process. This results in wide scatter in the data, when the corrosion loss is plotted against log PS₂/PO₂, especially for alloy C. However, when the H₂S partial pressure is constant and the PO₂ is controlled by the steam content of the gas a closer correlation is obtained.

In summary, the correlation of corrosion loss with PS₂/PO₂ ratio confirms the existence of a "kinetic boundary" for alloys containing strong oxide formers. This kinetic boundary is close to the Cr₂S₃/Cr₂O₃ phase boundary at 540°C, but does not correspond to a detectable protective oxide layer. The other alloys do not show a "kinetic boundary" in the range of gas mixtures studied, but generally show a maximum corrosion rate at a log PS₂/PO₂ of about 18. This disagrees with the corrosion model developed by John et al.⁵³, which postulates a monotonic increase of corrosion rate, with increasing PS₂/PO₂. In the following sections the available microstructural evidence will be examined to elucidate the anomalous behavior found in this study.

6.1.2 Scale Growth and Corrosion Mechanisms for Base Alloy A

Two corrosion morphologies can be identified for alloy A, roughly dependent on the PS₂/PO₂ ratio of the gas. The two morphologies are generally more distinct and easily recognizable when the PS₂/PO₂ ratio is manipulated by varying only one gas constituent, such as the steam content or H₂/H₂O ratio of the gas. The morphologies are labeled Type A and Type B corrosion here. Type A corrosion occurs in gases with a high PS₂/PO₂ ratio. Transition to the second corrosion regime occurs when the Log PS₂/PO₂ ranges from about 18.6-19.4. Type B corrosion occurs in gases with an intermediate to low PS₂/PO₂ ratio. Peak corrosion rates occur, when the Log PS₂/PO₂ is in the 17.5-18.4 range. At lower PS₂/PO₂ ratios the corrosion rate gradually decreases and becomes more variable, possibly signaling the transition to a regime in which protective scales are stable. However, under the test conditions used in this study, a continuous protective oxide scale was not formed.

Corrosion in gas compositions at the boundary of the two regimes is usually irregular and sometimes shows a distinct pitting type of attack. Apparently here two corrosion mechanisms are possible simultaneously, thus creating differences in local corrosion rates. Since the corrosion rate of the two regimes differs considerably, wide variations in penetration depth can occur both on the same specimen as well as between different corrosion tests with nominally the same PS₂/PO₂ ratio.

A. Corrosion in gases with high PS_2/PO_2 ratios (Type A)

Corrosion in this regime was extensively studied both as a function of time, 1.5-1350 hrs, and as a function of the oxygen and sulfur pressure of the gas. Corrosion kinetics at $\text{Log } PS_2/PO_2 = 19.7$ and 18.5 were shown previously in Figures 5.2 and 5.3. The available data do not support either strict linear or parabolic kinetics, although generally the corrosion rate decreases with time. The plots of recession rate as a function of \sqrt{t} suggest changes in K_p as a function of time, despite the absence of spallation. A detailed study of scale development during isothermal exposures ranging from 1.5-1224 hrs in gas 1 (0% H_2O , 0.8% H_2S), was presented in Section 5.3.2, is summarized here and correlated with information from tests in syngas with 0.2% H_2S .

The corrosion product formed in the first 1.5 hrs consists mostly of Ni, Fe sulfides with some oxygen present. It is very loose and is almost certainly formed by the reaction of H_2S in the gas with outward diffusing Ni and Fe. Below this outward growing scale a FeS scale is present, which also contains some chromium and nickel. After 15 hrs exposure an oxygen free 5-10 μm thick $FeCr_2S_4$ scale has formed on the alloy, below the Fe (Cr, Ni) sulfides. This is shown schematically in Figure 6.3A. It is concluded that corrosion initially consists mainly of sulfidation and that the scale is largely epitactical. After 600 hrs exposure a mixed oxide-sulfide topotactical scale has formed under the $FeCr_2S_4$ layer, which is generally sulfur rich near the scale/metal interface and oxygen rich near the epitactical scale. Crystallites of Cr_2O_3 are present in a sulfur rich matrix [Figure 5-10, Table 5.10]. Islands of partially converted alloy, generally iron rich, are occasionally present and become more prevalent, when the H_2S content of the gas is lowered to 0.2% H_2S [Figure 5.53, Table 5.43]. This is shown schematically in Figure 6.3B. After 1224-1350 hrs exposure, the scale near the alloy scale-interface remains sulfur rich, but contains more oxygen and numerous Cr_2O_3 precipitates. Lowering the H_2S content to 0.2% results in an irregular scale alloy interface, with oxygen rich scales in areas of deepest penetration.

The corrosion mechanism suggested by the microstructural evidence is as follows:

1. Formation of a two, possibly three layer epitactical scale, consisting of an outer layer of Fe, Ni sulfides, a middle layer of FeS containing some Cr and Ni and a bottom layer of dense, stoichiometric $FeCr_2S_4$.
2. Formation of a topotactical scale below the nonprotective $FeCr_2S_4$ layer by intergranular corrosion and oxide/sulfide precipitation. This leads to a granular sulfur rich scale containing "islands" of partially converted alloy and Cr_2O_3 precipitates. At lower H_2S partial pressure, local differences in oxygen or sulfur pressure can lead to differences in penetration depth. The deepest penetration occurs in oxygen rich areas.

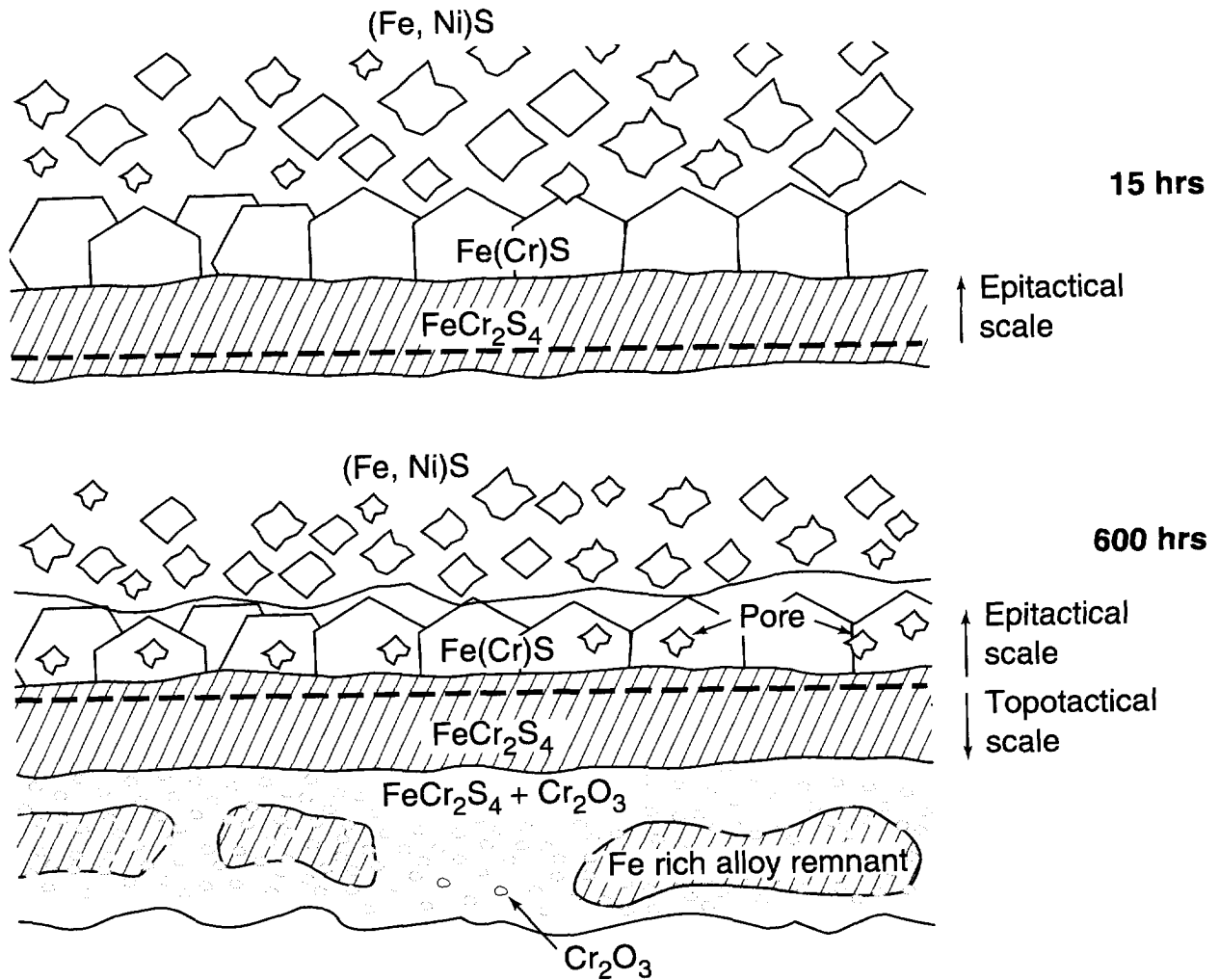


Figure 6.3
Schematic of Scale Development on Alloy A in Syngas With a High PS_2/PO_2 Ratio (Type A Corrosion)

The rate controlling step in the above corrosion mechanism is probably the diffusion of oxidants through the dense $FeCr_2S_4$ scale and corroded grain boundaries. Diffusion of oxidants into the alloy is quite irregular and frequently leads to significant metallic remnants, rich in iron. It would appear that the local corrosion rate is dependent both on local differences in diffusing gas species as well as differences in alloy composition resulting from selective oxidation or sulfidation. Thus it is not surprising that straight forward parabolic corrosion kinetics, defined by a single rate constant K_p do not apply, but that the corrosion rate constant varies with exposure time.

The scenario depicted above requires changes in the oxygen and sulfur pressure of the gas diffusing into the alloy surface. The composition of the alloy remnants indicates that they consist of Cr_2O_3 precipitates in a matrix of Fe, Cr and Ni, with minor amounts of S, Si and

Mn. For instance the metallic remnant from Table 5.43 contains approximately 50% Cr_2O_3 , 29% Fe, 12% Cr and 5% Ni. Thus the composition of the metal is 58% Fe, 24% Cr and 10% Ni. This would indicate that the local gas composition was located in the stability fields of Fe and Ni, close to the $\text{Cr}_2\text{O}_3/\text{Cr}$ boundary. Nearby, completely corroded areas have the following approximate composition: Cr_2O_3 54, Fe Cr_2S_4 35, Fe S 11. Thus here the gas composition is located in the FeS stability field close to the $\text{Cr}_2\text{S}_3/\text{Cr}_2\text{O}_3$ boundary i.e. fairly close to the original gas composition. Relative stability fields of the principal alloying elements are shown in Figure 6.4.

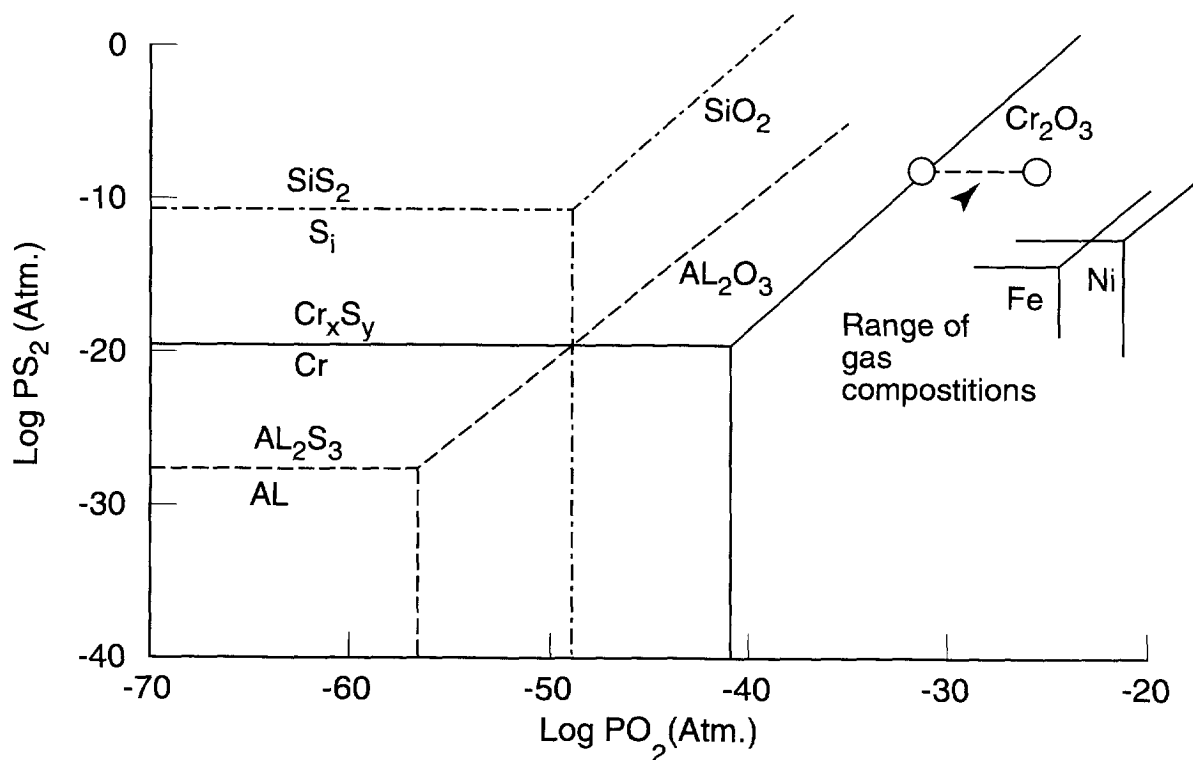


Figure 6.4
Schematic Phase Diagrams for AL, Si, Fe and Ni at 550°C

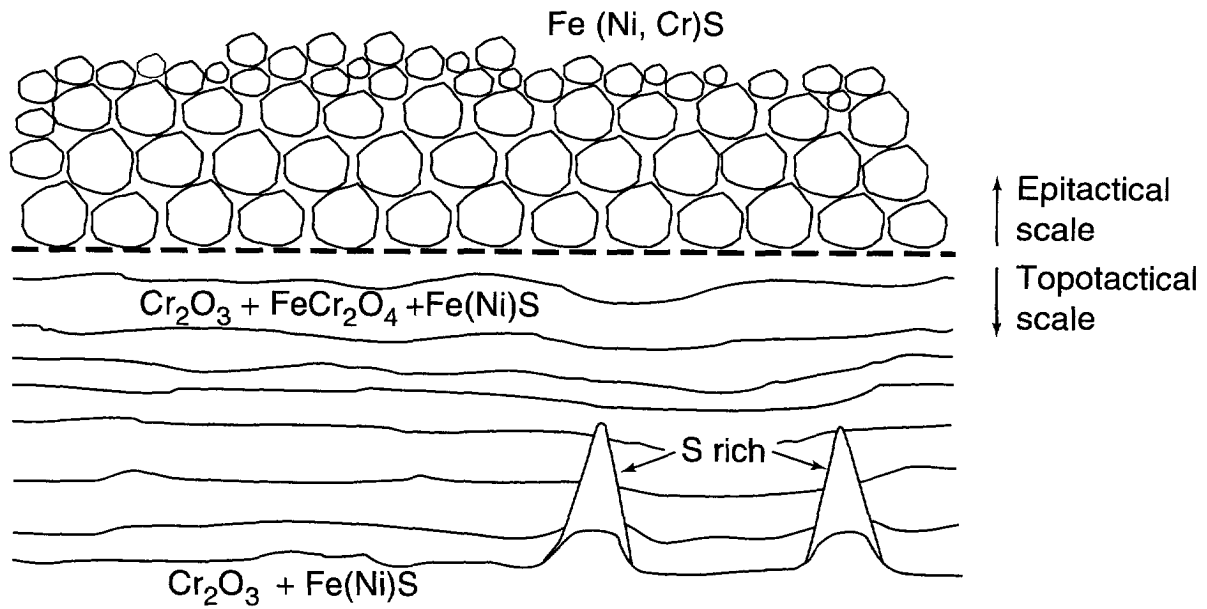
B. Corrosion at intermediate PS_2/PO_2 ratios (Type B)

Very high corrosion losses were experienced in gases with a $\text{Log PS}_2/\text{PO}_2$ of about 18, independent of the H_2S partial pressure of the gas. The epitactical scale here consisted mostly of iron sulfide, enriched in Ni at the outside and Cr on the inside. The Fe Cr_2S_4 layer is generally absent or very thin. The voluminous coarse grained topotactical scale is oxygen rich (35-45 at% O). The oxygen content generally increases away from the scale alloy interface [Table 5.26, Figures 5.29, 30]. The scale alloy interface is generally smooth. Where irregularities occur, the scale is rich in oxygen in the pits [Table 5.45, Figure 5-55]. The oxygen rich topotactical scale is already present after 15 hrs exposure as shown in Figure 5.24. Here the oxygen content of the scale was 26 at % and the sulfur content 22%,

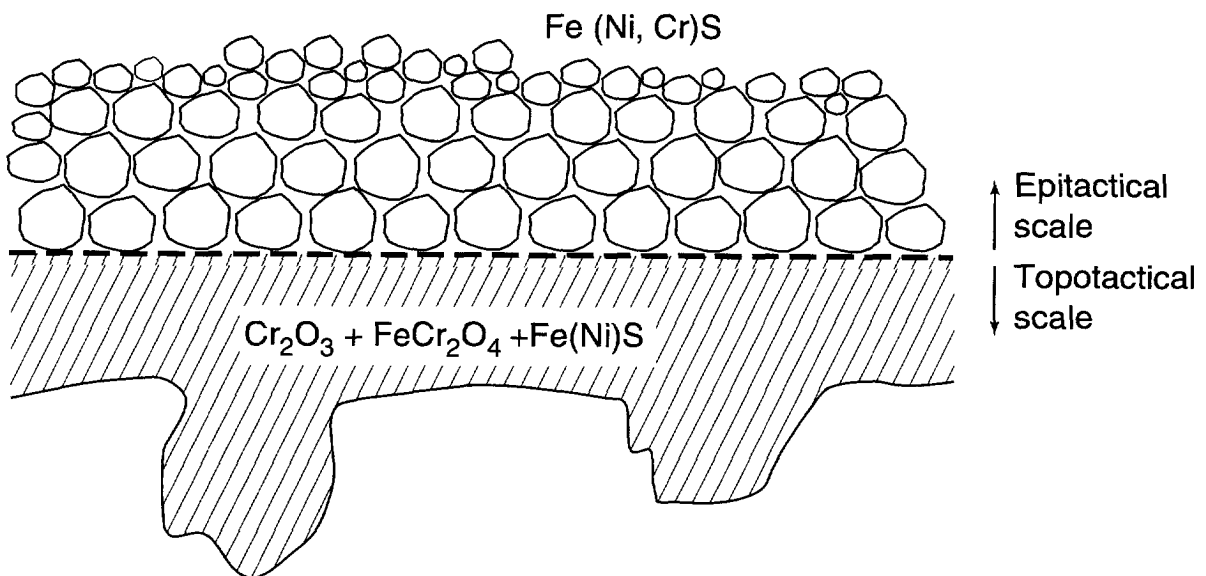
possibly indicating that the scale contained some metallics or substoichiometric sulfides or oxides. Further exposure does not greatly change scale composition or morphology, except for an increase in oxygen and decrease in sulfur near the scale surface. In general the sulfur content of the scale near the alloy surface is similar to or slightly higher than the Fe+Ni content indicating that the scale consists of a mixture of Cr_2O_3 (~75%) and Fe(Ni)S (~35%). Scale morphology and composition is schematically shown in Figure 6.5A. When the PS_2/PO_2 ratio of the syngas is further reduced, corrosion losses decrease gradually and the scale/alloy interface becomes irregular again, indicating a local tendency to form a more protective scale or healing layer [Figure 5.31, 5.56]. The composition of the scale becomes more homogeneous, as the difference in sulfur content between the top and bottom of the topotactical scale largely disappears. Typically the scale composition is (at %) O 46, S 7, Cr 28, Fe 15, Ni 3, the mineral composition calculated from the analysis is approximately: Fe(Ni)S 14, FeCr_2O_4 56, Cr_2O_3 30. Scale morphology and composition is schematically shown in Figure 6.5B.

The corrosion mechanism suggested by the microstructural evidence is as follows: Simultaneous formation of a porous epitactical scale consisting mainly of Fe and Ni sulfides, with some chromium at the base of the scale and a topotactical scale consisting mainly of Cr_2O_3 and FeS with only minor amounts of Ni, Mn and Si. Although the scale has a coarse granular texture, individual Cr_2O_3 and FeS grains cannot be detected in the scale, using a $(1 \mu\text{m})^2$ electron beam EDS system. The sulfur content of the scale is generally higher near the scale/alloy interface and also in the 15 hr exposure. This suggests simultaneous oxidation and minor sulfidation of Cr and sulfidation of Fe+Ni initially, followed by reoxidation of chromium sulfides. This sequence apparently produces a very porous scale which provides little resistance to further corrosion. At lower PS_2/PO_2 ratios the sulfur content of the scale decreases sufficiently to suggest the simultaneous formation of Cr_2O_3 , FeCr_2O_4 and FeS. This scale can become locally quite protective as shown by the irregular scale/alloy interface. However even at the lowest PS_2/PO_2 ratio corrosion losses are still significant, and may lead to unacceptably high corrosion rates, especially if corrosion kinetics are not parabolic.

An alternate explanation of the accelerated corrosion observed is that internal oxidation of Cr and precipitation of Cr_2O_3 in the alloy surface takes place, concurrently with sulfidation of outward diffusing Fe and Ni species, which form a non protective FeNiS scale. The volume fraction of the Cr_2O_3 precipitates in the alloy surface is not high enough to significantly reduce inward diffusion of oxygen or outward diffusion of Fe and Ni. The result is a porous, nonprotective but oxygen rich topotactical scale. At low PS_2/PO_2 ratios a protective Cr_2O_3 layer may form locally at the alloy/scale interface, while at high PS_2/PO_2 ratios chromium sulfides may also form.



(a) Intermediate PS_2/PO_2 Ratio (3% H_2O , 0.8% H_2S)



(b) Low PS_2/PO_2 Ratio (3% H_2O , 0.2% H_2S)

Figure 6.5
Schematic of Scale Development on Alloy A in Syngas With Intermediate to Low PS_2/PO_2 Ratio
(Type B Corrosion)

6.1.3 Effect of Minor Alloying Additions

A. Vanadium (alloy B)

Under most exposure conditions the addition of 3.25%V results in slightly lower corrosion losses, but no significant changes in corrosion mechanism: at high PS_2/PO_2 ratios type A corrosion occurs and corrosion losses are relatively low. Corrosion kinetics are close to being fully parabolic. At intermediate PS_2/PO_2 ratios type B corrosion occurs and corrosion losses are much higher, while at the lowest PS_2/PO_2 ratios the corrosion losses decrease again.

15 hr exposure in a gas causing type A corrosion indicates the formation of a vanadium rich sulfide layer, below a $FeCr_2S_4$ scale [Table 5.12, Figure 5.12]. This layer is an almost fully converted precipitation zone, consisting of $(Cr, V)_x S_y$ precipitates with probably some nickel and iron rich metallic remnants. A similar V rich layer is present after 1224 hrs exposure in the same gas, although it contains more metallic remnants here. This layer was apparently not protective as a fully converted topotactical scale was able to form below the V rich layer. In general the topotactical scale on alloy B is more inhomogeneous than that on the base alloy A and also contains more metallic remnants especially close to the alloy/scale interface. It is therefore likely that the precipitation of vanadium sulfides in the alloy surface somewhat reduces the diffusion of corrosive species into the alloy, thus lowering the corrosion rate.

At intermediate PS_2/PO_2 ratios rapid type B corrosion occurs. Corrosion losses are significantly lower than that of the base alloy. A 15 hr exposure indicates that the topotactical scale initially contains considerably more sulfur than that of the base alloy especially near the scale metal interface. Here the scale consists mainly of Cr (V) sulfides with only minor amounts of Cr_2O_3 and FeNiS [Figure 5.25, Table 5.22]. After 600 hrs exposure in the same gas the oxygen content of the topotactical scale varies from 30-50%. Areas of high (17 at %) to low (6 at %) sulfur are randomly distributed. Areas with a high oxygen content are associated with the deepest scale penetration into the alloy. It appears that the Cr, V sulfides initially precipitated in the alloy have been reoxidized upon further exposure and are relatively ineffective in slowing down the corrosion rate when the PS_2/PO_2 ratio of the gas decreases.

A special feature of the scale on alloy B is its irregular alloy/scale interface. This is especially prominent after exposure to a gas 2, containing 1% H_2O . Here the principal corrosive attack is in the form of deep pits [Figure 5.32, 33]. The scale in the pits has a composition typical of type B corrosion, while the scale above protected areas has a higher sulfur content, similar to that of type A corrosion. It is concluded that both corrosion mechanisms occur simultaneously here.

In summary it can be concluded that vanadium additions, most likely result in (Cr,V)S precipitates near the alloy surface. These are beneficial in retarding the growth of the topotactical scale. This effect is most pronounced in gases with high PS_2/PO_2 ratios, causing type A corrosion.

B. Titanium (alloy C)

At very low PS_2/PO_2 ratios alloy C exhibits classic type A corrosion, forming a topotactical sulfur rich scale with frequent metallic remnants [Figure 5.49, Table 5.39]. However the transition to type B corrosion occurs here at higher PS_2/PO_2 ratios. In gases with a log PS_2/PO_2 of 19.7 type A scales are formed in some exposures, type B scales in other exposures in the same nominal gas composition. Short term exposures in the above gas show the formation of a Ti free, presumably epitactical, $FeCr_2S_4$ scale, containing 6% O, above a precipitation zone or subscale containing Ti, Cr and Fe sulfides and probably metallic nickel. These precipitates are apparently effective in reducing the corrosion rate in the 150 and 1224 hr exposures, where high sulfur, partially converted type A topotactical scales are formed. In contrast an oxygen rich, fine grained type B scale is formed during the 600 hr exposure. Here the corrosive attack is in the form of very broad pits.

When the Log PS_2/PO_2 ratio is lowered to 18.5 by lowering the H_2S content in the gas, only type B corrosion occurs, again in the form of very large pits. This form of corrosion is especially well developed after the 1350 hrs exposure [Table 5.50, Figure 5.61]. This figure also shows clearly that corrosion rates are lower in areas where the sulfur content of the scale is higher, i.e. when local conditions are more sulfidizing. In such areas the underlying alloy is enriched in Ni and depleted in Cr and Fe, while no depletion occurs under fast growing oxygen rich scales. Other exposures, for instance Figure 5.62, Table 5.51 show that the oxide rich pits are covered with a thin titanium and sulfur rich layer, which probably represents the original alloy surface containing sulfide precipitates.

When the Log PS_2/PO_2 is lowered to about 18 the pitting attack changes to general corrosion. Corrosion losses increase in gases containing 0.8% H_2S , resulting in a maximum corrosion loss at Log $PS_2/PO_2=18$, which is typical for type B corrosion. However the maximum is less pronounced here, and is not present in gases containing 0.2% H_2S . Here the corrosion loss after 600 hrs remains relatively high at about 100 μm , when the Log PS_2/PO_2 varies from 18.5 to 16.9.

In gases with a Log PS_2/PO_2 of 16.7 the corrosion loss drops to 20-40 μm , suggesting the formation of a more protective oxide or healing layer. The scale contains again a considerable amount of $FeCr_2O_4$. The lowest corrosion rate is obtained in a dry gas with a high CO_2 content. Here a thin subscale with a high Cr_2O_3 content is present (~15% TiO_2 , 70% Cr_2O_3) [see Table 5.42, Figure 5.52]. This suggests the presence of a healing oxide layer at the scale/metal interface.

In summary it is concluded that titanium additions accelerate the formation of an oxide rich scale, but at the same time reduce the magnitude of the rapid oxidation attack at intermediate PS_2/PO_2 ratios, presumably through the precipitation of TiO_2 , which may accelerate the formation of Cr_2O_3 .

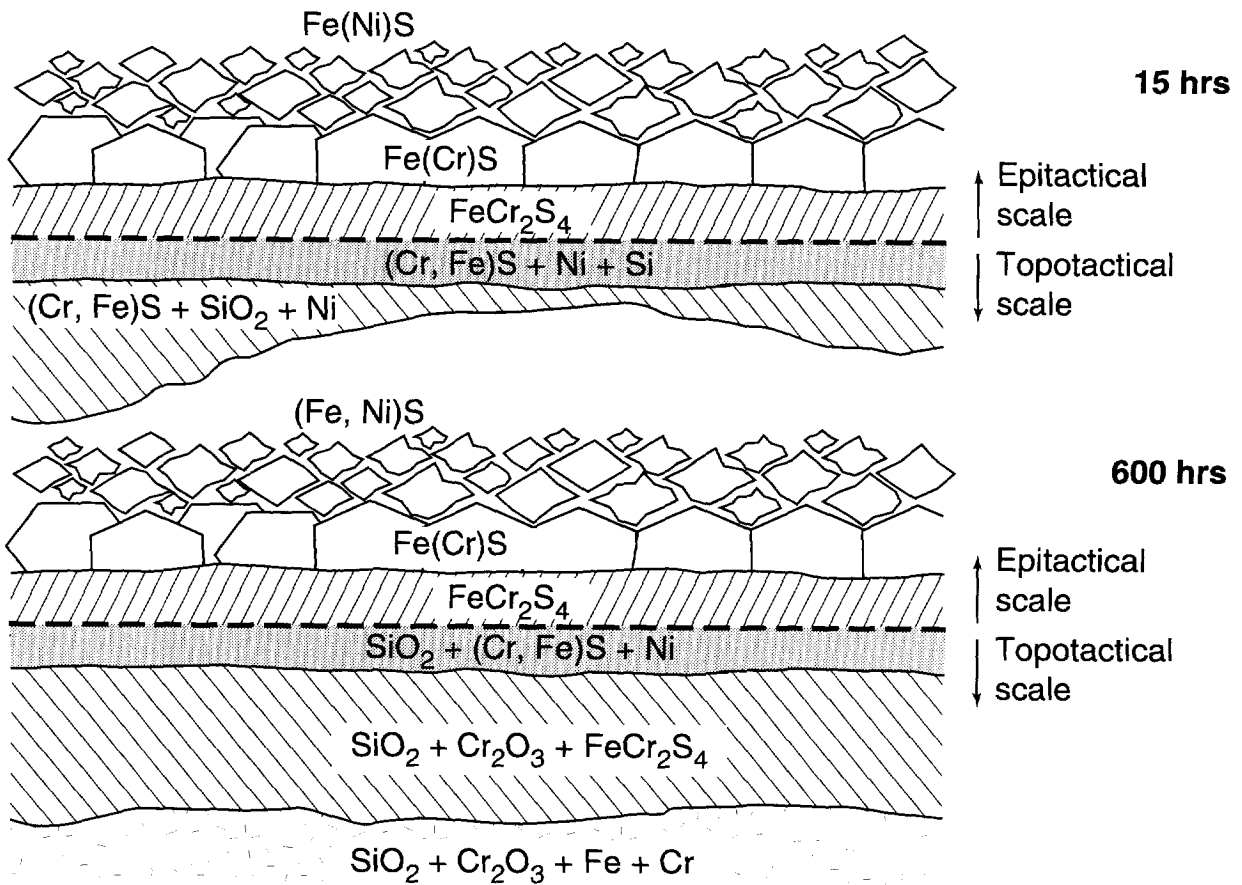
C. Silicon and Aluminum (alloys D and E), type C Corrosion

Aluminum and silicon additions will be considered together, as these strong oxide formers have the same effect on the corrosion mechanism. At high PS_2/PO_2 ratios (>18.5), both alloys exhibit type A corrosion, although corrosion losses, especially that of the Si containing alloy are lower than those of the base alloy [Figure 6.6A]. Short term exposures (15 hrs) indicate the presence of an alloy layer enriched in nickel and silicon containing mainly sulfide precipitates [Table 5.17, Figures 5.19-20]. Most of the silicon must be present as metal as silicon is more stable than SiS_2 under highly reducing conditions [Figure 6.4]. Below this layer, which has partially spalled, a mixed oxide-sulfide topotactical scale has formed, containing metallic remnants. The epitactical scale consists again of a relatively thin $FeCr_2S_4$ layer with a thick (Fe, Ni) sulfide outer layer. The 600 hr exposure in the same gas shows a relatively oxide rich topotactical scale, only partially converted near the alloy scale interface. A thin silicon and nickel rich layer, now fully oxidized and sulfidized, is still present [Table 5.19, Figure 5.21].

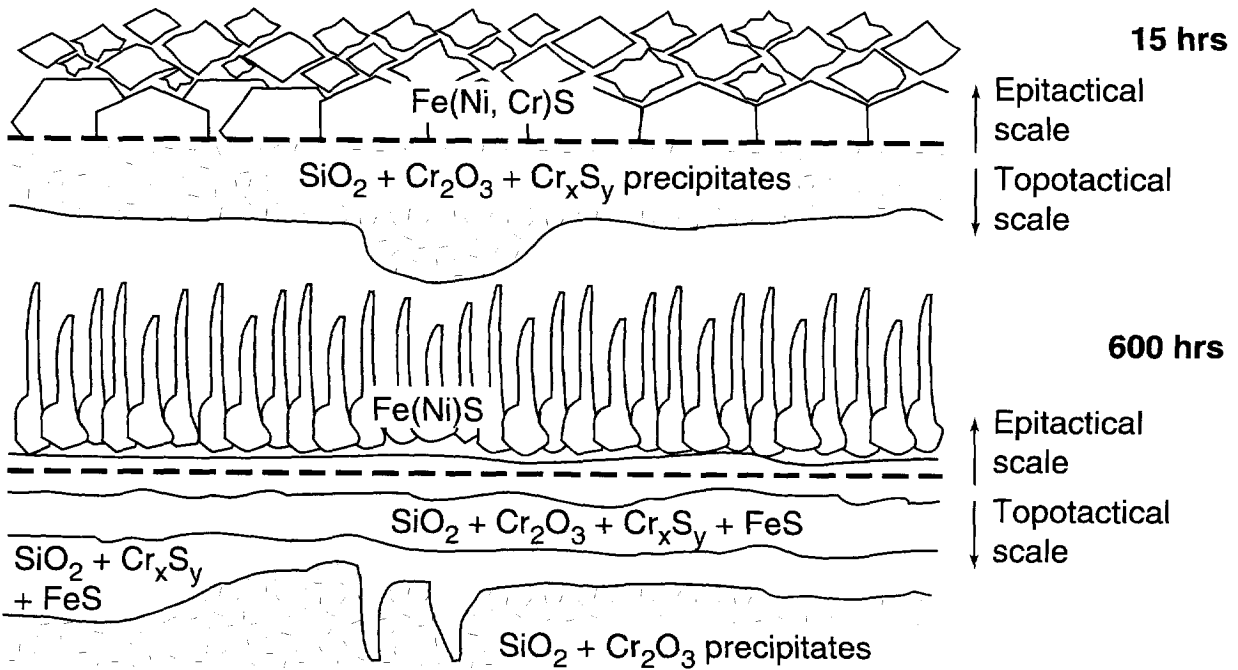
Increasing the PS_2/PO_2 ratio does not lead to type B corrosion. Instead, a new corrosion regime, designated type C, starts in gases with a $\text{Log } PS_2/PO_2$ of 18.5 or lower. This is schematically shown in Figure 6.6B. Short term exposure indicates the precipitation of SiO_2 , Cr_2O_3 and Cr sulfides in the outer layers of the alloy (~21% SiO_2 , 15% Cr_2O_3 and 28% Cr_3S_4) [Table 5.29, Figure 5-27]. Apparently these precipitates suffice to block inward diffusion of the corrosive species. After 600 hrs the corrosion loss of the alloy is only 3 μm , an order of magnitude less than at higher PS_2/PO_2 ratios. Scale analysis shows that the topotactical scale has an oxide rich top layer with small sulfur rich pits underneath. Both areas contain about 30 at % SiO_2 . No evidence of a protective SiO_2 layer was detected by E.D.S. Even Auger spectroscopy line scans (with a beam width of 50 nm) across the scale alloy interface were not able to detect a coherent, SiO_2 rich oxide scale. However the silicon, and chromium-oxide content remained high in the first 2 microns of the alloy indicating SiO_2 and Cr_2O_3 precipitation here [Table 5.33, Figures 5.40-41]. This suggests internal oxidation of Si and Cr.

Decreasing the $\text{Log } PS_2/O_2$ to 16.7 did not change scale thickness or composition. A careful E.D.S. analysis of the alloy surface layers indicated a precipitation zone containing about 20-30% SiO_2 and an equal amount of Cr_2O_3 [Table 5.34, 35, Figures 5.42, 43].

Examination of alloy E containing Al confirmed the corrosion mechanism described above. Negligible corrosion rates occurred over the same range of oxygen and sulfur partial pressures, in the presence of about 25% Al_2O_3 precipitates in the alloy surface.



(a) Type A Corrosion



(b) Type C Corrosion

Figure 6.6
Schematic of Scale Development on Alloy D

In summary Al and Si additions to the base alloy result in completely protective corrosion kinetics when the $\log P_{S_2}/P_{O_2}$ is 18.5 or less. The available microscopic evidence indicates that the resulting low corrosion rates are due to the precipitation of Al_2O_3 or SiO_2 in the alloy surface [Figure 6.6]. These precipitates together with Cr_2O_3 precipitates completely block the diffusion of corrosive species in the alloy and largely prevent the outward diffusion of Fe and Ni, as the epitactical scales on Al and Si containing alloys are considerably thinner than on the base alloy.

6.1.4 Corrosion Kinetics

In sections 6.1.2 and 6.1.3 three broad corrosion regimes have been identified, which can serve to classify the wide variety of microstructures found after exposure in non equilibrium gas compositions with a wide range of oxygen and sulfur partial pressures as well as different oxidant species. Here we will discuss the corrosion kinetics associated with each corrosion mechanism.

The limited corrosion rate data in this study have been obtained in dry syngas with a $\log P_{S_2}/P_{O_2}$ of 19.7 and 18.5 respectively. Under these conditions most alloys experienced type A corrosion, characterized by a somewhat protective $FeCr_2S_4$ epitactical subscale and a mixed oxide/sulfide topotactical scale frequently containing alloy remnants. The data presented in Section 5.1 indicate that the corrosion rates are quite variable and vary from nearly linear to subparabolic. Comparison of the scale composition and microstructure with the corrosion rate data indicates that the corrosion rate generally declines when the type A corrosion mechanism becomes more pronounced, i.e., when the $FeCr_2S_4$ layer is well developed and the topotactical scale is sulfur rich. Under such conditions corrosion kinetics are subparabolic, as exhibited by alloy B in gas 1A (0.2% H_2) and alloy C in gas 1 (0.8% H_2S).

The corrosion kinetics of alloys with a more oxide rich scale become sublinear, which considerably increases the predicted annual corrosion rate. Alloy C in gas 1A exhibits type B corrosion, be it in the form of large pits. Not surprisingly its corrosion kinetics are close to linear and actual and predicted corrosion rates are the highest of all alloys tested (>0.7 mm/yr). Since type B corrosion losses of most alloys after 600 hrs exposure in water containing gases are considerably higher, it can be safely assumed that they will also have unacceptably high corrosion rates. Similar to low alloy steels they will probably also exhibit pseudo linear corrosion behavior as described by Perkins⁵¹. It is therefore concluded that such alloys are not suitable for service under conditions where type B corrosion is possible.

Corrosion rate studies of alloys D and E under conditions where type C corrosion occurs have not been carried out. However corrosion losses after 600 hrs are about an order of magnitude less than those of alloys experiencing type A corrosion. These alloys were shown to have parabolic corrosion kinetics, resulting low annual corrosion rates. It is

therefore safe to assume that Si or Al containing alloys will also exhibit protective corrosion kinetics. A commercial alloy containing silicon exposed for 1224 hrs under conditions where type C corrosion occurred showed a negligible increase in corrosion loss between 150 and 1224 hrs exposure⁵⁴.

The conditions under which type A and type B corrosion occur are not clearly defined, as they depend not only on the PS_2/PO_2 ratio in the gas but also on the type of oxidant present. For instance gas 1A and gas 3 have the same $\log PS_2/PO_2$ (18.5). However alloy A suffers from type A corrosion in gas 1A and from type B corrosion in gas 3. The resulting difference in corrosion loss is 97 μm . The difference in corrosion loss of alloy B is even more pronounced: 162 μm . Alloy C on the other hand exhibits type B corrosion in both gases, which explains the relatively small difference in corrosion loss (40 μm). Differences between wet and dry gases with a lower PS_2/PO_2 ratio are less pronounced, because no shift in corrosion mechanism is involved. Corrosion of alloys A and B is considerably higher in a water free syngas (8) than in a wet syngas (7) with the same PS_2/PO_2 ratio. In case of alloy A the difference is 68 μm , while alloy B shows a difference of 55 μm in corrosion loss after 600 hrs exposure. Thus corrosion rates are dependent on the type of oxidant present as well as the oxygen and sulfur pressures of the resulting gases. In extreme cases this can give rise to a shift in corrosion regime and result in vastly different corrosion rates.

Gas compositions with PS_2/PO_2 ratios on the boundary between two corrosion regimes can give rise to erratic corrosion behavior. In most cases the result is an irregular alloy/scale boundary, where small local differences in gas composition produce large differences in corrosion rate. In extreme cases pronounced pitting can occur. A good example is alloy B after exposure to gas 2, Figure 5-32. Most alloys exposed in gas 3A show a similar behavior. In one case, alloy C in gas 1, specimens exposed to the same gas can exhibit either type A or type B corrosion. Here the specimens exposed for 150 and 1224 hrs show classic type A behavior i.e. they form sulfur rich topotactical scales with an abundance of metallic remnants. However the specimen exposed for 600 hrs shows type B corrosion, with large broad pits filled with an oxide rich scale. This explains why the corrosion loss after 600 hrs is higher than that after 1224 hrs (80 μm vs. 72 μm).

A similar behavior as that of alloy C in gas A has been described by Perez and Larpin⁵⁵ for the sulfidation of Fe-Mn alloys in sulfur vapor. High linear corrosion rates are experienced when a porous (Fe, Mn) sulfide is formed, while much lower parabolic corrosion rates prevail when a compact duplex scale of Mn (Fe) S (inner) and Fe (Mn) S (outer) is formed. The chaotic character of the corrosion rate is temperature dependent here: below 973 K slow parabolic corrosion kinetics occur, while above 1023 K only fast, linear corrosion rates were found. It would appear that the regime in which unstable chaotic corrosion can occur is more limited in our study. However, the relatively wide spread occurrence of pitting type corrosion, suggests that the possibility of unpredictable corrosion behavior certainly exists in the system studied.

6.2 COMPARISON WITH PREVIOUS WORK

6.2.1 Laboratory Studies

Before comparing the data gathered in this study with other recent studies on mixed oxidant corrosion it is useful to briefly summarize data on the widely studied commercial alloys Incoloy 800 and SS 310 obtained under the same conditions by the present author and published elsewhere^{54, 56}. Figure 6.7 shows corrosion losses of both alloys as a function of the water content of syngas with a fixed, 0.8% H₂S content. It is clear that Incoloy 800 behaves similar to alloy A, as expected from its composition. However the maximum corrosion in the "type B" region is considerably less than that of alloy A. The small additions of Al and Ti to Incoloy 800 apparently reduce the rate of accelerated oxidation, but do not suppress it. SEM analysis shows that the topotactical scale indeed consists mainly of chromium oxide with lesser amounts of FeS. SS 310 does not show accelerated corrosion in syngas with 1-10% H₂O. Its behavior is similar to the alloys D and E containing Si or Al, except that fully protective scales not form until the water content of the gas is increased to about 15%. SEM analyses presented in Figure 6.8, indicate that SS 310 still shows type A corrosion i.e. it forms a sulfide/oxide topotactical scale with metallic remnants, in gas 4, containing 3% H₂O i.e. where maximum type B corrosion occurs in alloys with 20% chromium. In syngas 7, containing 15% H₂O, the

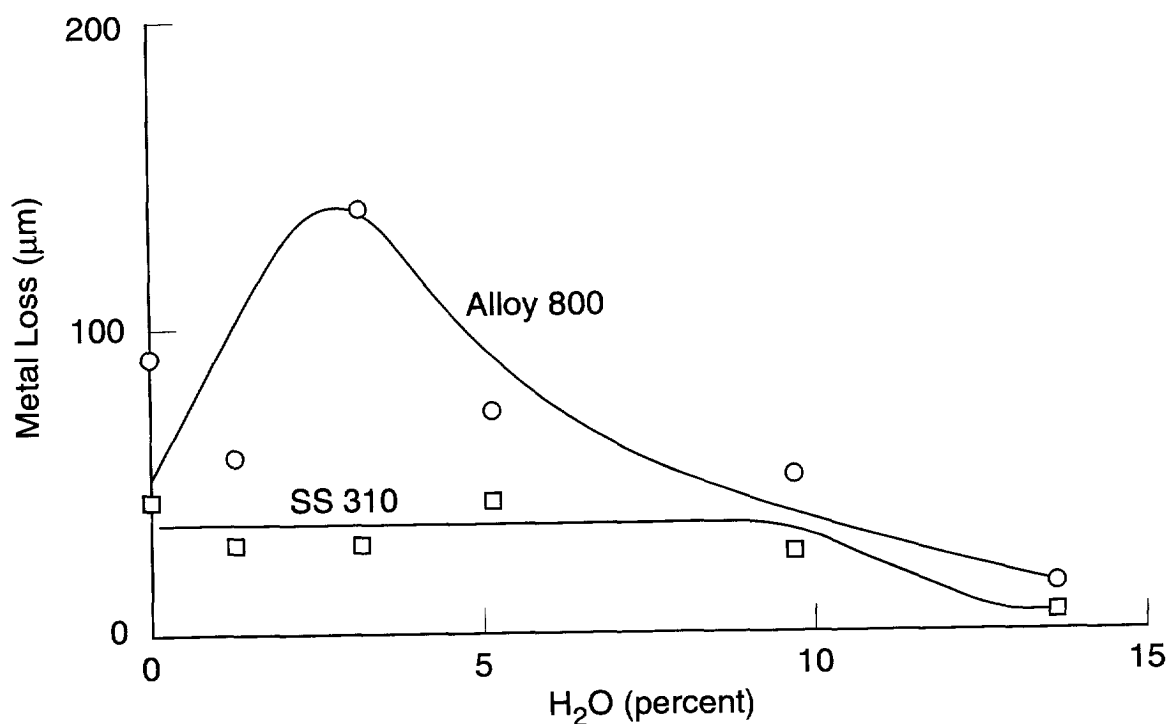
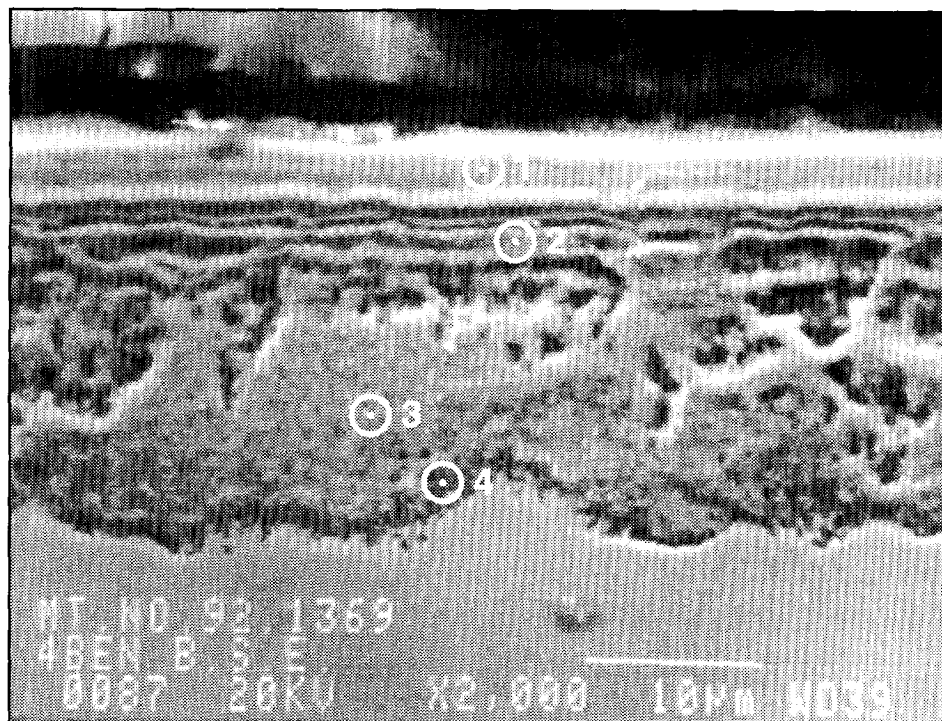


Figure 6.7
Corrosion Loss of Alloy 800 and SS310 as a Function of Water Content in Syngas, 600 hrs, 540°C



E.D.S. Analysis (at %)

Area	O	Si	S	Cr	Mn	Fe	Ni
1	19	4	35	31	2	9	<1
2	20	2	33	34	2	8	<.5
3	22	2	2	27	2	43	1
4	29	2	7	27	2	23	<.5

Figure 6.8

BSE Image and E.D.S. Analyses of Scales on SS310, 600 hr Exposure, Gas 4, 540°C

corrosion loss of SS 310 becomes very small and only a very thin topotactical scale is formed. Again a protective oxide rich scale was not present. It is suspected that dense oxide precipitates are responsible for the protective scaling behavior. Corrosion rate data presented in Figure 6.9, indicate that the scaling behavior of SS 310 in water free gas 1 follows parabolic corrosion kinetics with a K_p of $1.4 (\mu\text{m})^2/\text{hr}$, which would result in a commercially acceptable corrosion rate of about 0.1 mm/yr. The corrosion kinetics of Incoloy 800 on the other hand are not completely parabolic and will probably result in unacceptably high corrosion rates even under the type A corrosion conditions of water free gas 1A.

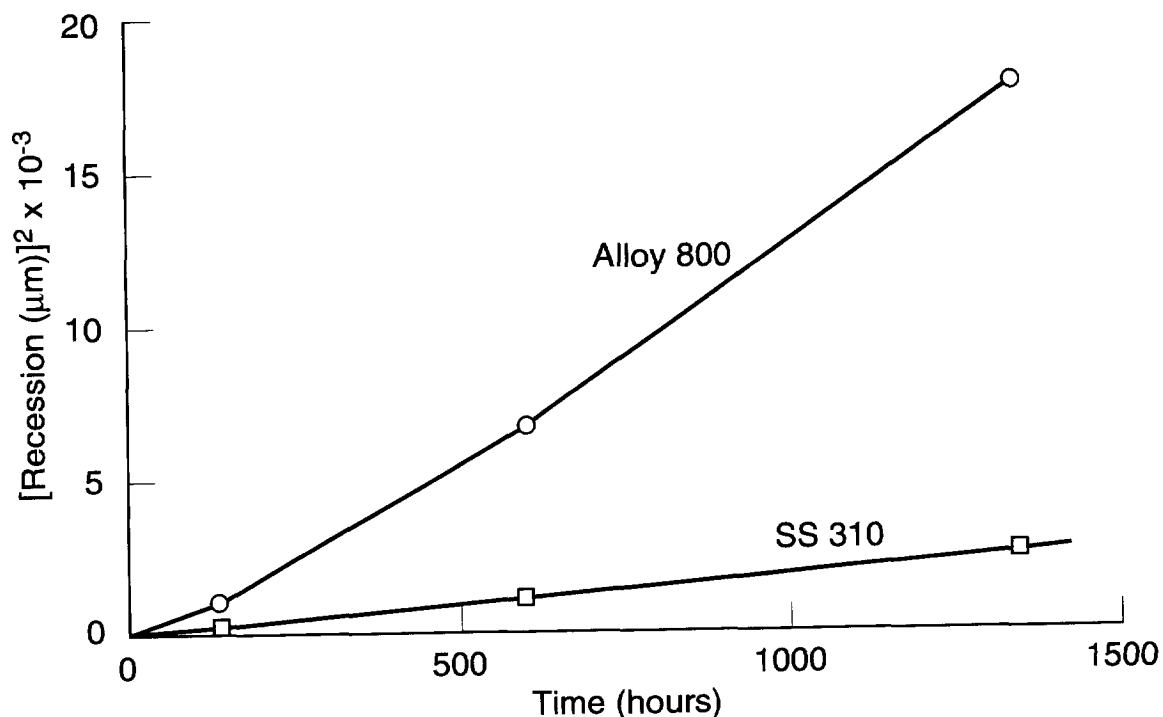


Figure 6.9
Isothermal Corrosion Loss of SS310 and Alloy 800 in Syngas 1A (0% H₂O, 0.2% H₂S)

The "type A" corrosion mechanism has been recognized by many previous authors. Since most studies were done at temperatures above 700°C, type A corrosion has generally been described as "catastrophic" sulfidation^{27,51}. This term is probably correct at higher temperatures, above the eutectic melting temperature of Fe and Ni sulfides. However temperatures of greatest commercial interest ($\leq 600^\circ\text{C}$) are well below the melting point of any sulfide mixtures. Sulfidation rate constants also decrease exponentially with temperature. It is therefore possible that sulfidation rates are sufficiently slow to provide acceptable corrosion losses. Data published by Natesan⁵⁸ indicate that the parabolic rate constant for sulfidation of chromium at 500-600°C is about the same as its oxidation rate constant at 1100°C. Chromium containing austenitic stainless steels generally form protective oxide scales at 1000-1100°C, although alloys forming alumina or silica are generally preferred at temperatures over 1000°C because of the volatility of chromium oxide above 1000°C.

Work carried out recently by Norton and Levi⁵⁹ confirms the proposition that protective parabolic corrosion kinetics are possible under highly sulfidizing conditions. Tests were carried out in a non equilibrium dry syngas, containing 0.2% H₂S, similar to gas 1A in this study, except for the 400 ppm HCl addition. The study was limited to alloys containing at least 25% Cr. Corrosion losses were generally lower at 600°C than found in our study at 540°C. Corrosion losses for all alloys increased slowly with time after an initial rapid increase in the first 150 hrs. Corrosion kinetics were subparabolic. In a parallel study⁶⁰ a

609 hr exposure at 600°C, using gas 1A (with 400 ppmv HCl), was therefore carried out in our laboratory. Comparative results for a few alloys are shown in Table 6.1. They clearly demonstrate that the corrosion losses in our study are significantly higher. Microscopic analysis indicates the presence of a thicker and more completely converted topotactical scale on alloys exposed in our study. In the study of Norton and Levi the topotactical scale is less well developed and consists mainly of intergranular corrosion and sulfide precipitates. Figure 6.10 shows the difference for alloy 310. It is unlikely that small differences in experimental conditions between the two laboratories are responsible for the large difference in corrosion behavior observed. It is more plausible that the addition of 400 ppm HCl in our test is responsible for the observed differences in corrosion loss and scale development. Evidence that HCl additions may indeed play a significant role will be presented later, when discussing type B corrosion.

Table 6.1
Corrosion Losses (μm) in Dry Syngas 1A, With and Without 400 ppmv HCl

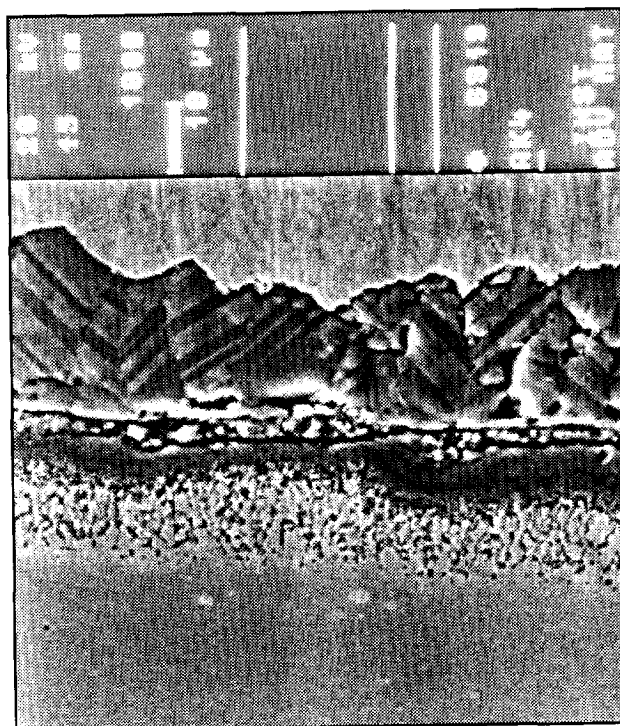
Alloy	Hours Exposure				
	600°C			540°C	
	500*	1000*	609**	600**	1350**
20Cr-35Ni (Alloy A)	–	–	214	80	134
SS 310/HR3c	20	20	46	34	46
27Cr-36Ni-3V	16	17	67	40	38
20Cr-35Ni-3V (Alloy B)	–	–	166	40	49

* From ref. 59. no HCl in gas

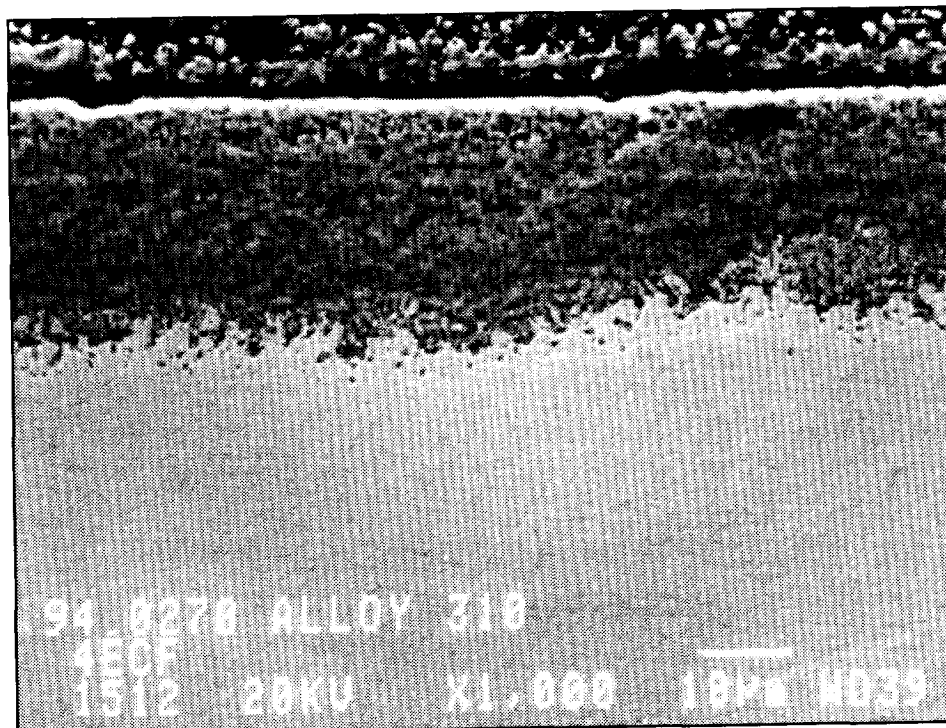
** This study, 400 ppmv HCl

Low temperature corrosion studies in dry non equilibrium syngas containing both H_2S and HCl similar to those used in this study have also been reported by R. John et al.⁵³. Unfortunately the study only gives detailed data on high nickel alloys, such as alloy 625 (21% Cr). A rough extrapolation from the graphical data presented indicates a corrosion loss of 80-200 μm after 600 hrs exposure at 500-600°C, which is in reasonable good agreement with type A corrosion losses found for alloy A in this study at 540°C (66-80 μm), especially considering the large differences in alloy composition. Unfortunately no microstructural information was given.

In summary it can be concluded that recent publications confirm that relatively low corrosion rates are possible under highly sulfidizing conditions, where the corrosion products consist mainly of sulfides, with smaller amounts of oxides mainly in the topotactical scale.



(a) No HCL (From Ref. 58)



(b) 400 ppmv HCL (This Study)

Figure 6.10
Scale on Alloy 310 After Exposure to Syngas 1A With and Without 400 ppmv HCL

To our knowledge, type B corrosion has not been observed previously. As discussed in the introduction most authors describe mixed oxidant corrosion in terms of a kinetic boundary, separating "protective" oxidation from "catastrophic" sulfidation. Some of the alloys tested in this study also show this behavior, but most alloys show rapid unstable oxidation at intermediate PS_2/PO_2 ratios, which we have labeled type B corrosion.

A study by Löbnig and Grabke⁶¹ indicates an increase in corrosion rate with increasing H_2O partial pressure of the gas. However this occurs only in the initial, transient stage of corrosion. Here the corrosion rate is linear and depends on the rate of gas transport to the metal surface. The increase in corrosion rate is attributed to the formation of fast diffusion paths at the grain boundaries between oxides and sulfides. After 120 minutes exposure, diffusion controlled parabolic corrosion kinetics become predominant and the effect of H_2O pressure disappears. It is unlikely that this transient effect of H_2O pressure, observed by Löbnig, is applicable to type B corrosion. R. John, et al.⁵³ also carried out corrosion tests in a non equilibrium syngas containing 2% H_2O , in which 20% Cr alloys may be expected to exhibit rapid type B corrosion. Unfortunately again no microstructural data are provided and corrosion loss data are presented only as annual corrosion losses, assuming parabolic corrosion kinetics. For alloy 625 an annual loss of about 0.4 mm/yr at 550°C is indicated. This is about the same as that for alloy A in a dry syngas undergoing type A corrosion [Table 5.3] and might indicate that accelerated corrosion did not occur. It is perhaps significant that the gas containing 2% H_2O did not contain HCl.

To further clarify type B corrosion a 600 hr corrosion test was carried out in gas 4, containing 3% H_2O , without HCl in a separate study⁶⁰. Some results are given in Table 6.2, which shows a significant decrease in corrosion loss in the HCl free gas for all the alloys exhibiting type B corrosion. However the corrosion loss of SS 310 which experiences type A corrosion was not affected. Limited SEM analyses indicated that alloy A still had an oxide rich type B scale, although more fine grained and dense in appearance (similar to that on alloy C). The scale on alloy B on the other hand was mixed. Some areas have sulfide rich scales containing metallic remnants (type A corrosion), other areas were richer in oxide and showed higher corrosion losses, resulting in pitted appearance. Thus small amounts of HCl in the syngas may promote the occurrence and increase the rate of type B corrosion. Therefore an effort was made to determine the presence of chlorine in scales on alloys exposed to HCl containing gases. Not even small amounts of chlorine were detected, either on surface scales before mounting or after preparation of a polished section, using non aqueous polishing liquids. This lack of chlorides is probably due to the high vapor pressures of chlorides, especially $FeCl_2$, which may have resulted in complete removal of HCl from the scale. This behavior is similar to the role of HCl in high temperature oxidation. Various studies^{62, 63, 64} have shown that the formation of volatile chlorides may lead to scale cracking and accelerated corrosion. Intergranular corrosion below the oxide scale is also frequently observed. In extreme cases catastrophic oxidation may occur⁶⁵. Iron base alloys are generally more affected than Ni or Co based alloys due to the higher vapor pressure of iron chlorides. In most cases chlorides are not found in

the corrosion products, but sometimes condense elsewhere in cooler parts of the furnace. The very porous, powdery nature of the epitactical (Fe, Ni) S scales found in this study may well be the result of outward diffusing chlorides, which are converted to sulfides at the scale/gas interface.

Table 6.2

Corrosion Losses in Wet Syngas 4, With and Without 400 ppmv HCl
3% H₂O, 0.8% H₂S, 600 hrs, 540°C

Alloy	No HCl	400 ppm HCl
20Cr-35Ni (Alloy A)	175	343
20Cr-35Ni-3V (Alloy B)	80	200
Incoloy 800	50	141
SS 310	30	30

The preliminary data on the effect of HCl on corrosion loss, together with the effect of chlorides on the oxidation rate of steels, indicate that the presence of HCl in the syngas plays a major role in the type B corrosion mechanism. A possible corrosion sequence is as follows. 1) An epitactical Fe (Ni, Cr) sulfide scale is formed on the alloy, due to reaction of H₂S with outward diffusing Fe, Ni and Cr ions. This reduces the sulfur pressure of incoming gas, but does not block the inward diffusion of oxide and chloride species. 2) Below the epitactical scale Cr₂O₃ is precipitated in the alloy surface, but iron and Ni are neither oxidized nor sulfidized in the local environment. This allows the formation of FeCl₂ and possibly NiCl₂ which will subsequently evaporate, diffuse away from the alloy through the porous epitactical scale and react with H₂S in the flowing syngas to form a powdery deposit of (Fe, Ni) sulfide. The remaining topotactical scale consists mainly of unconsolidated Cr₂O₃ precipitates with minor FeS. This scale is highly porous, allowing rapid attack of the underlying alloy by HCl and oxidants such as H₂O and CO₂. The corrosion mechanism proposed above is in principle similar to that proposed earlier in which the outward diffusion of Fe and Ni cations was driven by concentration gradients caused by the formation of a (Fe, Ni) S only. The presence of HCl accelerates removal of Fe and Ni and thus increases the corrosion rate.

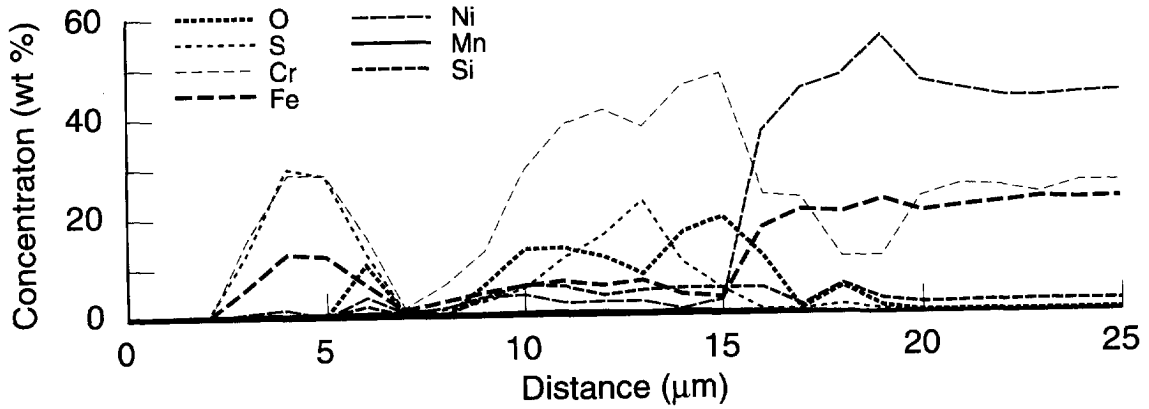
Type C corrosion will occur when the type B corrosion mechanism is prevented by the formation of an impervious layer which will block the diffusion of chloride species into the alloy. This occurs when strong oxide formers are added to the base alloy. Here a large number of submicroscopic SiO₂ or Al₂O₃ particles are precipitated in the alloy surface. The SiO₂ and Al₂O₃ precipitates probably also serve as nuclei for Cr₂O₃ precipitates. The resulting surface layer effectively blocks the diffusion of corrosive species into the alloy thus greatly reducing the corrosion loss. It also largely blocks the outward diffusion of Fe and Ni ions. The net effect is similar to the formation of a continuous protective oxide scale. It can be argued that a continuous very thin oxide scale indeed exists, but is too thin

to detect. If this is true the protective scale would have to be less than 50 nm thick. All the data gathered in this study support the existence of a dense precipitation zone as the main barrier to rapid corrosion, probably about 2-3 microns thick, containing 20-30 at % each of SiO_2 or Al_2O_3 and Cr_2O_3 .

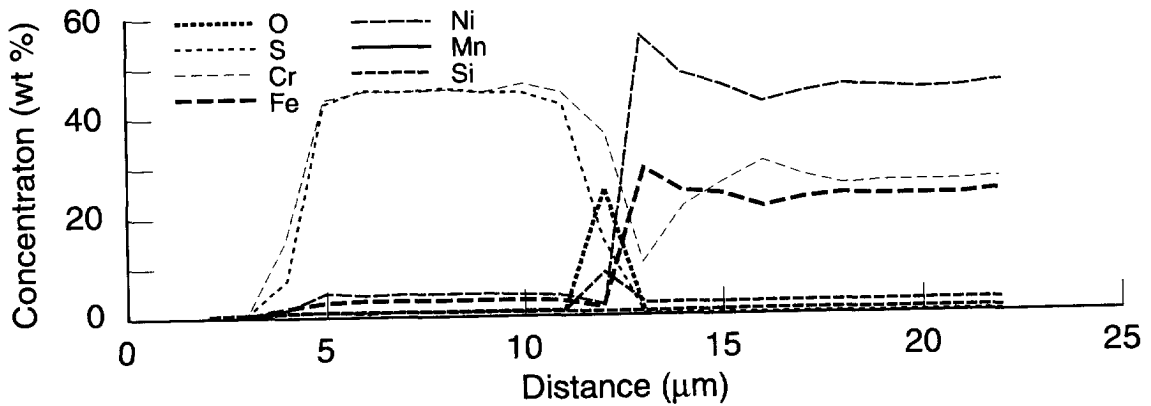
There is evidence in the literature that oxide precipitates can indeed reduce the rate of oxidation or sulfidation. As a first example we like to quote the extensive studies on the oxidation of austenitic Cr-Co and Cr-Ni alloys carried out by Kofstad and Hed⁶⁶, Wood, Wright, Hodgkiess, Wittle^{67, 68, 69} and others. Scale morphologies of very dilute alloys (<10% Cr) described by the above authors, resemble those in the type A regime of our study. These include the formation of precipitates and intergranular corrosion loops, below a partially protective CoO or NiO epitactical scale, resulting in metallic remnants within the topotactical scale/penetrated area. The corrosion rate, which usually follows diffusion controlled parabolic kinetics, is partially controlled by the amount of the Cr_2O_3 or MCr_2O_4 precipitates in the alloy surface or the inner scale respectively. Inward diffusion of oxygen and more importantly outward diffusion of Co or Ni cations is reduced by the presence of the precipitates, in which the diffusion rates are orders of magnitude slower than in CoO, NiO or the alloy. Once a critical precipitate density has been achieved, the corrosion rate will decrease rapidly with increasing chromium content until a minimum is reached at which a continuous MCr_2O_4 or Cr_2O_3 scale is formed. This decrease in corrosion rate usually starts at about 10-12% Cr and reaches a minimum at about 23% Cr in the alloy.

The next example is from the previously cited study by Norton and Levi⁵⁹. They studied an alloy containing 27% Cr and 3% Si in a gas mixture similar to gas 1A of this study, without a HCl addition. Under the conditions of the test the alloy showed protective type C corrosion, with little or no increase in corrosion loss between 100-2000 hr exposure. A careful analysis of the EPMA line scans in Figure 6.11 shows that areas of the scale, close to the alloy surface, which contain only oxygen and metallic elements, always contain less oxygen than required to fully oxidize the available metals. This strongly indicates the presence of a precipitation zone in the metal surface, rather than a complete oxide scale. Usually the precipitation zone contains 50-60% oxides and occasionally some sulfides as well. The amount of sulfur generally increases when the alloy is fully converted to scale. Corrosion losses are very small after the first 100 hr exposure. This confirms that a dense oxide precipitation zone can indeed inhibit mixed oxidant corrosion.

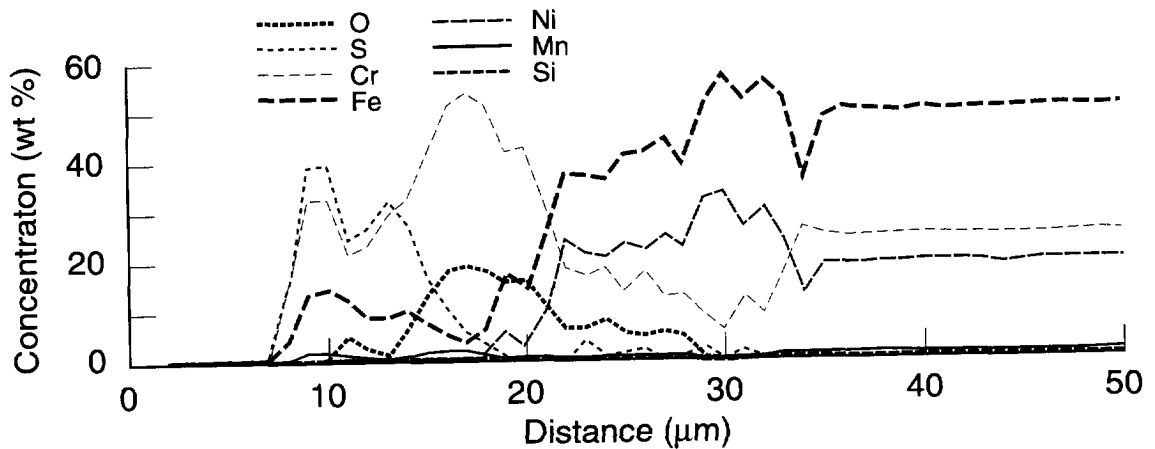
In summary, it is concluded that type B corrosion can be eliminated by adding small amounts of strong oxide formers to the base alloy A. However the formation of a continuous oxide scale is not a prerequisite for protective corrosion kinetics. The microstructural evidence clearly points to the existence of a narrow precipitation zone containing 20-30 at % SiO_2 (or Al_2O_3) and a similar amount of Cr_2O_3 as the main barrier to rapid corrosion, at least in the 600 hrs exposures in this study. Smaller amounts of oxide formers will reduce the rate of type B corrosion, as is shown by the much lower



(a) Cronifer 45, 1000 hr Exposure



(b) Cronifer 45, 2000 hr Exposure



(c) 310 CbN, 2000 hr Exposure

Figure 6.11
EPMA Line Scans of Cronifer and SS310 CbN After Exposure to Gas 1A Without HCL After Norton ⁽⁵⁸⁾

corrosion loss of Incoloy 800, containing 0.4% Al and 0.4% TiO₂ as compared to base alloy A.

6.2.2 Plant Experience

The literature on high temperature mixed oxidant corrosion occurring in coal gasification plants is limited, for reasons given in Section 2.1.2. Therefore our examples are drawn mainly from the extensive database collected by EPRI and KEMA, of which only a small part has been published.

An example of classic type A corrosion has been published by Schellberg et al.⁷⁰ Figure 6.12 shows the microstructure of an SS 310 sample exposed for 2100 hrs in a syngas cooler of an entrained slagging gasifier at 570°C. The steam content of the gas varied between 0 and 2% and the PO₂ of the gas was comparable to gases in our study in which SS 310 experienced type A corrosion. The scale morphology is similar to that found in the laboratory with an epitactical (Fe, Ni) S scale and a topotactical mixed oxide sulfide scale containing metallic remnants. The only difference in microstructure are the coarse precipitates below the topotactical scale. The authors suggest that this is caused by temperature excursions, as the exposed samples were not cooled. It is well known⁷¹ that the size of internal oxide precipitates will increase with temperature.

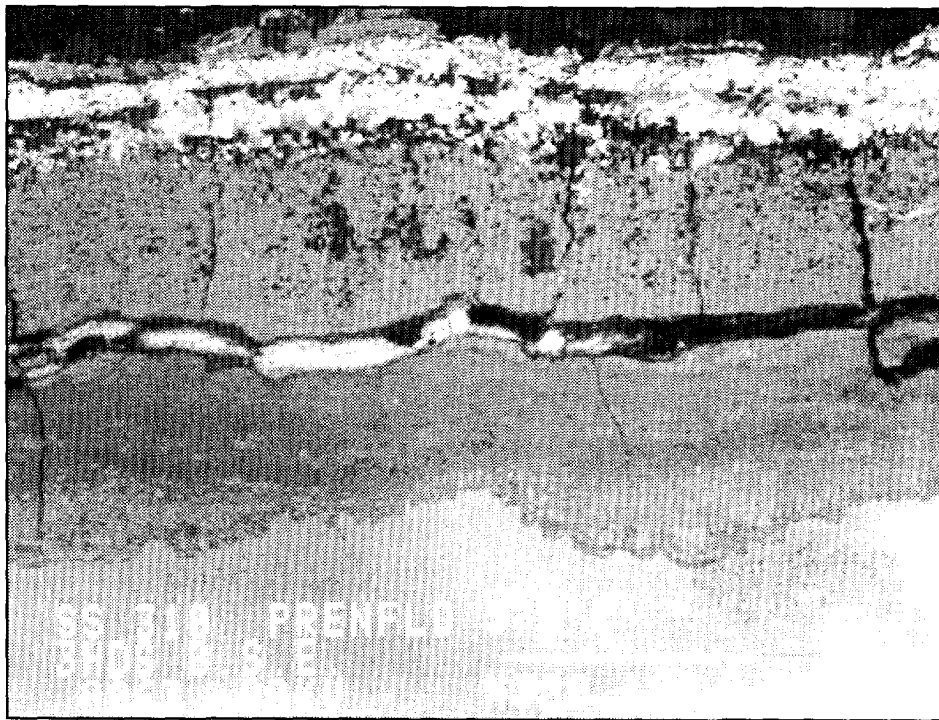


Figure 6.12
BSE Image of SS310 After 2100 hr Exposure in the PRENFLO Demonstration Plant at 570°C

Examples of type B corrosion are somewhat more difficult to find. Figure 6.13 shows the scale on an Incoloy 800 sample exposed for 3600 hrs in a coal-water slurry fed gasifier at 550°C¹⁹. The gas contained 13-17% steam, i.e. gas with a lower PS_2/PO_2 ratio than that causing maximum type B corrosion. Such gases frequently caused pitting type attack in our study (see Figure 5.56 for instance). Composition of the topotactical scale of the plant sample was also similar to that in the laboratory study i.e. it consists mainly of Cr_2O_3 with lesser amounts of Fe (Ni, Mn) S. The pitting type corrosion of Incoloy 800, was previously ascribed to incipient carburization of the alloy²¹. However in view of the high steam content of the gas the occurrence of type B corrosion appears more likely.

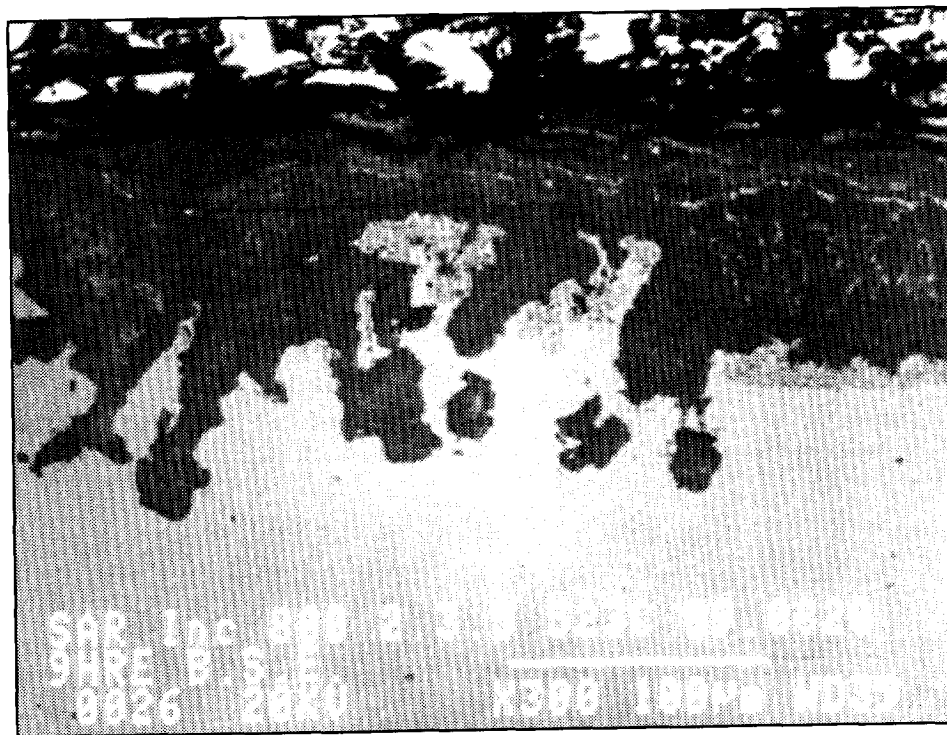
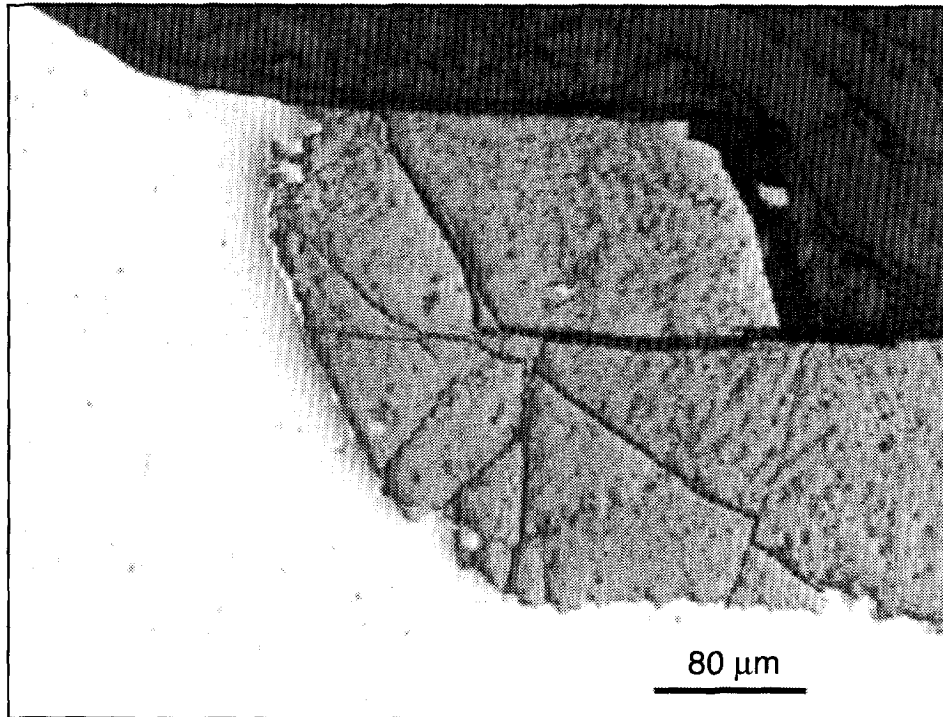


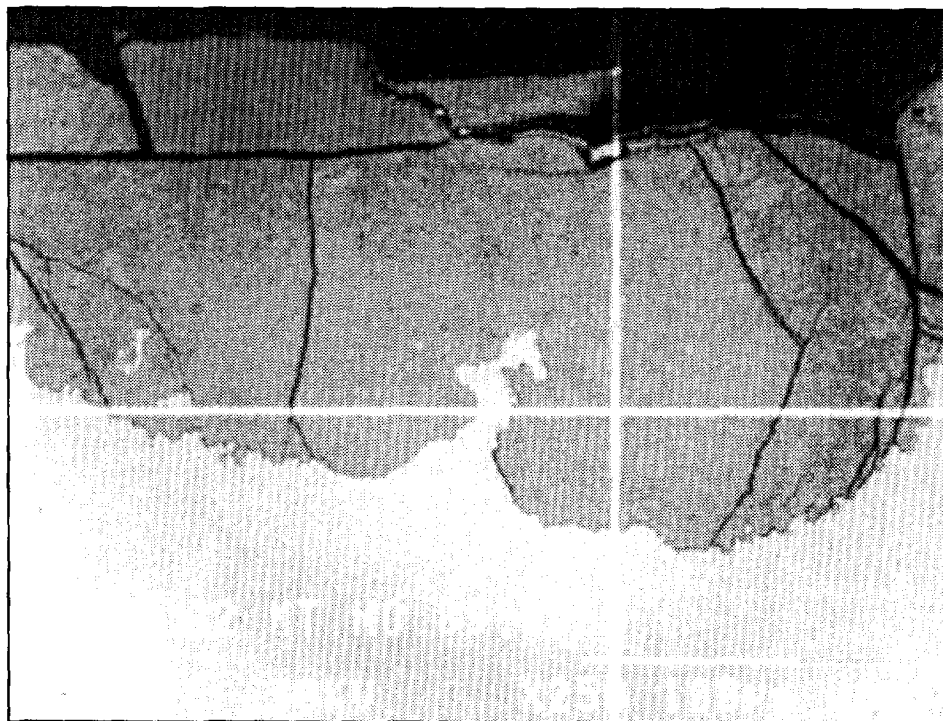
Figure 6.13
BSE Image of Alloy 800 After 2600 hr Exposure in SAR Gasification Plant at 523°C

The accelerated corrosion of Inco 82 weld metal, (80% Ni, 20% Cr, Nb, Mn) exposed in the same gasifier as Incoloy 800 at 450°C, is probably also an example of type B corrosion. This weld metal does not contain strong oxide formers and therefore would be expected to be as susceptible to rapid type B corrosion as base alloy A in this study. Figure 6.14 shows that it indeed corrodes considerably faster than the adjoining alloy¹⁸, which contained 27% Cr and 31% Ni. Maximum corrosion penetration was 280 μm in 3600 hrs at about 450°C. In comparison the corrosion loss of Incoloy 800 was only 150 μm at 550°C in the same environment.

Reference 70 also compares the corrosion loss of Incoloy 800 and SS 310 with that of silicon containing alloys. The latter show very low corrosion rates at all temperatures up to



(a) Optical Photomicrograph



(b) BSE Image

Figure 6.14
INCO82 Weld Metal After 3600 hr Exposure in SAR Gasification Plant, 406°C

570°C, thus confirming the beneficial affect of small silicon additions. A thorough analysis to detect the presence of SiO₂ precipitates or a continuous scale was not made, but the presence of the latter was not obvious from a cursory SEM/EDS analysis.

In summary it can be concluded that the three corrosion regimes identified in this study all have been found in alloys exposed in gasifiers.

6.3 UNIFIED CORROSION MODEL

After careful consideration of the pertinent literature and the microstructural evidence, the three corrosion regimes identified earlier can be described by a single corrosion model. The basis of the model is that a protective continuous Cr₂O₃ oxide layer does not form under the experimental condition explored in the present study. Internal oxidation and Cr₂O₃ precipitation occurs instead, with the simultaneous formation of a Fe (Ni) S external scale through the outward diffusion of Fe and Ni cations. According to Wagner's classical theory⁷², the transition between internal and external oxidation is dependent on the atom fraction of the alloying element, producing the most stable oxide under the experimental condition.

$$N_{\text{cr}} (\text{crit}) = \left[\frac{\pi g^*}{3} \cdot N_{\text{o}}(s) \cdot \frac{D_{\text{o}} V_{\text{m}}}{D_{\text{cr}} V_{\text{ox}}} \right]^{1/2}$$

$N_{\text{cr}} (\text{crit})$ = minimum fraction Cr in alloy to form external Cr₂O₃ scale.

g^* = critical volume fraction of oxide scale

$N_{\text{o}}(s)$ = oxygen solubility in alloy

D_{o} = diffusivity of oxygen in alloy

D_{cr} = diffusivity of chromium in alloy

V_{m} = molar volume of alloy

V_{ox} = molar volume of oxide

The controlling parameters in the above equations are the solubility and diffusivity of oxygen in the alloy and the diffusivity of chromium. A decrease in the first two parameters and an increase in the last one will favor the formation of an external scale. Oxidation studies in austenitic chromium containing alloys⁶⁶⁻⁶⁹ have shown that at about 1000°C continuous Cr₂O₃ rich oxide scales will usually form when the Cr content of the alloy is in the 15 (Ni alloys) to 25% (Co alloys) range. However the parameters controlling the $N_{\text{cr}} (\text{crit})$ change with decreasing temperature and the critical volume fraction of

chromium could increase, thus allowing internal oxidation of chromium even in alloys containing 20-25% chromium. Perkins, et al. have shown a transition of internal oxidation of Al in Nb-Ti-Al alloys to external oxidation between 1100°C and 1400°C for instance^{73,74}. Because of the change to external oxidation corrosion losses decreased significantly with increasing temperature. Thus it is probable that N_{cr} (crit) of austenitic Fe-Ni-Cr alloys will also increase with decreasing temperature. Unfortunately reliable diffusion and solubility data to substantiate this were not found. The presence of a second oxidant (sulfur) may further increase the critical chromium content, as part of the available chromium may form sulfides, thus reducing V_{ox} and possibly D_{cr} by trapping diffusing Cr ions as sulfides. It is therefore concluded that the observed internal oxidation of chromium and precipitation of Cr_2O_3 is theoretically possible and even probable under the conditions of this study.

It should be remembered here that the size of the internal oxide precipitates decreases with decreasing temperature and can therefore not be observed directly by S.E.M.⁶⁹. However occasionally the precipitates grow when engulfed by an inward growing sulfide rich scale and can be identified as Cr_2O_3 [see Figures 5.10 and 11 for instance].

The corrosion model described above can produce different scale morphologies and corrosion kinetics, ranging from highly protective to almost catastrophic. The type of scale formed and the associated corrosion kinetics depend mainly on the PS_2/PO_2 ratio in the gas and the composition of the alloy. In this study we have earlier identified three broad types of behavior: partially protective type A corrosion, largely nonprotective type B corrosion, and highly protective type C corrosion.

Type A Corrosion. This type of corrosion occurs in gases where chromium sulfide is the most stable corrosion product. This results in a duplex epitaxial scale with a porous Fe(Ni)S outer layer and a dense somewhat protective Fe Cr_2S_4 inner layer. This layer reduces the inward diffusion of sulfur more than that of oxygen. Thus below the scale both Cr_2O_3 and Cr_xS_y can form along grain boundaries and as internal precipitates. Here the oxygen and sulfur partial pressures are frequently low enough to make iron a stable phase, as demonstrated by iron rich metallic remnants in the scale. The rate of type A corrosion of the base 20 Cr-35 Ni-Fe alloy varies little with changes in PS_2/PO_2 ratio and is diffusion controlled. Alloying additions do not affect the corrosion mechanism but generally reduce the corrosion rate somewhat, probably through the formation of additional precipitates in the alloy surface, which further impede the diffusion of oxidant into the alloy and Fe + Ni ions out of the alloy. Thus both V a sulfide former and Si an oxide former reduce the corrosion rate.

The effect of HCl additions on type A corrosion has not been investigated directly in this study. Comparisons with work carried out by Norton et al.⁵⁹ would indicate that the presence of 400 ppm HCl increases the corrosion rate somewhat and may enhance the

formation of oxides in the topotactical scale/alloy surface. This trend has also been observed by Saunders⁷⁵. However the effect of HCl on mixed oxidant corrosion is needs further study.

Type B Corrosion. When the $\text{Log PS}_2/\text{PO}_2$ is lower than about 18.5, Cr_2O_3 becomes the most stable phase both in contact with the bulk gas as well as below the epitactical scale. In the base alloy the result is accelerated internal oxidation, i.e. type B corrosion. In this corrosion regime the major alloy constituents Fe and Ni sulfidize readily. This results in thick, but rather porous and granular external scales, which generally also contain a minor amount of chromium. Below the epitactical scale, Cr_2O_3 precipitates in the alloy surface. The volume fraction of the Cr_2O_3 precipitates is not high enough to slow down or prevent the simultaneous outward diffusion of Fe and Ni cations or the inward diffusion of oxidants. This results in rapid corrosion. Eventually most Fe and Ni diffuses out leaving a porous granular topotactical scale consisting mainly of Cr_2O_3 , with a minor amount of FeS. Apparently neither the epitactical FeNiS scale nor the topotactical Cr_2O_3 rich scale offers much resistance to the inward diffusion of the oxidants or outward diffusion of Fe and Ni, as demonstrated by the very high corrosion losses which peak when the $\text{Log PS}_2/\text{PO}_2$ is about 18. At lower PS_2/PO_2 ratios, a healing Cr_2O_3 layer gradually begins to form at the scale alloy interface. This lowers the overall corrosion rate and quite often results in a pitting type corrosion, in areas where the healing layer is absent.

Alloying additions strongly influence the rate of type B corrosion and may prevent type B corrosion altogether. The sulfide former vanadium has the least effect. It only reduces the peak corrosion rate of the base alloy by about one third. Titanium additions accelerate the onset of type B corrosion at higher PS_2/PO_2 ratios but reduce the peak corrosion rate by at least a factor 2 and also facilitate the formation of Cr_2O_3 layers at lower PS_2/PO_2 ratios. The presence of submicron TiO_2 precipitates in the alloy surface and the topotactical scale is probably responsible for this behavior. Strong oxide formers Si, Al and to a lesser extent Cr prevent the occurrence of type B corrosion altogether and will be discussed separately under type C corrosion.

The effect of even small additions of HCl on type B corrosion is very significant and is the subject of an ongoing study. Preliminary corrosion experiments in gases where the type B corrosion rate peaks, indicate a 2-3 fold reduction of corrosion loss for the base alloy, as well as that of alloys containing Ti and V. It is speculated at this point that HCl accelerates the outward transport of Fe and Ni through the formation and evaporation of $(\text{Fe,Ni})\text{Cl}_2$ in the topotactical scale and decomposition of $(\text{Fe,Ni})\text{Cl}_2$ at the scale/gas interface. The role of HCl needs further study and clarification.

Type C Corrosion. When strong oxide formers Si or Al are added to the base alloy, corrosion losses drop 5-10 fold when the $\text{Log PS}_2/\text{PO}_2$ drops to about 18.5. The protective corrosion kinetics are attributed to the formation of a continuous, dense oxide

precipitation zone, containing 20-30% SiO₂ or Al₂O₃ precipitates and an equal amount of Cr₂O₃ precipitates. Due to the low temperature all precipitates are submicron and cannot be resolved by optical or Scanning Electron Microscopy. The precipitation zone is apparently able to slow down the corrosion of Si or Al containing alloys to a few microns/500 hrs. It can be argued that a very thin continuous SiO₂ or Al₂O₃ rich scale can also explain the low corrosion rate. However Auger spectroscopy indicated that such a layer must be less than 50 nm if present at all, while a 2-3 μm precipitation zone in the alloy surface is well documented. It is therefore concluded that the presence of a dense precipitation zone is sufficient to explain the low corrosion rate of Al and Si containing alloys.

Adding more chromium to the base alloy also eliminates type B corrosion, but relatively fast type A corrosion persists until the PS₂/PO₂ ratio is about 16.5. At this point the scale morphology is very similar to that of Si or Al containing alloys and the corrosion rate is reduced 5-10 fold, suggesting the onset of type C corrosion.

The presence of HCl does not appear to have a major effect on type C corrosion. This may be mainly due to the low corrosion rates, which would make a reduction in corrosion loss hard to measure.

7

CONCLUSIONS

1. Laboratory mixed oxidant corrosion experiments carried out at low temperatures to simulate heat exchanger surfaces in gasifiers must be carried out in non equilibrium CO-CO₂-H₂-H₂O-H₂S-HCl containing gases.
2. Non equilibrium gases have lower oxygen and sulfur pressures than equilibrated gases at the same temperature. Therefore studies with equilibrated gases do not properly simulate conditions in coal gasification plants.
3. Corrosion losses after exposure in non equilibrium gases do not only depend on the PS₂/PO₂ ratio of the gas, but also on the type of oxidant present. In general gases containing steam as the major oxidant are more "oxidizing" than gases containing CO₂ as the major oxidant. Thus artificial gas mixtures simulating only the PS₂/PO₂ ratio of the syngas will not necessarily produce the same relative corrosion losses. Laboratory corrosion studies should therefore use gas mixtures closely similar to those in actual gasifiers.
4. Dense, continuous oxide scales do not form readily on alloys containing Cr, Si or Al at temperatures below 600°C. Internal oxidation is usually observed at least during relatively short exposures up to 1350 hrs.
5. Epitactical sulfide scales were present on all alloys in all gas mixtures used in this study. In gases with a high PS₂/PO₂ ratio the epitactical scale is layered and consists of a porous outer Fe(Ni)S layer and dense inner FeCr₂S₄ layer. In gases with a low PS₂/PO₂ ratio the epitactical scale consists only of a porous Fe(Ni)S layer, which usually contains some chromium near the original alloy surface.
6. FeCr₂S₄ scales formed in gases with a high PS₂/PO₂ ratio are relatively dense and result in reasonably protective parabolic corrosion kinetics, especially when a well developed oxide or even a mixed oxide/sulfide precipitation zone is present below the sulfide scale.
7. The absence of Fe Cr₂ S₄ scales in gases with a low PS₂/PO₂ ratio will lead to very rapid internal oxidation under a nonprotective Fe(Ni)S epitactical scale, when the alloy contains an insufficient amount of oxide formers. The volume fraction of precipitates formed in such alloys is not high enough to reduce the inward diffusion of oxidants or the outward diffusion of the base alloy constituents Fe and Ni. The

end result is a nonprotective porous, chromium rich topotactical scale below an equally porous epitactical FeNiS scale.

8. Addition of strong oxide formers, especially Si or Al can completely prevent rapid internal oxidation in gases with low PS_2/PO_2 ratios. Apparently the additional oxide formers increase the volume fraction of oxide precipitates in the alloy surface enough to largely prevent further corrosion. This leads to parabolic corrosion kinetics with rate constants well below $1(\mu\text{m})^2 \text{ hr}$, with corresponding annual corrosion rates well below 0.1 mm/yr.
9. In gases with a PS_2/PO_2 ratio between two corrosion regimes, corrosion can become chaotic. This expresses itself either through large differences in penetration depth in the same specimens or large differences in corrosion morphology and rate for different samples of the same alloy exposed in nominally the same environment.
10. Reports on mixed oxidant corrosion in syngas coolers of slagging gasifiers indicate that the corrosion regimes and morphologies identified in this study have also been found in service.
11. The presence of 400 ppm HCl in the simulated syngases used in this study significantly affects the corrosion rates reported here, especially when corrosion rates are high due to unstable internal oxidation. It is believed that the presence of HCl facilitates the outward transportation of Fe and Ni as $(\text{Fe, Ni}) \text{Cl}_2$, and may well be the main cause of the accelerated corrosion observed at intermediate PS_2/PO_2 ratios. However this needs further confirmation, as no chloride species have been detected in the scales so far, and the HCl content of the gas was not a variable in this study.

8

REFERENCES

1. K. Yeager, "An R&D Agenda for the Second Electrical Revolution", p. 107, Proc. *Electricity Beyond 2000*, F. Kalhammer, Editor, EPRI 1991.
2. R. Balzhiser, "Impact of Research on Electric Utilities", p. 27, Ref. 1.
3. J. van Liere, "Advanced Power Generation by Means of Coal", p. 143, Ref. 1.
4. R.P. Allen, et al., "Characteristics of An Advanced Gas Turbine with Coal Derived Fuel Gases", p. 13-1, Proc. *Ninth EPRI Conference on Gasification Power Plants*, N. Holt, Editor, EPRI Report TR-100466, July 1992.
5. J. van Liere, W.T. Bakker, "Coal Gasification for Electric Power Generation", *Workshop on Materials for Coal Gasification Power Plants*. Petten, June 1993, J.F. Norton, W.T. Bakker, editors. Butterworth-Heinemann, Dec. 1993, *Mats at High Tech*, Vol. 11, 1-4, p. 4, 1993.
6. H.H. Lowry (ed.), *Chemistry of Coal Utilization, Supplementary Volume*, J. Wiley & Sons, Inc., New York, 1963.
7. E.V. Clark, N.A. Holt, ed., *Coolwater Coal Gasification Program: Final Report*, EPRI Report GS-6806, December 1990.
8. J. van Liere, et al., "Dutch IGCC Developments in 1992, Demkolek Plant Status", Proc., *11th EPRI Conference on Gasification Power Plants*, N. Holt, Ed., in print.
9. W. de Priest, K.K. Gupta, "Review of Potential Cycle Improvements for an IGCC Plant", Proc. *8th Annual EPRI Gasification Conference*, p. 3-1, N. Holt, Editor. EPRI Report GS-6485, August 1989.
10. J.E. Notestein, "Update on Department of Energy Hot Gas Cleanup Programs", p. 14-1, in Ref. 9.
11. R.C. Dobbyn, H.M. Ondyk, "Materials Research for the Clean Utilization of Coal Task 4 Failure Prevention", Proc. *Third Annual Conference on Materials for Coal Conversion and Utilization*, 1978. DOE Report. Conf. 781018, p. 1-3, 1978.

8. References

12. D.R. Diercks, "A Review of Failure Analysis Experience on Coal Gasification Components", Proc. *Materials for Coal Gasification*. W.T. Bakker, Ed., ASM 1987, p. 223.
13. K.J. Barton, et al., "Corrosion Performance of Metals in Pilot Plant Coal Gasifiers", Proc. *The Properties and Performance of Materials in the Coal Gasification Environment*. V. Hill, Editor. ASM 1981, p. 65.
14. R.R. Judkins, R.A. Bradley, "Materials Performance in Coal Gasification Plants", p. 239, Ref. 12.
15. N. Ullrich, et al., "Materials Exposures in the PRENFLO Plant, Uncooled Samples", p. 101, Ref 5.
16. W.T. Bakker, et al., "Corrosion in Syngas Coolers of Coal Gasification Combined Cycle Power Plants", *Materials Performance* [24], 9, 1985.
17. J. van Liere, et al., "Materials Testing at the Ruhrkohle-Ruhrchemie, 165 tpd Demonstration Plant", p. 211, Ref. 12.
18. J. van Liere, et al., "Materials Performance at the SAR Coal Gasification Plant", p. 22-1, Ref. 4.
19. W.T. Bakker, et al., "Materials Testing in Syngas Coolers of Coal-Water Slurry Fed Gasifiers", Ref. 5, p. 133.
20. A.M. Sarosiek, et al., "Shutdown Corrosion in Syngas Coolers of Entrained Slagging Gasifiers". Paper 98, Corrosion 86, NACE 1986.
21. W.T. Bakker, et al., "Carburization in Coal Gasifier Environments". Paper 63, Corrosion 91, NACE 1991.
22. W. Schellberg, "Materials Performance at the PRENFLO Coal Gasification Plant", p. 23-1 in Ref. 4.
23. E.A. Gulbransen, S.A. Jansson, "General Concepts of Oxidation and Sulfidation Reactions, A Thermodynamical Approach", *High Temperature Metallic Corrosion by Sulfur and Its Compounds*, p. 3-54, Z.A. Foroulis, Ed., Electrochemical Soc. 1970.
24. R.A. Perkins, S.J. Vonk, *Materials Problems in Fluid Bed Combustion Systems, IV Corrosion Chemistry in Low Oxygen Activity Atmospheres*, EPRI Report FP-1280, 1979.

25. J. Stringer, "Corrosion and Erosion in Complex High Temperature Environments", *Behavior of High Temperature Alloys in Aggressive Environments*, I. Kirman et al., Ed., The Metals Society, London 1979, p. 739.
26. G.H. Meier, et al., "Thermodynamic Analyses of the High Temperature Corrosion of Alloys in Gases Containing More Than One Reactant", *High Temperature Corrosion*, R.A. Rapp, Ed., NACE 1981, p. 327.
27. K. Natesan, "High Temperature Alloy Corrosion in Coal Conversion Environments", p. 336, in Ref. 26.
28. V.L. Hill, J.F. Blough, B.A. Humphreys, "The Performance of Alloys in the MPC Gaseous Corrosion Study", p. 225 in Ref. 13.
29. G.Y. Lai, et al., "The Corrosion Behavior of a New Sulfidation Resistant Alloy in a Sulfidizing/Oxidizing/Carburizing Atmosphere". *Proc. Heat Resistant Materials*, K. Natesan, D.J. Tillack, Ed., Sept. 1991, ASM 1991.
30. I.G. Wright, J.A. Coldwell, *Effect of Minor Alloying Additions on the Formation of Protective Scales Under Sulfidizing Conditions at 700°C*. ORNL/Sub/86-57444/02, 1990.
31. R.A. Perkins, W.T. Bakker, "Beyond Mixed Oxidant Corrosion - Corrosion Phenomena in Gasifiers", *Proc. Corrosion-Erosion-Wear of Materials at Elevated Temperatures*, A. Levy, Ed., January 1990. NACE 1991.
32. R.C. John, "Rapporteurs Review on Laboratory Corrosion Studies", p. 129 in Ref. 12.
33. J.H. de Van, "Corrosion Performance of Iron Aluminide (Fe_3Al) in Coal Conversion Process Environments", Ref. 29, p. 235.
34. R.A. Perkins, *Corrosion in Syngas Coolers of Entrained Slagging Gasifiers*, EPRI Report GS-6971, 1990.
35. K. Natesan, "Corrosion Behavior of Materials in Low and Medium BTU Gasifier Environments", *Proc. Corrosion-Erosion-Wear in Emerging Fossil Energy Systems*, Berkeley, January 1982. A. Levy, Ed., NACE 1982, p. 100.
36. W.H. Gibb, "The Nature of Chlorine in Coal and Its Behavior During Combustion", *Proc. Corrosion Resistant Materials for Coal Conversion Systems*, D.B. Meadowcroft, M.I. Manning, Ed., Applied Science Publishers, London 1983, p. 25.

8. References

37. J. Norton, Personal Communication, 1991.
38. R.A. Perkins, et al., *Materials for Syngas Coolers*, EPRI Report AP-2518, 1982.
39. Dr. Stall, H. Prophet, *JANAF Thermochemical Tables*, 2nd Edition, NSRDS - WBS-37. U.S. Gov. printing office 1971.
40. E.A. Gulbransen, "Thermochemical Stability Diagrams for the Condensed Phases of Four Metal-Oxygen-Sulfur Systems at 550°C (823K)", unpublished results.
41. W.T. Bakker, R.A. Perkins, "Laboratory Study of Superheater Corrosion in Coal Gasification Power Plants", Paper 525, Corrosion 89, NACE.
42. K. Natesan, D.J. Baxter, Proc. *Corrosion-Erosion Wear of Materials for Advanced Energy Applications*, p. 1, A. Levy, Ed., NACE 1987.
43. D.B. Roach, *The Potential Use of Duplex Stainless Steels for Utility Applications*, EPRI Report RD-3401, 1984.
44. H. Schusten, "Magnetitbildung Im verdamper von Benson kesseln", Allianz. Berichte [16] p. 28, April 1971.
45. M. Hansen, *Constitution of Binary Alloys*, McGraw Hill, New York, 1958.
46. R.P. Elliott, *Constitution of Binary Alloys*, First Supplement, McGraw Hill, New York, 1965.
47. F.A. Shunk, *Constitution of Binary Alloys*, Second Supplement, McGraw Hill, New York, 1959.
48. R.L. Hammings, R.A. Perkins, *Thermodynamic Phase Stability Diagrams for Analysis of Corrosion Reactions in Coal Gasification/Combustion Atmospheres*, Report FP-539, EPRI, Palo Alto, 1977.
49. P.A. Flint, G.A. Waychunas, "A New X-ray Diffractometer Design for Thin Film Texture, Strain and Phase Characterization". *J. Vac Sc. Techn.* B6(6), 1988.
50. J.A. Bain, unpublished results, 1992.
51. R.A. Perkins, *Corrosion in Syngas Coolers of Slagging Gasifiers*, EPRI Report GS-6971, August 1990. EPRI, Palo Alto.

52. R.A. Perkins, *Evaluation of Coated and Clad Heat Exchangers for Syngas Coolers*, EPRI Report AP-4406, Vol. 2, EPRI, Palo Alto, 1986.
53. R.C. John, et al., "Prediction of Alloy Corrosion in the Shell Coal Gasification Corrosion Process", Ref. 5, p. 124.
54. W.T. Bakker, "Effect of Gasifier Environment on Materials", p. 81, Ref. 5.
55. M. Perez, J.P. Larpin, "Sulfidation Properties of Austenitic Fe-Mn and Fe-Mn-Al Alloys Under Low Sulfur Vapor Pressure in the Temperature Range 873-1173 K", *Ox. Metals*, Vol. 24, p. 29, 1985.
56. W.T. Bakker, J. van Liere, "Construction Materials for IGCC Plants", *Proc. Materials for Advanced Power Eng.*, 1994. Liege (B), Oc. 1994, D. Coutsouradis et al. ed. Kluwer A.C. Publ. 1994, p. 1413.
57. J.F. Norton, S. Canetoli and K. Schuster, "Nucleation and Growth of Surface Oxides and Sulfides", *Proc. Microscopy of Oxidation 1*, Cambridge 26-28 March. M.J. Bennett, G.W. Lorimer editors, p. 387, Institute of Metals, 1991.
58. K. Natesan, "Alloy and Coating Development for Coal Gasification Applications", p. 137 in *Materials for Coal Gasification*, W.T. Bakker, S. Dapkunas, V. Hill eds. ASM, 1988.
59. J.F. Norton, et al., "High Temperature Corrosion of Candidate Heat Exchanger Alloys in Dry Feed Entrained Slagging Gasifier", Ref. 56, p. 1617.
60. W.T. Bakker, unpublished work.
61. R.E. Lobnig, H.J. Grabke, "Mechanism of Simultaneous Sulfidation and Oxidation of Fe-Cr and Fe-Ni-Cr Alloys", *Corrosion Sc.*, Vol. 30, No. 10, p. 1045, 1990.
62. P. Mayer, A.V. Manolescu, "Influence of HCl on Corrosion of Boiler Steels in Synthetic Fluegas", *Corrosion*, 36 (1980) p. 369.
63. P. Elliott, C.J. Tyreman, R. Prescott, "High Temperature Alloy Corrosion by Halogens". *J. of Metals*, July 1985, p. 20.
64. F.H. Stott, R. Prescott, P. Elliott, "Corrosion Resistance of High Temperature Alloys in Gas Containing HCl". *Mat. Sciences & Technology*, Vol. 6, April 1990, p. 364.

8. References

65. Y. Ihara, et al., "The Corrosion of Iron in HCl and HCl-O₂ at High Temperatures", *Corr. Sc.*, Vol. 21, No. 12, p. 805, 1981.
66. P.K. Kofstad, A.Z. Hed, "High Temperature Oxidation of Co-10 %Cr Alloys", *J. Electro Chem. Soc.*, Vol. 116, No. 2, p. 224, Feb. 1969.
67. G.C. Wood, T. Hodgkiess, "Characteristic Scales on Pure Ni-Cr Alloys at 800-1200°C", *J. Electrochem. Soc.*, Vol. 113, No. 5, April 1966.
68. G.C. Wood, T. Hodgkiess, D.P. Wittle, "A Comparison of the Scaling Behavior of Pure Iron Chromium and Nickel Chromium Alloys in Oxygen", *Corrosion Science*, Vol. 6, p. 129, 1966.
69. G.C. Wood, I.G. Wright, T. Hodgkiess, D.P. Wittle, "A Comparison of the Oxidation of Fe-Cr, Ni-Cr and Co-Cr Alloys in Oxygen and Water Vapor", *Werkstoffe und Korrosion*, Vol. 21, p. 900, Nov. 1970.
70. W. Schellberg, et al., "Materials Experience in the PRENFLO Plant". Proc. 12th EPRI Coalgasification Conference, San Francisco, Nov. 1993, in print.
71. R.A. Rapp, "Kinetics, Microstructure and Mechanism of Internal Oxidation. Its Effect and Prevention in High Temperature Alloy Oxidation", *Corrosion*, Vol. 21, p. 382, Dec. 1965.
72. C. Wagner, *Z. Elektrochem*, 63, 772, 1959.
73. R.A. Perkins and G.H. Meier, "The Oxidation Behavior and Protection of Niobium", *JOM*, Vol. 42, No. 8, p. 17, 1990.
74. R.A. Perkins and G.H. Meier, "Metallographic Characterization of the Transition From Internal to External Oxidation of Nb-Ti-Al Alloys", p. 183, Ref. 56.
75. S.R.J. Saunders, et al., "Behavior of High Alloy Steels Used as Heat Exchanger Components in Coal Gasification Plants", p. 51, Ref. 5.

9

SAMENVATTING

INLEIDING EN EXPERIMENTELE AANPAK

De belangrijkste toepassing van roestvast staal in KV-STEG (Kolenvergassing, Stoom en Gasturbine) centrales, voor de opwekking van elektriciteit is als warmtewisselaars in de syngaskoeler van de kolenvergasser. Hier wordt de voelbare warmte van het syngas omgezet in stoom, dat later wordt gecombineerd met stoom, geproduceerd in de afgas ketel van de gasturbine. Via een generator, gekoppeld aan de gas- en stoomturbine wordt elektriciteit opgewekt.

De temperatuur van het gas in de syngaskoeler daalt snel van ongeveer 1200 °C tot 250°C. Bovendien ligt de temperatuur van de warmtewisselaar aanzienlijk lager dan die van het gas. De samenstelling van het syngas is daarom niet in evenwicht met de temperatuur van het staal in de warmtewisselaar, waarop de corrosie plaatsvindt.

Over het algemeen is de gassamenstelling gelijk aan de evenwichtssamenstelling op ongeveer 1100°C, terwijl de temperatuur van de warmte wisselaars ongeveer 300-600°C is, afhankelijk van hun gebruik als verdamperwand (350-450°C) of als oververhitter (500-600°C). Om deze redenen is het huidige onderzoek uitgevoerd in "non equilibrium" syngas, waarvan de samenstelling gelijk is aan die geproduceerd in kolen vergassers van bijvoorbeeld de Dow, PRENFLO, Shell en Texaco processen. Deze gassen bestaan grotendeels uit CO en H₂, soms met aanzienlijke hoeveelheden CO₂ en H₂O en altijd geringe hoeveelheden H₂S en HCl. Vooral de laatste 2 ingredienten maken het gas corrosief.

Het H₂S en HCl gehalte is afhankelijk van het zwavel en chloor gehalte van de kolen. H₂S gehalten van 0,2 % en 0,8%, representatief voor kolen met laag en hoog zwavelgehalte, werden gekozen voor deze study. Het HCl gehalte van het gas werd constant gehouden op 400 ppm. Dit is representatief voor kolen met 0.1-0,15% chloride.

Kolenvergassers, die met poeder kool gevoed worden, produceren gas met een laag CO₂-en H₂O-gehalte, terwijl vergassers, die met een koolwater slurry gevoed worden, gas produceren met ongeveer 10-15% CO₂ en 13-23% H₂O.

Het H₂O-en CO₂-gehalte van de gassen, gebruikt in deze studie, werd daarom gevarieerd tussen 0 en 15%.

De zuurstofdruk (PO_2) van een "non-equilibrium" gas, kan berekend worden uit de CO_2/CO en H_2O/H_2 verhoudingen. Figuur S-1 toont de zuurstof druk als een functie van het vochtgehalte van het gas. Op dezelfde wijze kan de zwaveldruk (PS_2) berekend worden uit de H_2S/H_2 verhouding. Omdat het waterstofgehalte van de gassen weinig varieert, is de PS_2 voornamelijk afhankelijk van het H_2S -gehalte: $\log PS_2 = -9,3$ voor een gas met 0,8 % H_2S en $\log PS_2 = -10,5$ voor een gas met 0,2% H_2S .

Alle corrosie proeven werden uitgevoerd op $540^\circ C$, een gebruikelijke temperatuur voor een oververhitter.

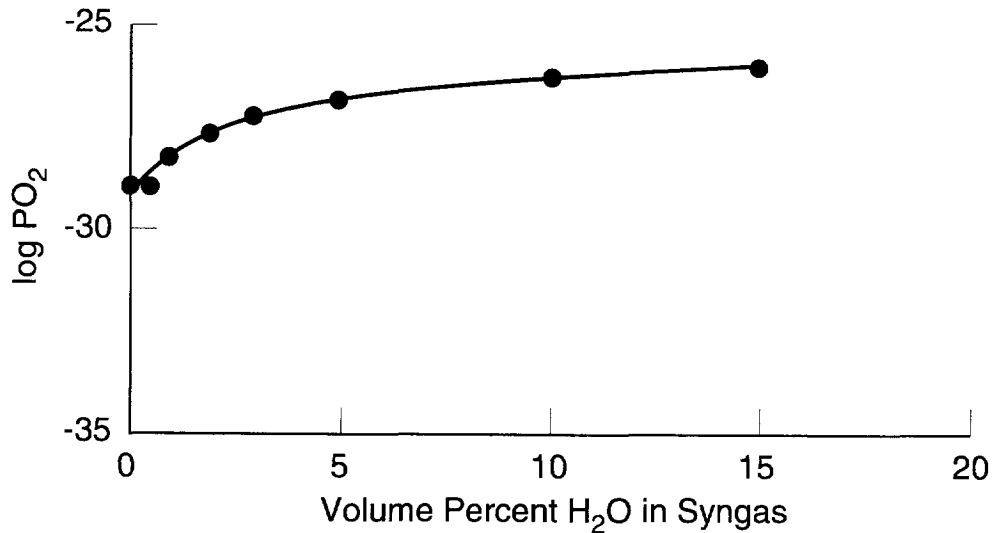
Austenitische roestvaste staalsoorten combineren een hoge kruip sterkte met een goede corrosie bestendigheid. Daarom werden de volgende typen roestvaststaal voor deze studie gekozen. Basis staal :20%Cr, 35%Ni,1%Mn, 0.3% Si, rest Fe. Stalen van dezelfde samenstelling, met toevoeging van respectievelijk 3% V,Ti,Al en Si, werden gekozen om het effect van sulfide en oxide vormende elementen te onderzoeken.

Monsters van de verschillende staalsoorten werden blootgesteld aan syngas gedurende 1.5 tot 1350 uur. Na afloop werd de wanddikte afname bepaald door het meten van de dikte van de korrosie schaal, zowel als uit de dikte afname van het monster. Corrosie produkten werden onderzocht met een raster elektronen microscoop en bijpassend EDS apparatuur dat het mogelijk maakte om de samenstelling van het korrosie produkt kwantitatief te meten. Verder werd ook nog gebruik gemaakt van licht microscopie, Röntgenanalyse en Augerspectroscopie.

RESULTATEN

Figuur S-2 toont het corrosieverlies van de verschillende staalsoorten als een functie van het vochtgehalte van het gas, bij een vast H_2S -gehalte van 0.8%. Het corrosieverlies van stalen A,B en C is maximaal bij een vochtgehalte van 3%. Op dit punt is de $\log PS_2/PO_2$ gelijk aan 18. Het corrosie verlies van de staalsoorten D en E, die 3% Si of Al bevatten, is ongeveer gelijk aan dat van de andere staalsoorten in gassen met een laag vocht gehalte, maar zeer laag, wanneer het vochtgehalte van het gas groter of gelijk is aan 2%. Op dit punt is de $\log PS_2/PO_2$ gelijk aan 18,5. Variaties in de PS_2 of van het oxidatie middel (CO_2 i.p.v. H_2O) veranderen dit algemene patroon niet. Wel wordt de variabiliteit in de data veel groter. Dit betekent, dat corrosie verliezen niet alleen afhankelijk zijn van de PS_2/PO_2 verhouding maar ook van het type oxidatiemiddel en de partiaalspanning van H_2S .

Het corrosiegedrag, hierboven beschreven, kan verklaard worden door het volgende model: alle stalen vormen een externe(epitaktische)Fe,Ni(Cr) S laag in contact met syngas. Waar Cr_2S_3 de stabiele fase in contact met het gas is, vormt zich een $FeCr_2S_4$ laag



Figuur S-1

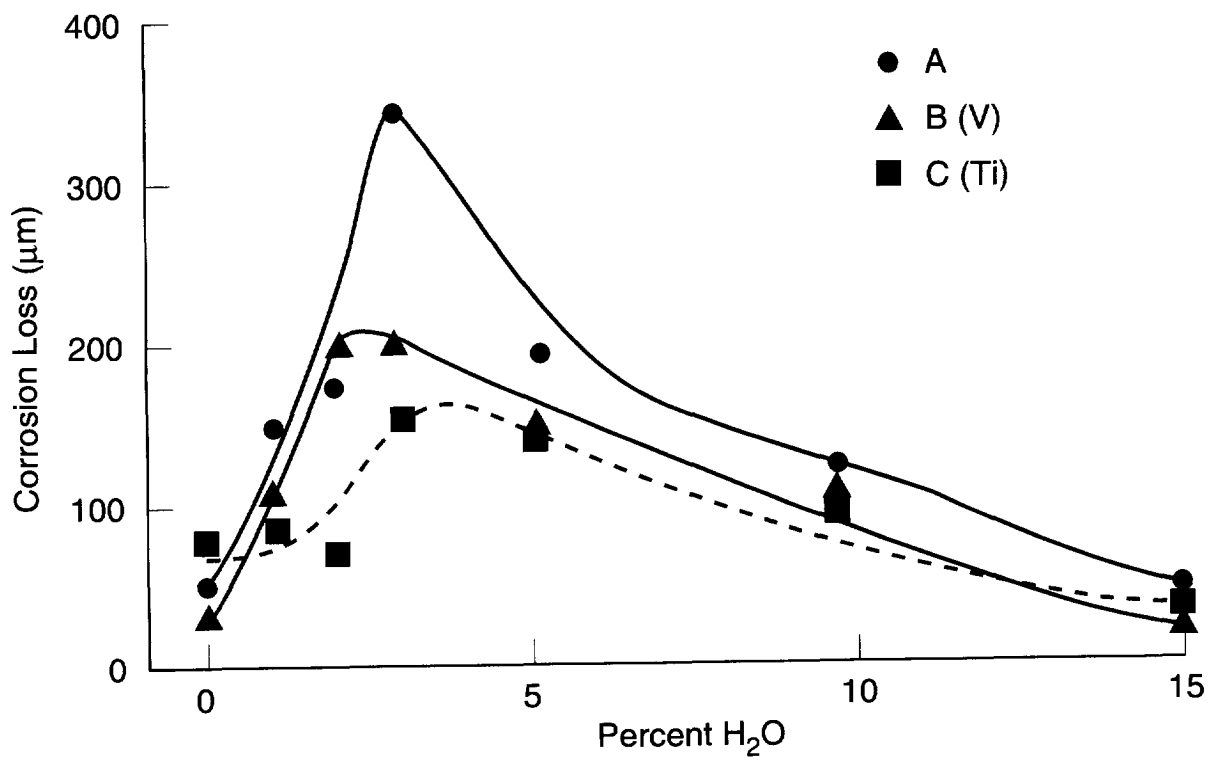
"Non-equilibrium" zuurstof spanning van syngas als functie van het vochtgehalte op 540°C

onder de (Fe,Ni)S laag, i.e. als de PS_2/PO_2 verhouding hoog is. Deze laag wordt dunner en verdwijnt eventueel, als de PS_2/PO_2 verhouding lager wordt. Interne oxidatie van Chroom tot Cr_2O_3 vindt plaats in het staal oppervlak onder de epitaktische laag. Cr_xS_y precipitaten kunnen zich tegelijkertijd vormen bij een hoge PS_2/PO_2 verhouding. Het resultaat is een interne (topotaktische) laag, gevormd door samengroeien van de oxide en sulphide precipitaten. Deze laag bevat vaak aanzienlijke hoeveelheden metaal, meestal ijzer. Wanneer de PS_2/PO_2 verhouding van het gas afneemt, wordt het ijzer- en zwavelgehalte van deze laag over het algemeen lager en neemt het Cr_2O_3 -gehalte toe.

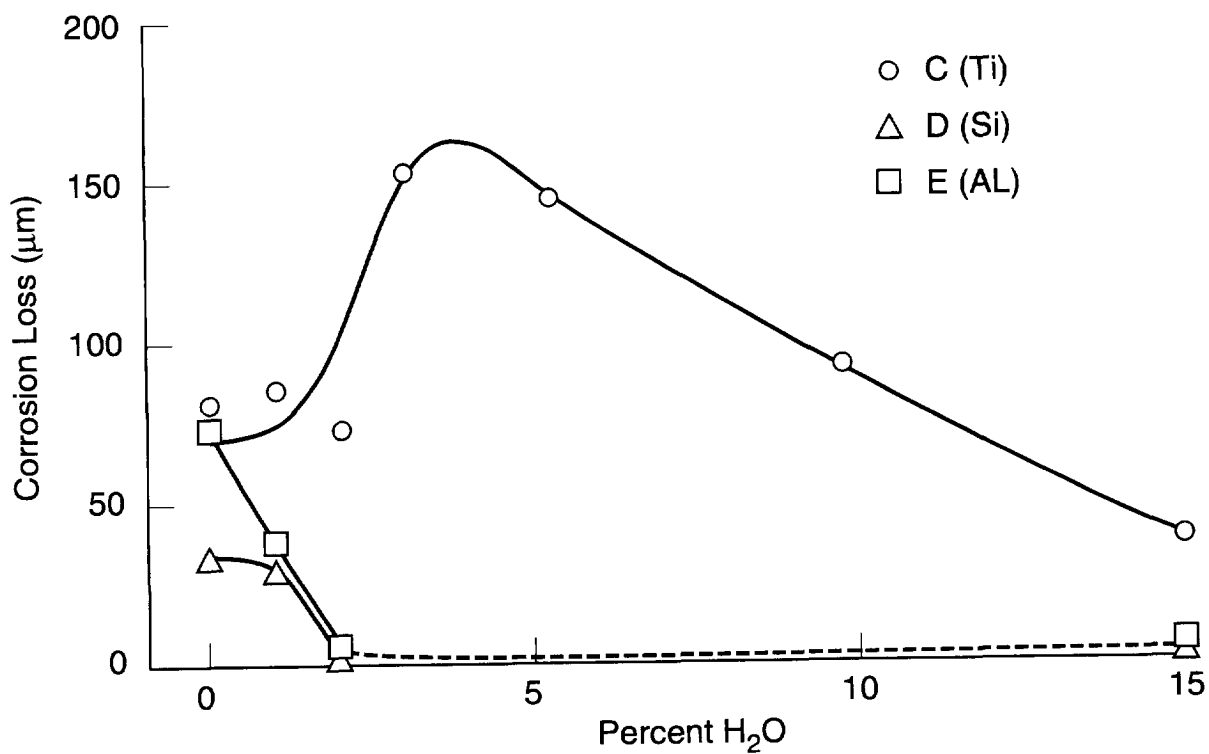
Afhankelijk van de gassamenstelling en de staalsoort, leidt het hierboven beschreven korrosie model tot 3 verschillende corrosie regimes, hier genoemd type A, B en C corrosie (Figuur S-3).

Type A corrosie vindt plaats in alle staalsoorten onder hoge PS_2/PO_2 verhoudingen (Cr_2S_3 stabiel). Hier vormt zich een $FeCr_2S_4$ laag met een beschermend karakter. Dit leidt tot relatief lage parabolische corrosie snelheden met een K_p variërend tussen 1 en 17 $(\mu m)^2/u$, leidend tot corrosie snelheden tussen 0,1 en 0,4 mm/jr.

Type B corrosie vindt plaats in gassen met lage PS_2/PO_2 verhoudingen en is alleen waargenomen in staalsoorten A, B en C. Een beschermende $FeCr_2S_4$ laag ontbreekt hier, omdat nu Cr_2O_3 stabiel is in contact met het gas. Het resultaat is een zeer snelle interne oxidatie van chroom, onder een poreuze (Fe,Ni(Cr))S schaal, gevormd door de uitwaardse diffusie van Fe en Ni. De chroom rijke topotaktische schaal, die ontstaat door het samengroeien van de Cr_2O_3 precipitaten, is poreus en biedt weinig bescherming tegen verdere corrosie. Corrosie verliezen tot 0,35 mm/600 uur zijn gemeten. De dikke corrosielagen bladderen gemakkelijk af, met als gevolg snelle pseudo lineaire corrosie.

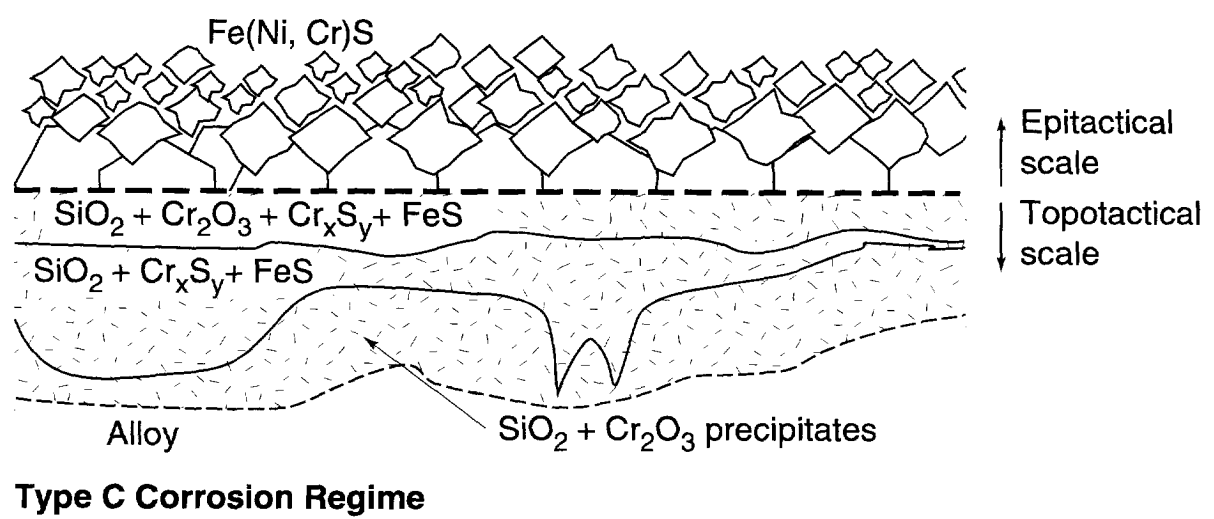
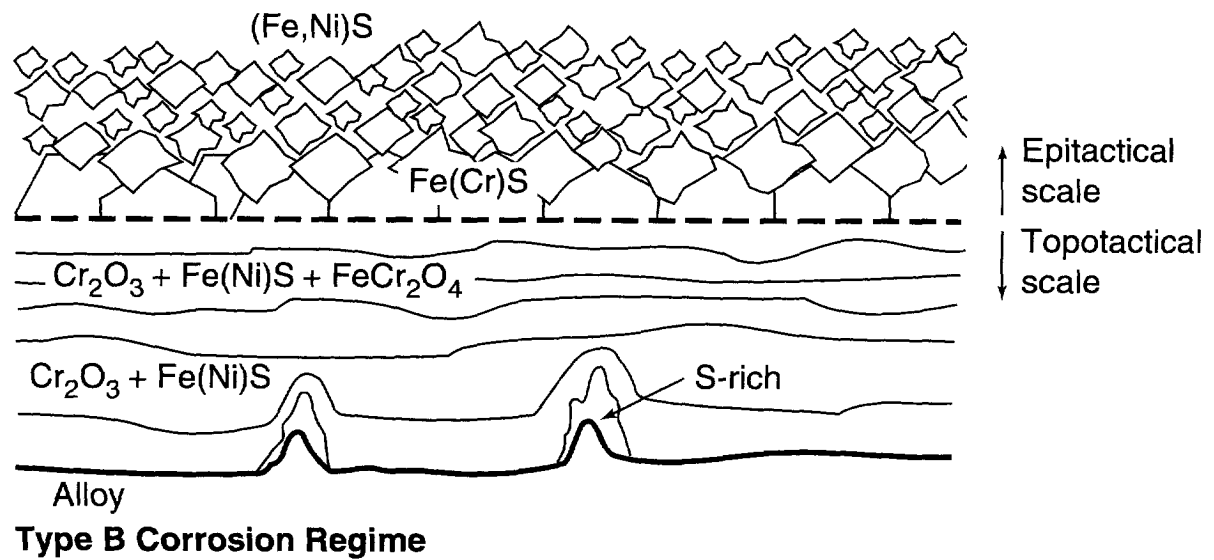
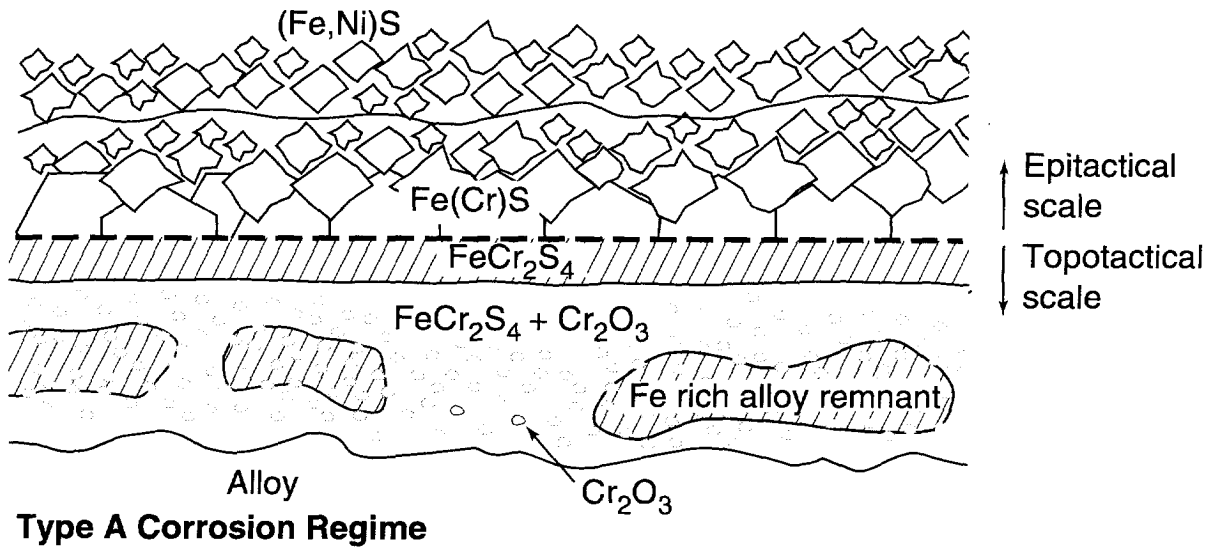


(a)



(b)

Figuur S-2
Corrosie als Functie van het vochtgehalte van syngas. (540°C, 0,8% H₂S)



Figuur S-3
Vereenvoudigde schaal morfologie en samenstelling

Type C corrosie vindt plaats onder dezelfde omstandigheden als type B, wanneer het staal 3% Si of Al bevat. In dit geval vormen zich niet alleen Cr_2O_3 , maar ook SiO_2 of Al_2O_3 precipitaten in het staal onder de poreuze $(\text{Fe},\text{Ni}(\text{Cr}))$ epitaktische laag. De grote hoeveelheid oxideprecipitaten in het staaloppervlak remt de inwaardse diffusie van de oxidatie middelen in het staal zowel als de uitwaardse diffusie van Fe en Ni. Het gevolg is een zeer lage korrosie snelheid, minder dan 0,1mm/jr.

Het zojuist beschreven corrosie model heeft veel gemeen met de oxidatie van Ni-Cr en Co-Cr legeringen met relatief laag chroom gehalte. Ook hier zijn Cr_2O_3 precipitaten in het metaaloppervlak, samen met $(\text{Ni},\text{Co})\text{Cr}_2\text{O}_4$ precipitaten in de $(\text{Ni},\text{Co})\text{O}$ laag in staat om de corrosie snelheid aanzienlijk te verminderen.

Tenslotte verklaart het model ook sommige corrosieverschijnselen, waargenomen in materialen afkomstig van kolenvergassers. Bij voorbeeld, de snelle korrosie van het lasmetaal INCO 82 is een duidelijk een voorbeeld van type B korrosie. Topotaktische schalen met een hoog vrij ijzer gehalte zijn gevonden op monsters van type 310 roestvast staal, afkomstig van een syngas koeler van een met poederkool gestookte vergasser.

10

CURRICULUM VITAE

Wate T. Bakker was born on March 28, 1933 in Stiens (Fr). He attended the Christian Elementary School in Stiens (Fr) and the Christian Reformed Gymnasium in Leeuwarden (Fr), where he graduated in 1951. From 1951 to 1957 he studied mining engineering at the Technical University in Delft, where he graduated "Cum Laude" on September 16, 1957. Following his graduation he joined the Shell Oil Company as an exploration geophysicist and participated in oil and gas exploration in Pakistan and Bangladesh. In 1961 he emigrated to Canada and joined the Aluminum Company of Canada as a research chemist in Arvida, Quebec. Here he was responsible for research and development of alumina based raw materials for the ceramic and refractory industries. In 1966 he joined General Refractories Co. in Baltimore, Md. as a research associate. He was responsible for the development of alumina based refractory brick, plastics and castables. In 1975 he joined the US Department of Energy in Washington, D.C. as Branch Chief, Materials, for fossil energy applications. Finally he joined EPRI (The Electric Power Research Institute) at Palo Alto, Ca. in 1979, where he is now Manager of High Temperature Materials Technology.

As part of his responsibilities he has carried out extensive studies on corrosion of materials in coal gasifiers. The present thesis is a result of one of these studies, which was carried out in collaboration with the Palo Alto research laboratory of Lockheed Missile and Space Company.

During his career, Wate Bakker, has published over 50 papers in the areas of refractory technology, ceramics and high temperature corrosion. He also obtained 11 patents. He was elected as a fellow of the American Ceramic Society in 1976 and served as the Chairman of its refractory division in 1983. In 1985 he received the Allen W. Allen award for his paper "Refractory Practice in Slagging Gasifiers".

Propositions

1) Corrosion by liquid alkali iron sulfates is over-emphasized as the leading cause of metal wastage in superheaters of coal-fired boilers. Erosion-corrosion, reducing conditions and overheating can cause similar failure features. Superheater wastage should, therefore, only be blamed on alkali iron sulfate corrosion, when this ingredient is found to be present.

2) Abrasive wear in coal pulverizers is not only dependent on the quartz and pyrite content of coal, but also on the size distribution of both minerals

R.T. Donais, A.L. Tyler, W.T. Bakker p. 637
"Advances in Materials Technology for Fossil Power Plants",
R. Viswanathan, R.I. Jaffee, eds., ASM, 1987.

3) Silicon is the preferred alloying additive to Fe-Cr-(Ni) steels to reduce corrosion loss in coal gasifier environments, because the parabolic rate constant for the oxidation of silicon decreases less with temperature than that of Cr or Al; and is actually higher than that of Cr below 650°C.

N. Birk, G.H. Meier, p. 54 in "Introduction to High Temperature Oxidation of Metals", E. Arnold Ltd., London, 1983.

4) The mechanism of accelerated corrosion in syngas coolers, apparently resulting from combined aqueous corrosion during downtime and high temperature corrosion during service, has not been adequately determined nor duplicated under laboratory conditions.

W.T. Bakker, J.B.M. Kip, H.P. Schmitz, "Materials Testing in Syngas Coolers of Coal-Water Slurry Fed Gasifiers",
Materials at High Temperature, 1993, Vol. 11, p. 133.

5) Results of short term high temperature corrosion tests in gases containing multiple oxidants cannot be extrapolated to predict long term corrosion behavior at lower temperatures, especially when such tests are carried out above the eutectic melting points of Fe and Ni sulfides and oxides.

6) Materials problems, including corrosion, in high temperature components, can often more easily be corrected by design changes than by materials upgrades. This is especially true for erosion related failures.

7) Coal gasification combined cycle power plants will only become a significant part of the electric power production industry, when their capital cost can be reduced to that of ultra supercritical pulverized coal plants, unless the public is willing to pay somewhat higher prices for electricity to enjoy cleaner air.

- 8) "Re-engineering" of companies will only be successful if company management is willing to be included in the exercise. This is seldom the case.
- 9) The supposition that the high crime rate in certain countries can be reduced by increasing the police force is questionable, as policemen spend already a significant amount of time to catch and fine ordinary citizens for minor traffic violations and are unlikely to reduce such activities in favor of pursuing dangerous criminals.
- 10) The most effective mode of technology transfer is the movement of people from basic research to applied research where new results are exploited. Therefore, the movements of researchers between national laboratories, universities and industry should be encouraged.

J.A. Armstrong, "Is Basic Research a Luxury our Society Can No Longer Afford?", p. 117, *Adv. Materials Processes*, Vol. 146 [5], November 1994.

- 11) The model of Robertson and Forrest on the formation of non-protective, laminated Magnetite scales on carbon and low alloy steels in high temperature acid chloride solutions does not adequately explain the formation of the laminated microstructure. Especially the highly segmented scales found on steels containing 0.5-2% Cr remain unexplained.

J. Robertson, J.E. Forrest, "Corrosion of Carbon Steels in High Temperature Acid Chloride Solutions", p. 521, *Corr. Sc.*, Vol. 32, 1991.
J.E. Forrest, J. Robertson, "Corrosion of Cr Steels in High Temperature Acid Chloride Solutions", p. 541, *Corr. Sc.* Vol. 32, 1991.

Stellingen

- 1) Wanddikteafname van oververhitters in kolengestookte ketels wordt te gemakkelijk geweten aan corrosie, veroorzaakt door ijzer-alkalie sulfaten. Het kan echter ook het gevolg zijn van erosie-corrosie, reducerende omstandigheden en/of abnormaal hoge temperaturen. De aanwezigheid van ijzer-alkalie sulfaten moet daarom positief vastgesteld worden, als bewijs dat corrosie de hoofdoorzaak is van de wanddikteafname.
- 2) Slijtage in kolenmolens is niet alleen afhankelijk van het Quartz- en Pyrietgehalte van de kool, maar ook van de korrelgrootte verdeling van beide mineralen.

R.T. Donais, A.L. Tyler, W.T. Bakker: p. 637 "Advances in Materials Technology for Fossil Power Plants", R. Visvanathan, R.I. Jaffee, eds, ASM, 1987

- 3) Als legeringselement in roestvast staal is silicium effectiever dan chromium of aluminium ter bestrijding van corrosie in kolenvergassers, omdat de reactieconstante (K_p) voor de oxidatie van silicium bij afnemende temperatuur minder snel daalt dan die van chromium of aluminium. De K_p voor de oxidatie van silicium is zelfs hoger dan die van chromium bij temperaturen onder 650°C.

N. Birk, G.H. Meier, p. 54 in "Introduction to High Temperature Oxidation of Metals", E. Arnold Ltd., Londen, 1983.

- 4) Het mechanisme van versnelde corrosie in syngaskoelers, ogenschijnlijk het resultaat van een combinatie van stilstandscorrosie en hoge temperatuur gas corrosie, is onvolledig opgehelderd en nog niet in een laboratorium gesimuleerd.

W.T. Bakker, J.B.M. Kip, H.P. Schmitz, "Materials testing in Syngas Coolers of Coal-Water Slurry Fed Gasifiers", Mats at High Temp., 1993, Vol. 11, p. 133.

- 5) Resultaten van kortdurige corrosieproeven op hoge temperatuur in gassen, bestaande uit meerdere oxiderende componenten, kunnen niet gebruikt worden om corrosiesnelheden op lagere temperaturen te voorspellen, vooral als deze proeven zijn uitgevoerd boven het eutectische smeltpunt van ijzer en nikkel sulfiden.
- 6) Moeilijkheden met materialen, inclusief corrosie, kunnen vaak gemakkelijker opgelost worden door ontwerpwijziging dan door het gebruik van betere (en duurder) materialen. Dit geldt vooral voor schade veroorzaakt door erosie.

- 7) KV-STEG centrales kunnen alleen een belangrijk onderdeel van de elektriciteitsvoorziening worden, als de investeringskosten daarvan op gelijk niveau liggen met die van moderne poederkoolgestookte centrales, omdat het onwaarschijnlijk is dat het publiek bereid is om meer voor elektriciteit te betalen ten behoeve van het milieu.
- 8) Herstructurering van bedrijven kan alleen maar met succes tot stand gebracht worden, als de bedrijfsleiding bereid is actief deel te nemen in het proces. Dit is echter zeldzaam.
- 9) De veronderstelling dat een hoog niveau van criminaliteit verlaagd kan worden door het inzetten van meer politie, is onjuist. Politieagenten besteden namelijk al een aanzienlijk gedeelte van hun tijd met het bekeuren van gewone burgers voor kleine verkeersovertredingen. Het is onwaarschijnlijk dat deze activiteit zal verminderen ten gunste van het vervolgen van gevaarlijke criminelen.
- 10) De beste manier om spuurwerk resultaten in de praktijk te brengen is het overplaatsen van personeel van fundamenteel naar toegepast onderzoek, om de nieuwe resultaten in de praktijk te brengen. Om deze reden moet de uitwisseling van wetenschappelijke medewerkers tussen universiteiten, researchinstututen en industrie aangemoedigd worden.

J.A. Armstrong, "Is basic Research a Luxury our Society can no longer Afford?" p. 117, Adv Mats Proc., Vol. 146 (5) , nov. 1994.

- 11) Het model van Roberson en Forrest betreffende de vorming van een niet beschermende, gelaagde corrosiehuud op koolstofstaal in chloridehoudend water verklaart het ontstaan van de gelamineerde microstructuur onvoldoende. Vooral het ontstaan van de sterk gelaagde corrosiehuud op staal met 0.5-2.0% chromium blijft een raadsel.

J. Robertson, J.E. Forrest, "Corrosion of Carbon Steels in High Temperature Acid Chloride Solutions" p. 521, Corr. Sc., Vol. 32, 1991. J.E. Forrest, J. Robertson, Corrosion of Cr Steels in High Temperature Acid Chloride Solutions, *ibid*, p. 541.